UNIVERSITY OF SOUTHAMPTON

Faculty of Natural & Environmental Sciences

School of Ocean and Earth Science

Seepage of Hydrocarbon Bearing Fluids at the Carlos Ribeiro and Darwin Mud Volcanoes (Gulf of Cadiz)

by

Heleen L.A.E. Vanneste

Thesis for the degree of Doctor of Philosophy

November 2010

UNIVERSITY OF SOUTHAMPTON

ABSTRACT

FACULTY OF NATURAL & ENVIRONMENTAL SCIENCES
SCHOOL OF OCEAN AND EARTH SCIENCES

Doctor of Philosophy

SEEPAGE OF HYDROCARBON BEARING FLUIDS AT THE CARLOS RIBEIRO AND DARWIN MUD VOLCANOES (GULF OF CADIZ)

Heleen L.A.E.Vanneste

Submarine mud volcanism is an important pathway for transfer of deep-sourced fluids enriched in hydrocarbons and other elements into the ocean. Mud volcanoes (MVs) occur in abundance on all oceanic plate margins, so fluxes of methane (CH_4) and other chemical constituents from mud volcanism are likely to be significant for the oceanic budgets of some elements. Here, I present a detailed study of the spatial and temporal variation in fluid and chemical fluxes and mud flow activity at the Carlos Ribeiro and the Darwin MVs in the Gulf of Cadiz. Analyses of the chemical composition of pore fluids, sediments and authigenic carbonates are combined with a 1-D transport-reaction pore fluid model. Pore fluids from both MVs contain high concentrations of hydrocarbons (up to 16 mM), while pore fluids from Carlos Ribeiro MV (CRMV) are also enriched in lithium (Li^+) and boron (B) but depleted in chloride relative to seawater. Oxygen, hydrogen and strontium isotope data suggest that the pore fluids are derived from depth and are affected by the transformation of smectite to illite. This process also produces pore fluids that are depleted in chloride and potassium, while B and Li^+ appear to be leached from the sediments during this transformation process. The CRMV is the most active of the two MVs: fluid flow velocities are as high as 4 cm yr^{-1} at the eye of the MV but rapidly decrease to 0.4 cm yr^{-1} at the periphery. The associated fluxes of B, Li^+ and CH_4 are 7-301, 0.5-6 and 0-806 mmol m^{-2} yr^{-1}, respectively. Fluid flow velocities at the Darwin MV are lower, ∼0.09 cm yr^{-1}, and show little spatial variation: seepage activity appears to be controlled by the distribution of slabs of authigenic carbonate that are found on the seafloor at the summit of the MV. Results of radiocarbon dating of the hemipelagic sediments covering the CRMV suggest that there has been recent mudflow activity at the eye of the MV, and frequent mud expulsions over the past ∼1000 Cal yrs BP. The distribution of barite fronts at the margin of the MV and within the mudflow to the SE of the summit suggests that fluid advection has ceased over the past 340 Cal yrs, but degassing of these mudflows is ongoing and is potentially an important source of CH_4. Geochemical and petrographic analyses of carbonates from the Darwin MV suggest that the MV formed in stages, with periods of intense fluid flow alternating with phases of mud extrusion and tectonic uplift. The results of this study demonstrate that fluid (and chemical) fluxes from MVs vary over relatively small time and space scales and that mud volcanism may contribute significantly to the oceanic inventories of Li^+ and B. Moreover, anaerobic oxidation of methane appears to be an important control on methane emissions into the overlying water column, and a better understanding of this process is urgently required to properly quantify the impact of mud volcanism on the global oceanic methane budget.

Contents

List of Figures

List of Tables

declaration of authorship

I, Heleen L.A.E. Vanneste, declare that the thesis entitled **Seepage of Hydrocarbon Bearing Fluids at the Carlos Ribeiro and Darwin Mud Volcanoes (Gulf of Cadiz)** and the work presented in the thesis are both my own, and have been generated by me as the result of my own original research. I confirm that:

- this work was done wholly or mainly while in candidature for a research degree at this University;
- where any part of this thesis has previously been submitted for a degree or any other qualification at this University or any other institution, this has been clearly stated;
- where I have consulted the published work of others, this is always clearly attributed;
- where I have quoted from the work of others, the source is always given. With the exception of such quotations, this thesis is entirely my own work;
- I have acknowledged all main sources of help;
- where the thesis is based on work done by myself jointly with others, I have made clear exactly what was done by others and what I have contributed myself;
- parts of this work has been published as: **Vanneste, H.**, Kelly-Gerreyn, B. A., Connelly, D. P., James, R.H., Haeckel, M., Fisher, R. E., Heeschen, K., Mills, R. A. 2011. Spatial variation in fluid flow and geochemical fluxes across the sediment-seawater interface at the Carlos Ribeiro mud volcano (Gulf of Cadiz). Geochimica et Cosmochimica Acta 75, 1124 - 1144 (doi:10.1016/j.gca.2010.11.017).

Signed: .....

Date: .....

Acknowledgements

This PhD has been a long and adventurous journey and I would not have been able to finish it successfully without the support and contributions of a number of people whom I would like to thank.

First of all, to my supervisors, Rachael James, Rachel Mills and Boris Kelly-Gerreyn as well as the GG group, for giving me the opportunity to do this PhD and for their support during the course of my PhD. In particular Rachael for doing an excellent job in taking over the main supervising job half way through my PhD. Although maybe not registered as an official supervisor this thesis would not have been what it is without the contributions of Matthias Haeckel who initiated me into the world of seeps and mud volcanoes and taught me numerical modelling. Thank you very much for the good guidance when I was in Kiel and for answering all my questions by e-mail so quickly once back in Southampton. Many thanks to Doug Connelly for supporting me in the good and the bad times, the quick chats and for helping out with the methane analyses.

I am also really thankful to the World Universities Network which gave me this fantastic opportunity to go overseas and work for two months with experts in my field at Scripps Institution of Oceanography. Miriam Kastner was a very enthusiastic and generous host during my stay at SIO and made me feel at home in no time. Thank you for the many scientific and non-scientific discussions which gave me inspiration and a real boost to keep on going. Thanks to Gustaf Arrhenius for letting me use his XRD lab and teaching me the principles of X-ray diffraction.

Then there are a couple of people I would like to thank for their helping hand with the many analyses. They are Darryl Green, Belinda Alker, Andy Milton, Matthew Cooper and Richard Pearce all based at NOCS. Thanks to Gretchen Robertson and Saul Perez-Montano for guiding me in the SIO labs. This PhD also benefited from conversations with Phil Weaver, Damon Teagle and Guy Rothwell.

I was very lucky to be part of the HERMES project through which I met a lot of nice people: thank you Lois for the microbiological talks and Carolina for having been a short but lovely office mate. And then last but not least to all my friends in Southampton and Belgium for all the fun times, long talks, laughs, trips to the south coast, enjoyable

lunches, delicious dinners, walks in the New Forest, giving me a shoulder to lean on when necessary, many skype hours,.. AND my family for supporting me all the way through.

Definitions and abbreviations

AI	North Atlantic inflow water
ANME	anaerobic methanotrophic archaea
AOM	anaerobic oxidation of methane
AS	Alboran Sea
BSR	bottom simulating reflector
CAMV	Captain Arutyunov mud volcano
CRMV	Carlos Ribeiro mud volcano
DPMV	Deep Portuguese Margin mud volcano Field
GHSZ	gas hydrate stability zone
GC	Gulf of Cadiz
MAR	Mid-Atlantic Ridge
ML	Mediterranean Lower Water
MOW	Mediterranean Outflow Water
MV(s)	mud volcano(es)
MU	Mediterranean Upper Water
NACW	North Atlantic Central Water
NADW	North Atlantic Deep Water
NASW	North Atlantic Surface Water
ODE	ordinary differential equation
ROV	Remotely operated vehicle
SMTZ	sulphate methane transition zone
SRB	sulphate reducing bacteria
TA	total alkalinity

It is not a pleasant idea, - that of a sluggish torrent of exceedingly dirty water, or thin paste, issuing from a crack in the earth, and gradually building up a conical hill of mud of a dirty black color, cracked all over when dry, and too slimy to give foothold while moist. There is in it none of the dignity of danger, none of the grandeur that belongs to a sudden outburst of smoke accompanied by the roaring of subterranean artillery, a "mitraill" of red-hot stones, and a current of white-hot lava threatening to destroy a town some twenty miles distant. A mud volcano is decidedly tame and repulsive compared to a volcano of the ordinary kind. And yet a real honest eruption of a mud volcano, and the result seen in a large district where such phenomena have been frequent, and have lasted a long while, is an event worth recording, and not without a good deal of interest of its own.

Every Saturday: A Journal of Choice Reading, selected from foreign current literature.
Vol I Saturday, June 16, 1866.

Chapter 1

Introduction

Mud volcanoes have been described from all over the world, both on land and offshore, and are one of the most dynamic and unstable sedimentary structures known to exist on our Earth. A total number of MVs has been estimated to be approximately 6500 of which 5500 occur offshore (Dimitrov, 2002; Judd and Hovland, 2007; Milkov, 2000; Milkov et al., 2003). The first scientific reports on mud or "dirt" volcanoes go back to the 19th century; they were considered a variety of magmatic volcanoes (Kholodov, 2002b and references therein). Since they harbour a unique ecosystem, are of interest for hydrocarbon exploration and are a potential hazard for humans, MVs are still intensively studied at the present day. Furthermore, their popularity might increase in the future as there are recent indications for the presence of MVs on Mars (e.g. Oehler and Allen, 2010; Skinner and Tanaka, 2007).

1.1 Mud volcanism

1.1.1 What are mud volcanoes?

Mud volcanoes (MVs) are sedimentary structures constructed mainly of mud which periodically or continuously vent a mixture of mud, element-enriched fluids, oil and hydrocarbon gases, especially methane, originating from over-pressured sediment layers in the subsurface (Hedberg, 1974; Higgins and Saunders, 1974; Kugler, 1933). The semi-fluidized extruded material is called mud breccia which is for 99% composed of a mud matrix containing a variable amount of chaotically distributed angular to rounded rock clasts (Dimitrov, 2002). The clasts range in size from 1 mm to 10 m and more, and their lithology reflects the stratigraphical horizons the mud has passed through during its way up to the surface. The mud breccia is generally extruded from a central vent called the feeder channel or conduit forming mudflows up to several hundred meters wide and kilometres long (Fig. 1.1). These mudflows accumulate as wedge-shaped deposits, thinning away from the crater (i.e. the area where the conduit crops out at the surface) and thus build up the main body of the MV. The summit crater of the MV may be a flat or bulging plat-

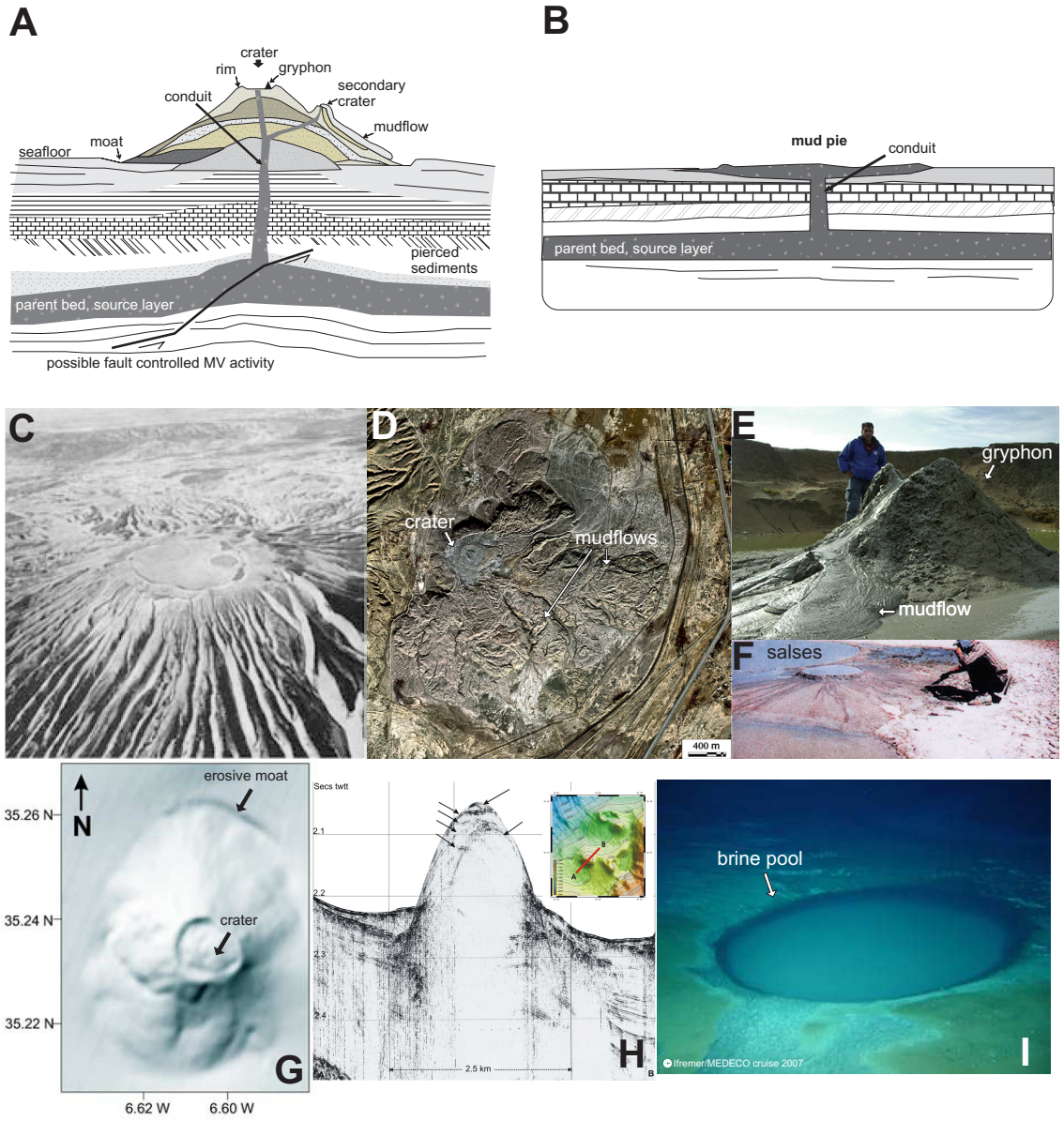

Figure 1.1 **A** Schematic cross-section of a conical mud volcano illustrating the basic structure and main elements, modified after Dimitrov (2002) and Kopf (2002). **B** Schematic cross-section of a mud pie illustrating the basic structure, modified after Kopf (2002). Land mud volcanoes: **C** Air photo of the cone shaped Touragay MV, Azerbaijan (Huseynov and Guliyev, 2004). **D** Satellite image of the mud pie Dashgil MV, Azerbaijan (Mazzini et al., 2009). **E** Picture of a small gryphon in the crater of Dashgil MV erupting mud (Mazzini et al., 2009). **F** Picture of salses lakes in the Bulganak MV, Ukraine (Dimitrov, 2002). Submarine mud volcanoes: **G** Shaded relief map of the cone shaped Al Idrissi MV, Gulf of Cadiz (Van Rensbergen et al., 2005a). **H** Seismic profile of the Kula MV, eastern Mediterranean Sea. Arrows indicate buried MVs or eruption centres (Lykousis et al., 2009). **I** Brine pool on the summit of the Napoli MV, eastern Mediterranean Sea (Vanreusel et al., 2009).

eau as well as a depression, called caldera, surrounded by a rim (i.e. a topographical high, Kopf, 2002). The latter forms as the result of either an explosive eruption or a summit collapse (e.g. Evans et al., 2008). On land, these may partly fill with water forming pools called salses (Fig. 1.1F) while offshore summit craters may be occupied by brine pools (Fig. 1.1I). Large MVs can have several active vents around the crater or on the flank, each surrounded by a small cone or 'gryphon' (Fig. 1.1E). A moat may occur at the base of the MV. There are two basic MV morphologies. The first is the 'classic' MV which resembles that of magmatic volcanoes: conical hills with a summit crater (Fig. 1.1A, C and G), and the second are flat shaped MVs with a slope angle of less than 5°, called mud pies (Fig. 1.1B, D and B; Le Pichon et al., 1990). Nevertheless MVs of various shapes and sizes have been described both controlled by the mud breccia properties (e.g. viscosity, density, grain size), nature and frequency of the extrusions (fast, slow, explosive) as well as the volumes of sediments and fluids produced and the width of the conduit (Dimitrov, 2002; Kopf and Behrmann, 2000; Shih, 1967). Generally, the more frequent the activity, the larger the structures; the lower the viscosity the larger and flatter the body (Lance et al., 1998); the larger the amount of lithified clasts within the mud breccia the higher the MV (Huguen, 1998). MVs vary in size with a crater of a few centimetres to several kilometers in width and a base of maximum 4-5 km across (e.g. Al Idrissi MV in the Gulf of Cadiz, Fig. 1.1G; Van Rensbergen et al., 2005a). MVs up to 500 m high have been observed in Azerbaijan (e.g. Touragay MV, Fig. 1.1C; Jakubov et al., 1971).

1.1.2 Worldwide distribution

Mud volcanoes are mainly clustered in tectonically active areas which coincide with convergent and transform plate boundaries (Fig. 1.2). The highest number of onshore MVs is situated along the Alpine-Himalayan collision belt including the largest land MVs in the world in Azerbaijan (Aliyev et al., 2002). Submarine MVs have been intensively studied from active convergent margins such as at the Nankai Trough (Kobayashi et al., 1992), Eastern Mediterranean Ridge (Cifci et al., 1997), the Barbados (Henry et al., 1996) and Costa Rica (Hensen et al., 2004; Zuleger et al., 1996) margins, where tectonic plates move towards one another, resulting in subduction of one of the plates (1.2B). During this process the subducting plate scrapes its sediment burden against the overlying plate to form a compressed wedge of sediments or accretionary prism, over the subduction zone. However several MV fields have also been reported at passive margins including the Gulf of Mexico (Macdonald et al., 1994), the Norwegian shelf (Ginsburg et al., 1999) and the Niger Delta (Graue, 2000) where the MVs are mostly associated with rapidly accumulating sediments. Accordingly the occurrence of MVs seems to be controlled by recent tectonic activity, particularly compressional forces, sedimentary or tectonic loading and active hydrocarbon generation (Dimitrov, 2002). From hereon the focus will be on the submarine MVs as they are the subject of this study.

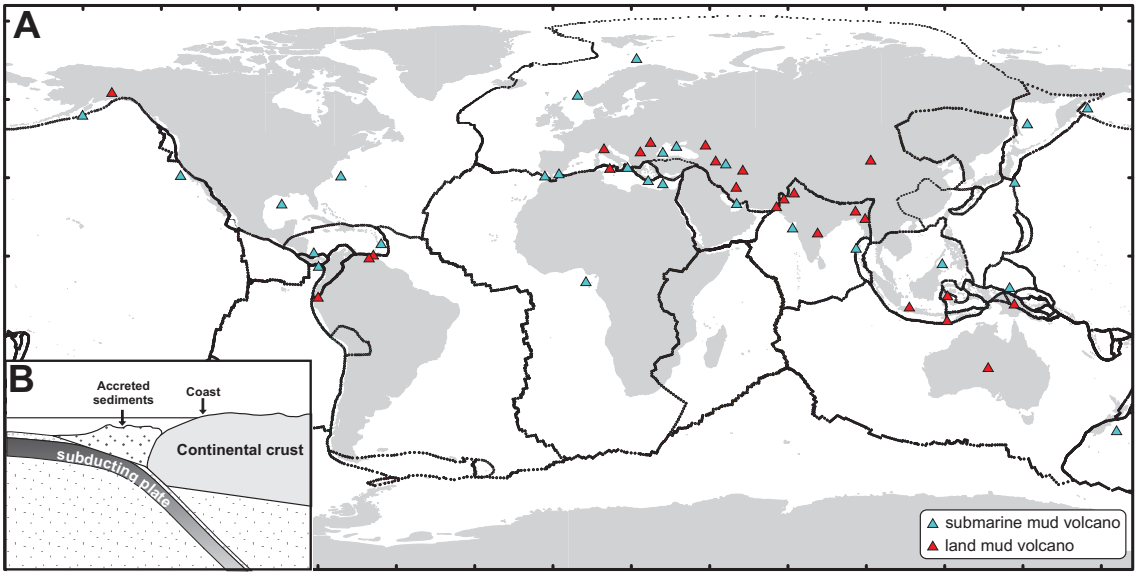

Figure 1.2 **A** Global distribution of land and submarine mud volcanoes, modified from Kopf (2002) and Milkov (2000). Black lines represent present plate boundaries on the Earth from Bird (2003). **B** A schematic structural section across a convergent margin.

1.1.3 Driving forces of mud volcanism

As a result of many detailed studies on MVs there is now a consensus on the main driving forces of mud volcanism (e.g. Brown, 1990; Hedberg, 1974; Kholodov, 2002a; Kopf, 2002; Mazzini, 2009; Mazzini et al., 2009; Medialdea et al., 2009; Van Rensbergen et al., 1999; Yassir, 2003). The ascent of mud and fluids to the surface during mud volcanism, is thought to be the result of buoyancy forces and/or pore fluid overpressure. The former is a function of bulk density contrast (Brown, 1990): layers composed of minerals with a low grain density such as halite (ρ_{grain}= 2.16-.217 g cm^{-3}) and gypsum (ρ_{grain}=2.30-2.37 g cm^{-3}) will rise when overlain by general marine sediments composed of quartz (ρ_{grain}= 2.65 g cm^{-3}) and feldspar (ρ_{grain}= 2.55-2.76 g cm^{-3}; Deer et al., 1992). In addition marine sediments that retained their fluid content because of fast burial (and thus are underconsolidated) or in which fluids are accumulated such as in certain clays (e.g. smectites), have often a low bulk density compared to overlying 'normally consolidated' sediments (Fitts and Brown, 1999).

Pore fluid overpressure occurs when the interstitial fluid pressure exceeds hydrostatic pressure. The involved mechanisms can be grouped into two categories: (1) reduction of the pore space and (2) increase of fluid volume in the pore space. Forces of mechanical and/or chemical nature such as consolidation, gas hydrate formation (creating a seal; Reed et al., 1990) and secondary precipitation of cementing materials can reduce the pore space. On deposition, sediments may have porosities as high as 70-80% (Brown, 1994). As they are buried effective stresses increase and consolidation commonly reduces porosities to below 30-40% at a few km depth (Bray and Karig, 1985). This reduction of pore volume is

accompanied by the movement of fluids out of the porous sediment. Where sedimentary sequences contain units with low permeabilities (e.g. muds), fluid expulsion can be retarded leading to the development of excess pore pressures (von Huene and Lee, 1983). Generally, significant overpressuring is associated with thick mud-rich sequences and rapid burial by sedimentary (e.g. high sediment accumulation rates at passive margins) and/or tectonic processes (e.g. overriding thrust sheets, accreting and folding at active margins; Brown, 1994). Mechanical processes such as consolidation can only reduce the intergranular porosity to a certain level while pressure solution and cementation of minerals such as carbonates can result in the almost total destruction of the pore volume, reducing it from 20-40% at a few km depths to below 1-2% by the time sediments reach metamorphic depths (Brown, 1994). On the other hand chemical reactions related to diagenesis and methamorphism may release significant quantities of fluid and gas which can lead to overpressuring in low permeability formations. Mineral dehydration reactions (Kastner, 1981; Kastner et al., 1991) in particular the smectite to illite transformation releases large amounts of freshwater (Brown et al., 2001; Spinelli and Underwood, 2004). Biogenic and/or thermogenic decomposition of organic matter results in the formation of methane which may take in a significant amount of volume when it occurs as a free gas, e.g. during the decompression of a rising mud layer (Brown, 1990; Hedberg, 1974; Hovland and Judd, 1988). Nevertheless, its low density will increase pore fluid pressures either way in the dissolved or gaseous phase (e.g. Kopf, 2002). Accordingly buoyancy forces and overpressure are unanimously related to one another.

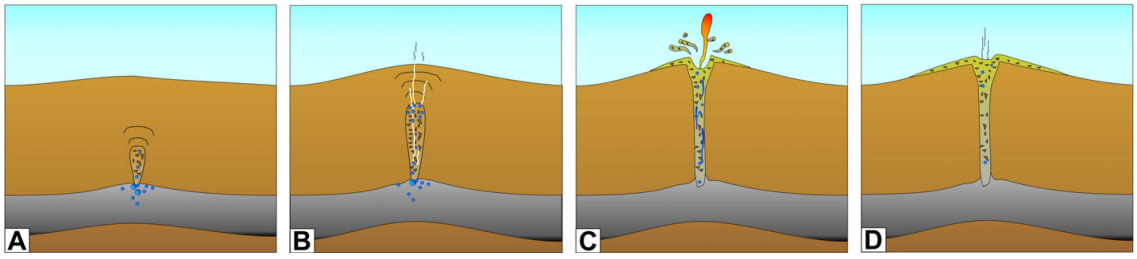

Figure 1.3 Sketch of growth stages of a mud volcano from its initial subsurface formation to final manifestation on the surface with eruption of mud breccia, gas and fluids after Mazzini (2009). **A** Fluid overpressure in impermeable sediments, diapiric structure formation and brecciation during diapiric growth. **B** Overpressured diapir reaches critical depth. Overburden cannot hold down the gas saturated diapir. **C** Blast of gas. The sudden pressure release allows large amounts of fluidized and gas saturated sediments to reach the surface. **D** Fluid-rich mud eruption following the initial blast. Slow seepage continues even during dormant period releasing remaining fluids.

The following MV formation mechanism has been put forward by Mazzini (2009) based on what is known about MVs so far (Fig. 1.3). At those sites where excess pore pressure occurs at depth, fluids intend to migrate along morphological discontinuities and geological structures such as fault planes, anticline axes and preexisting deformations. Simultaneously, the overpressure leads to the formation of a diapir-shaped feature of brecciated sedimentary units in the subsurface. Once fluid migration and diapirism has been initi-

ated, it is likely to be partly self-sustained by buoyancy and by the constantly increasing volume of fluids at shallower depth. Subsequently, when the over-pressured diapir reaches a critical depth, i.e. where the overpressure exceeds the sedimentary load, the overlying unit will fracture and breach. This results in a pressure drop facilitating the brecciated sediments with a reduced cohesion, to fluidize and flow to the surface. Seismic activity such as earthquakes, likely facilitates the break through of the diapir.

1.1.4 Life cycle of mud volcanoes

Once a mud volcano is formed its activity does not stay constant over time. Mud volcanoes have a life cycle as do their magmatic equivalents. The perception of present-day activity of MVs depends on whether fluid, gas or mud expulsion is considered. Accordingly MVs are categorised as being active, dormant or extinct depending on whether recent mud eruptions, only fluid and gas seepage or no seepage at all, have respectively been observed. Several techniques have been used to assess the temporal variability of mud volcanism. The most straight forward indicator of activity is the presence or absence of a hemipelagic veneer on top of the MV (e.g. Van Rensbergen et al., 2005b), whereas seismic profiles can provide information on eruption frequency. The latter can be quantified by AMS radiocarbon dating of shells from seep fauna (e.g. mussels; MacDonald and Peccini, 2009) and/or relative chronology of interbedded pelagic sediments (e.g. Lykousis et al., 2009). Variability in gas and fluid seepage is far more difficult to assess. Fluid expulsion rates are commonly estimated by applying transport-reaction models to pore water concentration profiles of conservative chemical constituents (e.g. chloride) and/or temperature data (Feseker et al., 2008; Haese et al., 2006; Wallmann et al., 2006b). Remotely operated vehicle (ROV) technology improved in situ observations and consequently the measurement of the volume and rate of fluid and gas seepage at present (de Beer et al., 2006; Lichtschlag et al., 2010; Sahling et al., 2009). Authigenic products such as carbonates and barite fronts have only been used to a limited extent to assess past hydrocarbon outflow at cold seep sites (e.g. Dickens, 2001). Unfortunately, all of these techniques are flawed, e.g. seismic profiles often have a limited resolution and/or range because of the presence of free gas causing acoustic blanking, making the identification of multiple mud expulsion events and minor extrusion events difficult to detect. In addition, mud flows often exceed the vertical sediment core dimensions and radiocarbon dating of carbonate shells is problematic due to contamination of 'dead' carbon from reservoir sources as well as seawater carbon (Aharon et al., 1997). Accordingly, data on the extent, frequency and timing of seepage and mud eruptions for submarine MVs is still limited.

1.1.5 Global significance and interest

The interest for studying mud volcanism is high and comes from a range of disciplines. First of all mud volcano gases are generally dominated by methane, an important 'green-

house' gas. A large number of MVs, offshore and onshore, are known to date and thus their emissions may contribute significantly to the global atmospheric greenhouse gas budget (e.g. Dimitrov, 2003; Sauter et al., 2006). The flow of methane and other reduced compounds (e.g. H_2S) at MVs fuel highly productive and specialised ecosystems containing organisms with unique functions that range in size from bacteria to fish. As the composition of MV communities varies from MV to MV, even within a single region (e.g. in the Gulf of Cadiz), the link between MV environments and these chemosynthetic ecosystems, clearly needs to be better understood. Particularly in a changing ocean if we are to be able to distinguish between natural and anthropogenic effects (Vanreusel et al., 2009). Furthermore, the spasmodic violent eruptions of MVs have proven to be hazardous to seafloor pipelines, cabling and, in coastal areas, they can threaten human lives. The latter was most recently demonstrated in East Java where the MV called 'LUSI', started to form on the 29th May 2006 displacing more than 30 000 people (e.g. Davies et al., 2008). Since MVs are closely associated with petroleum reservoirs, they are of interest for hydrocarbon exploration. Also gas hydrates are frequently observed at MVs which are likely to be exploited in the future (Mazzini et al., 2009). However the occurrence of high pressure at depth creates difficulties for exploration and production drilling through which there is a demand from the industry for a better understanding of the possible triggers and causes that lead to mud volcano eruptions.

1.2 Methane dynamics at cold seeps

Hydrocarbon in particular methane seepage, is unanimously related to mud volcanism and a major point of interest. Therefore an introduction is given in this section on the methane cycle in marine sediments from its production to the major processes on its pathway to the seafloor.

1.2.1 Methane production

Methane is largely formed by the digestion of organic compounds by microorganisms (microbial origin) and the thermal decomposition of organic matter (thermogenic origin). Bacterial methane production (= methanogenesis) occurs in anoxic sediments by anaerobic archaea, also known as methanogens. As these bacteria are generally outcompeted by sulphate reducers in their hunt for nutrients, methane is only formed when sulphate is nearly exhausted (Van Der Weijden et al., 1992). Methanogenesis follows two main pathways acetate fermentation (Eqn. 1.1) and CO_2 reduction (Eqn. 1.2; Jenden and Kaplan, 1986; Schoell, 1980, 1988; Woltemate et al., 1984).

$$CH_3COOH \rightarrow CH_4 + CO_2 \tag{1.1}$$

$$4H_2 + CO_2 \rightarrow CH_4 + CO_2 \tag{1.2}$$

The former predominates in very young, recently deposited marine sediments (Coleman et al., 1988; Jenden and Kaplan, 1986) while the latter is thought to represent the trapped gases in deeper strata (Schoell, 1988). Organic matter that survives microbial degradation in the early phase of diagenesis evolves in the formation of kerogen. Eventually with increasing burial depth, higher temperatures cause the thermal degradation of kerogen resulting in the formation of petroleum and natural gas (Hunt, 1996). The carbon and hydrogen isotopic composition of methane is generally used to discriminate between methane of different origins. This is demonstrated in Fig. 1.4 after Whiticar (1999).

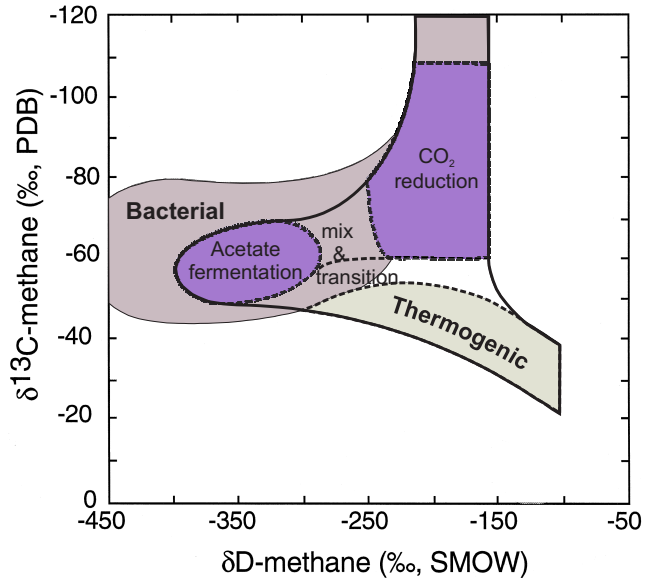

Figure 1.4 The use of carbon and hydrogen isotopes to discriminate between methane of different origins after Whiticar (1999).

1.2.2 Upward methane migration through the sediment column

The produced methane at depth is transported to the seafloor as a free gas phase (bubbles) and/or dissolved in the pore fluid depending on methane saturation. Methane saturation is a property of the fluid related to the relative amount of dissolved methane (Clennell et al., 2000). A fluid is saturated when it holds the maximum amount of methane in solution under the given conditions which is determined by methane solubility. The latter is a function of pressure, temperature and brine composition and thus varies from site to site (Duan et al., 1992). Under high pressure and temperature e.g. at great depths, methane generally occurs in solution while free gas bubbles may form when fluids migrate to the surface when the methane saturation of the pore fluid is exceeded because of the pressure and temperature drop. Both phases are buoyant and thus tend to migrate to the surface (Clennell et al., 2000; Park et al., 1990). Since the low solubility of methane in water, the migration of dissolved methane via advection and diffusion is very inefficient unless cracks, fractures or high permeable layers are present to increase the fluid flow rates.

Methane transport in the free gas phase on the other hand is far more efficient because of its strong buoyancy: free methane has even beneath 3-4 km of water a density of only 0.2-0.3 g cm^{-3} compared with 1.024 g cm^{-3} for seawater (Clennell et al., 2000). However, besides the methane saturation level, the occurrence of methane gas is also defined by the size of the sediment pore space and the elastic and fracture properties of the sediment which influence the nucleation and growth of gas bubbles (Boudreau et al., 2005; Clennell et al., 2000). Fine grained sediments such as clays hamper gas bubble formation because of an increased capillary pressure (Claypool, 1996). This property may partly explain why sometimes a stream of free gas bubbles is only seen at cold seeps when the sediment is disturbed by sampling activity.

1.2.3 Hydrate formation

Where environmental conditions allow, methane can also occur in marine sediments in a solid phase, i.e. as gas hydrates (Fig. 1.5). These are crystalline, ice-like solid compounds where water molecules form cage-like structures (= clathrates) in which low molecular weight gases (e.g. CO_2, H_2S and CH_4) are enclosed as guest molecules (Sloan, 1998). The presence of gas hydrates is mainly controlled by the temperature and pressure conditions of the environment, ionic strength of the water (de Roo et al., 1983) and the abundance and composition of gas (Sloan, 1998). The stability field of gas hydrates in marine sediments is illustrated on Fig. 1.5B. Thermodynamic conditions for hydrate stability are satisfied throughout most of the world's oceans, bottom water temperatures are generally $< 10°C$ in depths of more than 500 m and the geothermal gradient (i.e. the rate of temperature rise beneath the seabed because of the heat emanating from deep within the earth) is most commonly about 30 °C km^{-1}. Accordingly, the availability of methane is generally the most limiting factor because of the low concentration of organic matter in pelagic sediments. However, where the methane supply is abundant e.g. at mud volcanoes, the geothermal gradient and pore water salinity seem to determine the gas hydrate stability zone (Egorov et al., 1999; Feseker et al., 2009; Haeckel et al., 2007).
Although biogenic methane is thought to be the dominant methane source for gas hydrates (Kvenvolden, 1995), methane of thermogenic and/or mixed origin has been observed at several continental margins such as in the Gulf of Cadiz (Stadnitskaia et al., 2006), Gulf of Mexico (Brooks et al., 1984) and Hydrate Ridge (Milkov et al., 2005). An alternative supply of methane is the recycling of methane gas at the base of the gas hydrate stability zone (GHSZ). It has been cited as an important process to concentrate gas hydrates in areas where not sufficient labile organic matter is deposited to produce an appreciable quantity of methane hydrates by in situ biogenic production, (Kvenvolden and Barnard, 1983; Paull et al., 1994). This 'recycled' methane is released by the dissociation of deep-seated hydrates as a result of progressive burial and subsidence of the sediment column. Both the formation and the dissociation of gas hydrates are believed to play a role in the mechanism of mud volcanism. Hydrates are lighter than water and therefore thick layers

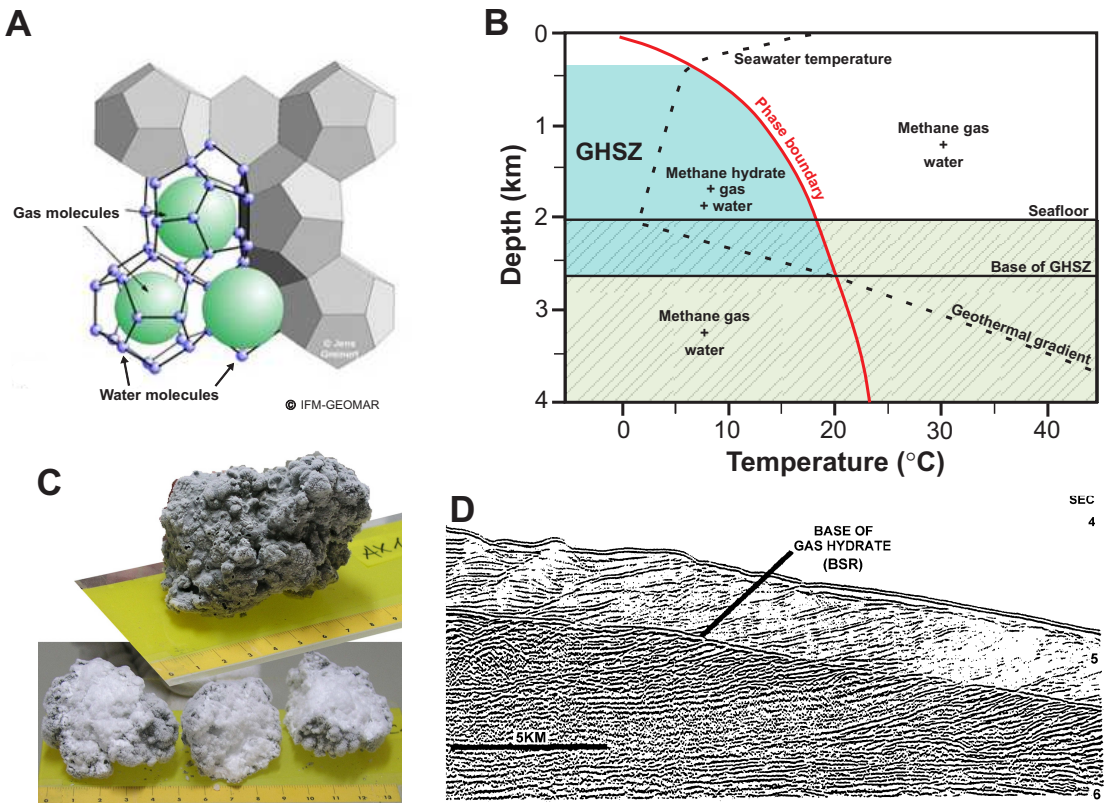

Figure 1.5 **A** Schematic diagram of gas hydrate crystal structure I. **B** Stability field of methane hydrates at normal seawater salinity within the water column and sediments. Intersections of the temperature profiles (dashed line) with the phase boundary define the area of the gas hydrate stability zone (GHSZ), modified from Bohrmann and Torres (2006). **C** Gas hydrate lump (top) and broken into pieces (bottom) recovered from the Amsterdam MV, eastern Mediterranean Sea (Lykousis et al., 2009). **D** Multichannel seismic profile from the crest and the eastern flank of Blake Ridge showing a strong bottom-simulating reflector (BSR) caused by the presence of gas hydrates (Hesse, 2003).

may be gravitationally unstable and as well form a seal within the sediment column and cause overpressure at depth. During gas hydrate dissociation large volumes of freshwater and methane gas are released and thus may lead to overpressure.

For a long time the presence of bottom-simulating reflectors (BSRs) on seismic profiles, have been used as evidence for the occurrence of gas hydrates (Fig. 1.5D). The BSR is believed to develop at the hydrate base as a consequence of the acoustic contrast between relatively high-velocity gas hydrate-charged sediments above low-velocity gas-rich sediments (e.g. Paull and Dillon, 2001). However ODP results indicate that this is not always the case, gas hydrates were found where there was no BSR and vice versa (Paull, 1997). Accordingly the complete relationship between BSRs and gas hydrates remains unknown. Other methods used to assess the presence of hydrates are sampling by means of coring, analysing pore fluids for chloride (Cl) concentrations and their oxygen ($^{18}O/^{16}O$) and hydrogen (D/H) isotopic composition as well as temperature measurements (e.g. Hesse, 2003; Kvenvolden and Kastner, 1990). During gas hydrate formation, dissolved ions (e.g.

sodium and chloride) are excluded from the crystal structure while the isotopically heavier water molecules (^{18}O and D) are preferentially incorporated into the gas hydrate (Hesse and Harrison, 1981; Ussler and Paull, 1995). Consequently, water in the residual pore fluid becomes enriched in Cl and enriched in ^{16}O and H during gas hydrate growth whereas the dissociation of gas hydrates e.g. during core retrieval, results in the release of freshwater enriched in ^{18}O and deuterium. Hence the recovered pore waters will be diluted and have a more positive oxygen and hydrogen isotopic signature compared to seawater. In addition hydrate melting is an endothermic reaction lowering the temperature down to 0°C and less. Visual recognition can be very difficult as for example in fine-grained sediment the hydrates often occur as highly dispersed small crystals which do not survive core retrieval (e.g. Hesse, 2003).

1.2.4 Methane consumption

Even before the methane-rich fluids can reach the seafloor, the majority of the methane is consumed by the anaerobic oxidation of methane (AOM; Reeburgh, 2007) performed by a consortium of methanotrophic archaea (ANME) and sulphate-reducing bacteria (SRB) (Boetius et al., 2000) according to the following net reaction (Reeburgh, 1976):

$$CH_4 + SO_4^{2-} \rightarrow HCO_3^- + HS^- + H_20 \tag{1.3}$$

AOM takes place in a strictly anoxic zone referred to as the sulphate-methane transition zone (SMTZ; Reeburgh, 1976), i.e. where the methane-charged fluids from below meet the sulphate rich pore waters from above (Fig. 1.6). Depending on the burial rate of reactive organic matter, the depth of methane production, the transport velocity of methane and sulphate and their consumption rates, the SMTZ may be found at decimetres to tens of meters below the seafloor (Knittel and Boetius, 2009). The SMTZ in mud volcanoes, which are characterised by high advective transport, is generally localised at the seafloor down to 50 cm depth (de Beer et al., 2006). Three groups of archaea have been identified to date: ANME-1 (Hinrichs et al., 1999), ANME-2 (Boetius et al., 2000; Orphan et al., 2001), and ANME-3 (Knittel et al., 2005). Within cold seep environments, ANME-2 and ANME-3 are most frequently observed in near-surface sediments (e.g. Håkon Mosby MV, Niemann et al., 2006b) whereas ANME-1 is known to dominate in only two seep systems, i.e. in the Gulf of Mexico (Lloyd et al., 2006) and in the Black Sea (Knittel and Boetius, 2009; Knittel et al., 2005). Although subgroups of ANME-2 seem to have preferences for either *Beggiatoa* (ANME-2a) or *Calyptogena* (ANME-2c) fields (Knittel et al., 2005) (see below), there is still no consensus at the present-day on whether different archaea groups can be associated with different environmental conditions, e.g. the size of the methane flux from depth.

As AOM leads to a significant increase of inorganic carbon, alkalinity and reduced sulphur in the pore waters, it has an important impact on the chemistry of the environment and

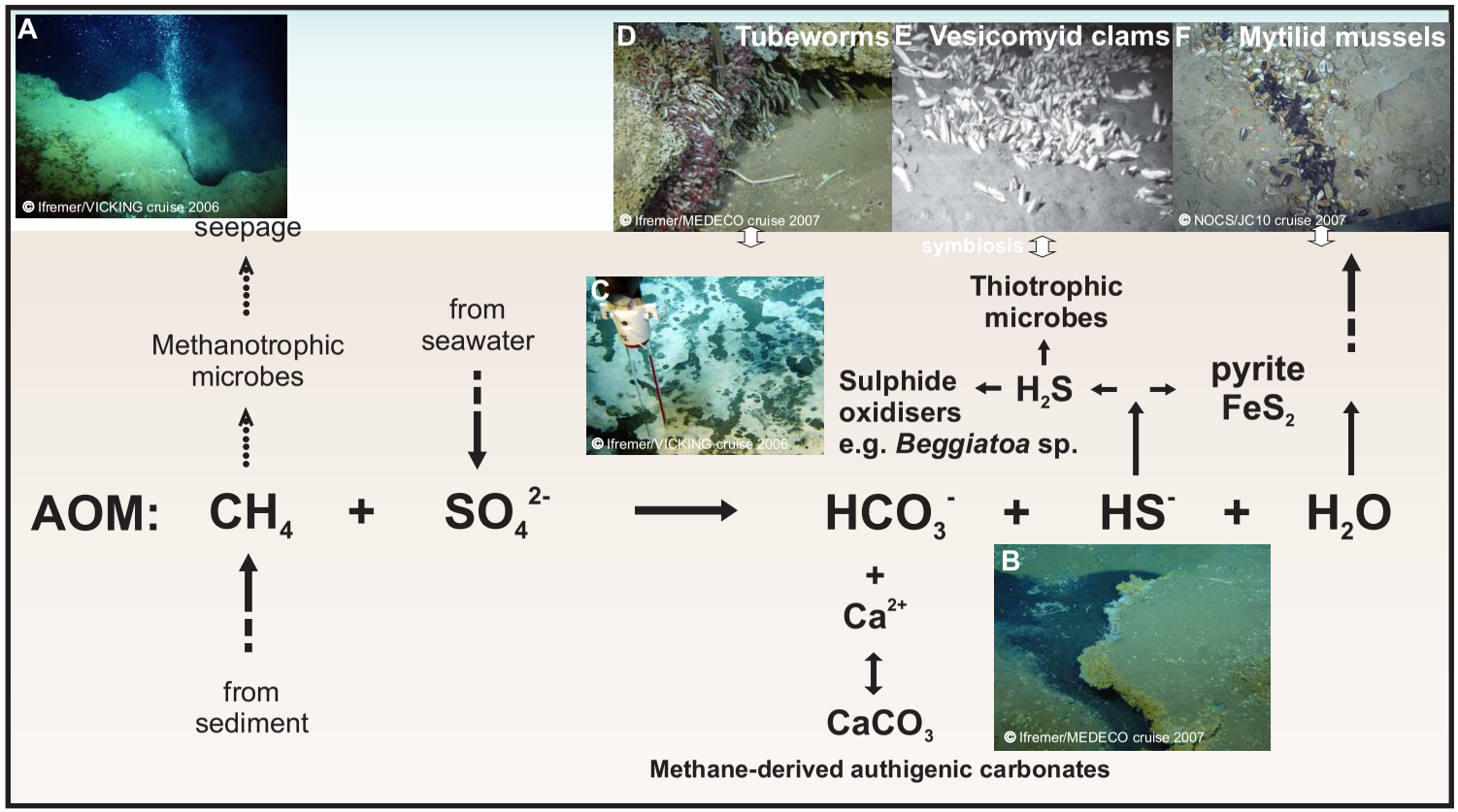

Figure 1.6 Anaerobic oxidation of methane: reactants (methane and sulphate), products (hydrogen carbonate, hydrogen sulphide ion and water) and by−products (pyrite and methane-derived authigenic carbonates). Excess methane is available for utilisation by methanotrophs (free-living and symbiotic) and any remaining methane seeps at the seafloor. Hydrogen sulphide (derived from HS^{-}) is available for utilisation by thiotrophic microbes: free-living e.g. *Beggiatoa* sp. and in symbioses e.g. tubeworms, vesicomyid clams and mytilid mussels. **A** String of free hydrate-coated methane bubbles rising from a seabed fissure at the surface of the Håkon Mosby MV, Norwegian Shelf (Foucher et al., 2009). **B** Carbonate crusts surrounded by black coloured reduced sediments at the Napoli MV, eastern Mediterranean Sea. **C** White thick bacterial mats surrounding the centre of the Håkon Mosby MV, Norwegian Shelf (Vanreusel et al., 2009). **D** Tubeworms (*Lamellibrachia*) in the pockmark area in the Nile Deep Sea Fan. **E** Vesicomyid clams (*Calyptogena phaseoliformis*) at the Kodiak Seep, Gulf of Alaska (Levin, 2005). **F** Mytilid mussels (*Bathymodiolus mauritanicus*) at the Darwin MV, Gulf of Cadiz (Vanreusel et al., 2009).

likewise provides the energy for distinct chemosynthetic communities (Fig. 1.6; Levin, 2005; Sibuet and Olu, 1998). The most characteristic and commonly observed seep biota include bacterial mats, siboglinids or tubeworms, mytilid mussels from the genus *Bathymodiolus* and vesicomyid clams (including *Calyptogena*). The bacterial mats consist of sulphide-oxidizing bacteria (thiotrophs) thriving at the interface between anoxic, sulphidic sediments and aerated seawater (Fig. 1.6C). The most widespread bacteria are from the genus *Beggiatoa* forming mats generally less than 1 cm thick but may be as thick as 10 cm. The presence of *Beggiatoa* mats has been associated with high methane effluxes and AOM rates (Reeburgh, 2007). To be able to survive in the anoxic sulphide-rich environment of cold seeps, 64 species including siboglinids and bivalves live in symbiosis with sulphur-oxidizing and/or methanotrophic bacteria inside their bodies (Sibuet and Olu, 1998). Both siboglinids (Fig. 1.6D) and vesicomyid clams (Fig. 1.6E) live in symbiosis with sulphur-oxidizing bacteria. The former form dense bushes on the seabed while the vesicomyid clams live partly buried in soft sediment extending their foot down into the sulphide-rich sediment but providing themselves with oxidants through a short siphon. *Bathymodiolus* species may use either methane or sulphide depending on the location, species and symbionts (Roberts and Carney, 1997). Family members with sulphide- and methane-oxidizing symbionts, prefer soft sediment where flow is more diffuse while others with methanotrophic symbionts occur on hard, carbonate substrate where fluid flows velocities and methane concentrations are higher (Olu et al., 1996). Principal mineralogical products of AOM are calcium carbonate precipitation ($CaCO_3$, Fig. 1.6B; Aloisi et al., 2002) and the formation of pyrite (FeS_2), both are discussed in detail in Chapter 5.
The efficiency of methane oxidation has been estimated to ranges from 66% in the Beggiatoa mats to 83% in the clam sites, so a fraction of the advective methane flux escapes to the ocean where it is oxidized by bacteria by means of oxygen (Fig. 1.6A; Higgins and Quayle, 1970; Reeburgh, 2007):

$$CH_4 + 2O_2 \rightarrow CO_2 + 2H_20 \tag{1.4}$$

1.3 Diagenetic modelling for a quantitative understanding of cold seep chemistry

The application of continuum models in early diagenesis was introduced by Robert A. Berner (1980) and became popular with a growing desire to understand and quantify the complex relations between numerous dissolved and solid components involved in diagenetic processes over the past 40 years (e.g. Aller, 1980; Boudreau, 1996; Meysman et al., 2005; Middelburg, 1989; Van Cappellen et al., 1993; Van Der Weijden et al., 1992). A diagenetic model is an idealized mathematical representation of diagenesis and a very useful tool in studies which deal with processes that occur on long time scales (e.g. carbonate precipitation) or in locations inaccessible for direct observations (e.g. deep sea). Furthermore, sampling techniques often disturb the system that we try to study (Boudreau, 1997). Cold seeps are one of these natural systems where sedimentary and biogeochemical

processes interact on variable timescales and are generally difficult to access. Methane seepage is the driving force of all biological and chemical reactions at cold seeps. Its volatile character makes it however difficult to study and quantify the related processes (e.g. rates of anaerobic oxidation of methane) without disturbing the system. Hence numerical modelling has become a very common tool in cold seep studies. A widespread application is the determination of upward fluid flow rates and the associated benthic fluxes of dissolved species from the subsurface to the overlying water column (e.g.Haese et al., 2006; Torres et al., 2002; Wallmann et al., 1997). Other applications include the quantification of calcite/aragonite precipitation rates (e.g. Luff and Wallmann, 2003), determination of the controls on the mineralogy of the authigenic precipitates (e.g. Aloisi et al., 2004b), quantification of hydrate formation (e.g. Davie and Buffett, 2001; Haeckel et al., 2004; Hensen and Wallmann, 2005) and methane fluxes in the past (e.g. Dickens, 2001).

1.4 Rationale and project objectives

Previous work on mud volcanoes have established that they are major pathways along which hydrocarbon gases and element-enriched fluids migrate up to the seafloor where they are expelled into the water column, altering the pore fluid and sediment geochemistry and providing a habitat for a distinct chemosynthetic community (e.g. Aloisi et al., 2000; Brown, 1990; Camerlenghi et al., 1992; Dählmann and de Lange, 2003; de Beer et al., 2006; Ginsburg et al., 1999; Kopf, 2002). However, a comprehensive and complete understanding of mud volcanism is still lacking because of the inaccessibility of these structures as well as their high diversity. Outstanding challenges include possible triggers for eruptions, fluid sources, geochemical reactions altering pore fluid chemistry on its way up to the seafloor, spatial and temporal variability of mud eruptions and seepage activity and the correlation between fluid chemistry and biodiversity.

Mud volcanoes are abundant on the European continental margin concentrated in five areas the (Nordic margin (Milkov et al., 2004b), the Alboran Sea (Sautkin et al., 2003), the eastern Mediterranean Sea (Cita et al., 1981), the Black Sea (Woodside et al., 1997) and the Gulf of Cadiz (Gardner et al., 2001)) and they have drawn the attention of scientists for several decades. The HERMES (Hotspot Ecosystem Research on the Margins of European Seas) project, an international multidisciplinary four year research programme has investigated the effects of physical processes (e.g. land slides, mud volcanism, deep-water currents) on Europes margin ecosystems and surroundings (Weaver et al., 2009). As part of this project, this PhD focussed on the spatial and temporal variability of mud eruptions and gas and fluid seepage at MVs using geochemical and sedimentological tools. Samples were collected from two MVs located in the Gulf of Cadiz, i.e. Carlos Ribeiro and Darwin MV. The presence of MVs in the Gulf of Cadiz was for the first time hypothesised in 1992 based on results of a sidescan sonar and multibeam survey. Only in 1999, samples were obtained from the respective geological structures, confirming the occurrence of five MVs in the Gulf of Cadiz, at least two of them active at the time (Gardner et al., 2001).

Many cruises followed resulting in the discovery of more than 40 MVs to date (Medialdea et al., 2009) all having distinct geochemical characteristics.
The main aim of this study is to better understand the spatial and temporal variability of methane and fluid seepage at mud volcanoes.
The specific objectives are:

- To estimate the velocity of upward fluid flow and the resulting lithium, boron and methane fluxes from the subsurface to the overlying water column at the Carlos Ribeiro MV, in order to determine the impact of fluid expulsion from mud volcanoes on the oceanic inventories of lithium, boron and methane.
- To determine the possible fluid sources at the Carlos Ribeiro MV
- To assess the utility of barite horizons as recorders of past variations in methane release from mud volcanoes.
- To reconstruct the venting history of the Darwin MV by means of a petrographic, chemical and isotopic investigation of authigenic carbonate precipitates recovered from the MV crater.

1.5 Thesis structure

First the reader is introduced to the basic concept of mud volcanism in chapter one: what are MVs, where do they occur and what are the driving forces behind them but also the processes related to gas and fluid seepage observed at MVs are discussed briefly. Chapter 2 describes the geological and oceanographical setting of the study area which is the Gulf of Cadiz and what is known so far about the MVs in that area. The results of geochemical and sedimentological analyses performed on samples from Carlos Ribeiro and Darwin MV are presented and discussed in Chapters 3 to 5. Chapter 3 focuses on the spatial variation in fluid flow and geochemical fluxes across the sediment-seawater interface at the Carlos Ribeiro MV including a detailed description of the 1-D transport-reaction model which was constructed to estimate fluid flow velocities and element and methane fluxes from the MVs. Chapter 4 shows the usefulness of barite horizons as a proxy for the methane venting history of Carlos Ribeiro MV while a detailed study of authigenic carbonate crust from Darwin MV described in Chapter 5 reveals the distinct phases of activity at the MV. Chapter 6 summarizes the key findings in Chapters 3-5 and discusses possibilities for future work. Each of Chapters 3-5 have been prepared/submitted as individual papers and therefore contain some overlapping introductory information. As the methods sections in these chapters are generally brief, a more detailed description of certain methods and the obtained precision and accuracies of the analyses is given in the Appendix.

Chapter 2

Study area: Gulf of Cadiz

The Gulf of Cadiz is located on the European continental margin between the Iberian and African mainlands, west of the Gibraltar Strait in the North Atlantic (Fig. 2.1A). It encompasses the boundary between the Eurasian and African plates (Fig.2.1B) and is part of a wide deformation band from the Gorringe Bank and Coral Patch in the west to the Gibraltar Arc and Alboran Sea in the east (Fig. 2.1C). The plate tectonic setting of the area yields a complex geodynamic history which is reflected in a variety of morphological features including mud volcanoes (Gardner, 1999; Pinheiro et al., 2003; Somoza et al., 2003; Van Rensbergen et al., 2005a), diapiric ridges (Fernandez-Puga et al., 2007; Medialdea et al., 2009), pockmarks (Baraza and Ercilla, 1996; Casas et al., 2003; León et al., 2006) and carbonate mud mounds bearing carbonate chimneys (Díaz-del Río et al., 2003; Foubert et al., 2008; León et al., 2007). In addition, the Gulf of Cadiz is characterised by a unique oceanographic setting dominated by the exchange of water masses through the Strait of Gibraltar.

2.1 Geological background

The geological history of the Gulf of Cadiz region is related to the plate tectonic interaction between Southern Eurasia and North Africa since the opening of the Central and North Atlantic Ocean (e.g. Gracia et al., 2003; Malod and Mauffret, 1990; Srivastava et al., 1990). The continental breakup started in the Triassic at the central African margin and propagated to the north until middle Late Jurassic resulting in seafloor spreading at the north-western African Margin and a transtensive tectonic regime between Africa and Iberia/Newfoundland (Fig. 2.2a). After Iberia separated from the North American plates (118 Ma), it moved independently from Eurasia and Africa until Late Cretaceous (84 Ma; Fig. 2.2b) when Iberia became attached to the African plate. The new plate boundary between Iberia and Africa was formed 35 Ma ago (Fig. 2.2c). However, the Iberian plate started to move as part of Eurasian plate only since the Early Miocene (20 Ma; Fig 2.2d) and has been doing ever since. The northward drift of the African plate star-

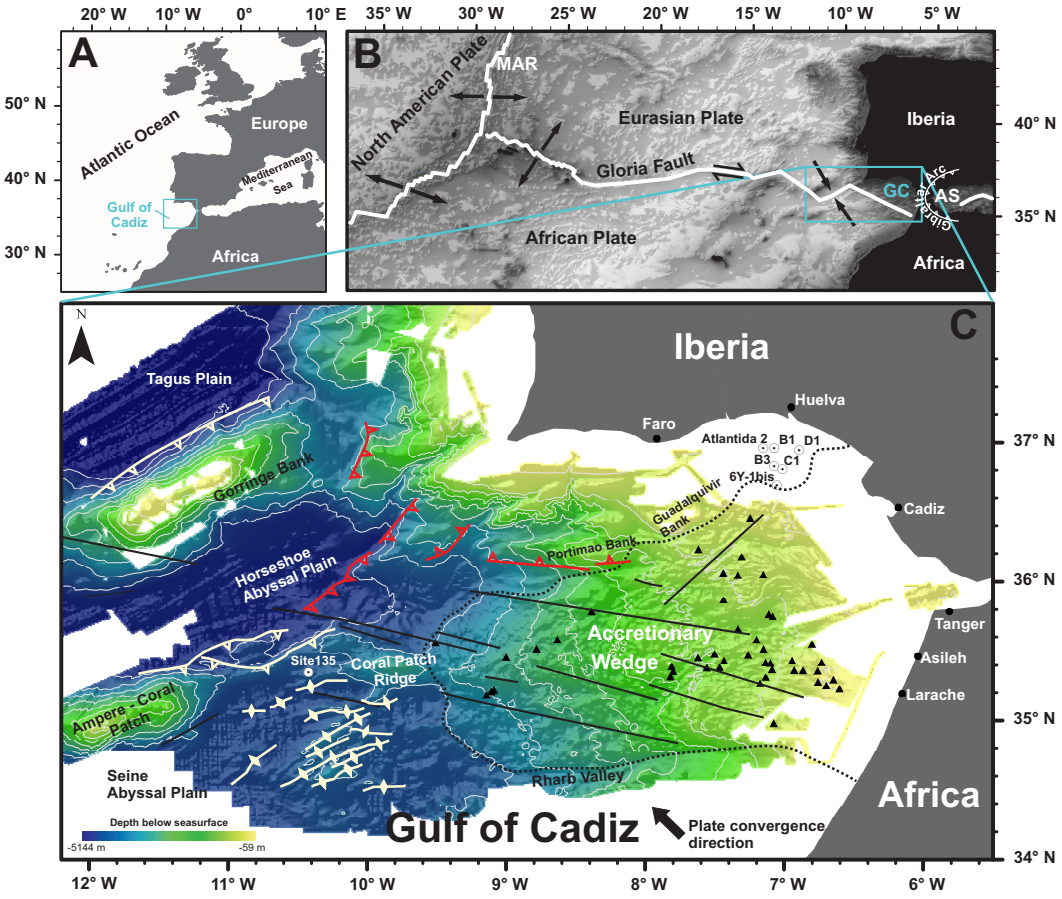

Figure 2.1 **A** Geographical map with the location of the Gulf of Cadiz. **B** Bathymetry map of Iberia, northwest Africa and the Central Atlantic Ocean (source: GEBCO) with the present-day plate boundary setting of the area. MAR: Mid-Atlantic Ridge; GC: Gulf of Cadiz; AS: Alboran Sea. Solid white line: plate boundaries from Bird (2003). Black arrows indicate the relative movements of the plates (Jiménez-Munt et al., 2001). **C** Bathymetry map of the Gulf of Cadiz (Zitellini et al., 2009) showing the main geological structures; black triangles: mud volcanoes; black dotted line: external boundary of the accretionary wedge; black lines: deep rooted faults that affect the seafloor; red lines with triangles: active reverse fault; yellow lines with triangles: inactive reverse fault; yellow lines with rhombuses: axis of inactive anticline (Medialdea et al., 2009; Zitellini et al., 2009). Dotted circles indicate the location of the Deep Sea Drilling Project site 135 (Hayes et al., 1972) and exploration wells on the Spanish margin (Maldonado and Nelson, 1999).

ted to dominate the tectonic evolution of the Gulf of Cadiz and lead to the closure of the Western Mediterranean area. Subsequently, the Gibraltar Arc domain moved westwards, overthrusting deformed Mesozoic and Tertiary sequences of the South Iberian and North African paleomargins resulting in the present plate tectonic setting (Dewey et al., 1989; Maldonado et al., 1999). In the Gulf of Cadiz this thrusting produced the emplacement of a large sedimentary body in the Late Tortonian (11.2 - 7.1 Ma; Maldonado et al., 1999; Medialdea et al., 2004; Torelli et al., 1996) resembling a subduction accretionary wedge (Fig. 2.1c; Gutscher et al., 2002). The wedge unit was reactivated in the Late Miocene as a result of the oblique collision of Iberia and Africa along a NW-SE boundary in this area which is still active today and concentrated in the central and northern sectors of the Gulf (Medialdea et al., 2009; Zitellini et al., 2009). After 25 years of research there is still a lack of consensus on the driving forces behind the motion of the Gibraltar Arc and behind the Africa-Eurasia plate boundary and the nature of the underlying crust, i.e. continental versus oceanic (e.g. Gonzalez et al., 1996; Gracia et al., 2003; Gutscher et al., 2002; Iribarren et al., 2007; Medialdea et al., 2004; Sartori et al., 1994; Torelli et al., 1996). Gutscher et al. (2002) argued in favour of active eastward subduction at present while the absence of seismicity in the accretionary wedge and its almost undeformed sediment seal (deposited since the Early Pliocene) has been considered as an indication of currently no or decreasing activity (Zitellini et al., 2009).

Information on the stratigraphy in the Gulf of Cadiz is limited to a Deep Sea Drilling Project site in the Seine Abyssal Plain (Hayes et al., 1972) and a few exploration wells on the Spanish and Moroccan margin (Fig. 1c; Flinch, 1993; Maldonado et al., 1999; Medialdea et al., 2004; Tortella et al., 1997). At all sites the base of the stratigraphic succession consists of marls and limestones from the Late Jurassic to Early Cretaceous. These are covered with Late Cretaceous to Eocene-Oligocene shales and basal carbonates followed by the accretionary wedge unit and a sedimentary seal ranging in thickness from 0.2 to 2 km of Late Tortonian to Holocene age (marly clays and sands; Maldonado et al., 1999; Zitellini et al., 2009). On the continental shelf and upper slope of the Iberian margin, this stratigraphic succession is underlain by Triassic evaporites (Maldonado et al., 1999). The accretionary wedge represents the thickest sedimentary unit being at least 10 km thick in the eastern sector gradually decreasing towards the west (Iribarren et al., 2007; Thiebot and Gutscher, 2006). Based on near shore wells on the Spanish margin and onshore Miocene units resembling the accretionary wedge, this wedge has been identified to consist of Triassic evaporites (anhydrite and gypsum), clays and rocks of heterogeneous lithologies of Triassic, Late Cretaceous and Paleogene age (including lime- and marlstones), (Flinch et al., 1996; Lanaja et al., 1987; Maestro et al., 2003; Maldonado and Nelson, 1999).

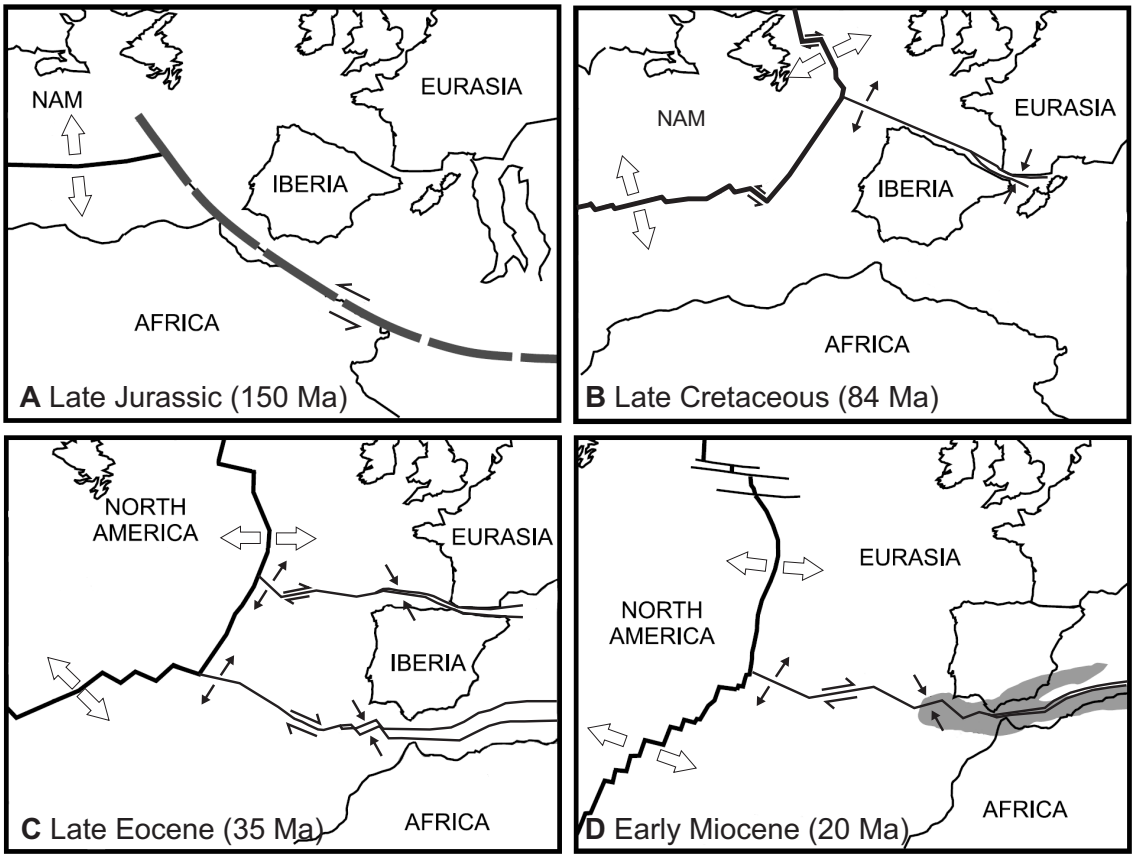

Figure 2.2 Sketch of the tectonic evolution of the African, Iberian and Eurasian plates from Late Jurassic till Early Miocene (after Gracia et al., 2003; Srivastava et al., 1990). Big white arrows show the direction of the relative plate motion which has stayed constant over time. Small black arrows show motions along plate boundaries specifically for the indicated geological time. Grey areas indicate compressional zones. NAM=North American plate

2.2 Oceanographic setting

Since the opening of the Strait of Gibraltar in the Early Pliocene (Loget and Van Den Driessche, 2006), the water circulation in the Gulf of Cadiz has been dominated by the exchange of water masses through the Strait (Fig. 2.3). The main water masses include the North Atlantic Inflow Water (AI) at the surface flowing into the Mediterranean Sea and the warm and saline near-bottom Mediterranean Outflow Water (MOW) flowing into the Atlantic Ocean (Ambar, 1983; Ambar and Howe, 1979). The AI comprises of the North Atlantic Surface Water (NASW) that occupies the top 100 m and the North Atlantic Central Water (NACW; 11 °C $\leq$ T $\leq$ 17 °C and 35.6 $\leq$ S $\leq$ 36.5) that flows between 100 and 700 m depth. Strictly speaking NASW is not a water mass but is the NACW modified by air-sea interactions with temperatures of more than 16 °C and a salinity of 36.4 (Criado-Aldeanueva et al., 2006). The pure Mediterranean water is characterised

by its high salinity values slightly greater than 38.4 (Baringer and Price, 1999). After exiting the Strait of Gibraltar (below 150 m), the MOW rapidly sinks and spreads along the northern continental slope in the Gulf of Cadiz, lying between 400 and 600 m water depth. As it moves downstream the MOW mixes with the NACW. As a result the water mass becomes fresher (S = 35.7 -37.5) and thicker (Ambar et al., 2002; Iorga and Lozier, 1999) and divides into two distinct but connected core layers: the Mediterranean Upper Water (MU; T=13.7 °C and S= 37.07) and the Mediterranean Lower Water (ML; T=13.6 °C and S=37.42) centred respectively at about 800 and 1200 m water depth (Ambar and Howe, 1979; Borenas et al., 2002; Bower et al., 2002; Daniault et al., 1994; Madelain, 1970; Zenk and Armi, 1990). The ML further splits into three minor branches, each following its own deep channel (Madelain, 1970). As these two main cores continue westwards and leave the Gulf of Cadiz, they follow slightly different routes. The ML spreads along three main pathways: one branch circulating cyclonically back into the Gulf of Cadiz spreading the salinity signal south of 34° N, a second turning westward of the St. Vincent Cape and a third flowing northward along the western Portuguese slope (Fig. 2.3b; Borenas et al., 2002; Iorga and Lozier, 1999). The MU bends northward staying closer to the continental slope (Bower et al., 2002; Daniault et al., 1994; Zenk and Armi, 1990). A shallower core at around 400-600 m depth has been observed in the region closer to the upper slope along the Iberian southern and western coasts (Ambar, 1983). Below the MOW, the colder (3 - 8 °C) less saline (34.95-35.2) North Atlantic Deep Water (NADW) is present at depths exceeding 1500 m.

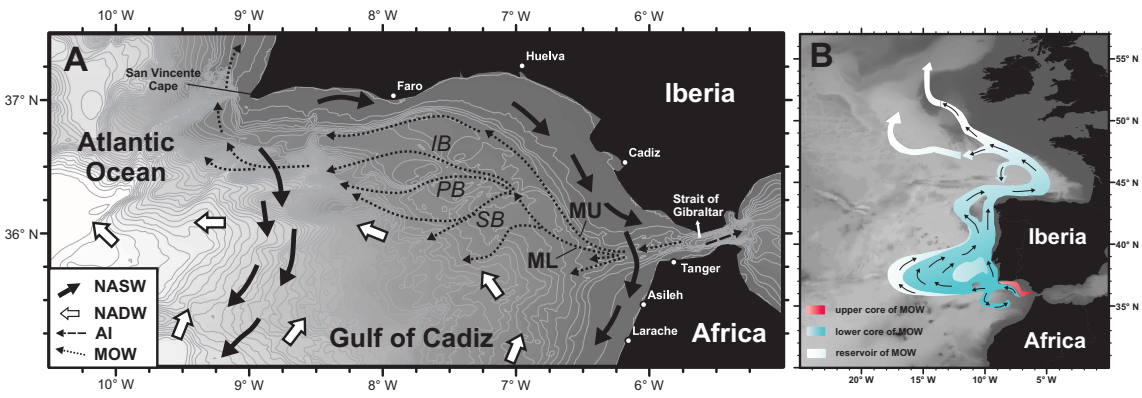

Figure 2.3 **A** Bathymetry map of the Gulf of Cadiz with the general circulation pattern of the main water masses in the area (Hernandez-Molina et al., 2006). NASW: North Atlantic Surface Water; NADW: North Atlantic Deep Water; AI: Atlantic Inflow Water; MOW: Mediterranean Outflow Water with MU: Mediterranean Upper Water and ML: Mediterranean Lower Water. ML is further subdivided into SB, PB and IB respectively the Southern, Principal and Intermediate Branch of ML. **B** General circulation pattern of the Mediterranean Outflow Water (MOW) in the eastern North Atlantic modified from Iorga and Lozier (1999).

2.3 Mud volcanism in the Gulf of Cadiz

To date 50 mud volcanoes have been confirmed by sampling in the Gulf of Cadiz since their first discovery in 1992 (Fig. 2.4; Gardner et al., 2001; Kenyon et al., 2000, 2006; Medialdea et al., 2009; Pinheiro et al., 2003; Somoza et al., 2002, 2000; Van Rensbergen et al., 2005b). They are mainly located on the Iberian (Tasyo and Guadalquivir Diapiric Ridge MV field) and Moroccan (Spanish-Moroccan Margin MV field) continental margins ranging in size from 800 to 4000 m in diameter and up to 200 m in height. Fewer MVs occur westwards on the lower slope at depths exceeding 2300 m (up to 3860 m; i.e. Deep Portuguese Margin MV Field; DPM). The MVs are mainly constructed from grey Miocene age plastic marls (Gardner et al., 2001; Ovsyannikov et al., 2003; Pinheiro et al., 2003) containing rock fragments (i.e. sand-, marl- and claystones) varying in age from the Late Cretaceous to Pliocene (Ovsyannikov et al., 2003). Note that since the MVs are located within the region of the accretionary complex, the oldest rock clasts do not necessarily originate from the source-strata but may belong to the overlying accretionary complex and thus come from the Iberian and Moroccan margins (Pinheiro et al., 2003).

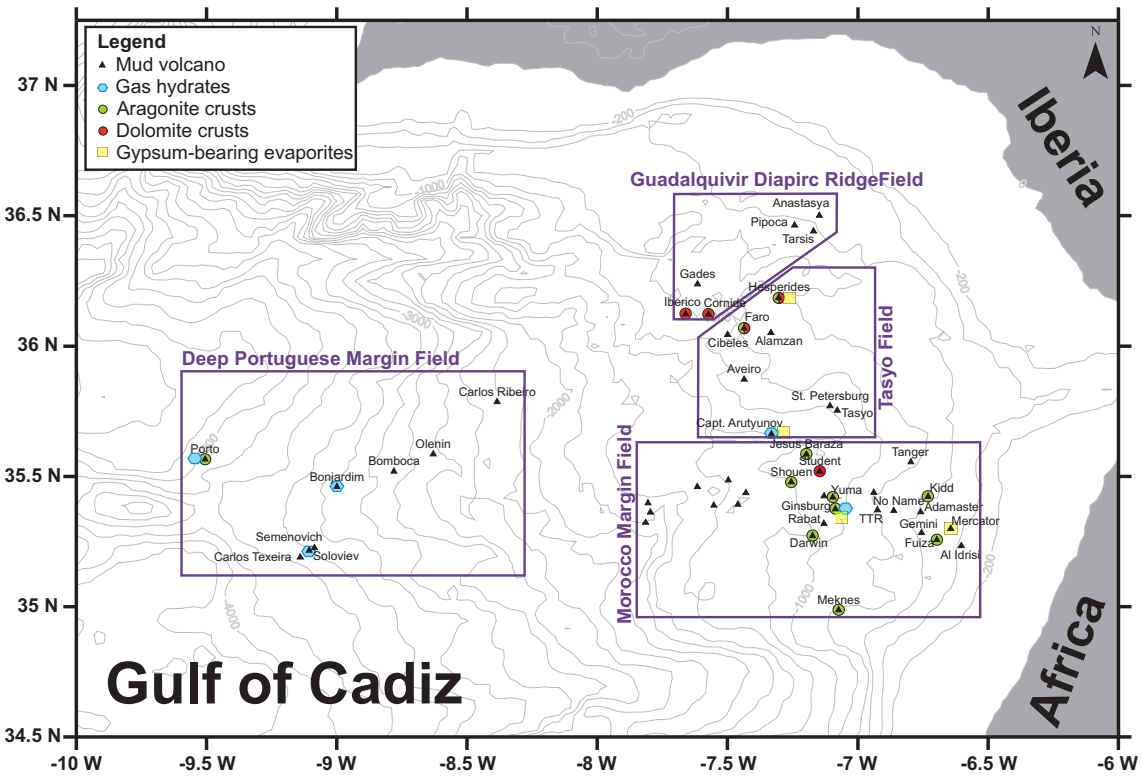

Figure 2.4 **A** Bathymetry map of the Gulf of Cadiz showing the locations of known mud volcanoes grouped into four mud volcano fields (compilation of Kenyon et al. 2006, 2000, 2002, 2003; Medialdea et al. 2009) with their geochemical characteristics known so far (compilation of Haeckel et al. 2007; Hensen et al. 2007; Niemann et al. 2006a; Somoza et al. 2003; Magalhães 2007; Stadnitskaia et al. 2006).

2.3.1 Seepage and mud extrusion activity

The presence of hydrate-bearing sediments (i.e. at the Ginsburg, Bonjardim, Captain Arutyunov, Soloviev and Port MV, Fig. 2.4; Mazurenko et al., 2002; Pinheiro et al., 2003), authigenic carbonates (e.g. the Hesperides, the Student and the Tasyo MV, Fig. 2.4; Díaz-del Río et al., 2003; Pinheiro et al., 2003) and seep related biota (e.g. the Captain Arutyunov, the Faro, the Ginsburg, and the Carlos Ribeiro MV; Gardner et al., 2001; Pinheiro et al., 2003) at some MVs suggests a high past and/or present methane seepage activity. However, spontaneous escape of methane from the seabed has only been observed by video observation at the Captain Arutyunov (CAMV) and the Mercator MV (Haeckel et al., 2007; Sommer et al., 2009). The most active fluid seeping MV in the Gulf of Cadiz to date, is considered to be the CAMV based on the estimation of fluid advection velocities (i.e. 10-15 cm yr^{-1}; Hensen et al., 2007) and methane turnover rates (Niemann et al., 2006a) followed by the Bonjardim, Mercator, Ginsburg and Gemini MVs (Haeckel et al., 2007; Hensen et al., 2007; Niemann et al., 2006a). The majority of the MVs do not show recent mud extrusion activity with the exception of the Bonjardim, Ginsburg Al Idrissi, Carlos Ribeiro and Gimini MV. This observation is based on the thickness of hemipelagic sediments covering the mud breccia at the summit of the MV (Pinheiro et al., 2003; Van Rensbergen et al., 2005b).

2.3.2 Driving forces

Seismic profile analysis (Gardner et al., 2001; Medialdea et al., 2009; Van Rensbergen et al., 2005b) as well as the geochemical study of hydrocarbon gases released from the MVs (Nuzzo et al., 2009), point out that mud volcanism in the Gulf of Cadiz is fault-controlled. Several structures such as extensional and strike-slip faults or fault zones perpendicular to anticlines along the margin have acted as efficient conduits for fluids and mud. This is also clear from the linear orientation of the MVs on the seafloor e.g. the Yuma, the Ginsburg, the Jesus Baraza and the Rabat MV, reflecting the NW-SE trend of the strike-slip fault system identifiable on side-scan imagery (Fig. 2.1C; Gardner et al., 2001). The orientation of the fault system is coherent with the direction of convergence between the African and the Eurasian plates (Díaz-del Río et al., 2003). However, the formation of the MVs in the Gulf of Cadiz is considered to be initially related to diapirism (including marly clay and salt diapirism; Medialdea et al., 2009). Several MVs have been detected in association with diapirs, i.e. either on top of outcropping diapirs (the Hesprides MV; Somoza et al., 2003) or above buried diapiric structures (e.g. the Anastasya, the Pipoca and the Tarsis MV; Fernandez-Puga et al., 2007). The start of mud volcanism has only been estimated for the Moroccan margin, which is at about 2.4 Ma ago (Van Rensbergen et al., 2005b).

2.3.3 Deep fluid characteristics

Fluids expelled from MVs in the Gulf of Cadiz are diverse in composition which seems to be controlled by the mineralogy of the underlying sediments, the fluids are passing through on their way up to the seafloor. The majority of the MVs vent fluids with low chloride concentrations but enriched in boron (up to 14 mM at the CAMV), lithium (up to 3.3 mM at the Mercator MV), strontium (up to 800 μM at the CAMV and the Mercator MV) and iodine (up to 182 μM at the Porto MV) relative to seawater (Hensen et al., 2007; Scholz et al., 2010, 2009). Clay mineral transformation and dehydration processes are most likely the major source of the freshened pore fluids and high iodine levels at all MVs while, the element enrichments have been attributed either to the input of hydrothermal fluids and/or to high temperature alteration of sediments and/or basement rocks (Hensen et al., 2007; Scholz et al., 2010, 2009). In contrast high chloride levels were measured in pore fluids of the Mercator MV and the CAMV and sulphate concentrations exceeding saturation values (i.e. with respect to gypsum) were recorded at the Mercator and the Ginsburg MV. The enrichment of both Cl and SO_4^{2-} in the pore waters, has been associated with the dissolution of gypsum-bearing evaporites (Haeckel et al., 2007; Hensen et al., 2007; Scholz et al., 2009).

2.3.4 Hydrocarbon sources and consumption

Hydrocarbon gases of different origin have been identified in the Gulf of Cadiz based on their molecular and isotopic compositions (Hensen et al., 2007; Nuzzo et al., 2009, 2008; Stadnitskaia et al., 2006). The majority of the MVs vent thermogenic gases, dominated by methane, of which the thermal maturity varies from one MV to the other (Nuzzo et al., 2009; Stadnitskaia et al., 2006). The most mature gases have been measured at the Ginsburg, Mercator and Jesus Baraza MV while MVs in the DPM MV field, the Meknes MV and the CAMV, vent thermogenic gases of a lower maturity. Hydrocarbon gases from the Porto MV on the other hand, show a major contribution from archaea microbes. However the low total organic carbon content of the sediments is unlikely to support a significant microbial activity and thus indicates the seepage of acetate enriched fluids which might originate from hydrothermal alteration of basement rocks (Nuzzo et al., 2009). A mixture of thermogenic and bacterial origins have been suggested for gases from the Bonjardim and the Carlos Ribeiro MV located at the DPM (Stadnitskaia et al., 2006). However a more recent study highlights that the isotopic signatures may be affected by partial recycling of thermogenic methane to microbial methane in shallow sediments by anaerobic oxidation of methane-related methanogenic archaea (Nuzzo et al., 2008). The variation in molecular composition, particularly the enrichment in methane relative to its heavier homologues at many of the 'low thermal maturity' sites is thought to be primarily caused by a transport effect. Indications of biodegradation have been observed at the Carlos Ribeiro MV and the CAMV but, most likely explain only partly the observed variations in hydrocarbon composition in samples from different cores (Nuzzo et al., 2009).

Selected lipid biomarkers indicate multiple sources of organic matter with different degrees of thermal maturity (Nuzzo et al., 2009; Stadnitskaia et al., 2008). Bitumen that has at least reached the oil window has been detected at the CAMV while thermally immature organic matter dominates at the Olenin MV. The majority of the MVs have organic matter that ranges in between these two extremes, indicating that thermally immature organic matter from the sediment is mixed with varying portions of petroleum that migrated upward into the shallow sediments. The presence of organic matter of mixed maturities in the mud breccia in the majority of the MVs and hydrocarbon gases with mature properties, suggests that the source-strata of the organic matter is likely shallower than the depth of origin of the gases (Nuzzo et al., 2009; Stadnitskaia et al., 2008). Although a diverse rate of gas maturities have been recorded in the Gulf of Cadiz, the gasses do not necessarily originate from different sedimentary units since the level and distribution of heat flow varies within the Gulf (Stadnitskaia et al., 2006; Thiebot and Gutscher, 2006). The bulk of the methane flux towards the sediment-seawater interface is considered to be consumed via AOM, a common process in the centres of the MVs, mediated by the methanotrophic archaea: ANME-1 and AMNE-2 (Hensen et al., 2007; Niemann et al., 2006a; Nuzzo et al., 2008). However AOM rates are low to moderate ($<$ 383 mmol $m^{-2}yr^{-1}$; Niemann et al., 2006a) compared to other fluid flow environments (e.g. $\sim$ 7100 mmol $m^{-2}yr^{-1}$ at the Håkon Mosby MV; Niemann et al., 2006b) and are generally lower than sulphate reduction rates ($<$ 690 mmol $m^{-2}yr^{-1}$; Niemann et al., 2006a) in MVs of the Gulf of Cadiz. The relatively higher sulphate reduction rates have been associated with the microbial consumption of higher hydrocarbons, besides methane, at least at Bonjardim, Carlos Ribeiro, Jesus Baraza, Ginsburg, Yuma, CAMV and Rabat MV (Niemann et al., 2006a; Nuzzo et al., 2008; Stadnitskaia et al., 2006). At Ginsburg MV, volatile fatty acids are also considered to contribute to the enhanced rates of sulphate reduction (Nuzzo et al., 2008).

2.3.5 Authigenic mineralisation

Authigenic carbonate precipitates occur primarily at MVs on the upper and mid-continental slope of the Iberian and Moroccan margins and consist mainly of aragonite (Fig. 2.4; Magalhães, 2007). They form crusts within the sediment column and or pavements on top of the MVs as a result of anaerobic oxidation of methane. Dolomite crusts are less abundant and have been mainly recovered from MVs on the Iberian margin (Díaz-del Río et al., 2003). The occurrence of authigenic carbonates in the Gulf of Cadiz has been associated with the dissociation of gas hydrates as a result of the influence of the warm MOW (Magalhães, 2007).

2.4 Conclusion

The unique location of the Gulf of Cadiz has attracted the attention of numerous scientist for decades. It is characterised by complex geological processes and a dynamic oceanographic setting which are intrinsically linked to one another. Consequently, many scientific questions remain unresolved and new ones have emerged. For instance, what causes the observed geochemical and biological diversity in the 50 MVs discovered to date? Is subduction active at the moment? And is there any link with the distribution of MVs? This study focusses on the spatial and temporal variability of mud eruptions and seepage activity at two MVs, Carlos Ribeiro and Darwin, to improve our knowledge on the dynamics of MVs. Potentially, the outcome of this study can then be related to the distribution and abundance of organisms and thus shed light on biodiversity.

Chapter 3

Spatial variation in fluid flow and geochemical fluxes across the sediment-seawater interface at the Carlos Ribeiro mud volcano (Gulf of Cadiz)[1]

3.1 Introduction

Submarine mud volcanoes (MVs) occur throughout the worlds oceans (Dimitrov, 2002; Kopf, 2002; Milkov, 2000). They are usually mound-like features on the seafloor that are characterised by a central conduit (through which mud and fluids are extruded), while the mound itself is generally made up of clasts in a clay mineral-rich matrix (i.e. mud breccia; Kopf, 2002). The main driving force of mud volcanism is pore fluid overpressurization at depth. This tends to occur where sediments accumulate rapidly, or in regions that are subject to tectonic stress and/or to hydrocarbon formation, and, as a result, MVs are commonly found close to subduction zones and orogenic belts (Brown and Westbrook, 1988; Dimitrov, 2002; Hedberg, 1974; Kopf, 2002; von Huene and Lee, 1983).

Until relatively recently, quantification of fluid and chemical fluxes associated with submarine mud volcanism has been intractable, principally because of their inaccessibility. However, with the advent of remotely operated vehicle (ROV) technology, this situation is now beginning to change, and the results of a number of studies suggest that mud volcanism can contribute significantly to the transfer of fluids and chemical elements from the subsurface to the ocean (e.g. Aloisi et al., 2004a; Kopf and Deyhle, 2002; Sauter et al., 2006). For example, most MV fluids are depleted in chloride (Cl^-) relative to seawater,

[1]This chapter has been published as **Vanneste, H.**, Kelly-Gerreyn, B. A., Connelly, D. P., James, R.H., Haeckel, M., Fisher, R. E., Heeschen, K., Mills, R. A. 2011. Spatial variation in fluid flow and geochemical fluxes across the sediment-seawater interface at the Carlos Ribeiro mud volcano (Gulf of Cadiz). Geochimica et Cosmochimica Acta 75, 1124 - 1144 (doi:10.1016/j.gca.2010.11.017).

which has been variably attributed to clay mineral dehydration (e.g. Brown et al., 2001; Dählmann and de Lange, 2003; Kastner et al., 1991), gas hydrate dissociation (Hesse and Harrison, 1981) and/or meteoric water inflow (e.g. Aquilina et al., 1997). In particular, MV fluids tend to have far higher levels of boron (B, e.g. Hensen et al., 2007; Kopf and Deyhle, 2002) and lithium (Li^+, e.g. Martin et al., 1996; You et al., 2004) relative to seawater. Although both elements are enriched in clay minerals that form at low temperature (Schwarcz et al., 1969; Spivack et al., 1987), they can be returned to solution during hydrothermal alteration at relatively low temperatures ($\sim 50°C$; James et al., 2003; You et al., 1996b) and by desorption and mineral dehydration reactions during burial (Deyhle and Kopf, 2002; James and Palmer, 2000; Teichert et al., 2005). At greater depths, higher temperature reactions with sediments and the oceanic or continental basement can produce very high concentrations of pore water Li^+ and B (Stoffyn-Egli and Mackenzie, 1984; You et al., 1995b). Nevertheless, although exchange of Li^+ and B between the solid phase and pore waters is strongly dependent on temperature, other variables, including pH and mineralogy, can also be important (Seyfried et al., 1984; Vigier et al., 2008; You et al., 1996b). Assessment of the role of mud volcanism in the oceanic budget of these elements is of pressing importance because they are increasingly being used as palaeoceanographic tracers of environmental change: B as a proxy for past seawater pH (Pearson and Palmer, 2000; Spivack et al., 1993) and Li^+ as a proxy for past rates of continental weathering (Hathorne and James, 2006). In addition to B and Li^+, MV fluids tend to contain high levels of methane, CH_4. Methane is an important greenhouse gas and, for this reason, a lot of work has gone into quantifying the flux of methane from MVs into the overlying water column (e.g. Dimitrov, 2002; Ginsburg et al., 1999; Haese et al., 2003; Kopf, 2003; Milkov et al., 2005, 2003). This includes analysis of pore water CH_4 concentrations and pore fluid modelling (e.g. Henry et al., 1996), as well as in situ measurements of gas bubbles (e.g. Sauter et al., 2006) and methane consumption rates (e.g. Linke et al., 2005; Niemann et al., 2006b; Sommer et al., 2009). It is now recognised that not all of the methane transported from depth in the MV system will be released into the water column. This is because of anaerobic oxidation of methane (AOM) by chemosynthetic organisms in the subsurface (Barnes and Goldberg, 1976; Nauhaus et al., 2002; Reeburgh, 1976, 2007; Treude et al., 2003). AOM is performed by a consortium of anaerobic methanotrophic archaea and sulphate reducing bacteria; together, these organisms oxidize methane (ultimately converting CH_4 to HCO_3^-) by the reduction of SO_4^{2-} (Boetius et al., 2000; Hinrichs et al., 1999; Orphan et al., 2001). In this way, fluid seepage at MVs supports a unique chemosynthetic ecosystem (Levin, 2005 and references therein) that strongly influences the biodiversity and spatial distribution of organisms across the MV surface (e.g. de Beer et al., 2006; Werne et al., 2004).

This study focuses on the Carlos Ribeiro MV (CRMV) in the Gulf of Cadiz. To date, there are only a handful of reports of the chemical composition of pore fluids expelled from MVs in the Gulf of Cadiz (Hensen et al., 2007; Mazurenko et al., 2002; Scholz et al., 2009), and these are, for the most part, based on only a single core, so they provide limited information on the spatial variation in chemical and fluid fluxes. In order to fill this gap,

and to provide more rigorous flux estimates, we have analysed a number of cores from a transect that runs from the apex of the CRMV to its periphery and a mudflow located SE of the summit. A transport-reaction model is applied to the pore fluid data to obtain estimates of fluid advection velocities, fluxes of Li^+, B and CH_4 from the subsurface to the overlying water column, and rates of AOM in the subsurface. The effect of AOM on the escape of CH_4 into the water column is also assessed. Finally, these results are extrapolated across the surface of the entire MV to assess the impact of mud volcanism on the Li^+, B and CH_4 inventories of the ocean.

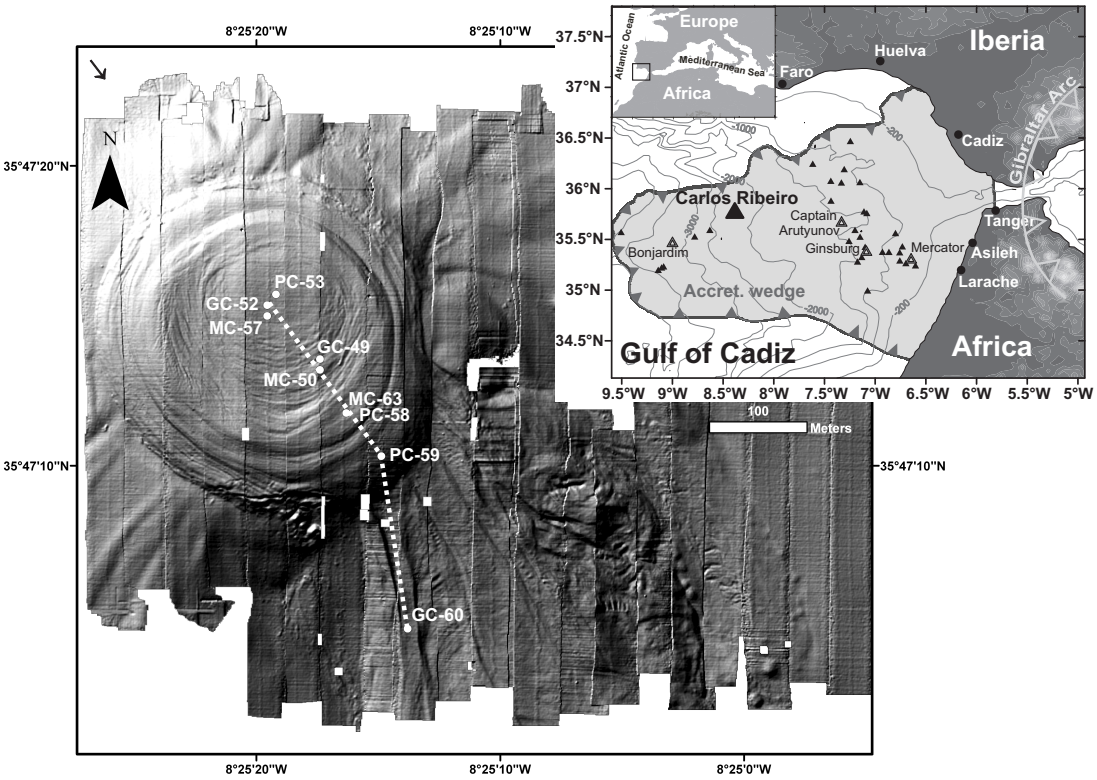

Figure 3.1 Simplified geological map of the Gulf of Cadiz (NE-Atlantic Ocean) showing the location of the accretionary prism (modified from Medialdea et al. (2009)) and of known mud volcanoes to date (compilation of Akhmetzhanov et al., 2007; Kenyon et al., 2000, 2003, 2006; Pinheiro et al., 2003; Somoza et al., 2003; Van Rensbergen et al., 2005b). The shaded relief map of the Carlos Ribeiro MV shows the core sites located along a 380m-long transect.

3.2 Geological Setting

The Gulf of Cadiz (Fig. 3.1) is the marine area that separates the Iberian and African mainlands west of the Gibraltar Strait, which encompasses the boundary between the Eurasian and African plates. It is part of a wide deformation band from the Gorringe Bank to the Alboran Sea (east of the Gibraltar Strait), which has experienced a complex tectonic history since the North Atlantic Ocean began to open, in the Triassic (200 Ma ago; Heyman, 1989).

The current tectonic plate arrangement in the Gulf of Cadiz was established 20 Ma ago, after the westward movement of the Gibraltar Arc domain (Dewey et al., 1989; Maldonado et al., 1999). This emplacement resulted in a complex of imbricated thrusts detached from a decollement surface, resembling a subduction accretionary wedge (Gutscher et al., 2002). The absence of seismicity, and the almost undeformed sediment seal, suggest that the subduction is currently not active (Zitellini et al., 2009). The presence of MVs (Gardner, 1999; Pinheiro et al., 2003; Van Rensbergen et al., 2005b), salt diapirs (Flinch et al., 1996; Berástegui et al., 1998) and other fluid escape structures (e.g. pockmarks and carbonate mud-mounds; Baraza and Ercilla, 1996; Casas et al., 2003; Díaz-del Río et al., 2003; Fernandez-Puga et al., 2007; León et al., 2006) piercing the sedimentary cover of the accretionary complex indicates that strike-slip and compressional deformation is occurring at the present-day (Gutscher et al., 2009; Rosas et al., 2009).

More than 30 MVs have been discovered in this area over the last decade. The MVs tend to be clustered on the slopes of the Gulf, in water depths ranging from ∼300 to ∼3800 m. The MVs vary in shape from conical to flat-topped, so-called mud pies that range in diameter from several tens of meters to ∼4 km and heights of up to 200 m (Pinheiro et al., 2003). They are mainly constructed from grey Miocene age plastic marls (Gardner et al., 2001; Ovsyannikov et al., 2003; Pinheiro et al., 2003). Fluids expelled from MVs in the Gulf of Cadiz are diverse in composition; they are both enriched and depleted in Cl^- relative to seawater, with high levels of Cl^- associated with evaporite dissolution (Hensen et al., 2007; Scholz et al. 2009), particularly on the Iberian and Moroccan continental margins (Medialdea et al., 2009). Strong enrichments in B (up to 14 mM; Hensen et al., 2007) and Li^+ (up to 3.3 mM; Scholz et al., 2009) have been recorded in pore waters from the Captain Arutyunov, Mercator and Bonjardim MVs, which have been attributed either to input of hydrothermal fluids and/or to high temperature ($> 150°C$) alteration of sediments or basement rocks (Hensen et al., 2007; Scholz et al., 2009). Hydrocarbon gases seeping from the MVs are predominantly of thermogenic origin (Hensen et al., 2007; Mazurenko et al., 2002; Nuzzo et al., 2009; Stadnitskaia et al., 2006). Some studies, based on isotope measurements, have suggested that the hydrocarbons may, in part, be derived from a shallow bacterial source (Stadnitskaia et al., 2006). However, a recent study has indicated that isotope signatures may be affected by partial recycling of thermogenic CH_4 in shallow sediments by AOM-related methanogenic archaea (Nuzzo et al., 2008).

The Carlos Ribeiro MV itself lies on the deep Portuguese Margin on the lower slope of the accretionary wedge at 2173 m below sea level (Fig. 3.1). Morphologically the MV is round with a flat-top, extending to ∼1500 m in diameter and ∼80 m in height (Pinheiro et al., 2003). The eye (i.e. the focus of activity) of the MV lies slightly to the north of its centre, and it is surrounded by a series of concentric ridges which build up the MV. A mudflow from the summit to the southeast flank is visible on the bathymetric map (Fig. 3.1).

Table 3.1 Location of studied coring sites. PC= piston core; GC=gravity core; MC=multi core

Core code	Region of Carlos Ribeiro MV	Latitude (°N)	Longitude (°W)	Core length (cm)	Water depth (m)
PC-43	2.9 km SW of Carlos	35°46.04'	8°26.551'	546	2344
MC-44	Ribeiro MV, reference	35°46.042'	8°26.554'	18	2344
GC-52	Summit, eye	35°47.255'	8°25.327'	201	2173
PC-53		35°47.259'	8°25.320'	548	2174
MC-57		35°47.250'	8°25.324'	33	2175
GC-49	Summit, off-centre, SE	35°47.224'	8°25.290'	124	2177
MC-50		35°47.221'	8°25.292'	20	2176
PC-58	Summit, margin, SE	35°47.196'	8°25.269'	231	2177
MC-63		35°47197'	8°25.269'	36	2177
PC-59	Summit, slope, SE	35°47.170'	8°25.248'	133	2179
GC-60	Mudflow, SE of summit	35°47.076'	8°25.229'	187	2189

3.3 Materials and Methods

3.3.1 Sample collection

A series of gravity, piston and multi cores were taken from the Carlos Ribeiro MV during RRS *James Cook* Cruise 10, in May-June 2007 (Table 3.1). The cores were taken from five sites, aligned along a transect connecting the eye of the MV with mudflow pathway on its southeast flank (Fig. 3.1). In addition, one piston and one multi core were taken away from the MV, at a background site that lies 2.9 km to the southwest of the CRMV (Table 3.1). Sampling of the cores was undertaken in a cold room ($\sim 6°C$) onboard the ship; piston and gravity cores were sampled every 20 cm while multi cores were sliced into 1-3 cm sections. Sub-samples were taken for hydrocarbon gas analyses, pore water chemistry and porosity analyses immediately after the cores were opened. For gas analyses, a slug of sediment ($\cong 3cm^3$) was withdrawn using a cut-off plastic syringe and placed in a 20 ml glass vial to which 5 ml of 1M NaOH was added to prevent further microbial activity (Hoehler et al., 2000). The vials were crimped shut, and the sample was then shaken vigorously for several minutes to release the adsorbed gases. Pore waters were extracted in a glove bag under a N_2-atmosphere by pressure-filtration through 0.2 μm cellulose acetate membrane filters, with an N_2-pressure of 3-4 bars. This is with exception of PC-59 for which Rhizon samplers were used to extract the pore water.

3.3.2 Analytical procedures

Total alkalinity (TA) was determined immediately after pore water extraction by titrating against 0.05M HCl while bubbling nitrogen through the sample (Ivanenkov and Lyakhin, 1978). Concentrations of hydrogen sulphide (H_2S) were also determined immediately, using standard photometric procedures (Grasshoff et al., 1999) adapted for pore waters with high ($\sim mM$) levels of dissolved sulphide.

Concentrations of all other chemical species were determined back onshore at the National Oceanography Centre in Southampton. Anion concentrations ($[Cl^-]$ and $[SO_4^{2-}]$) were determined by ion chromatography (Dionex ICS2500). The reproducibility of these measurements (determined by repeat analysis of a seawater standard as well as single anion standards) is better than 1%. Sodium ($[Na^+]$), potassium ($[K^+]$), lithium ($[Li^+]$) and boron ($[B]$) concentrations were determined by inductively coupled plasma optical emission spectroscopy (ICP-OES; Perkin Elmer Optima 4300DV). The accuracy and precision of these analyses is generally better than 5%, determined by replicate analysis (n=3) of IAPSO seawater. Analyses of stable oxygen ($\delta^{18}O$) and hydrogen (δD) isotopes in the pore waters were carried out at Royal Holloway, University of London. For oxygen isotopes, 0.2 ml of pore water was equilibrated with 5% CO_2 and 95% He for 7 hours at 40°C using a Multiflow injection system (GV Intruments/Isoprime Ltd.). δD was determined by pyrolysis of 2 ml of pore water. Isotope ratios were determined using an Isoprime isotope ratio mass spectrometer. $^{18}O/^{16}O$ ratios were normalized to the V-SMOW scale using an internal standard, DEW-1, that has a $\delta^{18}O$ value of -8.44‰, calibrated to V-SMOW and SLAP. Each sample was measured 7 times; the average precision of the $\delta^{18}O$ values is ~ 0.07‰. δD values were normalised to the V-SMOW scale using analyses of reference waters V-SMOW, GISP and SLAP. A mean precision of 0.7‰ for triplicate analysis of δD was obtained.

Concentrations of headspace hydrocarbon gases ($C_1 - C_5$) were determined by gas chromatography (Agilent 6850). Note that depressurisation and warming of the core during sediment retrieval is likely to have led to degassing, so the concentration of CH_4 (which is generally oversaturated in the pore waters) that we report is the minimum value.

Sediment porosity (φ) was calculated from the loss of water after freeze-drying of the sediment. The densities of the sediment and fluid were assumed to be 2.65 g cm^{-3} and 1.00 g cm^{-3}, respectively (note that the fluid evaporated by freeze-drying is freshwater).

Note that per site, one pore water concentration-depth profile is shown in this chapter. This profile is a compilation of the pore water data recovered from all sediment cores at each site (Table 3.1). For most sites this is a piston or gravity core and a multi core while for the eye site, pore water concentration-depth profiles were combined from a piston (PC-53), gravity (GC-52) and a multi core (MC-57).

3.3.3 Geochemical modelling

3.3.3.1 Modelling of fluid flow velocities

In order to estimate fluid flow velocities across the CRMV, a 1-D transport model was developed in MATLAB®, based on the FORTRAN model C.CANDI (Boudreau, 1996; Luff et al., 2001). Flow velocities were determined by fitting the model results to the measured pore water profiles of conservative elements, i.e. elements that are unreactive in the sediment column. In this case, this is true for Cl^-, Na^+ and B, at least for the depth of sampling. These species have concentration-depth profiles that are well mixed in the upper part of the core, either increasing or decreasing asymptotically with depth to a constant value in the lower part of the core (Fig. 3.2). Pore fluids in the shallow sediments are well-mixed because of bioirrigation (i.e. exchange of pore and bottom water over vertical distances in the surface sediment by the pumping activity and motion of mega and macro-fauna; Aller, 1980), while the changes in the concentrations of Cl^-, Na^+ and B below this mixed surface layer are characteristic of upward advection of a fluid with lower $[Cl^-]$ and $[Na^+]$, and higher [B], from deeper in the sediment column. The depth distribution of these conservative elements can thus be described by a partial differential equation that takes into account molecular diffusion, fluid advection and bioirrigation (e.g. Boudreau, 1996):

$$\frac{\partial \varphi C_i}{\partial t} = D_i \frac{\partial}{\partial x}\left(\frac{\varphi}{\vartheta^2}\frac{\partial C_i}{\partial x}\right) \quad - \quad \frac{\partial \varphi u C_i}{\partial x} \quad - \quad \varphi\alpha(x).(C_i(x) - C_i(0)) \qquad (3.1)$$

where C_i is the concentration of the dissolved pore water species i, D_i is the diffusion coefficient of species i corrected for salinity (34.2), temperature (4.3°C) and pressure (220 bar; Table 3.2), $\vartheta^2 (= 1 - ln(\varphi^2))$ is the tortuosity correction for diffusion (Boudreau, 1997), φ is the sediment porosity, u is the velocity of the upward fluid flow, $\alpha(x)$ is the irrigation exchange coefficient, $(C_i(x) - C_i(0))$ is the difference between the concentration of species i at depth and in bottom water, t is time and x is sediment depth. Values for each of these model parameters, at each of the core sites, are given in Table 3.2.

In order to account for the decrease in porosity with depth, the porosity profiles are approximated by least square fitting the following function to the measured porosity data (Boudreau, 1996):

$$\varphi(x) = (\varphi_0 - \varphi_\infty)e^{-\beta x} + \varphi_\infty \qquad (3.2)$$

where β is the porosity attenuation coefficient and the subscripts 0 and ∞ indicate porosity values at the sediment-water interface and at depth, respectively (Table 3.2).

Burial of pore water by sedimentation and the induced fluid flow by compaction of surface

Table 3.2 Parameter values used in the numerical model.

Parameter	Symbol	Unit	Eye	Off-centre	Margin	Slope	Mudflow
Molecular diffusion coefficient of chloride[a]	D_{Cl}	$[cm^2\ yr^{-1}]$	347.66				
Molecular diffusion coefficient of sodium[a]	D_{Na}	$[cm^2\ yr^{-1}]$	222.13				
Molecular diffusion coefficient of boron[b]	D_B	$[cm^2\ yr^{-1}]$	182.03				
Molecular diffusion coefficient of sulphate[a]	$D_{SO_4^{2-}}$	$[cm^2\ yr^{-1}]$	177.95				
Molecular diffusion coefficient of methane[c]	D_{CH_4}	$[cm^2\ yr^{-1}]$	289.38				
Length of model column[d]	L	[cm]	500.5	110	217	120	179.5
Porosity at sediment surface[e]	φ_0		0.75	0.76	0.75	0.78	0.69
Porosity at lower boundary[e]	φ_∞		0.58	0.57	0.53	0.54	0.51
Attenuation coefficient for porosity decrease[e]	β	$[cm^{-1}]$	0.0605	0.08	0.05	0.06	0.04
Cl^- concentration at sediment surface[f]	Cl0	[mM]	551	555	552	557	552
Cl^- concentration at depth L[f]	ClL	[mM]	199	252	296	461	461
B concentration at sediment surface[f]	B0	[mM]	0.5	0.5	0.5	0.6	0.6
B concentration at depth L[f]	BL	[mM]	10.0	10.2	8.5	2.3	2.9
Na^+ concentration at sediment surface[f]	Na0	[mM]	474	464	462	463	468
Na^+ concentration at depth L[f]	NaL	[mM]	185	228	294	459	433
CH_4 concentration at sediment surface[f]	CH40	[mM]	0.002	0.002	0.001	-	-
SO_4^{2-} concentration at sediment surface[f]	SO40	[mM]	28.2	28.5	28.2	-	-
SO_4^{2-} concentration at depth L[f]	SO4L	[mM]	0.1	0.2	0.2	-	-

[a] Calculated from equations given in (Boudreau, 1997) considering the in situ T (4.3°C), S (34.2) and P (220 bar) conditions.
[b] Calculated from equations given in (Boudreau and Canfield, 1988; Mackin, 1986) considering the in situ T (4.3°C), S (34.2) and P (220 bar) conditions.
[c] Calculated from equations given in (Hayduk and Laudie, 1974) considering the in situ T (4.3°C), S (34.2) and P (220 bar) conditions.
[d] Length of pore water profile.
[e] Obtained by least square fitting an exponential equation $\varphi(x) = (\varphi_0 - \varphi_\infty)e^{(-\beta x)} + \varphi_\infty$ to the measured porosity depth profile.
[f] Measured in pore waters extracted from sediment cores from this study
-:no data

sediments are much smaller at MVs than the upward fluid advection. Thus, they can be neglected and the pore fluid flow velocity u is then calculated as:

$$u = \frac{u_0 \cdot \varphi_0}{\varphi(x)} \tag{3.3}$$

where u_0 is the velocity of upward fluid flow at the sediment-water interface.

The irrigation exchange coefficient ($\alpha(x)$) varies with depth because of changes to burrow geometry, distribution and flushing (Meile et al., 2005) and can be described as follows:

$$\alpha(x) = \alpha' \cdot Exp\Big[- (x_b - x_{mix})\Big] \tag{3.4}$$

where α' is the pore water mixing coefficient, x_b is the depth exceeding the irrigation zone and x_{mix} is the depth of the mixing layer.

The discretization of Eqn. 3.1 was achieved by finite differencing, using backward differencing for the first-order derivatives of the diffusion and advection terms and central differencing for the second-order derivative of the diffusion term. The sediment surface was taken as the upper boundary while the lower boundary was set to the base of the cores retrieved at each site. Dirichlet boundary conditions (fixed concentrations) are applied at the top and base of the model domain. The vertical resolution of the model grid was set to 1 cm sediment depth; i.e. the minimum necessary to achieve numerical stability. The model was run to steady state starting from arbitrary initial conditions. The ordinary differential equation (ODE) solver in MATLAB® uses a variable time step and steady state was always reached within 1000 years simulation time. The fluid flow velocity, u_0, and irrigation parameters (α and x_{mix}) were determined by least square fitting the model results to the measured pore water concentration profiles of Cl^-, Na^+ and B simultaneously. Additional model runs were performed to test the sensitivity of the model to variations in the input parameters. The results of these tests are discussed in Section 3.4.

3.3.3.2 Modelling of methane fluxes at the seafloor

In seep environments, the turnover of SO_4^{2-} and CH_4 is mainly controlled by AOM (e.g. Borowski et al., 1996). Accordingly, the pore water distribution of these species is defined by the net stoichiometry of the AOM reaction (Reeburgh, 1976):

$$CH_4 + SO_4^{2-} \rightarrow HCO_3^- + HS^- + H_20 \tag{3.5}$$

Because of degassing during core recovery, concentrations of CH_4 measured in the pore fluids do not represent in situ concentrations and they therefore cannot be used to estimate CH_4 fluxes. However, according to Eqn. 3.5, the SO_4^{2-} flux must balance the CH_4

Table 3.3 Fluid flow and CH_4 budget characteristics at Carlos Ribeiro MV and other seeps sites across the globe.

Seep site	Fluid flow velocity	Water discharge	k_{AOM}	CH4L	RAOM	CH_4 flux from depth	CH_4 flux at the seafloor	CH_4 output at the seafloor	Method (References)
	[cm yr^{-1}]	[m^3 yr^{-1}]	[$(mM\ yr)^{-1}$]	[mM]	[mmol m^{-2} yr^{-1}]	[mmol m^{-2} yr^{-1}]	[mmol m^{-2} yr^{-1}]	x10^3 [mol yr^{-1}]	
Mud Volcanoes									
Gulf of Cadiz									
Carlos Ribeiro MV	0.4 - 4	836**	7-25	75 - 120	445 - 2810	445 - 3614	0 - 806	15	pore-fluid modelling (This study)
Capt. Arutyunov MV	10 - 15		0.1	85		6268.75*	n.d.		pore-fluid modelling (Hensen et al.; 2007)
					383				incubations (Niemann et al., 2006a)
								6	(Sommer et al., 2009)
Ginsburg MV	3		0.5	130	n.d.	2223*	n.d.	n.d.	pore-fluid modelling (Hensen et al.; 2007)
Bonjardim MV	1.3		0.1	62		459.42*	n.d.	n.d.	pore-fluid modelling (Hensen et al.; 2007)
					36				incubations (Niemann et al., 2006a)
Mediterranean Sea									
Kazan MV	3 - 5	5824**	25 - 37.5	130 - 165	5200 - 6500	6000	Negligible	n.d.	pore-fluid modelling (Haese et al., 2006; Haese et al., 2003)
Black Sea									
Dvurechenskii MV	8 - 25		20 - 100	85	6643 - 17228 (model)	7884 - 21279.5	1241 - 4052	1900	pore-fluid modelling (Wallmann et al., 2006b)
		94000			949 - 6095.5				radiotracer (Wallmann et al., 2006b, Aloisi et al., 2004a)
Norwegian continental slope									
Håkon Mosby MV	40-250	80000	n.d.			n.d.	n.d.		1-D evaluation of T profiles (de Beer et al., 2006, Ginsburg et al., 1999)
					0 - 7100				incubations (Niemann et al., 2006b)
								3.65 - 6.57 (dissolved CH_4)	Video observations & acoustic flow meter
								20196 (bubbles)	(Sauter et al., 2006)
Offshore Barbados									
Atalante mud diatreme	10 - 150	44500	n.d.		n.d.	n.d.	n.d.	185 000	T & pore-fluid modelling (Henry et al., 1996)
Cyclops mud diatreme		10750	n.d.		n.d.	n.d.	n.d.	14 000	T & pore-fluid modelling (Henry et al., 1996)
	7 - 50								pore-fluid modelling (Castrec et al., 1996)
Costa Rica convergent margin									
Mound 11	5	2721**	0.5	68	1840	2210			pore-fluid modelling (Schmidt et al., 2005);
					1800 - 51100		4400 - 32800	20486	distribution of chemosynthetic communities & water column meas. (Mau et al., 2006)
Mound 12	10	40715**	3	40	5877	10330			pore-fluid modelling (Linke et al., 2005);
					1800 - 51100		4400 - 32800	7 - 164	distribution of chemosynthetic communities & water column meas.(Mau et al., 2006)
Mound Culebra	n.d.		n.d.		50 - 20400	n.d.	0 - 200	0 - 4	distribution of chemosynthetic communities & water column meas. (Mau et al., 2006)
Other sites									
Cascadia margin									
Hydrate Ridge (southern summit)			0.1	68	9250	8733	14	n.d.	pore-fluid modelling(Luff and Wallmann, 2003);
	10 - 250								CAT measurements (Tryon et al., 2002)
Hydrate Ridge (S + N summit)	n.d.		n.d.		n.d.	n.d.	10950 - 36500 (bacterial mats) <365 (clam fields)	21900	pore-fluid modelling & benthic barrels (Torres et al., 2002)
Hydrate Ridge (S + N summit)	n.d.		n.d.		n.d.	n.d.	n.d.	21900 - 32850	water column measurements (Heeschen et al., 2005)
Gulf of Mexico									
Bush Hill	1.1 - 36		n.d.		n.d.	n.d.	890 (mussel field) 29000 (bacterial mats)	5200	in situ measurements (Solomon et al., 2008)

n.d. : not determined;

*calculated using the following formula: flux[mmol m^2 yr^{-1}]=porosity*CH4L[mM]*fluid flow velocity[cm yr^{-1}]*10

**calculated using the following formula: water discharge[m^3 yr^{-1}]=porosity*area[m^2]*fluid flow velocity[cm yr^{-1}]

flux from below (Borowski et al., 1996). Thus, estimates of CH_4 fluxes can potentially be obtained via modelling pore water profiles of SO_4^{2-}. In addition, SO_4^{2-} reduction (SR) is likely to be a negligible pathway in organic matter degradation because (1) the mud breccia from MVs in the Gulf of Cadiz have low TOC levels (0.3 wt% on average; Stadnitskaia et al., 2006) and (2) the fresh marine POC deposited at the sediment surface is highly reactive and therefore oxygen and nitrate are likely to be the most important oxidizers. Nevertheless, SR by organic matter degradation is incorporated into our model for completeness. In order to accommodate this, the depth distribution of CH_4 and SO_4^{2-} is described using a partial differential equation that incorporates an additional reaction term for SR, methanogenesis and AOM (Boudreau, 1996).

$$\frac{\partial \varphi C_i}{\partial t} = D_i \frac{\partial}{\partial x}\left(\frac{\varphi}{\vartheta^2}\frac{\partial C_i}{\partial x}\right) \quad - \quad \frac{\partial \varphi u C_i}{\partial x} \quad - \quad \varphi\alpha(x).(C_i(x) - C_i(0)) \quad + \quad \varphi \sum R_i \quad (3.6)$$

where

$$\varphi \sum R_{SO_4} = \varphi\left(- k_G \cdot \frac{C_{org}}{2} \cdot \frac{[SO_4^{2-}]}{K_{SO_4^{2-}+[SO_4^{2-}]}} - R_{AOM}\right) \quad (3.7)$$

$$\varphi \sum R_{CH_4} = \varphi\left(k_G \cdot \frac{C_{org}}{2} \cdot \frac{Ki_{SO_4^{2-}}}{Ki_{SO_4^{2-}+[SO_4^{2-}]}} - R_{AOM}\right) \quad (3.8)$$

and k_G represents the kinetic constant of organic matter degradation, $C_{org}/2$ is the organic matter concentration (mM), $K_{SO_4^{2-}}$ is the half-saturation constant of SR, $Ki_{SO_4^{2-}}$ is the inhibition constant for initiation of methanogenesis and R_{AOM} is the reaction rate of AOM. C_{org} is given a value of 0.3 wt% (i.e. 625 mM); this is the average value recorded in mud breccias from MVs in the Gulf of Cadiz (Stadnitskaia et al., 2006). As this organic carbon originates from deep within the sediment column, it is assumed to be refractory, with a k_G value typical of slowly degrading organic carbon in a deep sea environment (1x10^{-6} yr^{-1}; Hensen and Wallmann, 2005; Middelburg, 1989). As values for inhibition constants are poorly constrained in natural systems, $Ki_{SO_4^{2-}}$ is assumed to be equal to $K_{SO_4^{2-}} = 1$ mM.

R_{AOM} is the rate at which AOM takes place in the subsurface and it is defined by the following equation (Treude et al., 2003):

$$\varphi \sum R_{AOM} = k_{AOM} \cdot [CH_4] \frac{[SO_4^{2-}]}{K_{S,AOM} + [SO_4^{2-}]} \quad (3.9)$$

where $[CH_4]$ and $[SO_4^{2-}]$ are the concentrations of dissolved CH_4 and SO_4^{2-} in the pore water, k_{AOM} is the kinetic constant for AOM and $K_{S,AOM}$ is a Monod constant defining the inhibition of AOM at low $[SO_4^{2-}]$. Although this inhibition term has usually been

ignored in other studies (e.g. Hensen et al., 2007), it is included here for completeness because recent experimental data suggest that $[SO_4^{2-}]$ limits the rate of AOM when it is < 1 mM (Nauhaus et al., 2002). Thus, $K_{S,AOM}$ is set to 1 mM. No limitation factor is set for CH_4, because as long as there is CH_4 and sufficient SO_4^{2-}, then AOM will occur (Treude et al., 2003). k_{AOM} and $[CH_4]$ are derived by fitting the model results to the pore water SO_4^{2-} data. In this way, the model is used to determine dissolved methane fluxes and rates of AOM, SR and methanogenesis, at the eye, off-centre and margin stations.

Dirichlet boundary conditions are applied at the top of the model domain for SO_4^{2-} and at the top and base of the model domain for CH_4, while Neumann conditions (no flux) are applied at the base of the model domain for SO_4^{2-}. The concentration of CH_4 at the lower boundary (CH4L) was varied between 40 and 150 mM; i.e. within the range of values observed at all MVs that have been studied using pore fluid modelling (Table 3.3). The range of k_{AOM} values tested during the fitting procedure was 0.5 to 55 (mM yr)$^{-1}$ (Table 3.3). Values for the transport parameters u_0, α and x_{mix} were determined from modelling the pore water profiles of the conservative variables (Section 3.3.3.1). The uncertainty of the model results was assessed by sensitivity analyses.

3.4 Results

Fig. 3.2 shows concentration-depth profiles for Cl^-, Na^+, K^+, B and Li^+ in pore fluids recovered from all of the sediment cores. While the concentrations of all of these elements do not vary with depth at the background site (away from the MV), concentrations of Cl^-, K^+ and Na^+ are depleted, and B and Li^+ are enriched, relative to seawater, in the deeper sections of the cores at all of the MV sites. The Cl^- concentration is as low as ~200 mM in the eye of the MV, whereas concentrations of B and Li^+ are as high as ~10 mM and ~190 μM, respectively. In the case of B, this is ~25 times the seawater concentration. At the same site, concentrations of K^+ decrease with depth, and are close to zero below ~100 cmbsf. Na^+ concentrations are less than half that of background seawater (469 mM). Moving towards the mudflow site, the concentrations of Cl^-, K^+, Na^+, B and Li^+ in the deeper part of the core become progressively closer to those at the background site, but even on the flanks of the MV there is a steep concentration gradient between the pore fluids in the uppermost part of the core, and the pore fluids in the deeper part of the sediment column.

Concentration-depth profiles of pore water SO_4^{2-}, H_2S, CH_4, higher hydrocarbons ($C_2 - C_5$) and TA are shown in Fig. 3.3. These reveal that SO_4^{2-} concentrations fall to zero within 34-180 cm depth below the seafloor. The SO_4^{2-} penetration depth is shallowest (34 cm) in the eye of the MV, but it extends gradually to greater depths along the tran-

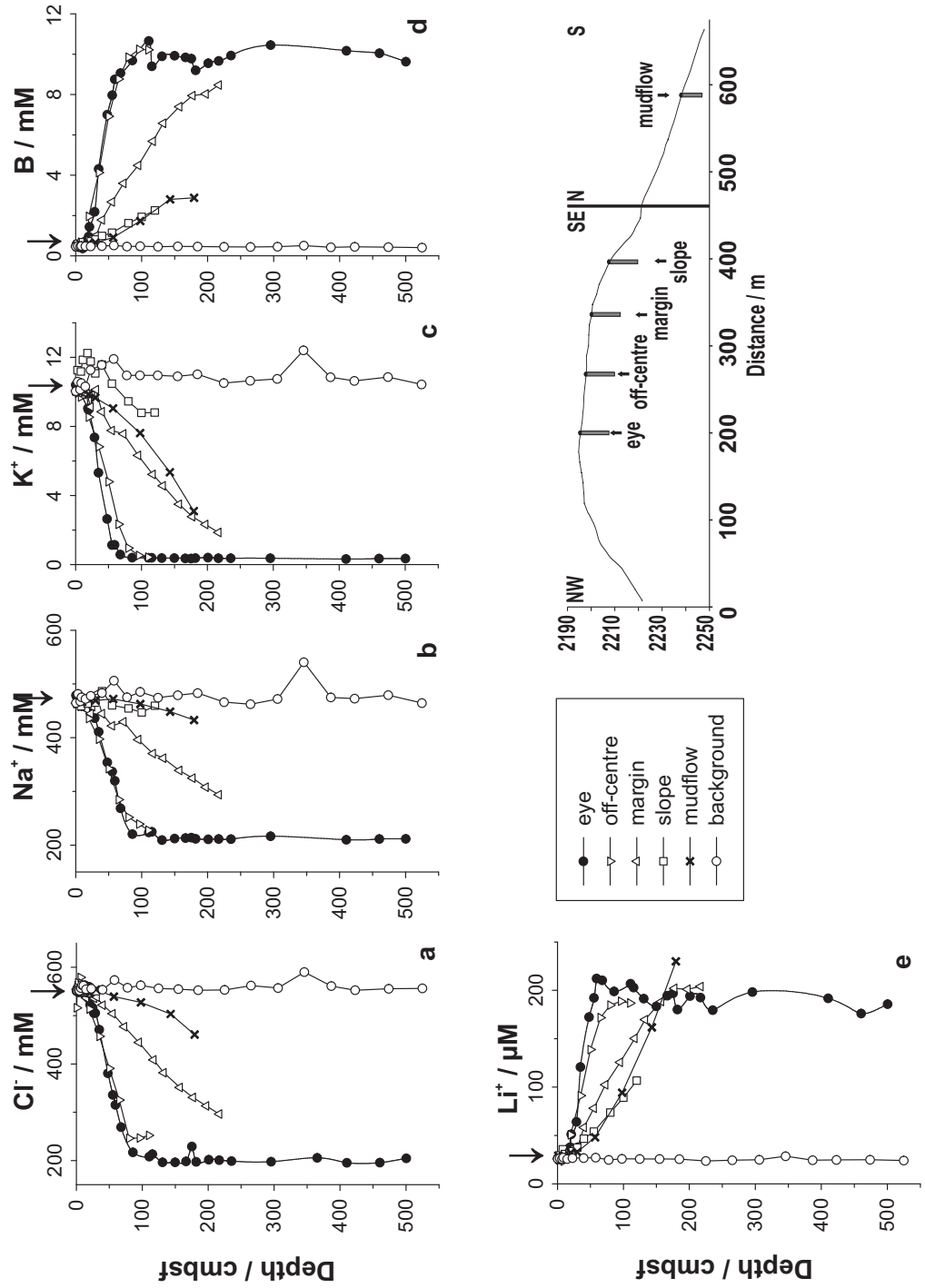

Figure 3.2 Pore water depth profiles of chloride (Cl^-), sodium (Na^+), potassium (K^+), boron (B) and lithium (Li^+) for the five stations at the Carlos Ribeiro mud volcano, and the background station. Vertical arrows indicate seawater values.

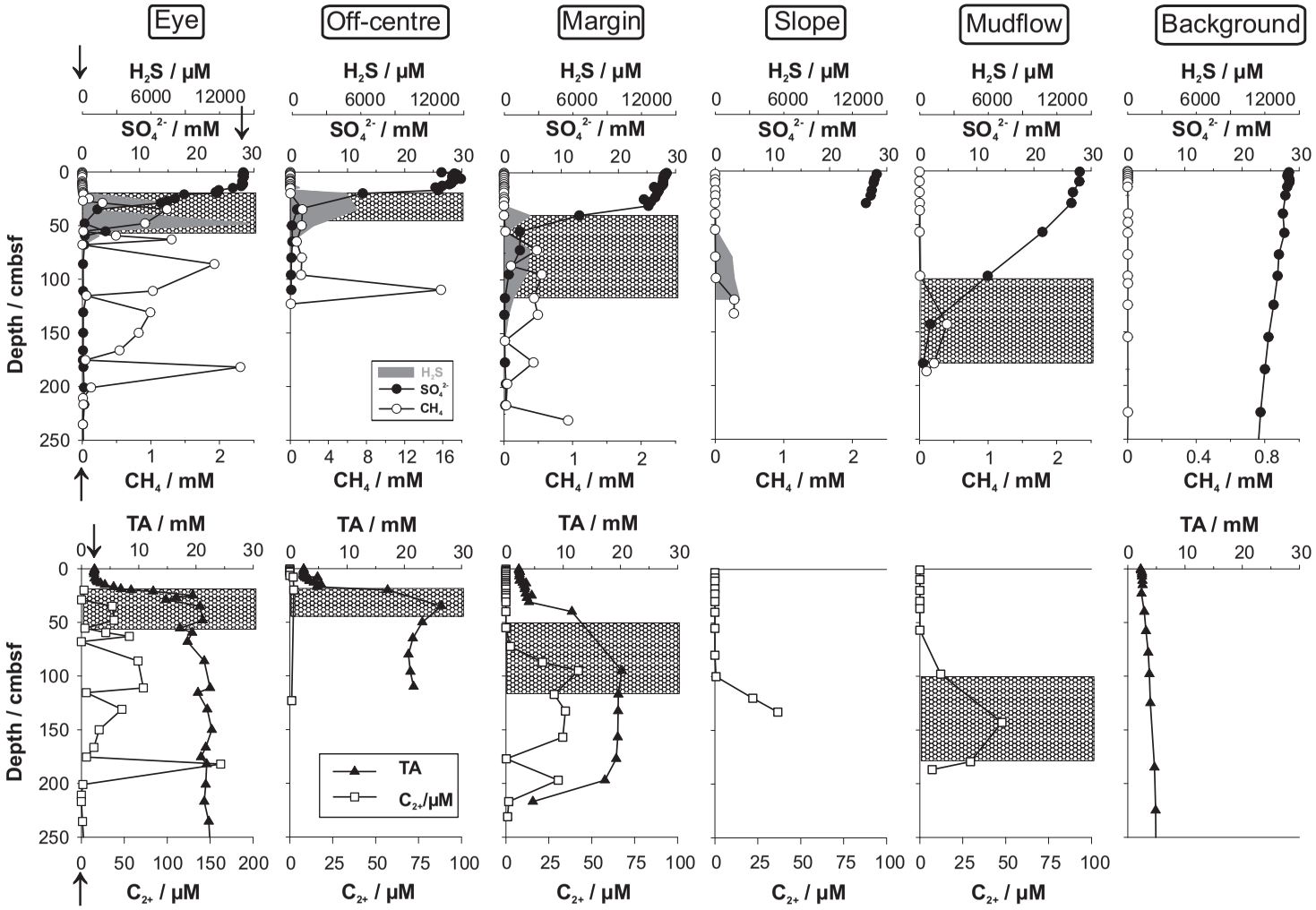

Figure 3.3 Pore water profiles of sulphate (SO_4^{2-}), hydrogen sulphide (H_2S), methane (CH_4), total alkalinity (TA) and higher hydrocarbons (C_{2+}) for the five stations on the Carlos Ribeiro mud volcano, and the background station. Vertical arrows indicate seawater values and shaded zones correspond to the sulphate-methane transition zone at the respective sites.

sect, reaching 180 cm at the outermost (mudflow) site. The depth of SO_4^{2-} penetration coincides with highest concentrations of H_2S; up to 14500 μM in the eye of the MV. TA also increases at this depth. (Note that TA was not measured in cores recovered from the periphery of the MV because of low volumes of pore fluid.) Very little change in $[SO_4^{2-}]$ or TA with depth is observed at the background station, and levels of H_2S are below the detection limit

CH_4 and C_{2+} are below the detection limit in pore fluids recovered from the background site. However, at the CRMV, concentrations of these species tend to increase with depth, attaining values of up to 2 mM CH_4 and 165 μM C_{2+} at the eye. At all MV sites, the headspace gas consists of on average 92±9 % CH_4 and 8 % of C_{2+}, of which 5.7±8 % is ethane and 1.6±2 % is propane, with only trace amounts (< 1%) of i-butane, n-butane and i-pentane.

Stable oxygen and hydrogen isotope ratios for the pore water samples are plotted in Fig. 3.4. Samples from the shallow subsurface tend to have δ^{18}O and δD values close to those of seawater (respectively, -1‰ and -1.5‰), while pore fluids recovered from greater depths have lower δD and higher δ^{18}O, such that there is a negative correlation between these two variables.

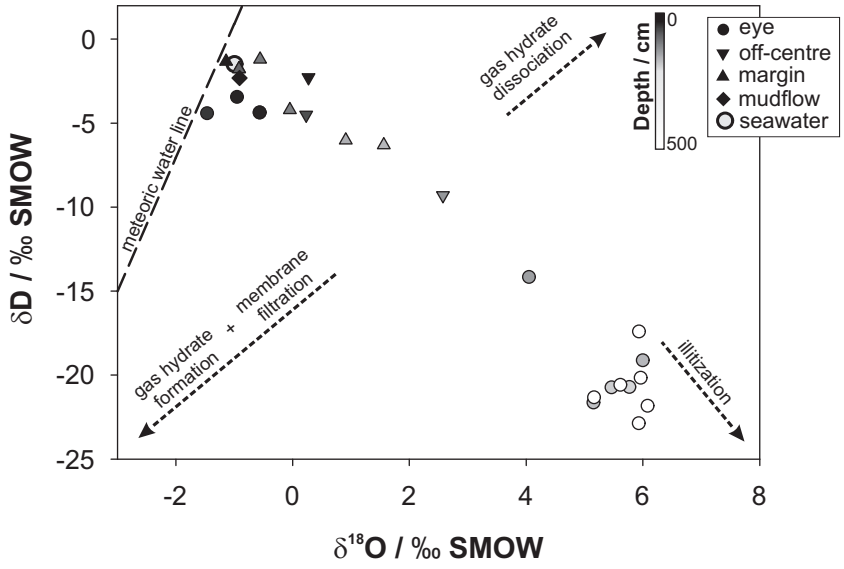

Figure 3.4 δ^{18}O versus δD (‰ SMOW) values for the pore fluids at Carlos Ribeiro mud volcano. The value for seawater and the meteoric water line (δD =8 δ^{18}O +10; Savin and Hsieh, 1998) are also shown.

The results of transport modelling of the pore fluid data are shown alongside the measured data in Fig. 3.5. The model parameters are given in Table 3.2 and the fitting parameters are given in Table 3.4. The model results indicate that fluids from the eye of the MV rise at a velocity of 4 cm yr^{-1}, but this value progressively decreases towards the periphery,

reaching 0.4 cm yr^{-1} at the margin site. Concentration-depth profiles of Cl^-, Na^+ and B, indicate that fluid flow must also occur at the outermost sites (slope and mudflow; Fig. 3.5) but, because the cores are relatively short, a good fit to the data could only be obtained by setting the fluid flow velocity to 0 cm yr^{-1}. Sensitivity analyses of the off-centre site indicate that the model fit is most sensitive to variations in x_{mix} and u_0. The effect of varying u_0 is shown in Fig. 3.5b; Increasing or decreasing the value of x_{mix} by a factor of two will change the value of u_0 by a factor of 0.4 to 3. However, the error on x_{mix} and thus u_0 can be minimized by applying the method of least squares (i.e. minimizing the sum of the squared differences between the model output and measured pore water data using the MATLAB® function lsqnonlin) for Cl^-, B and Na^+, simultaneously. Subsequently, an error of ∼10% is estimated on u_0 and the Li^+ and B fluxes using the MATLAB® function nlparci.

Depth-integrated turnover rates and fluxes obtained from the transport-reaction model for three of the MV sites are summarized in Table 3.5 and shown in Fig. 3.5c. In the eye of the MV, the best fit between the model and the measured SO_4^{2-} profile was obtained for a CH_4 concentration of 120 mM at the lower boundary (CH4L) and for $k_{AOM} = 7$ (mM yr)$^{-1}$. The calculated CH_4 flux from depth is 3614 mmol m^{-2} yr^{-1}. However, the majority (78%) of this methane will be consumed by AOM, which proceeds at a depth-integrated rate of 2810 mmol m^{-2} yr^{-1}. Consequently, only 806 mmol m^{-2} yr^{-1} of CH_4 is predicted to escape into the overlying water column. At the off-centre station, the CH_4 flux from depth is predicted to be 1.3 times lower (2738 mmol m^{-2} yr^{-1}) than it is in the eye. A considerably smaller proportion of this methane (14%) escapes from AOM and makes it into the overlying water column. Further along the transect, the CH_4 supply from depth decreases sharply (to 445 mmol m^{-2} yr^{-1} at the margin station), largely because of a weakened fluid flow. At all sites, rates of SR are significant lower than rates of AOM (Table 3.5), suggesting that AOM is the primary control on rates of sulphate reduction at the CRMV. Rates of methanogenesis are highest in the eye of the MV (0.6 mmol m^{-2} yr^{-1}) and decrease towards the periphery (to 0.1 mmol m^{-2} yr^{-1}).

Sensitivity analyses indicate that modelled values for methane fluxes at the seafloor are insensitive to variations (±50%) in $Ki_{SO_4^{2-}}$, $K_{SO_4^{2-}}$ and $K_{S,AOM}$, but changes in CH4L and, to a lesser extent, in k_{AOM} can be important. For example, at the off-centre site, a 50% decrease in CH4L reduces the methane flux by 80%, while a 50% increase in CH4L leads to a doubling of the flux reported in Table 3.5. A ±50% change in k_{AOM} will change the methane flux by a factor of between 0.2 and 2. However, in contrast to the transport model, the goodness of fit is not very sensitive to changes in the input parameters, which in this case are k_{AOM} and CH4L (Fig. 3.5c). This is demonstrated by the grey shading in Fig. 3.5c where a bigger shading area corresponds to a higher sensitivity of the goodness of fit. As a higher sensitivity allows a better fit, errors on flux calculations are

Table 3.4 Parameter values derived by fitting the model results to the data. The uncertainty of these values is discussed in the text.

Parameter	Symbol	Unit	Eye	Off-centre	Margin	Slope Mudflow	
Upward fluid flow velocity[a]	u_0	[cm yr^{-1}]	4	3.3	0.4	0	0
Irrigation depth[a]	x_{mix}	[cm]	32	32	40	39	50
Irrigation mixing coefficient[a]	α'	$[yr^{-1}]$	3.1	2.5	0.6	0.5	0.6
Rate constant of AOM[b]	k_{AOM}	$[(\text{mM yr})^{-1}]$	7	10	25	n.d.	n.d.
CH_4 concentration at depth L[b]	CH4L	[mM]	120	100	75	n.d.	n.d.

[a] Used to fit the transport model.
[b] Used to fit the transport-reaction model.
n.d.: not determined.

Table 3.5 Depth-integrated turnover rates and fluxes (in mmol $m^{-2}yr^{-1}$) calculated in the model. The uncertainty of these values is discussed in the text.

Parameter	Symbol	Eye	Off-centre	Margin	Slope	Mudflow
SR rate (= only via OM degradation)	SR	0.04	0.04	0.06	n.d.	n.d.
methanogenesis rate		0.6	0.1	0.2	n.d.	n.d.
AOM rate	R_{AOM}	2810	2368	445	n.d.	n.d.
CH_4 flux at depth		3614	2738	445	n.d.	n.d.
CH_4 flux at the seafloor		806	370	0	n.d.	n.d.
Percentage of CH4 flux from depth consumed by AOM [%]		78	86	100	n.d.	n.d.
B flux at the seafloor		301	260	35	8	7
Li^+ flux at the seafloor		6	5	0.8	0.3	0.5

n.d.: not determined.

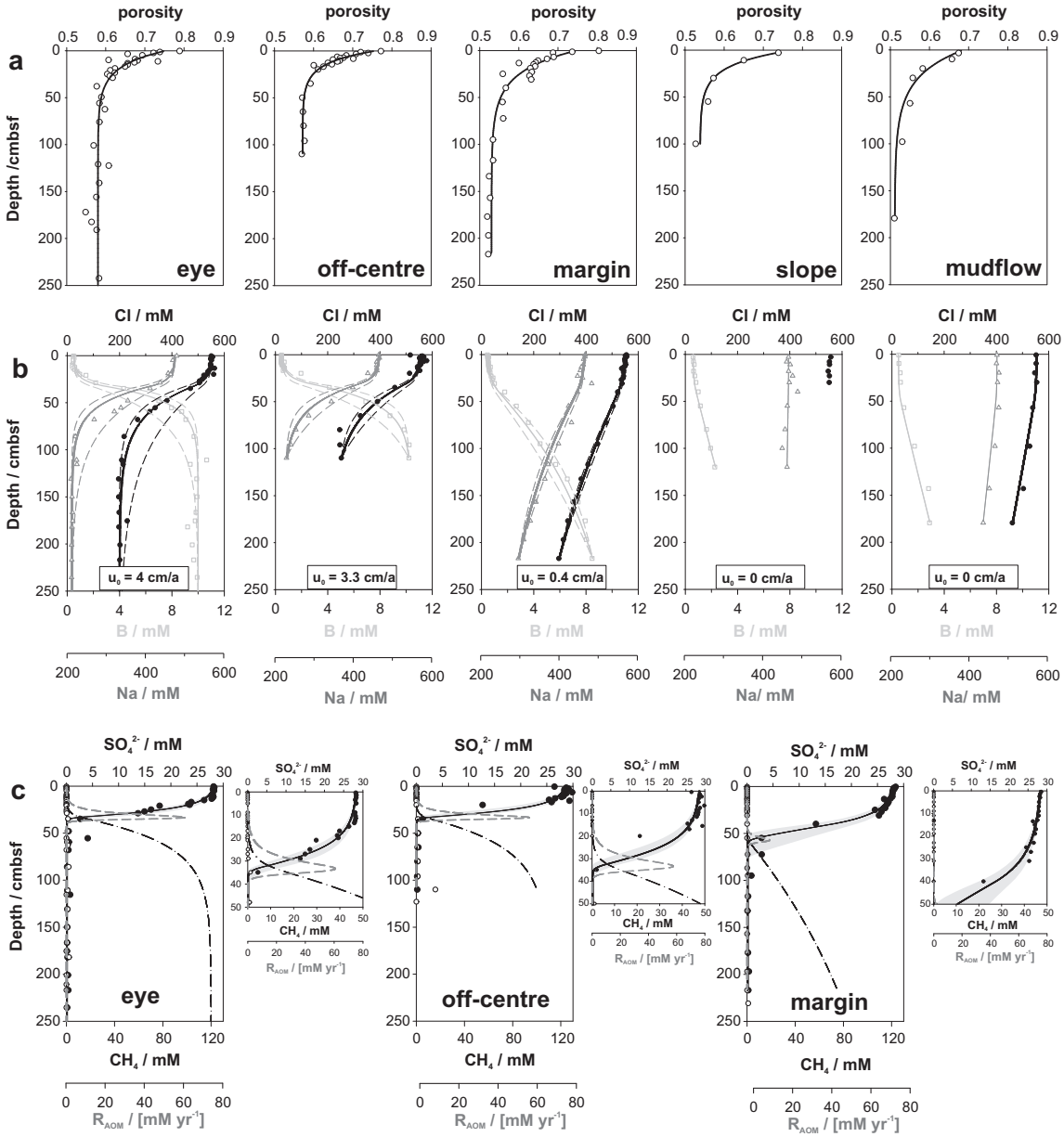

Figure 3.5 Results of numerical modelling of: **a** porosity data; **b** chloride (Cl^-; shown in black), sodium (Na^+; shown in dark grey) and boron (B; shown in light grey) data at the five stations investigated in this study. The solid lines represent the best fit between the model and the measured data; the dashed lines show the effects of doubling and halving the value of the upward fluid flow velocity (u_0; cm yr^{-1}) in the model simulation; **c** sulphate (SO_4^{2-}; solid line) and methane (CH_4; dash-dotted black line) data and reaction rate of anaerobic oxidation of methane (R_{AOM}; grey dashed line) at three stations across the CRMV (eye, off-centre and margin station). Small plots show a close-up of the top 50 cm of the respective concentration-depth profiles. The grey shading shows the effects of doubling and halving the value of CH4L in the model simulation. Measured data are represented by symbols. Note that even though the methane profiles show a $[CH_4]$ of 0 mM in the top 10 cm, methane does escape into the water column (Table 3.5). This is because CH_4 reaches the irrigation zone, i.e. up to 32 cm depth at eye and off-centre station (Table 3.4), where irrigation facilitates the transport of CH_4 to the seafloor.

reduced. Accordingly, the smaller shading area at the eye and off-centre site compared to the margin site, indicates a greater error on CH_4 fluxes at these sites. The uncertainty induced by the error in the fluid flow velocity (i.e. $\pm 10\%$) is quite low, $\sim 16\%$. Overall, these sensitivity tests indicate that accurate measurements of concentrations of pore water methane, and well-characterised values for the rate constant of AOM (k_{AOM}), are essential for meaningful application of 1-D transport-reaction models.

3.5 Discussion

3.5.1 Fluid seepage activity at the Carlos Ribeiro MV

Concentration profiles for the non-reactive species are concave in shape which is indicative of advective transport of fluid from below (Fig. 3.2). The concentration gradient is highest in the eye of the MV, and diminishes towards the periphery. There is no change in pore water concentrations of non-reactive species at the background site. Thus, our data indicate that the CRMV is actively emitting fluids. Numerical modelling confirms this; velocities of fluid flow are highest in the eye, indicating that the central conduit through which mud is transported to the seafloor is also the main pathway for fluid expulsion. The drop-off in the fluid flow velocity towards the periphery of the MV, that we record here, has also been observed at other MVs (e.g. Håkon Mosby MV; de Beer et al., 2006) and it seems to be a common characteristic of mud pies (i.e. flat-topped MVs; Kopf, 2002; Lance et al., 1998). Thus, the concentric ridges at the CRMV likely represent different episodes of mud extrusion, each with different geochemical and biological characteristics (de Beer et al., 2006; Lance et al., 1998). The speed of fluid flow advection in the eye of the CRMV (4 cm yr^{-1}) is moderate compared to other MVs in the Gulf of Cadiz (Table 3.3) but it is within the range reported for some MVs in the Eastern Mediterranean Sea and on the Costa Rica convergent margin (Table 3.3). Nevertheless, other MVs have far higher flow velocities, for example the Dvurechenskii MV in the Black Sea (8 - 25 cm yr^{-1}; Wallmann et al., 2006a) and the Håkon Mosby MV on the Norwegian continental slope (40 - 250 cm yr^{-1}; de Beer et al., 2006; Ginsburg et al., 1999).

The total fluid discharge from CRMV can be estimated by multiplying the surface area by the fluid flow velocity and the sediment porosity close to the surface, for each core site. To this end, the summit area of the MV is divided into a number of different zones that directly relate to the distribution of the concentric ridges present on the MV surface (Fig. 3.1). As the CRMV is also geochemically zoned, chemical fluxes are calculated by linear interpolation between the coring sites. In this way, we calculate that the total water discharge from the summit of the MV is $\sim$840 m^3 yr^{-1}. This value is modest relative to other MVs (Table 3.3) and especially for a mud pie, which are generally characterized by high fluid flow velocities and hence high water discharges (Kopf, 2002). However, most of the data given in Table 3.3 are based on only a few cores, usually sampled close to the

eye of the MV. What this study shows is that fluid expulsion velocities vary significantly across the surface of a MV, so the water flux values listed in Table 3.3 likely represent upper estimates. Crucially, our data demonstrate that there is a clear need to understand the spatial variation in fluid flow, if we are to more accurately determine the quantity of fluid discharge.

3.5.2 Chemical characteristics of the fluid source

Fig. 3.2 shows that, at depth, the pore fluids are depleted in Cl^-, K^+ and Na^+ and enriched in B and Li^+, relative to both seawater and pore fluids at the background station. Because the concentration of these elements is constant in the deeper part of the cores, the chemical composition of the deeper pore fluids is considered to represent that of the deep fluid source. This information can be used to assess the origin of the fluid.

3.5.2.1 Illitization as a freshwater source

Concentrations of Cl^-, Na^+ and K^+ in deep pore fluids at all sites on the CRMV are lower than seawater (Fig. 3.2). Low pore water salinities have been observed at a number of cold seep sites (Moore and Vrolijk, 1992) and are commonly attributed to clay mineral dehydration at depth (Kastner et al., 1991), including loss of interlayer water (Fitts and Brown, 1999) and temperature-driven clay mineral transformations (Colten-Bradley, 1987; Perry and Hower, 1972), gas hydrate dissociation (Hesse and Harrison, 1981; Martin et al., 1996) and meteoric water input (Aquilina et al., 1997; Moore and Gieskes, 1980). Other possible sources of freshwater include clay membrane ion filtration and opal dehydration (Kastner et al., 1991).

The Cl^- concentrations of pore waters from the CRMV are as low as ∼200 mM, i.e. 64% lower than seawater concentrations. Fig. 3.4 gives important clues as to which of the processes mentioned above could be responsible for the low levels of Cl^-. Firstly, input of meteoric water can be discounted, because this would produce pore fluids with positively correlated $\delta^{18}O$ and δD values, as indicated by the meteoric water line in Fig. 3.4 (Savin and Hsieh, 1998). Secondly, membrane filtration will produce fluids with low $\delta^{18}O$ and low δD (Coplen and Hanshaw, 1973), yet the pore fluids from CRMV have high $\delta^{18}O$. Thirdly, the low silica content of the mud breccias at the CRMV (Ovsyannikov et al., 2003) indicates that silica dehydration is unlikely to be an important process. Fourthly, gas hydrates are characteristically enriched in ^{18}O and D relative to the surrounding pore water (e.g. Hesse and Harrison, 1981; Kvenvolden and Kastner, 1990; Maekawa, 2004), so gas hydrate dissociation produces low Cl^-fluids that are enriched in the heavier isotopes. As the pore fluids from CRMV show a trend towards higher $\delta^{18}O$ but lower δD, a major fresh water contribution from gas hydrate dissociation is unlikely.

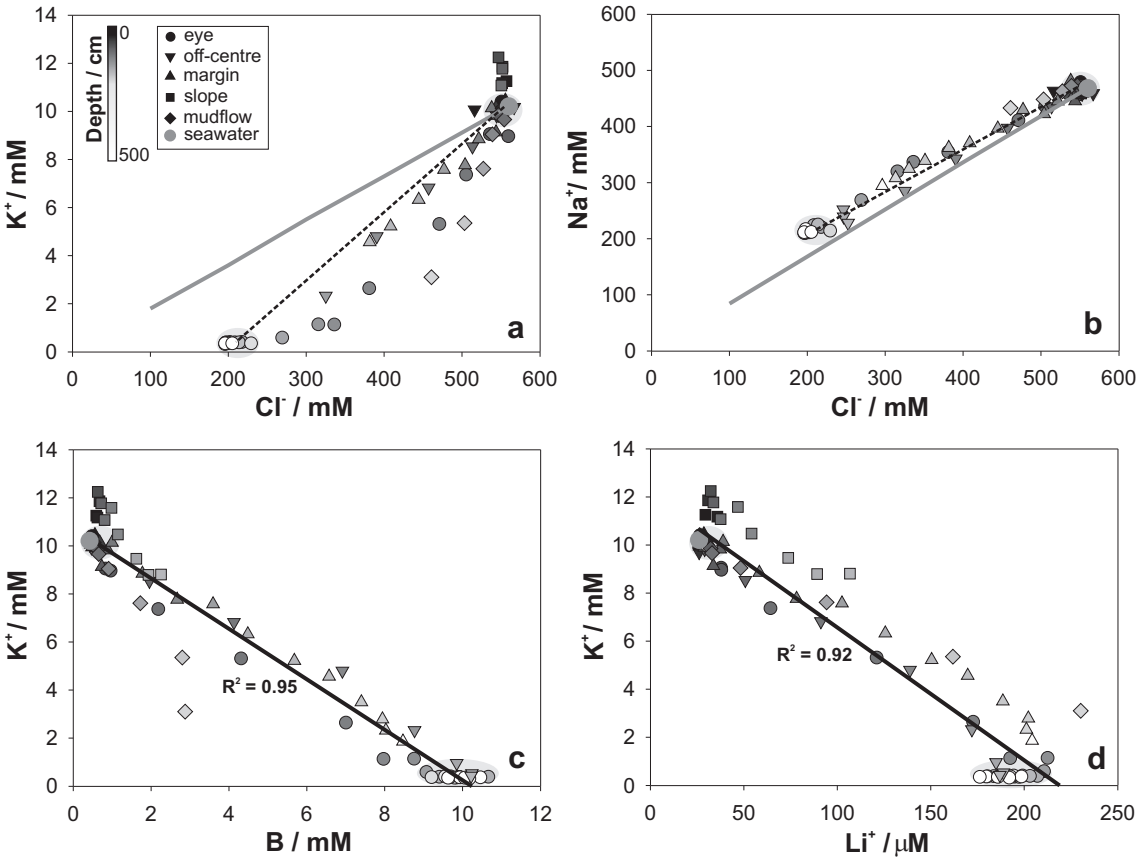

Figure 3.6 Pore fluid chloride ($^{-}$Cl) versus **a** potassium (K^+) and **b** sodium (Na^+). Dark grey line represents mixing between seawater and freshwater while the black dotted line represents mixing between seawater and the deep fluid source (grey shading). Pore fluid potassium (K^+) versus **c** boron (B) and **d** lithium (Li^+). Black solid lines are regression lines. Symbol colours become lighter with increasing sample depth in the core.

The negative correlation between $\delta^{18}O$ and δD is best explained in terms of extensive diagenetic fluid-rock reaction, in particular the transformation of smectite to illite (Dählmann and de Lange, 2003). This is also supported by Fig. 3.6a and 3.6b: the pore fluids are enriched in Na^+, and depleted in K^+, relative to $^{-}$Cl. The transformation of smectite to illite not only lowers pore water salinity (because of the release of interlayer and mineral-bound water), it also releases Na^+ from smectite interlayers and removes K^+, which is a required interlayer cation in illite (Hower et al., 1976). Thus, our data indicate that the main source of fresh water at the CRMV is illitization; this process is also thought to produce pore fluids with low [Cl^-] at other MVs in the Gulf of Cadiz (e.g. Hensen et al., 2007; Scholz et al., 2009). Given that illitization occurs at temperatures between ~60 and 150°C (Colten-Bradley, 1987; Srodon, 1999), and the geothermal gradient in the Gulf of Cadiz is on average 41 °C km^{-1} (Leon et al., 2009), the upwelling fluids must come from ~1.5 to 3.7 km depth.

3.5.2.2 Boron and lithium enrichment in the deep-sourced fluid

As is the case for other MVs in the Gulf of Cadiz (Hensen et al., 2007; Scholz et al., 2009), the pore fluids from the CRMV are enriched in Li^+ and B relative to seawater ($[Li^+]_{sw}$= 26 μM; $[B]_{sw}$= 0.42 mM; Fig. 3.2). During low temperature weathering reactions, both B and Li^+ are taken up into secondary minerals (e.g. Spivack et al., 1987; Stoffyn-Egli and Mackenzie, 1984). However, laboratory experiments demonstrate that both Li^+ and B can be released during alteration of marine sediments at moderate temperatures, ∼50°C (Chan, 1994; James et al., 2003; You et al., 1996a). As discussed in Section 3.5.2.1, there is strong evidence that the deep-sourced fluids rising through the CRMV have reached temperatures of ∼60 to 150°C, so alteration of marine sediments at moderate temperature could be a source of Li^+ and B. Experimental work by Chan (1994) suggests that, for a water/rock ratio of 3:1, as much as ∼200 μM of Li^+ is released to the pore fluids by the time a temperature of 150°C is reached (∼18 days). Sediments from CRMV contain on average 61 ppm Li (in Appendix B), and their mineralogy is similar to the sediments used in the Chan (1994) experiment. For a porosity of 35-50% and a mineral density of 2.65 g cm^{-3}, only ∼0.3-1.1% of the Li^+ hosted within the sediment would need to be mobilised to produce pore waters with ∼200 μM Li^+. Moreover, the water/sediment ratio at CRMV is substantially lower than 3:1 (note that sediment porosity is as low as 0.57 at 5 m depth, Fig 3.5a) and reaction times longer. Thus, all of this evidence would indicate that alteration of marine sediments at moderate temperature is capable of enriching the pore fluids in Li^+ (and, by analogy, B). Furthermore, the good correlation between pore fluid [B] and [Li^+] and [K^+] (Fig. 3.6c and 3.6d) suggests that these elements are supplied by the same (clay mineral transformation; section 3.5.2.1) process.

Recent work at the Bonjardim and Captain Arutyunov MVs in the Gulf of Cadiz has suggested that hydrothermal fluids (>150°C) may be an important source of Li^+ and B in the upwelling pore fluids (Hensen et al., 2007). As hydrothermal fluids are enriched in Li^+ relative to B (e.g. German and Damm, 2003), pore fluids from these MVs are characterised by low B/Li^+ ratios (< 30) and high Li^+ concentrations (> 350 μM; Hensen et al., 2007). Pore fluids from the CRMV have higher B/Li^+ (> 50), and lower [Li^+] (< 200 μM), which would suggest that any hydrothermal source is negligible.

3.5.3 Benthic geochemical fluxes at the Carlos Ribeiro MV

3.5.3.1 Quantification of boron and lithium fluxes from the Carlos Ribeiro MV

The diagenetically altered pore fluids expelled by the CRMV transfer material derived from great depths within the sediment column to the overlying ocean. The question is, is the flux of material sufficient to affect geochemical cycles on the global scale? Concentrations of Li^+ and B in pore fluids from the CRMV are, respectively, up to 10 and 25 times

higher than they are in seawater (Fig. 3.2) and similar levels have been recorded at other MVs (Dia et al., 1995; Hensen et al., 2007; You et al., 2004). The flux of Li^+ and B from the CRMV into the overlying water column can be calculated using the transport model, and results are given in Table 3.5. In the eye of the MV, 301 mmol B m^{-2} yr^{-1} and 6 mmol Li^+ m^{-2} yr^{-1} are released into the water column, but this value gradually decreases away from the summit, reaching 7 and 0.5 mmol m^{-2} yr^{-1}, respectively, at the outermost (mudflow) site. The total flux of Li^+ and B from the CRMV is ∼170 mol yr^{-1} of Li^+ and 8900 mol yr^{-1} of B. These values are lower than those reported for other submarine MVs (Aloisi et al., 2004a; Dia et al., 1995; Hensen et al., 2004; Martin et al., 1996); this is presumably due to lower fluid flow velocities at the CRMV, as concentrations of B, in particular, are amongst the highest reported to date.

On the global scale, submarine MVs are estimated to have an annual water discharge of ~ 0.2 km^3 yr^{-1}. This value is derived from the estimated number of 5500 submarine MVs on Earth (Judd et al., 2007) and an average water discharge of ∼35000 m^3 yr^{-1} per MV (based on water fluxes from the eight MVs described in Table 3.3). Li^+ and B concentrations in deep pore fluids range from 20 to 3400 μM and 2 to 14 mM, respectively (Emeis et al., 1996; Hensen et al., 2007; Scholz et al., 2009). Consequently, submarine MVs are estimated to contribute on average 0.3 x 10^9 mol Li^+ and 1.5 x 10^9 mol B per year to the oceans. These values are comparable to fluxes of Li^+ and B expelled at convergent margins (Chan, 1994; Kastner et al., 1991; Martin et al., 1991; You et al., 1993a, 1995b), and represent $\sim$ 5% of the flux of Li^+ and $\sim$ 20% of the flux of B supplied by hydrothermal vents (Chan et al., 2002a; Huh et al., 1998; Seyfried et al., 1984; Spivack et al., 1987; Stoffyn-Egli and Mackenzie, 1984; You et al., 1993a) (Table 3.6). Although there are large uncertainties in estimates of water discharge from MVs (see section 3.5.1), and also in the number of submarine MVs, this study along with other work on MVs (Aloisi et al., 2004a; Kopf and Deyhle, 2002), indicates that MVs supply $\sim$ 2% of the Li^+ and B delivered to the ocean.

3.5.3.2 Methane emissions at the Carlos Ribeiro MV

Constraining the CH_4 flux at MVs is of dual interest. First, a number of studies have shown that CH_4 is an important energy source for life at MVs (e.g. de Beer et al., 2006) and, secondly, CH_4 is a greenhouse gas. For these reasons, determinations of fluxes of methane from MVs are essential in order to understand the biodiversity at MVs and to assess whether MVs are a significant source of CH_4 in the global carbon budget.

Pore fluids from the CRMV contain elevated levels of CH_4 and higher hydrocarbons relative to the background station (Fig. 3.3), indicating that these gases are, in part, of thermogenic origin (Hensen et al., 2007; Mazurenko et al., 2002; Nuzzo et al., 2009;

Table 3.6 Boron (B), lithium (Li^+) and methane (CH_4) inputs into the ocean.

	B flux 10^9 mol yr^{-1}	Li^+ flux 10^9 mol yr^{-1}	CH_4 flux 10^{10} mol yr^{-1}	References
Rivers	54 (49 - 58)	8	-	(Huh et al., 1998; Lemarchand et al., 2000, Park and Schlesinger, 2002)
Hydrothermal fluids	7.4 (0.4 - 12)	6 (3 - 27)	0.1	(Chan et al., 2002a; Huh et al., 1998, Seyfried et al., 1984; Spivack et al., 1987, Stoffyn-Egli and Mackenzie, 1984; You et al., 1993b)
Fluid expulsion at convergent margins	1.9	0.08 - 0.6	-	(Chan and Kastner, 2000; Hathorne and James, 2006, Park and Schlesinger, 2002; You et al., 1995a)
Mud volcanoes	1.5 (0.4 - 2.7)*	0.3 (0.004 - 0.7)*	15.5	*See text for details; (Keir et al., 2005)
Seepage at continental shelves	-	-	205 (10 - 400)	(Hornafius et al., 1999; Hovland et al., 1993, Trotsyuk and Avilov, 1988)

Stadnitskaia et al., 2006). The pore fluid profiles of SO_4^{2-}, H_2S and TA suggest that CH_4 is the main driver of SO_4^{2-} consumption at the CRMV; SO_4^{2-} concentrations fall to zero within 34-180 cm depth below the seafloor (Fig. 3.3), yet they remain high throughout the sediment column at the background site which is not affected by the seepage of hydrocarbon rich pore fluids. Additionally, the drop in SO_4^{2-} is accompanied by a peak in H_2S and an increase in TA because HCO_3^- is produced by AOM (Eqn. 3.5). The presence of anaerobic methanotrophic archaea supports the geochemical evidence for AOM at this MV (Vanreusel et al., 2009). AOM has been shown to suppress the release of dissolved CH_4 into the water column also at other MVs in the Gulf of Cadiz (Niemann et al., 2006a) although, in this study, only diffusive CH_4 fluxes were taken into account. Our data indicate that the main mass transfer pathway at MVs is actually advective flow. Thus, we use our 1-D transport-reaction model to calculate dissolved CH_4 fluxes, both at depth and at the seafloor, and to assess the role of AOM in regulating the amount of CH_4 escaping into the water column at this MV.

For all sites, the model-derived methane concentration at the lower boundary (CH4L; Table 3.4) exceeds the methane saturation concentration required to form gas hydrates at CRMV (68 mM, calculated according to the methods described in Tishchenko et al., 2005). As the model presented here only simulates the dissolved phase, the values of CH4L greater than 68 mM suggest that CH_4 as a free gas must also be present, within the subsurface at CRMV. This is consistent with observations that document the coexistence of free gas and gas hydrates at a number of cold seeps (e.g. Milkov et al., 2004a) and streams of gas bubbles escaping from the seabed at MVs that are located within the hydrate stability zone (e.g. Sauter et al., 2006; Sahling et al., 2009). It is important to note that the model only provides an effective measure of the methane concentration at the lower boundary, and it does not simulate the exact physical processes (i.e. gas flow in porous media and subsequent (partial) dissolution). (This would require a model that incorporates multi-phase flow, which is beyond the scope of this paper.) Crucially, however, our model *can* provide the correct methane flux required for AOM, because methanotrophic archaea can only utilise dissolved methane (as opposed to methane gas) for AOM. Results of transport-reaction modelling (Fig. 3.5c; Table 3.5) also indicate that CH_4 fluxes at depth and at the seafloor decrease from the eye of the MV towards its periphery. This is partly because of (i) lower CH_4 concentrations in the subsurface at the peripheral sites (CH4L = 75 mM), and (ii) a drop in the fluid flow velocity towards the periphery (Table 3.4). Although advective flow could not be modelled at the outermost sites (slope and mudflow), SO_4^{2-}, H_2S and hydrocarbon data clearly show (Fig. 3.3) that there is some upward CH_4 flow. However, these data may also reflect lateral diffusion of solutes from the central vent channel. Nevertheless, regardless of the CH_4 source, our data indicate that most of the CH_4 is oxidized within the surface sediments, because of the low fluid flow velocities at these sites. Hence, the model outcome underlines the importance of pore water flow (Luff and Wallmann, 2003). Furthermore, if the supply of CH_4 from depth is low, the model predicts that CH_4 is consumed at a lower rate, but more efficiently: R_{AOM}

decreases while k_{AOM} increases from the eye of the MV towards its periphery (Table 3.5). This means that dissolved CH_4 will only escape from the seafloor into the overlying water column if it is supplied at a faster rate than it is consumed by CH_4 oxidizing archaea. This may be stating the obvious, but the fact that this is acknowledged by the model gives us confidence in its ability to reconstruct transport and reaction processes at cold seeps.

Derived values for k_{AOM} at the CRMV are consistent with those obtained by other modelling studies at cold seep sites (Table 3.3). The depth-integrated rate of AOM is generally low compared to other cold seeps in the Mediterranean and Black Sea, as well as on the Costa Rica and Cascadia margins (Table 3.3). This can be attributed on the one hand to lower CH_4 concentrations at the lower boundary of the model (e.g. Carlos Ribeiro MV: CH4L=75-120 mM versus Kazan MV: CH4L =130-165 mM) and/or to lower fluid flow velocities (e.g. Dvurechenskii MV: 8-25 cm yr^{-1}). R_{AOM} and the CH_4 flux are intrinsically linked via Eqn. 3.9; higher methane concentrations will result in higher R_{AOM} values. Thus, the CH_4 flux from depth plays an important role in setting k_{AOM} and R_{AOM} values in cold seep environments. As it is still difficult to accurately measure CH_4 concentrations in sediment cores, or in situ, modelling is the best way to constrain these parameters. Furthermore, rates of AOM obtained from laboratory experiments suffer in that they are averaged over only a few hours, while models are based on pore water data which correspond to timescales of months to years. Nevertheless, although the models work well, major advances in our understanding of CH_4 related processes in cold seep environments will only be possible with an improvement in our ability to make in situ measurements.

The total CH_4 output via quiescent dewatering across the sediment-seawater interface at the CRMV is estimated to be $\sim$ 15 x 10^3 mol yr^{-1} (Tabel 3.3); this is 15 % of the amount transported to the surface sediments from depth ($\sim$ 100 x 10^3 mol yr^{-1}). This value is within the range of that calculated at the Captain Arutyunov MV (Gulf of Cadiz), Mound 11 and Mound 12 (Costa Rica), which have similar fluid flow velocities (Table 3.3). MVs with higher fluid flow velocities tend to have considerably higher CH_4 emissions, e.g. Håkon Mosby MV, Dvurechenskii MV, Atalante and Cyclops. However, CH_4 emissions from Atalante and Cyclops are likely to have been overestimated as the majority of the CH_4 ascending from the periphery of the MVs is likely to have been oxidized by AOM, which was not taken into account. If all submarine MVs in the Gulf of Cadiz (i.e. >30) are considered to have the same level of activity as Captain Arutyunov MV and Carlos Ribeiro MV, submarine MVs in the Gulf of Cadiz would emit 3.3 x 10^5 mol yr^{-1} of CH_4 (= 11 x 10^3 mol yr^{-1} x 30). This is significantly lower than calculated for the Black Sea (1.2 x 10^8 mol yr^{-1}; Wallmann et al., 2006a) and for the Costa Rica margin (20 x 10^6 mol yr^{-1}; Mau et al., 2006).

Wallmann et al. (2006a) estimate that the total CH_4 emission into the ocean via fluid

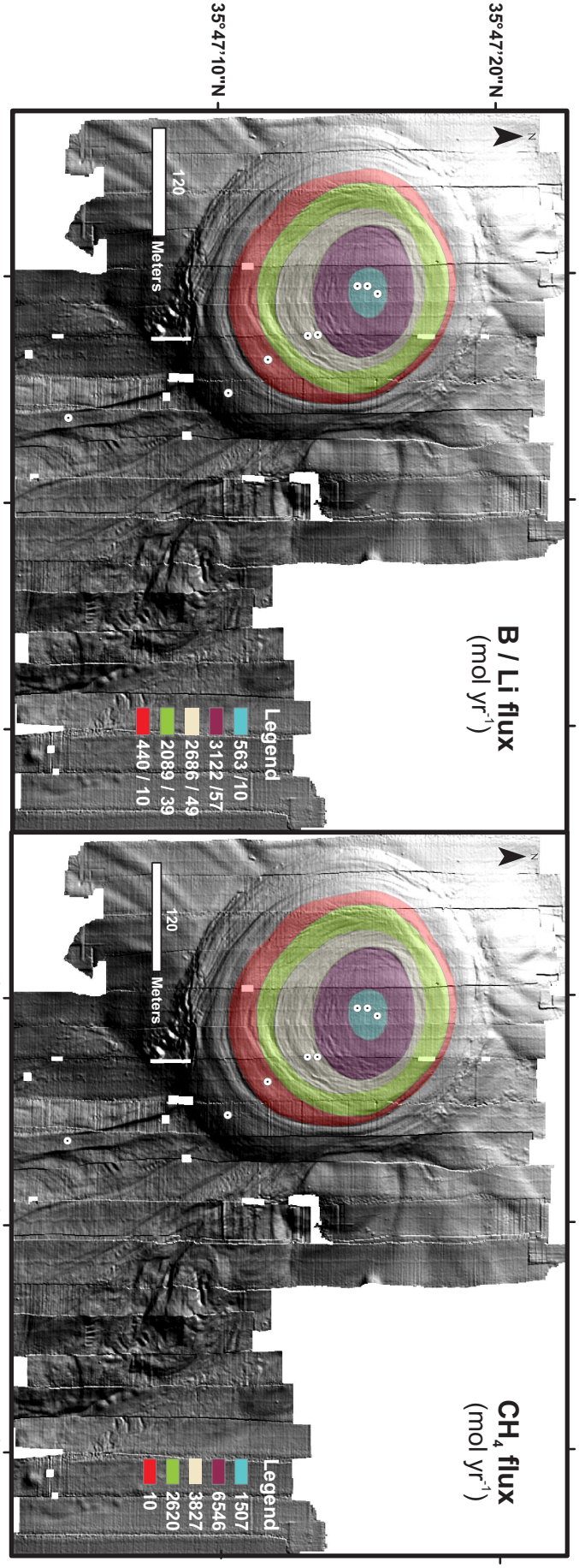

Figure 3.7 Spatial distribution of boron (B), lithium (Li^+) and methane (CH_4) fluxes across the Carlos Ribeiro mud volcano surface.

flow through submarine MVs is of the order of 10^{10} mol yr^{-1}, excluding the contributions from gas ebullition ($\sim$ 2 x10^{10} mol yr^{-1}) and mud extrusions ($\sim$12.5 x10^{10} mol yr^{-1}). Thus, although these estimates are based on very few data (Kopf and Behrmann, 2000; Sahling et al., 2009; Sauter et al., 2006), the magnitude of methane emissions via quiescent dewatering is very similar to gas ebullition. This is most likely because of the more constant and continuous nature of fluid flow and its widespread occurrence at MVs, in contrast to gaseous fluxes which are rich in CH_4 but episodic. Accordingly, results from seep sites such as on the Cascadia margin and in the Gulf of Mexico (Table 3.3), show that the size of the area of seepage is of key importance in defining the amount of CH_4 emitted from a single seep site. This is also demonstrated by the distribution of the CH_4 output across the CRMV (Fig. 3.7). The contribution of submarine MVs to the global methane budget of the ocean is relatively small ($\sim$8%) compared to marine seepage at continental shelves (Hornafius et al., 1999; Hovland et al., 1993; Trotsyuk and Avilov, 1988) but significantly higher than the input from hydrothermal circulation at mid-ocean ridges (e.g. 150 x emissions from the Mid-Atlantic Ridge; Keir et al., 2005) (Table 3.6).

Nevertheless, more work needs to be done to properly quantify CH_4 emissions from submarine MVs. So far well-constrained methane fluxes from MVs are limited to those on land, which have a direct influence on the atmospheric methane budget and are easier to study (Dimitrov, 2002; Etiope et al., 2002; Etiope and Milkov, 2004; Etiope, 2009). Nevertheless, although the contribution of methane emissions of submarine MVs to the atmosphere is likely to be small (McGinnis et al., 2006), they can have an indirect effect on global climate by reducing the buffering capacity of the deep ocean (Damm and Budéus, 2003).

3.6 Conclusions

The Carlos Ribeiro mud volcano in the Gulf of Cadiz has been systematically sampled along a transect to assess the spatial variation of fluid flow velocities and element and methane fluxes. Compared to other MVs, the CRMV currently shows only modest fluid expulsion activity. Fluid flow velocities are highest at the eye of the MV and generally decrease towards its periphery. Accordingly, geochemical fluxes across the seawater-sediment interface are also highest in the eye and very low at the edges. This pattern of concentric zonation seems to be a common characteristic of mud pies and needs to be taken into consideration when assessing the effects of fluid flow on chemical budgets in the ocean.

Like other submarine MVs, the CRMV expels fluids with very low Cl^- concentrations which are sourced at depth by the transformation of smectite to illite. Illitization takes place at temperatures of between $\sim$60 - 150°C, which results in leaching of Li^+ and B. Boron attains concentrations of up to 10 mM at the CRMV, amongst the highest ever reported for cold seep environments. We calculate that mud volcanism is an important

source of Li and B to the ocean, supplying up to 20% of the flux of B, and up to 5% of the flux of Li^+, from high-temperature hydrothermal activity.

Methane emissions into the overlying water column at the CRMV are relatively low compared to other MVs. This is probably because of low velocities of fluid flow coupled with efficient microbial methanotrophy. Microbial methanotrophy (or AOM) has been observed at almost all seep sites; understanding the controls on this process is therefore of urgent need if we are to properly quantify the impact of cold seeps on the global methane budget.

Chapter 4

Authigenic barite as a proxy for past methane emissions at the Carlos Ribeiro mud volcano, Gulf of Cadiz

4.1 Introduction

Large quantities of organic matter reach the seafloor along most continental margins and, over time, burial of this carbon results in the formation of hydrocarbons: biogenic methane (CH_4) in the shallow sub-surface and thermogenic methane and higher hydrocarbons at depth. The build up of large quantities of gas at depth causes overpressure within the sediment column resulting in the upward migration of hydrocarbons. While upward migration is usually driven by diffusion, advection can be dominant in some systems, such as cold seeps including mud volcanoes (MVs), which are usually confined to areas of tectonic activity (Dimitrov, 2002; Judd et al., 2007; Milkov, 2000; Milkov et al., 2003). Mud volcanoes are of particular interest as they are extremely efficient in transporting hydrocarbons (especially methane) along conduits to the overlying water column (Dimitrov, 2002). Furthermore, new mud volcanoes and cold seeps are being discovered all the time. Therefore it is important to understand the dynamic nature of cold seeps to estimate their impact on the methane budget of the ocean and, potentially, the atmosphere. Authigenic barite ($BaSO_4$) has been shown to be a useful proxy for assessing past fluxes of methane gas on continental margins (Dickens, 2001). The gas-charged fluids seeping in these areas generally lack sulphate (SO_4^{2-}) but contain elevated concentrations of dissolved barium (Ba^{2+}) (Torres et al., 1996b). During the ascent of these fluids through the sediment column, barite precipitates on contact with downward-diffusing seawater sulphate close to and/or at the seafloor (Aquilina et al., 1997; Fu et al., 1994; Gingele and Dahmke, 1994; Kasten et al., 2003; Torres et al., 1996a):

$$Ba^{2+} + SO_4^{2-} \quad \leftrightarrow \quad BaSO_4 \tag{4.1}$$

The pore water sulphate gradient at MVs is typically regulated by the methane flux from depth via the anaerobic oxidation of methane (AOM) at the Sulphate-Methane Transition (SMT; e.g. Aloisi et al., 2002; Bohrmann et al., 2003; Borowski et al., 1999; de Beer et al., 2006; Haese et al., 2003; Niemann et al., 2006a; Werne et al., 2004:

$$CH_4 + SO_4^{2-} \quad \rightarrow \quad HCO_3^- + HS^- + H_20 \tag{4.2}$$

As authigenic barite builds up just above the depth of sulphate depletion, they record the depth of the SMT and thus can potentially be used to document the history of gas venting at cold seep sites (Dickens, 2001; Kasten et al., 2003; Snyder et al., 2007a; Von Breymann et al., 1992a). A wide assortment of cold seep barite precipitates have been described: these vary from microcrystalline phases in sediments from the Peru Margin, Japan Sea (Torres et al., 1996b) and Aleutian subduction zone (Suess et al., 1998); nodules, crusts and dispersed concretions in the Monterey Canyon (Naehr et al., 2000b) and Gulf of Mexico (Castellini et al., 2006); to blocks and columns up to 10 m high in the Sea of Okhotsk (Greinert et al., 2002) and along the San Clemente fault (Lonsdale, 1979; Torres et al., 2002). Other authigenic minerals can also be found in association with the SMT; these include carbonates and pyrite. Their formation is triggered by AOM as this reaction increases the alkalinity and hydrogen sulphide concentrations within the pore fluids (Ritger et al., 1987).

$$Ca^{2+} + 2HCO_3^- \quad \leftrightarrow \quad CaCO_3 + CO_2 + H_2O \tag{4.3}$$

Carbonates formed as a result of AOM occur as crust pavements, chimneys and as carbonate horizons in the sediments, at the depth of SMT (e.g. Aloisi et al., 2000; Matsumoto, 1990; Mazzini et al., 2004; Naehr et al., 2000a). Similarly to barites that form at cold seeps, carbonate chimneys generally form at seeps that are characterised by high methane fluxes (e.g. 20-110 cm yr^{-1}; Aloisi et al., 2004b; Greinert et al., 2001, 2002), while authigenic horizons in sediments reflect gentle expulsion regimes (e.g. < 5 cm yr^{-1}; Aloisi et al., 2004c,a,b; Berelson et al., 2005; Rodriguez et al., 2000). Cold seep barite usually occurs with minor amounts of detrital silicates and pyrite (Torres et al., 2003), but the proportion of carbonate can range from low (San Clemente sites; Torres et al., 2002) to very high (Peru margin and Sea of Okhotsk; Aquilina et al., 1997; Dia et al., 1993; Greinert et al., 2002; Torres et al., 1996a). It is the competition between barium and methane for sulphate that controls the mineralogy of the authigenic precipitates: at low dissolved methane/barium ratios barite precipitation dominates whereas at higher methane/barium ratios the rate of anaerobic oxidation of methane increases promoting the formation of cal-

cium carbonate (Aloisi et al., 2004b). Accordingly, the morphology and mineralogy of cold seep precipitates gives clues as to the hydrological and biogeochemical conditions within the sediment column at the time of precipitation.

To date, only a handful of studies have used authigenic minerals (such as barite) as a proxy for the periodicity of mud volcanism (Castellini et al., 2006). Here, solid phase and dissolved element profiles in sediments from the Carlos Ribeiro mud volcano are combined with a numerical 1-D transport-reaction model to determine the methane flux dynamics at Carlos Ribeiro MV. In addition, radiocarbon dating of the hemipelagic drape on top of the Carlos Ribeiro mud volcano is used to provide additional insight as to the mud extrusion history of the mud volcano.

4.2 Methods

4.2.1 Sample collection

A suite of sediment cores were recovered from the Carlos Ribeiro MV during the RRS *James Cook* Cruise 10 (May 13th through June 7th, 2007). These include piston, gravity and multi cores from four sites along a transect that connects the eye of the MV to mudflow pathways to the southeast of the summit (Fig. 4.1 and Table 3.1). For comparison, a background site 2.9 km SW of the CRMV was cored. Upon retrieval, piston and gravity cores were immediately sampled every 20 cm, and multi cores were sliced into 1-3 cm sections in a cold room (∼6°C) onboard the ship. Sediment samples for porosity determinations were stored in airtight containers for onshore analyses. Pore waters were immediately extracted in a glove bag under a N_2-atmosphere by pressure-filtration through 0.2μm cellulose acetate membrane filters, with a N_2-pressure of 3-4 bars.

4.2.2 Onshore analyses

4.2.2.1 Pore fluid analyses

Pore water barium ($[Ba^{2+}]$), calcium ($[Ca^{2+}]$), strontium ($[Sr^{2+}]$) and magnesium ($[Mg^{2+}]$) concentrations were determined by inductively coupled plasma optical emission spectroscopy (ICP-OES; Perkin Elmer Optima 4300DV). The external reproducibility of these analyses, determined by repeat analyses (n=3) of IAPSO seawater, a seawater standard (CRM) and four pore water samples, is within 4%.
Note that per site, one pore water concentration-depth profile is shown in this chapter. This profile is a compilation of the pore water data recovered from all sediment cores at each site (Table 3.1). For most sites this is a piston or gravity core and a multi core

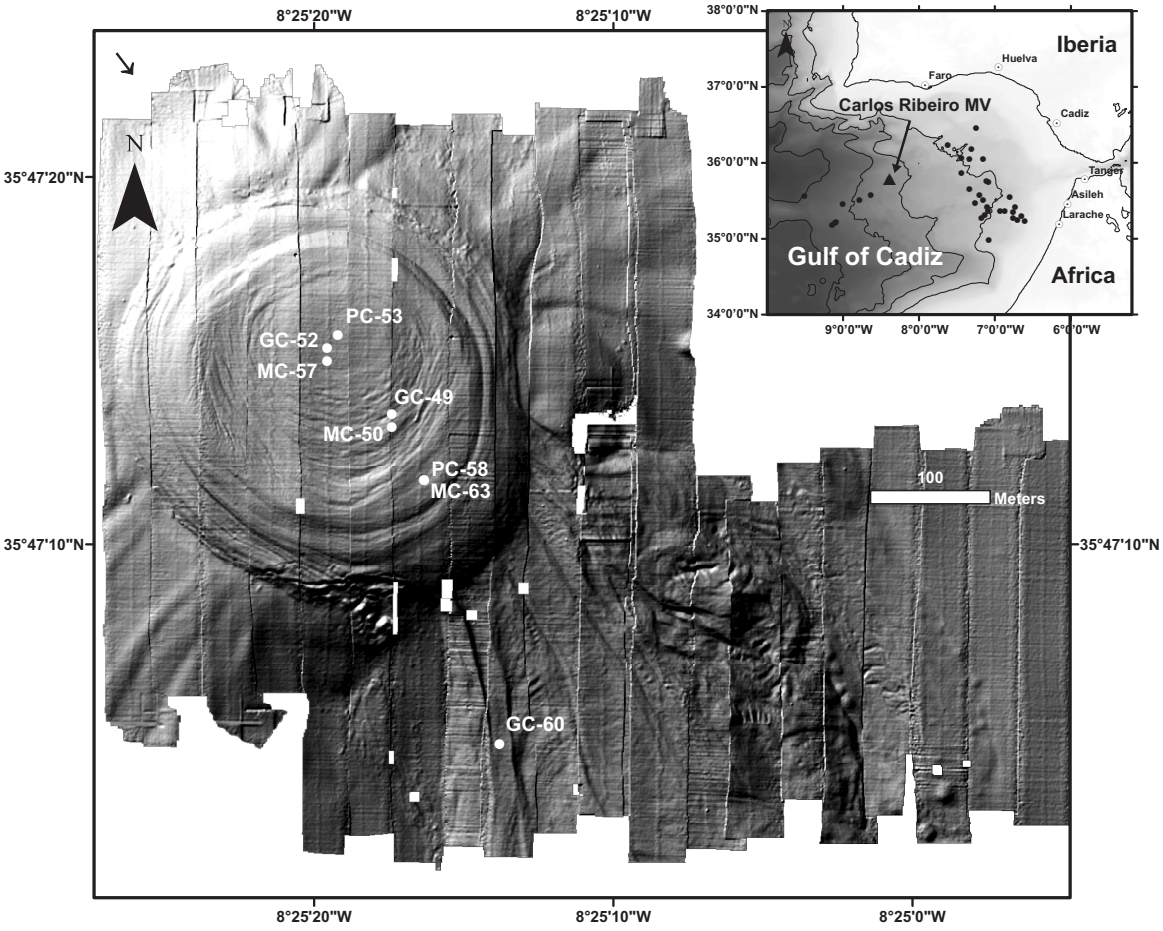

Figure 4.1 Shaded relief map of the Carlos Ribeiro mud volcano and its location within the Gulf of Cadiz (on the top right) showing the location of the studied core sites.

while for the eye site, pore water concentration-depth profiles were combined from a piston (PC-53), gravity (GC-52) and a multi core (MC-57).

4.2.2.2 Sediment analyses

To optimize the sediment sampling strategy, piston (PC-43 and 58) and gravity (GC-52, 49 and 60) cores were analysed using the ITRAX core scanner housed by BOSCORF at NOCS. This is a non-destructive method which provides in addition to optical and microdensity (X-radiography) information, preliminary geochemical data. The latter is acquired by the build-in X-ray fluorescence (XRF) spectrometer. As the XRF data are output as counts, the ITRAX provides geochemical data of semi-quantitative nature (Croudace et al., 2006). Calibrations were not performed during this study and thus the obtained XRF element profiles give only an indication of down-core geochemical changes. The voltage and current of the X-ray source, a 3kW Mo tube, was set to 30 kV and 30 mA respectively. A measurement step-size of 1000 μm and exposure time of 40s were used. The obtained data was processed using Q-Spec software (Croudace et al., 2006).

Based on the XRF data (shown in Figures 4.2-4.4d), 39 sediment samples were selected to measure the major and minor element composition of the sediment. The samples were taken either from the sediment core or from the squeeze-cakes (i.e. the sediment leftover after pore fluid extraction), dried in an oven at 50-60°C for 24 hours and ground to a powder using an agate mortar and pestle. Approximately 0.1 g of sediment was weighed out and subjected to a combined Aqua Regia, HF and $HClO_4$ total digestion and analysed by ICP-OES using a Perkin Elmer Optima 4300V ICP-OES at NOCS. Ba, Ca, Sr, Mg, Ti (titanium), Al (aluminium) and Fe (iron) data are presented here and the analytical reproducibility, based on replicate analyses (n=3) of five sediment samples is better than 2%. The accuracy of the measurements was assessed by analysis of two international certified reference materials (MAG-1 and Sco-1), and is better than 6%.

The total inorganic carbon content was determined in 24 sediment samples using a UIC CM 5012CO2 coulometer. Each sample was treated with 10% phosphoric acid to let the inorganic carbon evolve into CO_2. The carbonate content is then calculated from the measured TIC concentrations:

$$Carbonate(wt\%) = TIC \cdot \frac{60.01}{12.01} \tag{4.4}$$

Repeat analyses (n=3) of two sediment samples consistently gave concentrations within 1%.

In addition to barite, Ba can also be found in association with other sedimentary phases. Examples include witherite ($BaCO_3$), calcium carbonate ($CaCO_3$) and ferromanganese oxyhydroxides and clays (Gonneea and Paytan, 2006; Rutten and de Lange, 2002). Three of the sediment samples from the mudflow station (one from each of the Ba-enriched sediment layers) were therefore subjected to a sequential leaching procedure (Eagle et al., 2003; Paytan et al., 1993) to separate the barite grains. These samples were weighed and sequentially digested with acetic acid, sodium hypochlorite, hydroxylamine hydrochloride and an HNO_3: HF mixture. The residues were then treated with a 1:1 mixture of saturated $AlCl_3$ and HNO_3 (1 M) and subsequently ashed in a muffle furnace at 700 °C for 1 hour. After extraction the residual material was mounted onto a metal stub, coated with gold and examined using a Leo 1450VP Scanning Electron Microscope (SEM) equipped with an Energy Dispersive Spectrometer (EDS) at NOCS.

4.2.3 Radiocarbon analyses

Three cores from the eye (MC-57), the margin (MC-63) and the mudflow (GC-60) sites on the mud volcano were subsampled for radiocarbon analyses. The aim of these analyses was to determine the age of the mud extrusion episodes that build up the MV. Approximately $\sim$10 cm^3 of hemipelagic sediment (i.e. the sediment that sits on the top of the mud breccia) from each core was washed through 250 and 150 μm sieves with MILLI-Q water

and dried under a hot lamp. 10-15 mg of planktonic foraminifera were picked from each sample, coated in graphite at the NERC Radiocarbon Facility (Environment) in Scotland and analysed for ^{14}C at the SUERC AMS Laboratory. The age of the samples is reported in conventional radiocarbon years BP (i.e. relative to AD 1950), and converted to the calendar year timescale by applying the Marine04 dataset (Hughen et al., 2004). This was achieved using the calibration program CALIB 5.0 which incorporates a time-dependent global ocean reservoir correction of about 400 years (Stuiver and Reimer, 1993). The range in the calibrated radiocarbon age represents the 95% confidence interval (i.e. 2σ) of the analyses (Table 4.3).

4.2.4 Geochemical Modelling

A 1-D transport model, described in detail in Chapter 3, is applied to Ca^{2+}, Mg^{2+}, Ba^{2+} and Sr^{2+} pore water concentration-depth profiles to study sediment-pore fluid interactions at the Carlos Ribeiro MV. The same fluid flow velocities (u_0) and irrigation parameters determined in Chapter 3 for each site (as well as any other model setting), are used to generate the pore fluid profiles for Ca^{2+}, Mg^{2+}, Ba^{2+} and Sr^{2+} (Table 4.1). Note that this model only accounts for advection, diffusion and irrigation. Accordingly, the modelled pore fluid profiles for Ca^{2+}, Mg^{2+}, Ba^{2+} and Sr^{2+} do not take into account any chemical reactions between the pore fluids and the sediments. This is important because, unlike chloride, sodium and boron, Ca^{2+}, Mg^{2+}, Ba^{2+} and Sr^{2+} are known to be involved in diagenetic reactions at cold seeps, such as the precipitation of calcium carbonate, dolomite and barite. Thus, it can be expected that the model generated pore fluid profiles will not always match the measured pore fluid data for these elements. However, any discrepancies between the modelled and measured pore fluid data can be used to reveal whether exchange of Ca^{2+}, Mg^{2+}, Ba^{2+} and Sr^{2+} between the pore fluids and sediments was occurring, at the time of sampling.

4.3 Results

4.3.1 Element pore fluid profiles

Fig. 4.2 and 4.3 show pore fluid concentration-depth profiles for Ba^{2+} and SO_4^{2-} from respectively the four sites on CRMV and the background site. A detailed description of the pore fluid SO_4^{2-} data is given in Chapter 3. Pore fluid Ca^{2+}, Mg^{2+} and Sr^{2+} data are shown in figures 4.3 and 4.4a-4.4d. For all sites on the MV, there is no change in pore fluid $[Ba^{2+}]$ in the uppermost 50 cm of the sediment column, and the concentration of Ba^{2+} is low ($< 1\mu$M). Below 50 cm depth, dissolved Ba^{2+} concentrations rise. At the mudflow and margin sites, the increase in $[Ba^{2+}]$ is more gradual than it is at the eye

Table 4.1 Parameter values used in the numerical model.

Parameter	Symbol	Unit	Eye	Off-centre	Margin	Mudflow
Molecular diffusion coefficient of calcium[a]	D_{Ca}	[cm^2 yr^{-1}]	132.29			
Molecular diffusion coefficient of magnesium[a]	D_{Mg}	[cm^2 yr^{-1}]	122.59			
Molecular diffusion coefficient of barium[a]	D_{Ba}	[cm^2 yr^{-1}]	145.83			
Molecular diffusion coefficient of strontium[a]	D_{Sr}	[cm^2 yr^{-1}]	133.72			
Length of model column[b]	L	[cm]	500.5	110	217	179.5
Porosity at sediment surface[c]	φ_0		0.75	0.76	0.75	0.69
Porosity at lower boundary[c]	φ_∞		0.58	0.57	0.53	0.51
Attenuation coefficient for porosity decrease[c]	β	[cm^{-1}]	0.0605	0.08	0.05	0.04
Upward fluid flow velocity[d]	u_0	[cm yr^{-1}]	4	3.3	0.4	0
Irrigation depth[d]	x_{mix}	[cm]	32	32	40	50
Irrigation mixing coefficient[d]	α'	[yr^{-1}]	3.1	2.5	0.6	0.6
Ca^{2+} concentration at sediment surface[e]	Ca0	[mM]	11	10.6	10.5	10.1
Ca^{2+} concentration at depth L[e]	CaL	[mM]	1.9	2.1	3.2	5.5
Mg^{2+} concentration at sediment surface[e]	Mg0	[mM]	56.9	54.4	54.3	52
Mg^{2+} concentration at depth L[e]	MgL	[mM]	2.1	2.5	6.3	17.1
Ba^{2+} concentration at sediment surface[e]	Ba0	[mM]	0.7	0.2	0.3	0.5
Ba^{2+} concentration at depth L[e]	BaL	[mM]	43.3	49	68.3	28
Sr^{2+} concentration at sediment surface[e]	Sr0	[mM]	91.1	88.7	87.1	91.4
Sr^{2+} concentration at depth L[e]	SrL	[mM]	148	167	263	515

[a] Calculated from equations given in (Boudreau, 1997) considering the in situ T (4.3°C), S (34.2) and P (220 bar) conditions.
[b] Length of the pore water profile.
[c] Obtained by least square fitting an exponential equation $\varphi(x) = (\varphi_0 - \varphi_\infty)e^{(-\beta x)} + \varphi_\infty$ to the measured porosity depth profile (Fig. 3.5).
[d] Derived by fitting the transport model results to pore water profiles of conservative elements Cl^-, Na^+ and B (see Chapter 3).
[e] Measured in pore waters extracted from sediment cores from this study.

and off-centre sites. The depth of the increase in $[Ba^{2+}]$ differs at each site and coincides with the depth of the SMT (Fig 4.2). The maximum concentration of Ba^{2+} in the pore fluids is lowest at the mudflow site (28 μM) and highest at the margin site (78 μM). At the eye and mudflow stations Ba^{2+} concentrations are no higher than 47 μM and 52 μM, respectively. The pore fluid Ba^{2+} profile at the margin site shows one excursion consisting of a drop in $[Ba^{2+}]$ to a value of 27 μM. Note that the two excursions at the eye site are an artefact of combining pore fluid data from PC-53 and and GC-52 into one profile (Figure E.7 in Appendix E). The dissolved Ba^{2+} concentration at the background site is <0.5 μM throughout the core (Fig 4.3).

Concentrations of Ca^{2+} and Mg^{2+} in the pore fluids gradually decrease with depth at all sites, from seawater concentrations near the seafloor down to 2 - 6 mM Ca^{2+} and 2 - 17 mM Mg^{2+} at the base of the cores. Pore fluid Sr^{2+} concentrations are higher than measured in background seawater, in the deeper sections of the cores at all sites. At the mudflow site, $[Sr^{2+}]$ is ~6 times higher than it is in seawater, the highest value recorded in all of the pore fluids from the CRMV. The pore fluid profile at the eye station shows an enrichment in $[Sr^{2+}]$, relative to seawater, at 56 cm depth.

4.3.2 Sediment chemistry

Ba concentration profiles measured by the ITRAX XRF as well as the measured Ba content and Ba/Ti ratio of the sediments from the CRMV are shown in Fig. 4.2; profiles of sedimentary Ca, Mg, Sr and Fe for all sites are given in figures 4.4a-4.4d and in Fig. 4.3 for the background site. The XRF profiles coincide well with the measured sediment element/Ti profiles for all elements at all sites, with exception of Ba at the off-centre site. Accordingly, the X-ray fluorescence data appear to reliably reflect the elemental composition of the sediments at the CRMV.

Bulk sediment Ba concentrations range from 129 to 1740 ppm. The eye and background site show little variation in sedimentary Ba content throughout the core, with an average [Ba] value of, respectively, 266 and 403 ppm (Table 4.2). Higher [Ba] values are recorded at the other sites, although these are confined to narrow (13-27 cm) depth intervals. The off-centre site shows one Ba peak of 617 ppm at 25 cm depth. Note that because of the offset between the XRF and the measured Ba profile at the off-centre site, this peak is not considered in the discussion below. A maximum Ba concentration of 1740 ppm was measured at 18 cm depth at the margin site, while three Ba peaks occur at the mudflow site i.e at 45 (407 ppm), 85 (785 ppm) and 130 cm (748 ppm, excluding carbonate concretion shown in Fig. 4.5) depth (Table 4.2). The lowest [Ba] in sediments from the

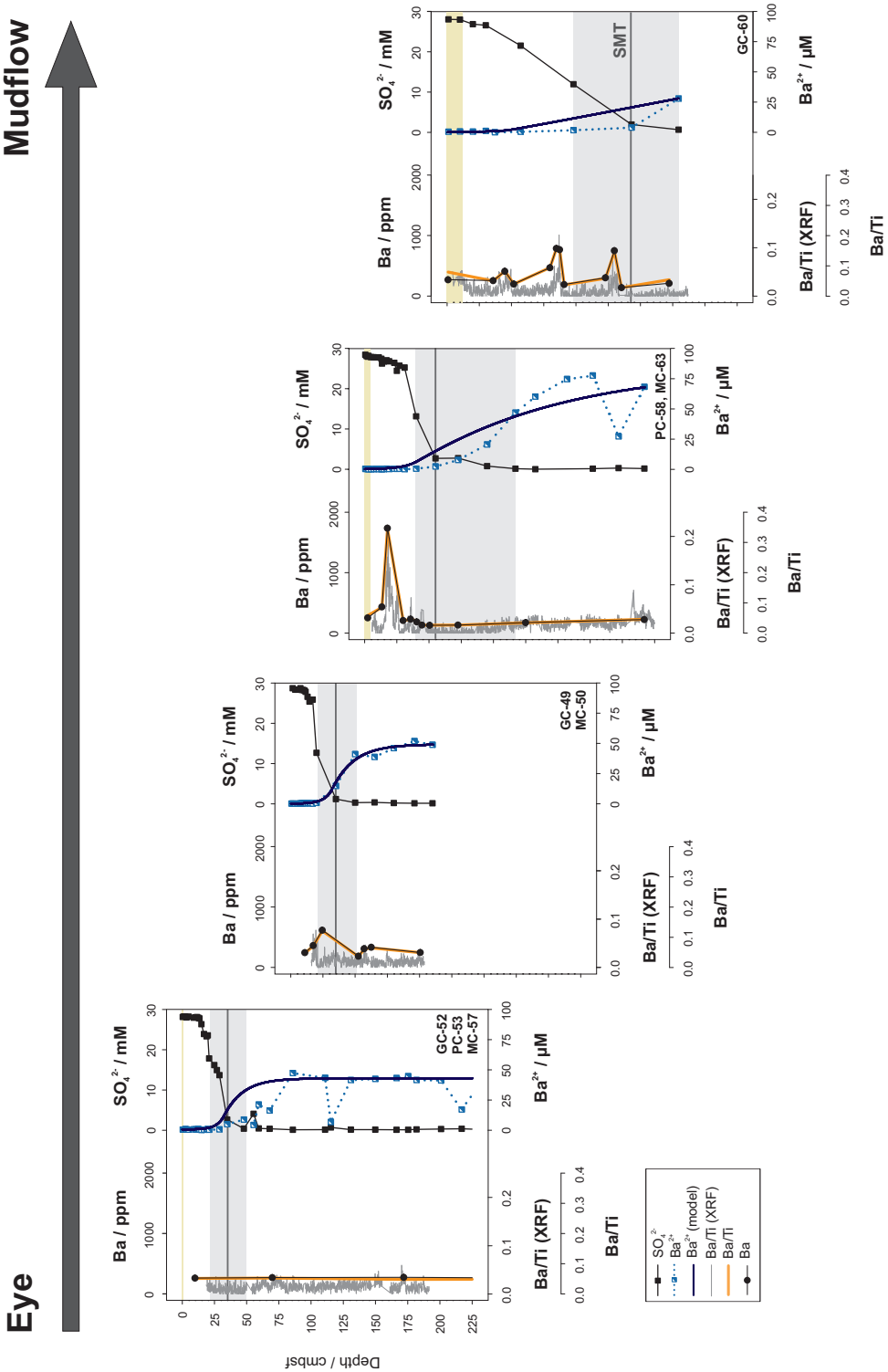

Figure 4.2 Profiles of solid phase barium (Ba), Ba/Ti, Ba/Ti (XRF), dissolved Ba^{2+}, SO_4^{2-} and results of numerical modelling of dissolved Ba^{2+} profiles for the four stations at the Carlos Ribeiro mud volcano investigated in this study. The yellow and grey areas represent the hemipelagic veneer and the sulphate-methane transition zone (SMTZ; ref. Chapter 3), respectively. The dark gray line indicates the depth of the SMT, i.e. the shallowest depth of sulphate depletion.

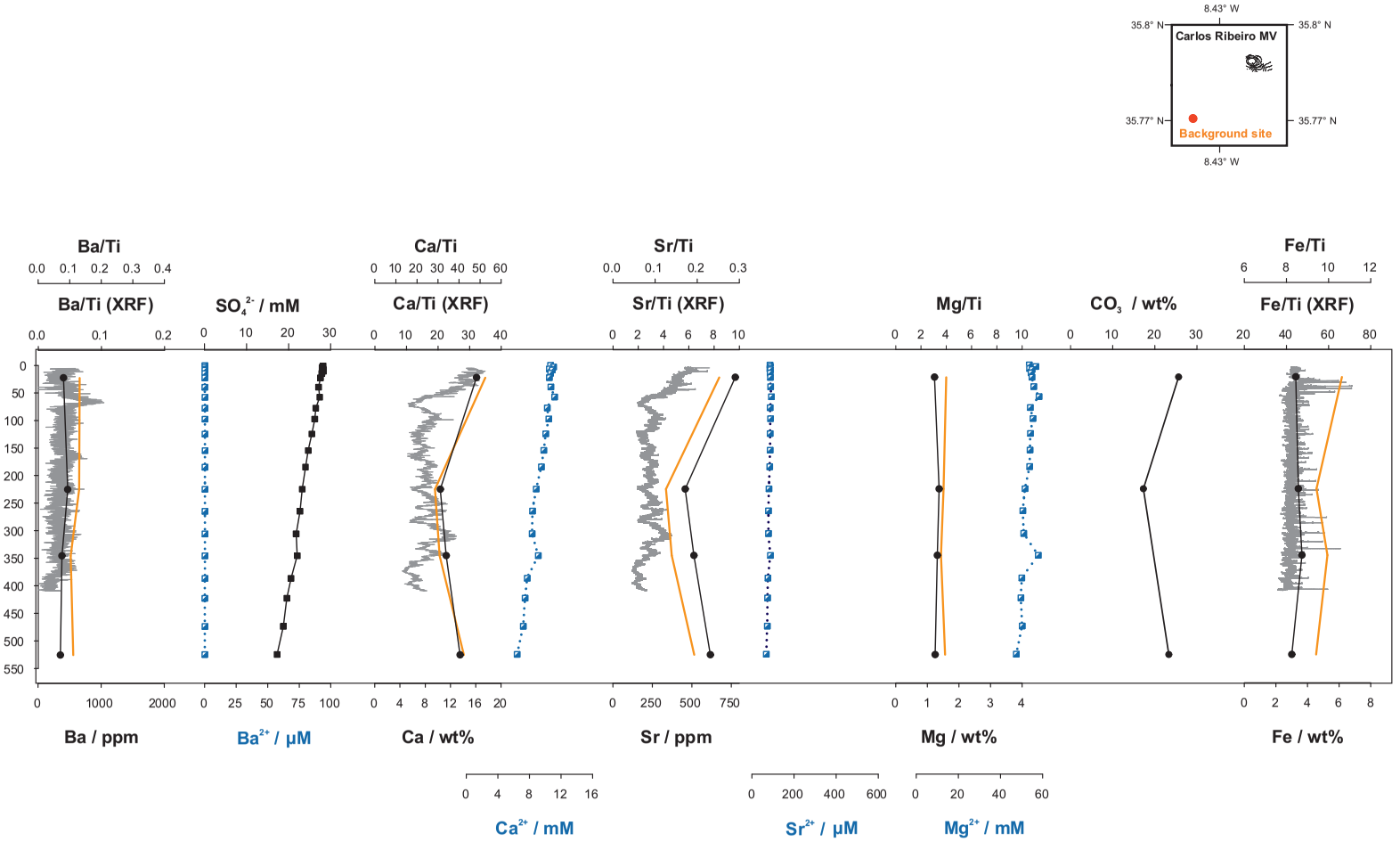

Figure 4.3 Profiles of solid phase barium (Ba), calcium (Ca), strontium (Sr), magnesium (Mg), iron (Fe) and carbonate (CO_3), Ba/Ti, Ba/Ti (XRF), Ca/Ti, Ca/Ti (XRF), Sr/Ti, Sr/Ti (XRF), Fe/Ti, Fe/Ti (XRF), Mg/Ti, dissolved Ba^{2+}, Ca^{2+}, Sr^{2+}, Mg^{2+} and SO_4^{2-} for the background site located 2.9 km SW of the Carlos Ribeiro mud volcano.

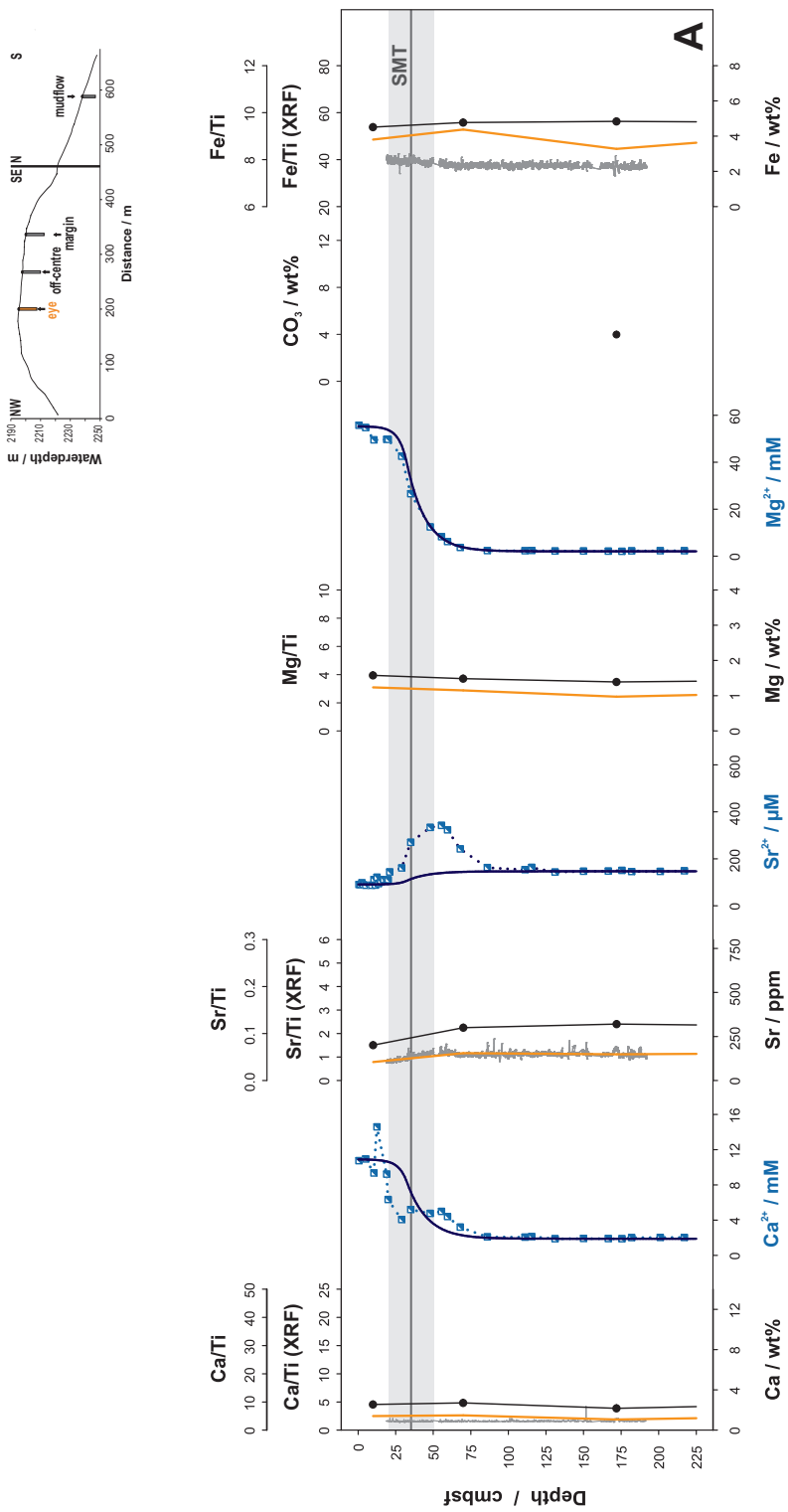

Figure 4.4a Profiles of solid phase calcium (Ca), strontium (Sr), magnesium (Mg), iron (Fe) and carbonate (CO_3), Ca/Ti, Ca/Ti (XRF), Sr/Ti, Sr/Ti (XRF), Fe/Ti, Fe/Ti (XRF), Mg/Ti, dissolved Ca^{2+}, Sr^{2+} and Mg^{2+} for the eye site at the Carlos Ribeiro mud volcano. The light grey area represents the sulphate-methane transition zone (SMTZ). Solid dark blue lines shown on profiles of dissolved constituents represent modelled data.

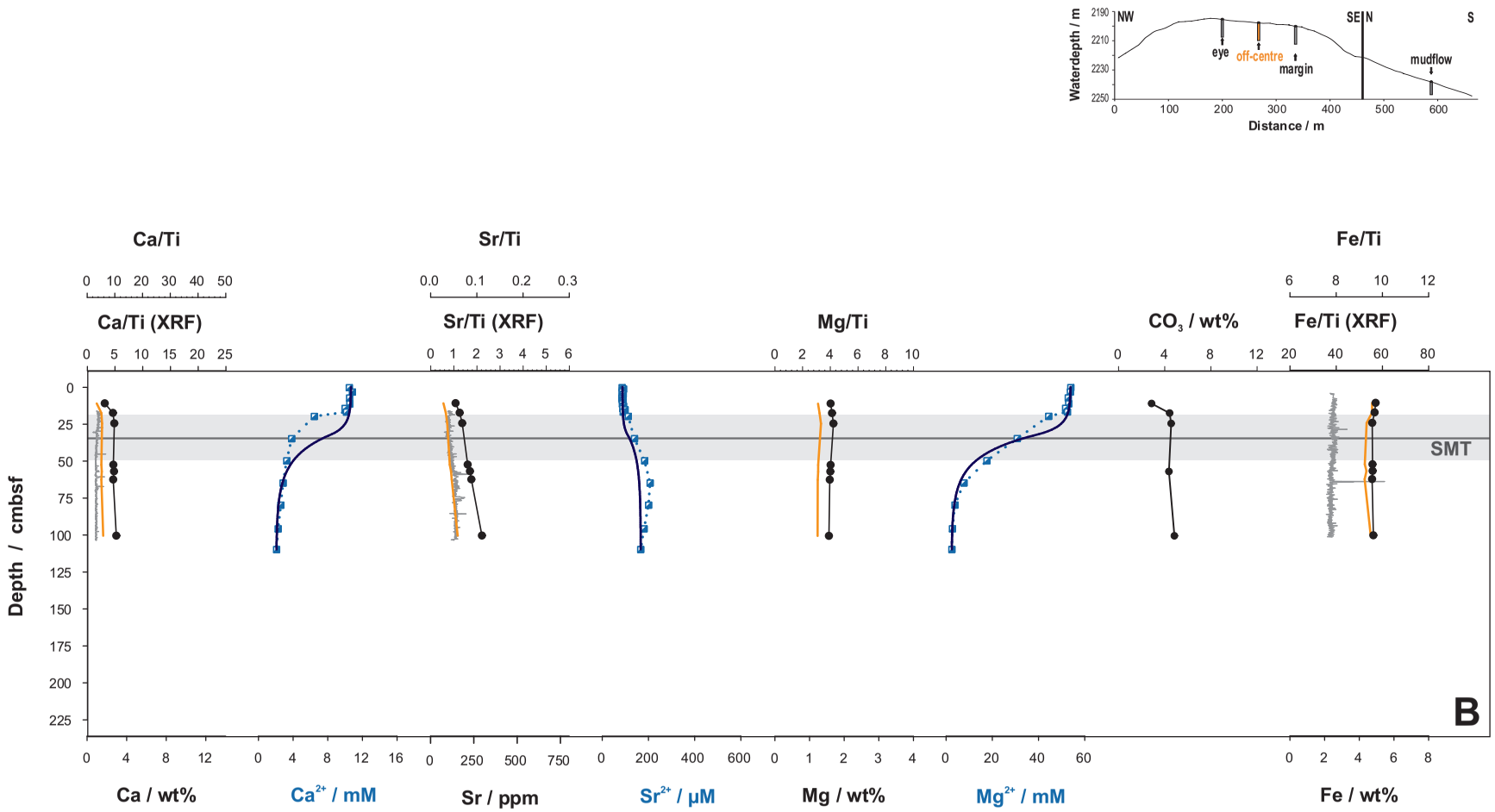

Figure 4.4b Profiles of solid phase calcium (Ca), strontium (Sr), magnesium (Mg), iron (Fe) and carbonate (CO_3), Ca/Ti, Ca/Ti (XRF), Sr/Ti, Sr/Ti (XRF), Fe/Ti, Fe/Ti (XRF), Mg/Ti, dissolved Ca^{2+}, Sr^{2+} and Mg^{2+} for the off-centre site at the Carlos Ribeiro mud volcano. The light grey area represents the sulphate-methane transition zone (SMTZ). Solid dark blue lines shown on profiles of dissolved constituents represent modelled data.

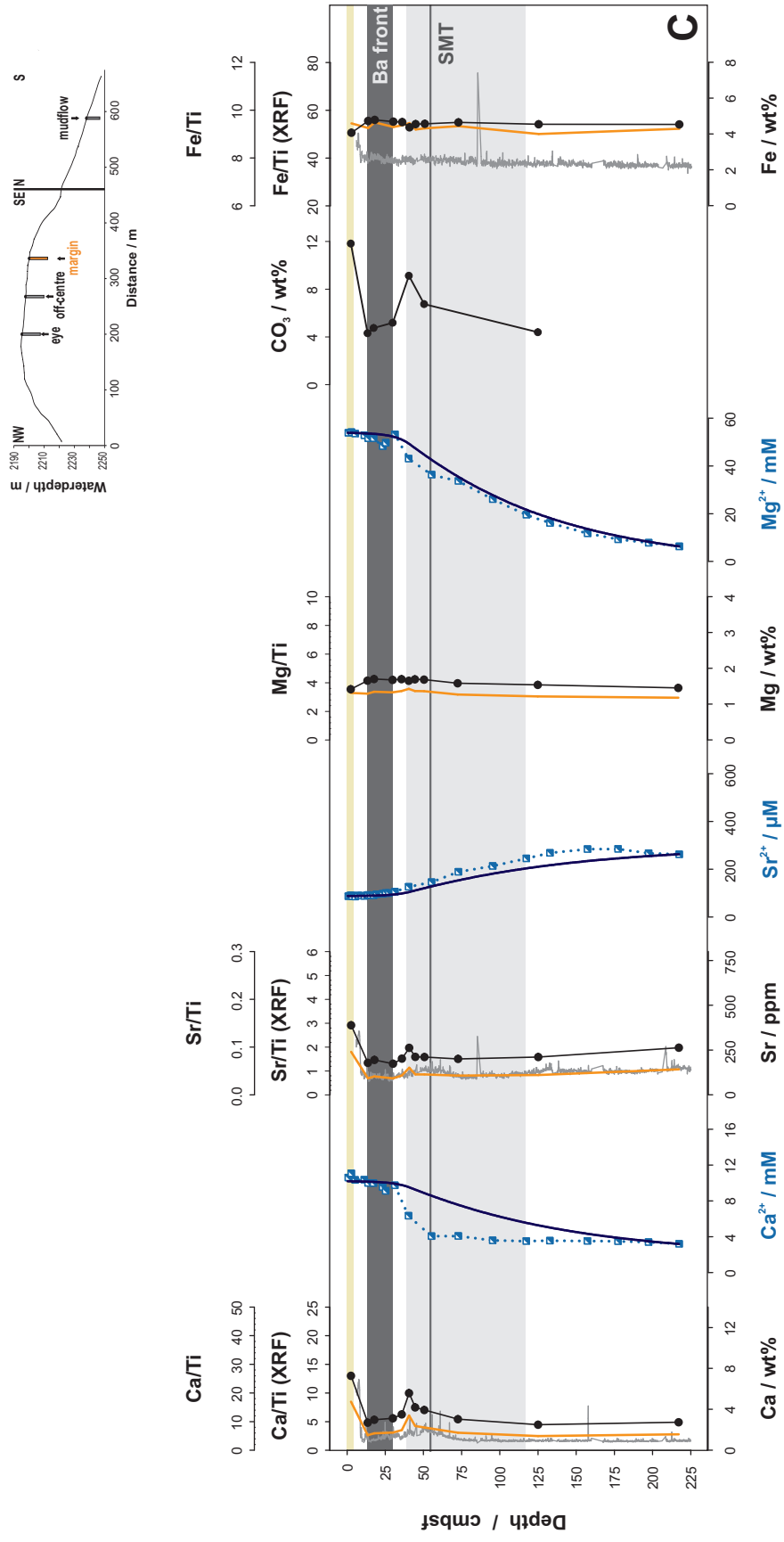

Figure 4.4c Profiles of solid phase calcium (Ca), strontium (Sr), magnesium (Mg), iron (Fe) and carbonate (CO_3), Ca/Ti, Ca/Ti (XRF), Sr/Ti, Sr/Ti (XRF), Fe/Ti, Fe/Ti (XRF), Mg/Ti, dissolved Ca^{2+}, Sr^{2+} and Mg^{2+} for the margin site at the Carlos Ribeiro mud volcano. The yellow, light grey and dark grey areas represent respectively hemipelagic veneer, the sulphate-methane transition zone (SMTZ) and the location of Ba fronts at each site. Solid dark blue lines shown on profiles of dissolved constituents represent modelled data.

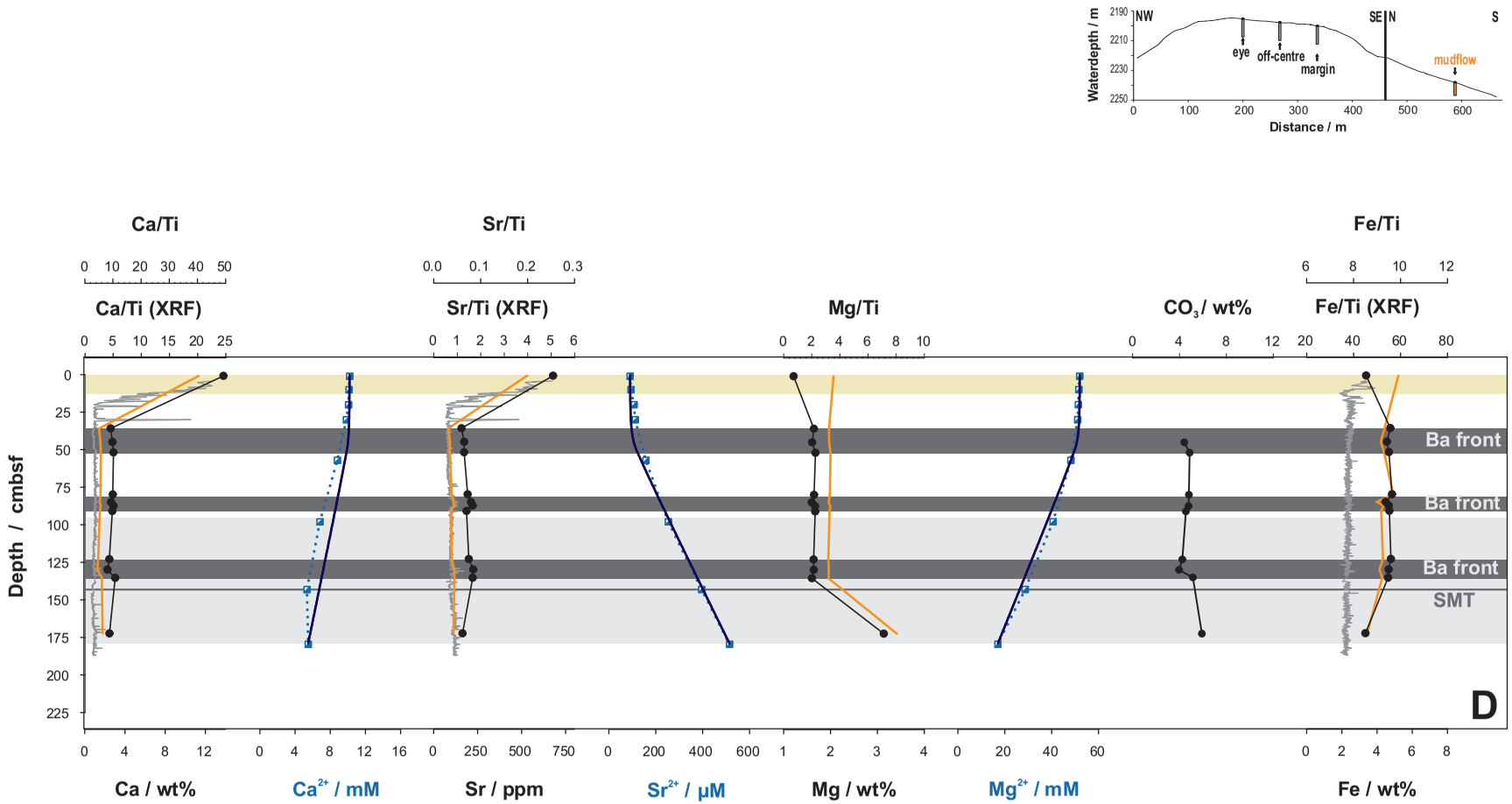

Figure 4.4d Profiles of solid phase calcium (Ca), strontium (Sr), magnesium (Mg), iron (Fe) and carbonate (CO_3), Ca/Ti, Ca/Ti (XRF), Sr/Ti, Sr/Ti (XRF), Fe/Ti, Fe/Ti (XRF), Mg/Ti, dissolved Ca^{2+}, Sr^{2+} and Mg^{2+} for the mudflow site at the Carlos Ribeiro mud volcano. The yellow, light grey and dark grey areas represent respectively hemipelagic veneer, the sulphate-methane transition zone (SMTZ) and the location of Ba fronts at each site. Solid dark blue lines shown on profiles of dissolved constituents represent modelled data.

CRMV are measured just below the enriched horizons. The highest [Ba] was measured in a concretion that was found embedded in the sediment at 130 cm depth at the mudflow site (Fig. 4.5). From the chemical data it is clear that this concretion is mainly composed of $CaCO_3$, and it seems likely that the high Ba concentrations can be attributed to the occurrence of transparent-white crystals of barite, on the side of the concretion (Fig 4.5; see below).

Primary elemental Composition

Weight %	
Ca	30.5
Mg	0.5
Al	1.5
Ti	0.1
Fe	1.2
CO_3	50
ppm	
Sr	946
Ba	4940

Figure 4.5 On the left: photograph of carbonate concretion with white-transparent barite crystals, recovered from sediment core GC-60 at the mudflow site at 130 cmbsf (Carlos Ribeiro mud volcano). On the right: elemental composition of the concretion.

In general, the sediments have relatively homogenous concentrations of Ca, Mg, Sr and Fe, while Ba is more variable (Fig. 4.4a-4.4d). At the eye and off-centre sites there is little variation in the chemical composition of the sediments. Further away from the centre of the MV, high Ca and Sr concentrations are recorded in material at the top of the core, in the hemipelagic layer. The Ca and Sr contents of the mud breccia underneath are, respectively, ∼4.5 and ∼2.5 times lower (Table 4.1). At 40 cm depth, just above the SMTZ, Ca and Sr sediment profiles of the margin station show a slight enrichment with concentrations of, respectively, 5.6 wt% and 261.9 ppm (Fig. 4.4c). This corresponds with an increase in the CO_3 concentration in the sediments. The sedimentary Mg concentration at the mudflow site slightly increases with depth at 173 cm; at the same depth, [Fe] decreases (Fig. 4.4d).

Downcore variations in the chemical composition of sediments not only reflect the precipitation or dissolution of mineral phases, they can also reflect changes in the relative proportion of different primary minerals. These primary minerals commonly include aluminosilicates (i.e. clays), which usually contain Mg, Ca, Fe, Sr and Ba in their crystal lattice, raising the possibility that variations in the concentrations of these elements in

Table 4.2 Elemental composition of sediments from Carlos Ribeiro MV

Core	Depth cm	Ca wt%	Mg wt%	Al wt%	Ti wt%	Fe wt%	CO3 wt%	Ba ppm	Sr ppm
Background site									
PC-43	23	16.1	1.2	5.5	0.3	3.3	26	405	775
PC-43	225.5	10.4	1.4	6.3	0.4	3.4	17	473	458
PC-43	346	11.3	1.3	6.2	0.4	3.7		380	514
PC-43	526	13.5	1.3	5.6	0.3	3	23	356	617
On Carlos Ribeiro MV									
GC-52	10	2.5	1.6	8.5	0.5	4.5		264	201
GC-52	70	2.7	1.5	8.6	0.5	4.8		273	301
GC-52	172	2.2	1.4	8.8	0.6	4.8	4	277	321
PC-53	372.5	2.8	1.5	8.2	0.5	4.8		256	300
PC-53	507.5	2.5	1.5	8.6	0.5	4.7	5	259	290
GC-49	11.5	1.8	1.6	8.9	0.5	4.9	3	245	145
GC-49	17.5	2.6	1.7	8.9	0.5	4.9	4	363	169
GC-49	24.5	2.8	1.7	8.8	0.5	4.8	5	617	184
GC-49	52.5	2.7	1.6	8.9	0.5	4.8		186	215
GC-49	57	2.7	1.6	8.9	0.5	4.8	4	311	228
GC-49	62.5	2.7	1.6	9	0.5	4.7		333	236
GC-49	100.5	3	1.6	8.8	0.5	4.8	5	248	297
PC-58	2.5	7.3	1.4	7.3	0.4	4.1	12	253	388
PC-58	13.5	2.7	1.7	8.6	0.5	4.7	4	435	179
PC-58	17.75	3	1.7	8.7	0.5	4.8	5	1740	195
PC-58	30	3.1	1.7	8.8	0.5	4.7	5	209	174
PC-58	35.75	3.5	1.7	8.7	0.5	4.7		230	202
PC-58	40.5	5.6	1.7	8.1	0.5	4.4	9	186	262
PC-58	44.5	4.2	1.7	8.6	0.5	4.5		132	212
PC-58	50.5	3.9	1.7	8.6	0.5	4.6	7	129	211
PC-58	72.5	3	1.6	8.2	0.5	4.6		133	200
PC-58	125	2.5	1.5	8.4	0.5	4.5	4	174	211
PC-58	217	2.7	1.5	8.2	0.5	4.5		224	263
GC-60	1	13.8	1.2	6	0.3	3.4		268	680
GC-60	36	2.6	1.7	9	0.5	4.8		253	159
GC-60	45	2.8	1.6	8.5	0.5	4.6	4	407	174
GC-60	52	2.9	1.7	8.8	0.5	4.7	5	197	174
GC-60	80	2.8	1.7	8.8	0.5	4.9	5	467	194
GC-60	85	2.6	1.6	8.5	0.5	4.5	5	785	213
GC-60	87.5	2.9	1.7	8.7	0.5	4.7	5	765	222
GC-60	91	2.8	1.7	8.9	0.5	4.7	5	188	187
GC-60	123	2.5	1.6	9	0.5	4.8	4	299	200
GC-60	130	2.3	1.7	8.6	0.5	4.7	4	748	226
GC-60	135.5	3	1.6	8.7	0.5	4.6	5	136	223
GC-60	172.5	2.5	3.1	5.9	0.4	3.3	6	208	165

sediments from the CRMV reflect variations in the clay content of the sediments. In this connection, it is important to note that the main component of mud breccia is clay. In order to negate the effect of variable clay content on the chemical composition of the sediments, element concentrations are normalised to Ti, a refractory element and major component of clays. Although Al normalisation is more common in sedimentary data analysis (Van der Weijden, 2002), it is not applied in this study because the ITRAX core scanner sensitivity for Al is imprecise at the present time (Croudace et al., 2006). Therefore, in order to link the XRF data with the bulk element data profiles, element concentrations are normalised to Ti. Nevertheless, Fig. 4.2 demonstrates that downcore profiles of Ba/Ti are in fact very similar in shape to the profiles of bulk sediment Ba. This is also true for Ca, Mg, Sr and Fe, at all sites (Fig. 4.4a-4.4d).

These results suggest that the Ba-, Ca- and Sr-rich horizons are not the result of changes in the proportions of primary minerals. Small differences between the normalised and non-normalised profiles do occur for Ba, Mg and Fe in the uppermost part of the cores from the margin and mudflow sites. This is likely because the uppermost sample is located within the hemipelagic sediment layer. In the following discussion, depth intervals with high [Ba] ($> 258 \pm 11$ ppm) are referred to as a 'Ba front'. The value of 258 ppm represents the average Ba concentration of the mud breccia in the uppermost part of the cores, here considered as 'background concentration'. In this interval pore waters are saturated in SO_4^{2+} and Ba^{2+} (the barite saturation index for the pore fluids at this depth is greater than 1, indicating saturation with respect to barite); thus, the mud breccia has not been subject to diagenesis since the mud was extruded.

4.3.3 Barium mineralogy

Fig. 4.6 shows the results of SEM analyses of the residues of the sequential extraction. Although the extracted residue is impure, as we still observed TiO_2 minerals (e.g. rutile) and some aluminosilicates, barite crystals were found in samples from the mudflow site. These were taken from 45 (Fig. 4.6 a), 85 (Fig. 4.6 c) and 130 cm (Fig. 4.6 d) depth. The barite crystals vary in size from ∼15-30 μm. The EDS spectrum is given for two of the samples; these confirm the presence of both Ba and S.

4.3.4 Age model

Results from the radiocarbon analyses of foraminifera recovered from within sediments from the CRMV are given in table 4.3 . The hemipelagic layer at the eye site contains a component of carbon of modern origin, which means that the mud breccia was extruded very recently. The mudflow at the margin of the MV is significantly older, between 255 and 304 Cal yr BP. The mudflow pathways to the southeast of the summit date from 997

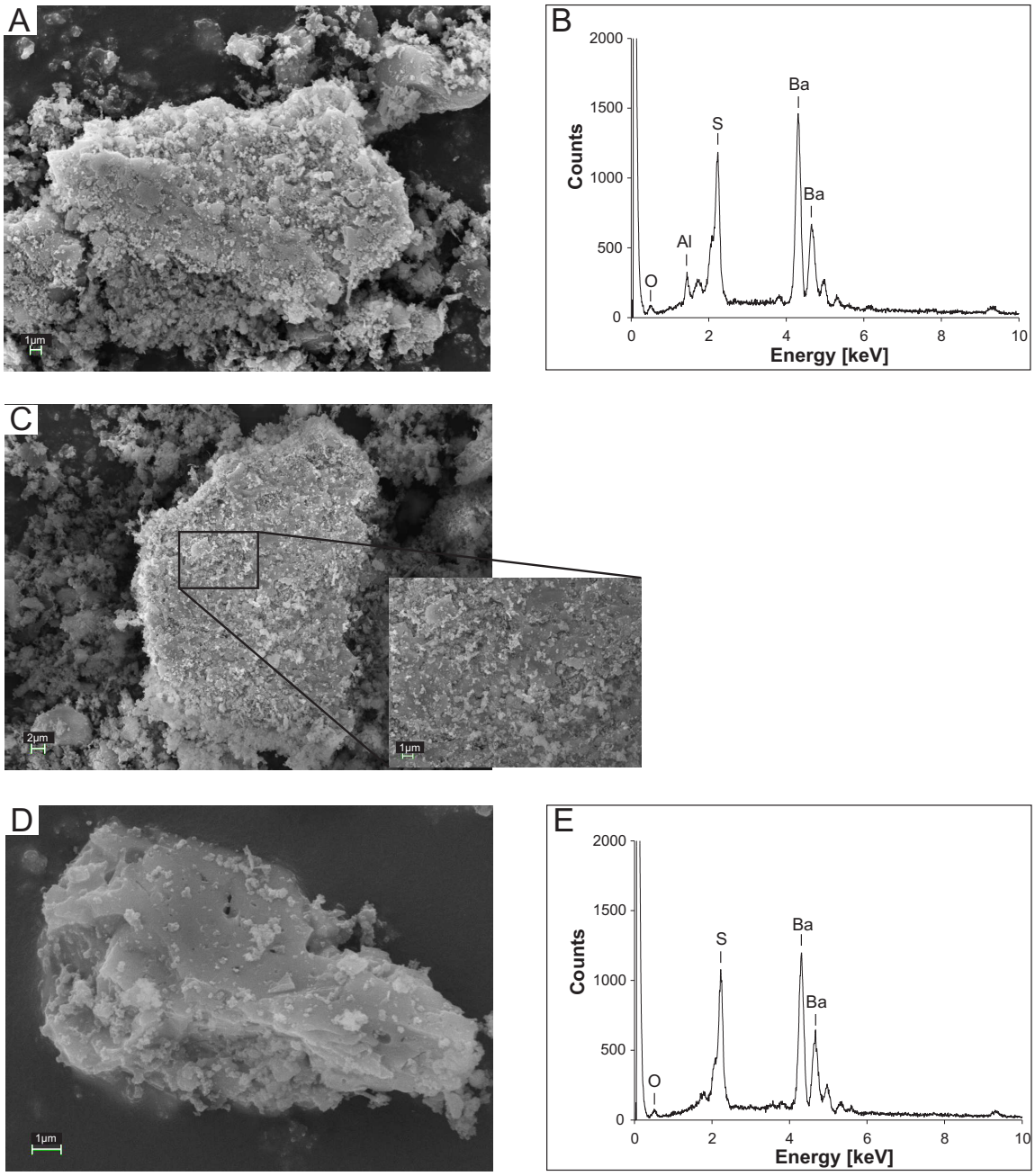

Figure 4.6 Scanning electron microscope (SEM) photograph of residue remaining after sequential extraction of sample **A** GC-60(45 cm); **C** GC-60(85-88 cm) and **D** GC-60(130cm). These intervals are characterized by high concentrations of Ba at the mudflow site at the Carlos Ribeiro mud volcano. **B** and **E** show EDS spectra for samples GC-60(45 cm) and GC-60(130cm), respectively.

to 1132 Cal yr BP.

Table 4.3 Conventional and calibrated radiocarbon ages of hemipelagic veneer

Core	Sample depth	Sample ID	Conventional Radiocarbon age	Error range	Calibrated Radiocarbon age range
	cm		yr BP	1σ	2σ Cal yr BP
MC-57	0-1	SUERC-26762	-	-	-
MC-63	2-4	SUERC-26763	636	37	255-304
GC-60	8-12	SUERC-26764	1512	35	997-1132

4.3.5 Model results

The results of transport modelling of the pore fluid data are shown alongside the measured data in Fig. 4.2 for Ba^{2+} and Fig. 4.4a-4.4d for Ca^{2+}, Sr^{2+} and Mg^{2+}. The model-generated profiles are in some cases (e.g. Ba^{2+} at the margin site and Sr^{2+} at the eye site) a relatively poor fit to the measured data. However, the measured and modelled Ba^{2+} profiles at the off-centre site do show an excellent match. Where the measured concentrations are lower than those predicted by the model, this suggests removal of dissolved constituents from the pore fluids into the solid phase; measured concentrations higher than those predicted by the model are indicative of release of a constituent from the solid into the dissolved phase.

4.4 Discussion

4.4.1 Origin of Ba fronts at the Carlos Ribeiro MV

All of the Ba fronts at the CRMV occur within the mud breccia that builds up the MV. This mud breccia originates from great depths (∼km) below the seafloor, and as a result of burial and compaction, it is likely that biogenic barite and $CaCO_3$ will have dissolved (see below). As a result the mud breccia contains low concentrations of Ca and Ba relative to the background site: Ca concentrations are ∼2.8 wt % in the mud breccia and 12.8 wt % in sediments from the background site, while Ba concentrations are ∼258 ppm in the mud breccia and ∼404 ppm in sediments from the background site (Table 4.2). This strongly suggests that the Ba fronts are authigenic in origin, i.e. they were formed after the eruption of the mud breccia within which they occur. Indeed, EDS investigations confirm the presence of microcrystalline barite within the Ba fronts at the mudflow site (Fig. 4.6).

Although no EDS information is available for the Ba front at the margin site, the absence of a Ca front indicates that the Ba front is generated due to the presence of barite rather than a Ba-rich carbonate phase. In conclusion, the sedimentary Ba enrichments observed at the CRMV must be due to the presence of authigenic barite.

The main source of Ba for the formation of authigenic barite in marine sediments is generally considered to be the dissolution of biogenic barite in sulphate-depleted pore waters (Brumsack, 1989; McManus et al., 1998; Torres et al., 1996b; Von Breymann et al., 1992b). Marine biogenic barite is formed in the water column within microenvironments of decaying biological debris (Bishop, 1988; Dehairs et al., 1980; Dymond et al., 1992; Gingele and Dahmke, 1994; Paytan et al., 1993). An increase in productivity results in an increased barite flux to the seafloor. During burial this barite dissolves if the pore waters become undersaturated with respect to sulphate (Torres et al., 1996b). Accordingly, authigenic barite fronts tend to be found in areas of high biological productivity e.g. along continental margins (Von Breymann et al., 1992b). At the present-day the surface waters in the centre of the Gulf of Cadiz have mainly an oligotrophic character while it is enclosed by upwelling systems in the north (along Portuguese Coast; Fiuza et al., 1982) and south (off NW African Coast; Pelegrí et al., 2005). However palaeoceanographic records indicate upwelling related biological productivity in the Gulf of Cadiz in the past and thus possibly also an increased supply of biogenic barite (Voelker et al., 2006; Wienberg et al., 2010). An additional source of Ba^{2+} is sedimentary material, detrital aluminosilicates can contain up to 1000 ppm of Ba (Dymond et al., 1992). Hence dissolved Ba^{2+} in the pore fluids from the CRMV might originate, as do dissolved Li^{+} and B, from pore fluid-sediment interactions at moderate temperatures at depth (see Chapter 3). Dissolved Ba^{2+} concentrations in seeping fluids vary greatly among seep sites from across the world ranging from < 60 μM in the Blake Ridge (Snyder et al., 2007a) to $\sim$12 mM in the Gulf of Mexico (Castellini et al., 2006). Although pore waters from the CRMV are enriched in Ba^{2+} relative to seawater concentrations, $[Ba^{2+}]$ from the CRMV are rather on the low side.

4.4.2 Present-day barium cycle at the Carlos Ribeiro MV

Methane and Ba-rich pore fluids are actively venting at the CRMV today, with the consumption of sulphate in the shallow subsurface as a result of AOM. The question is, are the barite fronts that we observe at the CRMV forming at the present time, or did they form in the past and therefore mark the position of a 'relict' SMT? In order to address this question, chemical analyses of the pore fluids and the solid phase are combined with modelling results.

As the pore fluid profiles of Ba^{2+} in the shallow sediments are similar to those observed at other methane-charged systems, the shape of the profile can be attributed to the dissolution and reprecipitation of barite across the SMT (Aloisi et al., 2004b; Von Breymann

et al., 1992a; Castellini et al., 2006; Dickens, 2001; Snyder et al., 2007a,b; Torres et al., 1996b). The application of the 1-D transport model to the Ba^{2+} pore fluid data confirms this; the model results show that Ba^{2+} is being removed from the pore fluid and taken up into the sediments at the eye, margin and mudflow sites (i.e. the measured values of $[Ba^{2+}]$ are lower than the model generated concentrations). The modelled data coincide with the measured $[Ba^{2+}]$ data only at the off-centre site, indicating that no significant sediment-pore fluid reactions are occurring at this site at the time of sampling. Nevertheless, a Ba front does occur at this site, at the depth of the pore water sulphate minimum, suggesting that conditions must have been favourable for barite precipitation at some point in the past, and that methane fluxes have remained stable ever since.

At the eye site, there are three depth intervals for which the measured $[Ba^{2+}]$ value is lower than that predicted by the model; this suggests that Ba^{2+} is taken up into the solid phase within these intervals. Note that at this site, the depth intervals for which the model indicates the uptake of Ba^{2+} into the solid phase tend to be located below the depth of the present-day SMT, which would inhibit the precipitation of barite. However, the Ca^{2+} pore water profile shows a concave-upwards inflection above the SMT, consistent with the precipitation of a carbonate phase within the SMT zone (as the model implies). Accordingly, it seems likely that Ba^{2+} is taken up into a carbonate phase at the eye site, rather than barite. Nonetheless, neither a Ba nor Ca front is observed in the sediment record. There could be a number of reasons for this. One possibility is that variation in the velocity of fluid flow has resulted in changes to the supply of Ba^{2+} and Ca^{2+}, and also CH_4, to the fronts which would lead to changes in the position of the SMT, thereby preventing the build up of significant quantities of barite or carbonate. In addition, radiocarbon analyses show that the date of the last mud extrusion event is indistinguishable from the present-day (Table 4.3). This means that any Ba and Ca fronts formed in the past, would have been broken up and mixed in with the new mud as it forced itself up to the seafloor. Thirdly, pore water chemistry adjusts much quicker to changes in hydrodynamic conditions than the solid phase. Accordingly, if the present-day hydrodynamic conditions were established only recently, it is unlikely that significant concentrations of Ba and Ca would have built up in sediments within the present-day SMT zone. This interpretation is in agreement with the central position of the eye site on the MV which is also the centre of activity today (Chapter 3).

At the mudflow site the model results also indicate that there is uptake of Ba^{2+} into the sediments. The sedimentary Ba profile supports this; a Ba front occurs just above the SMT and the inflection in the Ba^{2+} pore water profile below which Ba^{2+} abruptly increases with depth. In addition a carbonate concretion with barite crystals was found at 130 cm depth (Fig. 4.5). Given, the inflection in the Ca^{2+} profile at the same depth, both calcium carbonate and barite appear to be actively precipitating at the mudflow site at 130 cm depth. As that the authigenic barite front occurs immediately above the depth of SMT, the uppermost two Ba fronts would appear to delineate the position of relict SMTs

and thus a decrease in methane flux since the emplacement of the mudflow (ref. Dickens, 2001).

The margin site is the only site where the measured dissolved Ba^{2+} concentrations are higher than those predicted by the model (Fig. 4.2). The release of Ba^{2+} from the sediment is restricted to a relatively narrow depth interval of 58 cm which is preceded by a zone of barite precipitation. The shift from precipitation to dissolution coincides with the position of the SMT at 117 cm depth. The position of the largest Ba front at the CRMV is in the shallow subsurface above the SMT, and the absence of any fronts immediately above the SMT at present, suggest that the flux of methane from depth has fallen over time, resulting in a downward shift of the SMTZ. The sedimentary and pore water Ca data support this interpretation; Ca^{2+} uptake into the sediment (identified by differences in the measured and modelled values of Ca^{2+}) coincides with a Ca front which is located within the current SMT zone but below the Ba front (Fig. 4.4c). The Ba^{2+} excursion at the bottom of the core might be related to the spike in the Ba/Ti XRF profile.

In conclusion, the observed Ba fronts in the sediments from the Carlos Ribeiro MV mark both the present-day hydrodynamic conditions (mudflow site) as well as higher fluxes of methane in the past (margin and mudflow sites). Considered together, the geochemical data and transport modelling indicate that activity at the CRMV has been highly variable in the past, as well as in space (ref. Chapter 3).

4.4.3 Venting history of the Carlos Ribeiro MV

The solid phase and pore fluid data suggest that the single Ba front at the margin site, and the uppermost two sedimentary Ba peaks at the mudflow site, mark the location of relict SMTs and can thus potentially provide information about past methane fluxes at the CRMV (ref. Dickens, 2001). Indeed, the lack of oxidation fronts and/or hemipelagic sediments within the mud breccia at both sites (see core description, Appendix C) indicate that the sediment record represents one single mudflow and that the Ba fronts are the result of variations in methane fluxes.

In the case of the mudflow site, the barite fronts are likely to have formed as the mudflow degassed over time since its emplacement. Freshly-erupted mud is generally saturated in methane and will degas when emplaced onto the seafloor because of the drop in pressure (methane solubility decreases with decreasing depth; Duan et al., 1992). Because of this pressure drop, and also because of the strong contrast between the concentration of methane in the pore waters in the mudflow and the concentration of methane in the overlying water column, methane will rapidly escape into the water column as the mud extrudes. This might also explain why the uppermost Ba front is significantly smaller than the lowermost two. As the methane pressure within the pore fluid of the mudflow

will decrease rapidly during this process, the SMT will deepen just as fast and thus there is less time to accumulate barite at the front. To verify this interpretation, an attempt was made to reconstruct the sulphate pore water profiles at the time that each of the Ba fronts formed, using the 1-D transport-reaction model. This is based on the observation that Ba fronts are formed just above the sulphate pore water minimum (Torres et al., 1996b; Von Breymann et al., 1992a).

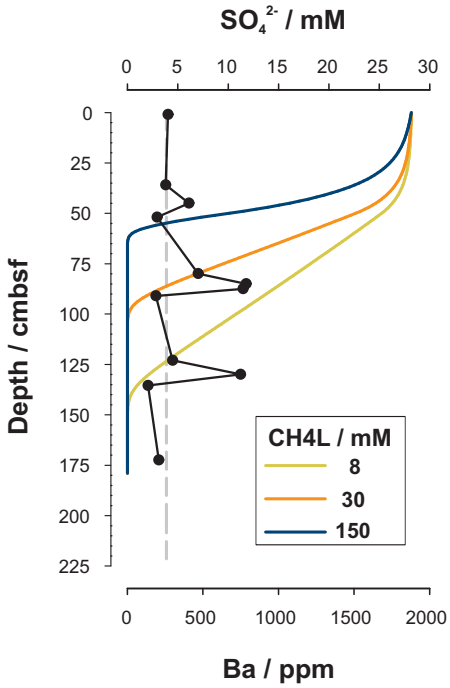

Figure 4.7 Solid phase barium (Ba; black symbols) and background Ba (dashed grey line) profiles and results of numerical modelling of dissolved sulphate (SO_4^{2-}; coloured lines) for the mudflow site at the Carlos Ribeiro mud volcano. CH4L is the dissolved methane concentration at the base of the core.

The dissolved sulphate profile within the sediments can largely be described by two parameters: (1) the advective fluid flow velocity (u_0) and (2) the dissolved methane concentration at the base of the core (CH4L). Assuming that the Ba fronts at the mudflow site are generated by degassing mud, then u_0 is zero (Chapter 3), while the concentration of methane at the lower boundary (CH4L) can be varied such that the depth of the SMT coincides with the base of the barite front, using the 1-D transport-reaction model described in Chapter 3. Modelling predicts that the value of CH4L must be >150 mM for the uppermost Ba front, 30 mM for the middle front, and 8 mM for the lowermost front (Fig. 4.7). These results demonstrate that the pore fluids in the extruded mud was initially oversaturated in methane (i.e. when $[CH_4]$>150 mM which is higher than 68 mM, the methane saturation concentration with respect to gas hydrates at the CRMV; Chapter 3), so the pore fluids must have contained a component of free methane gas. The model results there-

fore support the contention that the uppermost front is small because of the rapid escape of methane gas following the deposition of the mudflow. The estimated CH4L values for the two lowermost Ba fronts are significantly smaller than 68 mM, and thus suggest that the lowermost Ba fronts were formed as methane was transported towards the seafloor by diffusion, i.e. dissolved in the pore water driven by the concentration gradient between pore fluids and seawater. This process is slow (Clennell et al., 2000), and thus allows the formation of bigger Ba fronts at depth in the sediment column. Also the presence of a carbonate concretion at 130 cm depth indicates that the availability of bicarbonate was higher than in the upper two Ba fronts (both fronts occur at shallow depths and thus it is unlikely that any calcium carbonate concretions would have dissolved since the time of precipitation). The main source of bicarbonate at cold seep sites is AOM. Hence for pore fluids to reach the calcium carbonate saturation level, pore fluid methane concentrations need to be high (∼mM) but not higher than the solubility state as only dissolved methane is accessible for the methanotrophic archaea (Aloisi et al., 2004b). Accordingly, the model results are in line with the sediment geochemistry of the core supporting the process of degassing of the mudflow, as the underlying cause of Ba front formation at the mudflow site. These data also underline the importance of mudflows as possible contributors to the methane pool of the ocean which so far has mainly been neglected.

In case of the margin site, which is located on the summit of the MV, a drop in the methane flux and thus in the level of SMT, could have been caused either by a reduction in the fluid flux and/or by lower $[CH_4]$. It is likely that both of these parameters have changed over time. Unfortunately we are not able to determine the relative influence of each of the variables on the sulphate pore water profile at the time that the Ba front formed using a 1-D transport-reaction model. Nevertheless, we can assess the effect of varying these parameters, one at a time. This approach makes it possible to estimate the upper limit of fluid flow velocities and dissolved methane concentrations that enable the depths of the SMT and the base of the Ba front to coincide.
Past fluid flow velocities can be derived in two independent ways using the 1-D transport-reaction model. First, fluid flow velocities can be estimated by matching model-calculated dissolved Ba^{2+} fluxes to levels of 'excess Ba' (see below) and the age model. 'Excess Ba' is the difference between the Ba concentration measured in the Ba front and the Ba concentration in background sediment (258 ppm; see section 4.3.2). Following the approach used by Pruysers et al. (1993) for quantifying redox fronts, the integrated Ba peak area at the margin site (grey zone on Fig. 4.8) is estimated to be 12300 ppm cm. This value is then converted to volumetric units based on measured porosity values (i.e. 0.58, Chapter 3) and a grain density of 2.65 g cm^{-3}. Accordingly, the authigenic Ba front at the margin site contains ∼1 x 10^{-4} moles of excess Ba per cm^2 of sediment. Given that the Ba front at the margin station had 312-361 Cal yrs (relative to 2007, i.e. year of sampling) to form, a dissolved Ba^{2+} flux of 2.8-3.2 mmol m^{-2} yr^{-1} is required to supply the excess Ba in the sediments at the margin site. Subsequently, this Ba^{2+} flux is obtained from the model

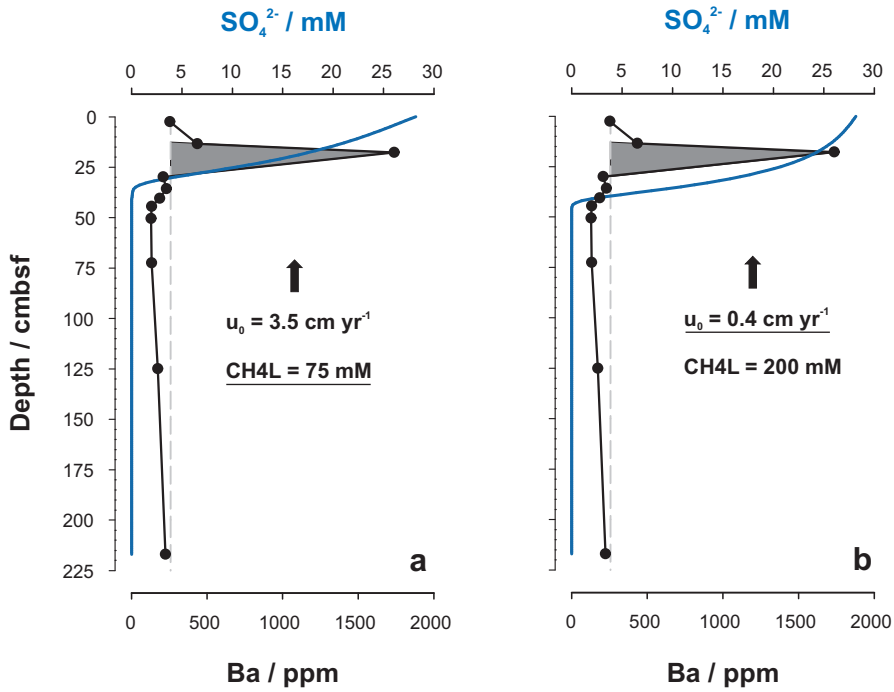

Figure 4.8 Solid phase barium (Ba; black symbols) and background Ba (dashed grey line) profiles and results of numerical modelling of dissolved sulphate (SO_4^{2-}; blue line) for the margin site at the Carlos Ribeiro mud volcano. **a** first assumption: CH4L stays constant **b** second assumption:u_0 stays constant. CH4L is the dissolved methane concentration at the base of the core and u_0 is the upward fluid flow velocity. The values of the underlined parameters were estimated for present day conditions (ref. Chapter 3).

by varying the fluid flow velocity (u_0). Assuming that $[Ba^{2+}]$ has remained constant over time, i.e. 0.07 mM (the Ba^{2+} concentration at the base of the core), a fluid flow of ~6 cm yr^{-1} is required in order to supply the quantity of Ba^{2+} in the front, over the measured time interval (312-361 Cal yrs). The alternative approach is similar to the method used for the mudflow site, except that in this case only u_0 is varied in order to fit the depth of the SMT to the base of the barite front. The obtained best-fit value for the fluid flow velocity is ~4 cm yr^{-1} (Fig. 4.8). Thus, both approaches generate fluid flow velocities of the same order of magnitude.

This approach can also be used to verify the assumption that a reduction in only $[CH_4]$ could have caused the depth of the SMT to increase over time. If this assumption is valid, then $[CH_4]$ would need to be >200 mM to form a Ba front at 18 cm depth (Fig. 4.8). This is rather unlikely as the pore waters currently being expelled at the centre of the CRMV only have a $[CH_4]$ value of <120 mM.

These results therefore suggest that the velocity of fluid flow at the margin site has changed within the last 255-304 Cal yrs BP. However, the magnitude of this change is difficult to quantify, because the change in $[CH_4]$ over this time interval cannot be specified, but it seems likely that u_0 was never greater than 6 cm yr^{-1}. These findings are in agreement with model results of Aloisi et al. (2004b) which indicate that microcrystalline phases and concretions of barite and calcium carbonate, similar to what was found at CRMV, are formed within the sediment column at low fluid flow velocities (0.14 - 20 cm yr^{-1}) while

more vigorous fluid flow (>20 cm yr^{-1}) would give rise to concrete barite-carbonate crust layers near the seafloor. Nevertheless, the estimated values of fluid flow, ∼4 and 6 cm yr^{-1}, are an order of magnitude greater than those estimated for this site at present (0.4 cm yr^{-1}; Chapter 3), underlining the dynamic nature of the CRMV.

4.5 Conclusions

Venting of Ba^{2+}- and methane rich fluids at the Carlos Ribeiro MV (Gulf of Cadiz) results in the precipitation of microcrystalline barite narrow zones within the sediment column; these coincide with the depth of the sulphate-methane transition. Possible sources of Ba^{2+} are the dissolution of biogenic barite in deeper, sulphate-depleted zones during the burial process and, sedimentary material that was involved in low to moderate temperature alterations at depth. In both cases Ba^{2+} is consequently transported upwards through the sediment column by advecting fluids.

Chemical data for pore fluids and the solid phase and the results of geochemical modelling can be used to understand the sediment-pore fluid interactions at the CRMV, both today and in the past. At the eye of the mud volcano, no Ca or Ba fronts can be identified within the sediment column, which suggests that upwelling of material from depth has been highly variable, both today and in the past. Towards the margin of the CRMV, the Ba fronts are observed in the sediment column, suggesting that at these sites, fluxes of material from below are less variable. However, the Ba front at the margin site is not the product of present-day precipitation; rather, it must have formed at a time when methane fluxes were higher than they are today. By contrast, the Ba fronts at the mudflow site are likely to have formed by gradual degassing of the mudflow since its extrusion.

For the first time, we have assessed the past variation in fluid fluxes and $[CH_4]$ at the CRMV, based on the occurrence of authigenic barite horizons in combination with pore fluid modelling. This is important, because it provides insights as to the periodicity of fluid expulsion at the CRMV. In addition, by determining the age of the hemipelagic veneer on top of the MV, we have been able to reveal that the muds have been extruded in the recent past. These results indicate that activity at the CRMV is dynamic, and that the position of barite fronts in the sediment column provide a viable tracer of the periodicity of mud volcanism.

In addition to barite, other authigenic minerals precipitate in the sediment column at the CRMV. High concentrations of Ca are found in narrow zones at the margin and mudflow sites. These appear to be actively forming today.

Chapter 5

Authigenic carbonates from the Darwin Mud Volcano (Gulf of Cadiz): a Record of (Palaeo)Seepage of Hydrocarbon Bearing Fluids.

5.1 Introduction

The study of submarine mud volcanoes (MVs) has gained importance over the past 10 years, as the ascending hydrocarbon rich fluids, not only provide an energy source for microorganisms (Hinrichs et al., 1999; Levin, 2005), but they also contribute significantly to the global carbon budget of the ocean (Damm and Budéus, 2003; Sauter et al., 2006). Attempts have been made to quantify the flux of methane from MVs into the water column, and its variability over short timescales, using video observations of bubble discharge (e.g. Sahling et al., 2009; Sauter et al., 2006) and pore fluid modelling (Aloisi et al., 2004a; Linke et al., 2005; Wallmann et al., 2006a). Nevertheless, the methane flux from a MV is known to vary on much longer timescales, from tens to hundreds of thousands of years (Lykousis et al., 2009) and thus an alternative approach is required to study these long term variations in carbon chemistry at MVs. One way to assess the long term variation in seepage activity at MVs is via the study of authigenic carbonates, which record the chemistry of the fluids from which they precipitate (Burton, 1993; Savard et al., 1996).
Hydrocarbon-derived seep carbonates are known from as far back as the Middle Devonian (Peckmann et al., 1999), and they have been documented on the seafloor on continental margins (e.g. Aloisi et al., 2000; Bahr et al., 2009; Bayon et al., 2007; Díaz-del Río et al., 2003; Greinert et al., 2001, 2002; Hovland et al., 1987; Matsumoto, 1990; Mazzini et al., 2004; Ritger et al., 1987), as well as in terrestrial outcrops (Campbell et al., 2002, 2008; Peckmann et al., 1999, 2002) from all over the world. They are the product of the microbi-

ally driven anaerobic oxidation of methane (AOM) and higher hydrocarbons (Joye et al., 2004; Omoregie et al., 2009) which takes place as the gas-rich fluids migrate towards the seafloor:

$$CH_4 + SO_4^{2-} \quad \rightarrow \quad HCO_3^- + HS^- + H_20 \tag{5.1}$$

Bicarbonate released during this process increases the pore fluid alkalinity and thus promotes the precipitation of carbonate minerals (Ritger et al., 1987):

$$Ca^{2+} + 2HCO_3^- \quad \leftrightarrow \quad CaCO_3 + CO_2 + H_2O \tag{5.2}$$

Hence, carbonate precipitation occurs in the sulphate methane transition zone (SMTZ). The depth of the SMTZ is defined by the methane flux from depth: high fluxes push the SMTZ upwards towards the seafloor, while a weak flux will result in authigenic carbonate formation at up to several meters depth below the sediment-seawater interface. The morphology of these seep carbonates is highly variable, ranging from centimetre-to-decimetre thick nodules within the sediment column (Feng et al., 2009a; Mazzini et al., 2004; Naehr et al., 2000a; Rodriguez et al., 2000), to thick slabs that pave the seafloor for several square meters (Aloisi et al., 2000; Gontharet et al., 2007), to chimney structures protruding more than 2 m above the seafloor (e.g. Díaz-del Río et al., 2003). The carbonate mineralogy consists typically of Mg calcites and aragonite, but dolomite and siderite have also been reported (e.g. Bayon et al., 2007). Carbonate morphology and mineralogy seems to be related to a number of factors, including pore fluid chemistry, fluid seepage rate and the type of sediments and biota present at the seep site (Greinert et al., 2001; Mazzini et al., 2004).

The Gulf of Cadiz is characterised by numerous fluid escape structures including pockmarks, mud volcanoes, mud diapirs, authigenic carbonate crusts and carbonate mud mounds (Baraza et al., 1999; Díaz-del Río et al., 2003; Foubert et al., 2008; Gardner, 1999; Kenyon et al., 2006). These are mainly concentrated on the Iberian and Moroccan continental margin, because of intense hydrocarbon seepage in this area. Two main lithologic types of authigenic carbonates have been identified in the Gulf of Cadiz: dolomite- and aragonite-dominated carbonates (Magalhães, 2007). They occur throughout the Gulf at depths of 500-4000 m, and their morphologies are highly variable. For example, fields of dolomite/ankerite chimneys on the Iberian margin (Díaz-del Río et al., 2003), irregular aragonitic blocks scattered over the seafloor associated with faults close to the Strait of Gibraltar, aragonitic crust pavements on top of MVs and nodular centimetre-sized concretions within the sediment column (Kenyon et al., 2006). The formation of the authigenic carbonates in the Gulf of Cadiz has been related to events of gas hydrate dissociation as a result of an increased influence of warm Mediterranean Outflow Water (MOW) on the Iberian margin (Gardner et al., 2001; Magalhães, 2007). However, gas hydrates have only been recovered from a few MVs so far (Mazurenko et al., 2003, 2002).

The Darwin MV is located on the Moroccan continental margin in the Gulf of Cadiz at a water depth of 1105 m (Fig. 5.1). The centre of its summit is covered by a carbonate pavement, which is broken up by a network of fissures. Here, I report the results of petrographic, chemical and isotopic analyses of these carbonates, to gain a better understanding of the venting history at the Darwin MV. In addition, pore fluid chemistry and 1-D transport modelling is used to examine the present-day seepage of hydrocarbon-bearing fluids, as well as present-day carbonate precipitation. In this way, this study contributes to the better understanding of variability in hydrocarbon venting at MVs, which is important for assessing their role in ocean chemical budgets.

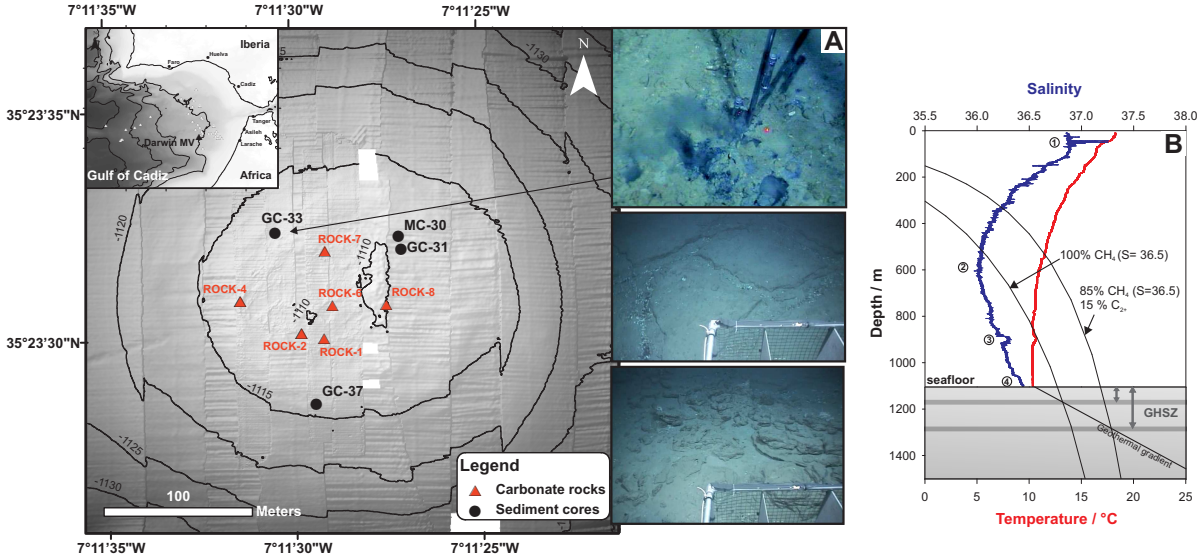

Figure 5.1 Shaded relief map of the Darwin mud volcano (MV) and its location within the Gulf of Cadiz (top left). Black dots depict the locations of the cores (GC-32, MC-30, GC-31 and GC-37) and red triangles depict the locations of the carbonate rock samples (rock-1, rock-2, rock-4, rocks 6-8). **A** Images of the seafloor taken from the ISIS ROV at the Darwin MV. Top: streams of bubbles produced by disturbing the sediments close to site GC-33. Note that this site is covered with soft black sediment. Middle: carbonate crust pavement broken up by a network of fissures. Note that the fissures are filled with living (black coloured shells) and dead (white coloured shells) mussels. Bottom: carbonate crusts exposed on the seafloor. **B** CTD profile and stability field of gas hydrates at the Darwin MV (salinity = 36.5; Bottom water temperature = 10.3 °C). The intersection of the geothermal gradient (41 °C; Leon et al., 2009) with the phase boundaries (for 100% CH_4 and 85% CH_4 + 15% C_{2+}) define the gas hydrate stability zone (GHSZ). Water mass ① is North Atlantic Surface Water (NASW), ② is the salinity minimum associated with the North Atlantic Central Water (NACW), ③ is the upper core of the Mediterranean Outflow Water (MOW) and ④ is the lower core of the MOW.

5.2 Materials and methods

5.2.1 Sample collection

All samples discussed in this chapter were collected from the Darwin mud volcano during the RRS *James Cook* Cruise 10 (May 13^{th} through June 7^{th}, 2007). The Darwin MV is cone shaped and has a height of ∼50 m. In the centre of the crater a patch of seafloor approximately 80 m in diameter is covered with a carbonate crust pavement that is broken up by a network of fissures. The individual carbonate slabs are up to 10 m in diameter and are often tilted creating local escarpments of up to 0.5 m high (Weaver and Masson, 2007). Video observations made with the ISIS Remotely Operated Vehicle (ROV) reveal that the cracks between the carbonate slabs are covered with banks of mainly dead mussels (i.e. *Bathymodiolus* mauritanicus; Vanreusel et al., 2009). Living mussels occur in small patches throughout the crater, suggesting that the authigenic carbonate crusts are associated with seepage of methane-rich fluids.

Three gravity cores (GC-31, GC-33 and GC-37) and one multi core (MC-30) were taken from three sites on the summit of the MV (Fig 5.1), and one piston core (PC-23) and one multi core (MC-26) were taken from a 'background site' that lies 1 km northwest of the Darwin MV (Table 5.1). The location of the sediment cores was mainly selected on the basis of video observations made with the ISIS ROV, prior to coring. However the choice was limited because of the wide spread occurrence of carbonate crusts. Core GC-33 is located close to a so-called 'black spot'; a small area with black coloured sediment on the surface and where gas-seepage was observed following disturbance of the sediment. The cores were subsampled onboard immediately after retrieval: sample intervals for gravity and piston cores were chosen based on visible changes in the sediment characteristics, while multi cores were sliced into sections of 1-3 cm in a cold room (∼6°C). Subsamples were taken for analyses of pore water hydrocarbon gas concentrations, porosity, and pore water chemistry. Samples for hydrocarbon gas analysis (ca. 3 cm^3) were withdrawn using a plastic syringe with a cut off tip and transferred to a 20 ml crimp cap glass vial containing 5 ml 1M NaOH to prevent further microbial activity (Hoehler et al., 2000). After closing and vigorous shaking for several minutes, dissolved gases become enriched in the headspace of the vial. Sediment samples for porosity analyses were stored in airtight containers and kept at 6°C until on onshore analyses. Pore waters were immediately extracted in a glove bag under a N_2-atmosphere by pressure-filtration through 2 μm cellulose acetate membrane filters, with a N_2-pressure of 3-4 bars.
The carbonate pavement on top of the Darwin MV summit was sampled by means of the ISIS ROV. Authigenic crusts (rock-1, rock-2, rock-4 and rocks 6-8) were recovered from six sites (Fig. 5.1), photographed and stored at room temperature for sectioning, subsampling and further analysis onshore.

Table 5.1 Location of studied coring and authigenic carbonate sampling sites. PC= piston core; GC=gravity core; MC=multi core

Core code	Region of Darwin MV	Latitude (°N)	Longitude (°W)	Core length (cm)	Water depth (m)
Cores					
PC-23	1 km NE of Darwin	35°23.962'	7°11.12'	505	1145
MC-26	MV, reference	35°23.965'	7°11.121'	36	1145
MC-30	Summit, NE	35°23.537'	7°11.454'	22	1104
GC-31		35°23.532'	7°11.453'	49	1104
GC-33	Summit, NW	35°23.539'	7°11.509'	40	1105
GC-37	Summit, S	35°23.476'	7°11.492'	24	1105
Authigenic carbonates				Number of samples	
Rock-1	Summit	35°23.500'	7°11.488'	2	1118
Rock-2	Summit	35°23.502'	7°11.498'	4	1118
Rock-4	Summit	35°23.514'	7°11.525'	2	1118
Rock-6	Summit	35°23.512'	7°11.484'	3	1119
Rock-7	Summit	35°23.532'	7°11.487'	2	1119
Rock-8	Summit	35°23.512'	7°11.460'	3	1118

5.2.2 Pore fluid, hydrocarbon and porosity analyses

Total alkalinity (TA) concentrations were determined onboard immediately after pore fluid extraction by manual titration against 0.05M HCl while bubbling nitrogen through the sample (Ivanenkov and Lyakhin, 1978). Concentrations of all other chemical species were determined back onshore at the National Oceanography Centre Southampton (NOCS, UK). Sulphate (SO_4^{2-}) pore water concentrations were measured using a Dionex ICS2500 ion chromatographer. The reproducibility of these measurements was determined by repeat analysis of a seawater standard as well as single anion standards and is better than 1%. Pore water boron (B), sodium (Na^+), calcium (Ca^{2+}), magnesium (Mg^{2+}), barium (Ba^{2+}) and strontium (Sr^{2+}) concentrations were determined by inductively coupled plasma optical emission spectroscopy (ICP-OES; Perkin Elmer Optima 4300DV). The accuracy and precision of these analyses is generally better than 4%. Headspace hydrocarbon gas abundances ($C_1 - C_5$) were measured using an HP Agilent® 6850 gas chromatograph equipped with a 30 m x 0.32 mm column and a flame ionization detector. This instrument was calibrated daily, using a certified gas standard purchased from Air Products® UK. Note that depressurisation and warming of the core during sediment retrieval is likely to have led to degassing, so the concentration of methane (which is generally oversaturated in the pore waters) that is reported here is the minimum value. Sediment porosity was calculated from the loss of water after freeze-drying of the sediment assuming a dry solid density of

2.65 g cm^{-3}.

5.2.3 Carbonate mineralogy, petrography and elemental composition

First, hand specimens of the carbonate rocks were examined in order to select representative samples for petrographic thin section analysis at Scripps Institution of Oceanography (SIO, California). A stained (using the Dickson's method; Dickson, 1966) and an unstained thin section of the same rock surface (cut perpendicular to the bedding) was prepared at NOCS for each rock. After examination under a petrological microscope, the surfaces of the carbonate slabs were subsampled using a hand-held microdrill. These subsamples were then ground to a fine powder using an agate mortar and pestle for further analyses.

The bulk mineralogy of each sample was determined by X-ray diffraction on random oriented powder slides using a diffractometer with CuKα radiation (λCuKα=1.542) at SIO. Quartz naturally present in the samples was used as an internal standard. Scans of bulk samples were run from 2° to 63° 2theta while scans of the insoluble residue (obtained after leaching the rock samples with 50 ml of 5% HCl), were run from 1° to 40° 2theta. The scanning speed was 1° 2θ/min with a step size of 0.1°. The 2theta position of the calcite d(104) peak was used to determine the amount of Mg^{2+} and/or Fe^{2+} that substitutes for Ca^{2+} in the calcite crystal structure: as both cations are smaller ($r_{Mg^{2+}}$=72 pm; $r_{Fe^{2+}}$=55 pm) than Ca^{2+} (r_{ion}=100 pm), the spacing between the crystal layers is reduced and d(104) is shifted to higher angles (Goldsmith et al., 1961). Calcite with less than 5 mol% MgCO_3 is referred to as low-Mg calcite (LMC), and calcite compositions of 5-20 mol% MgCO_3 are referred to as high-Mg calcite (HMC) (Burton and Walter, 1987). The relative proportion of the different carbonate minerals is determined from the peak intensities.

Cation concentrations (Ca, Mg, Sr, Ba, Fe, and Mn) in the carbonate precipitates were determined using a Perkin Elmer Optima 3000DV ICP-OES at SIO after treating each sample (ca. 200 mg) with 50 ml of 5% HCl solution, and separation of the carbonate fraction from the insoluble residue by vacuum filtration. Repeat analysis (n=3) of 2 samples consistently gave concentrations within 3.5%. The insoluble residue was dried and weighed, and the carbonate content was determined from the weight difference between the bulk and residue sample for each carbonate rock, i.e. $CaCO_3$ (wt%)= [(weight$_{bulksample}$ (g) - weight$_{residue}$(g)) / weight$_{bulksample}$ (g)] x 100.

5.2.4 Oxygen and carbon isotope analyses

Oxygen (δ^{18}O) and carbon (δ^{13}C) isotopic composition were determined for 11 of the powdered carbonate samples. Both isotopes were measured at NOCS using a PDZ Europa Geo 20-20 mass spectrometer equipped with a carbonate automated preparation system (CAPS). The CO_2 for analysis was obtained by reacting the samples with phosphoric acid

(H_3PO_4) at 70 °C. 'Raw δ^{18}O values were first corrected for temperature dependent isotope fractionation between the δ^{18}O of the carbonate sample and the δ^{18}O of the evolved CO_2, then for instrumental drift. The data are reported relative to the V-PDB standard for oxygen and carbon (CRAIG, 1957). Replicate analyses (n=6) of an in-house standard (SC-1) which is calibrated versus NSB-19, give an external precision and accuracy of better than, respectively, 0.05‰ and 2‰ for δ^{18}O and δ^{13}C.

Analysis of stable oxygen and carbon isotopes in the pore waters was carried out at Royal Holloway, University of London. Both isotopes were measured using a Multiflow injection system (GV Intruments/Isoprime Ltd.). For δ^{18}O, 2 ml of pore water was equilibrated with 5% CO_2 and 95% He for 7 hours at 40°C. δ^{13}C of dissolved inorganic carbon was determined by the equilibration of 0.5 ml of pore water with orthophosphoric acid for 4 hours at 40°C. The $^{18}O/^{16}$O ratios were normalized to the V-SMOW scale using an internal standard, DEW-1, that has a δ^{18}O of -8.44‰, calibrated versus V-SMOW and SLAP. Each sample was measured 7 times; the average precision of the δ^{18}O values is 0.07‰. The obtained carbon isotope ratios were normalised to the V-PDB scale using a bicarbonate laboratory standard, that has a δ^{13}C of -4.9‰, calibrated versus LSVEC and NBS-19. Replicate analyses of each sample (i.e. n=2) give an average precision of 0.12‰.

5.2.5 Geochemical modelling

A 1-D transport model, described in detail in Chapter 3, was applied to pore water concentration-depth profiles of B, Na^+, Ca^{2+}, Mg^{2+}, Sr^{2+} and Ba^{2+} from core GC-33, to calculate the fluid advection velocity and to assess the nature and extent of sediment-pore fluid reactions at the Darwin MV. Fluid flow velocities (u_0) were obtained by least square fitting of the model results to the measured pore water profiles of B and Na^+, which are both considered to behave conservatively at this site. The depth distribution of these two elements is described in the model in terms of molecular diffusion, fluid advection and bioirrigation (Boudreau, 1996), as follows:

$$\frac{\partial \varphi C_i}{\partial t} = D_i \frac{\partial}{\partial x}\left(\frac{\varphi}{\vartheta^2}\frac{\partial C_i}{\partial x}\right) \quad - \quad \frac{\partial \varphi u C_i}{\partial x} \quad - \quad \varphi\alpha(x).(C_i(x) - C_i(0)) \qquad (5.3)$$

where C_i is the concentration of the dissolved pore water species i, D_i is the diffusion coefficient of species i corrected for salinity (36.5), temperature (10.3°C) and pressure (110 bar; Table 5.2), ϑ^2(=1-ln(φ^2)) is the tortuosity correction for diffusion (Boudreau, 1997),φ is the sediment porosity, u is the velocity of the upward fluid flow, α(x) is the irrigation exchange coefficient, (C_i(x)-C_i(0)) is the difference between the concentration of species i at depth and in bottom water, t is time and x is sediment depth. Values for each of these model parameters, at each of the core sites, are given in Table 5.2.

Table 5.2 Parameter values used in the numerical model.

Parameter	Symbol	Unit	Site 33
Molecular diffusion coefficient of sodium[a]	D_{Na}	$[cm^2yr^{-1}]$	222.13
Molecular diffusion coefficient of boron[b]	D_B	$[cm^2yr^{-1}]$	182.03
Length of model column[c]	L	[cm]	68
Porosity at sediment surface[d]	φ_0		0.8306
Porosity at lower boundary[d]	φ_∞		0.5016
Attenuation coefficient for porosity decrease[d]	β	$[cm^{-1}]$	0.3416
B concentration at sediment surface[e]	B0	[mM]	0.3
B concentration at depth L[e]	BL	[mM]	0.5
Na^+ concentration at sediment surface[e]	Na0	[mM]	488
Na^+ concentration at depth L[e]	NaL	[mM]	484

[a] Calculated from equations given in (Boudreau, 1997) considering the in situ T (10.3°C), S (36.5) and P (110 bar) conditions.
[b] Calculated from equations given in (Boudreau and Canfield, 1988; Mackin, 1986) considering the in situ T (10.3°C), S (36.5) and P (110 bar) conditions.
[c] Length of the sediment core.
[d] Obtained by least square fitting an exponential equation $\varphi(x) = (\varphi_0 - \varphi_\infty)e^{(-\beta x)} + \varphi_\infty$ to the measured porosity depth profile (Fig D.1 in Appendix D).
[e] Measured in pore waters extracted from sediment core GC-33 from this study.

Values for fluid flow velocity and the irrigation parameters are then used to generate the pore fluid profiles of Ca^{2+}, Mg^{2+}, Sr^{2+} and Ba^{2+}. As the model does not account for any reactions between the pore fluids and the sediments, then any discrepancy between the measured and modelled pore water profiles of Ca^{2+}, Mg^{2+}, Sr^{2+} and Ba^{2+} are likely to indicate their involvement in diagenetic reactions such as the precipitation of calcium carbonate, dolomite and barite. In this way, the model can be used to assess whether there is an exchange of any of these elements between the pore fluids and the solid phase at the time of sampling.

5.3 Results

5.3.1 Pore fluid chemistry

Fig 5.2 shows pore fluid concentration-depth profiles for sulphate, total alkalinity, dissolved methane and higher hydrocarbons and the major (i.e. Na^+, Ca^{2+}, Mg^{2+}) and trace (i.e. B, Sr^{2+} and Ba^{2+}) cations for all of the cores from the Darwin MV and for the background site. Concentrations of all of these constituents in cores GC-37, GC-31 and MC-30, and the background site are similar to bottom seawater and show little variation with depth. However, pore fluids from core GC-33, which is located in the NW of the MV crater, show

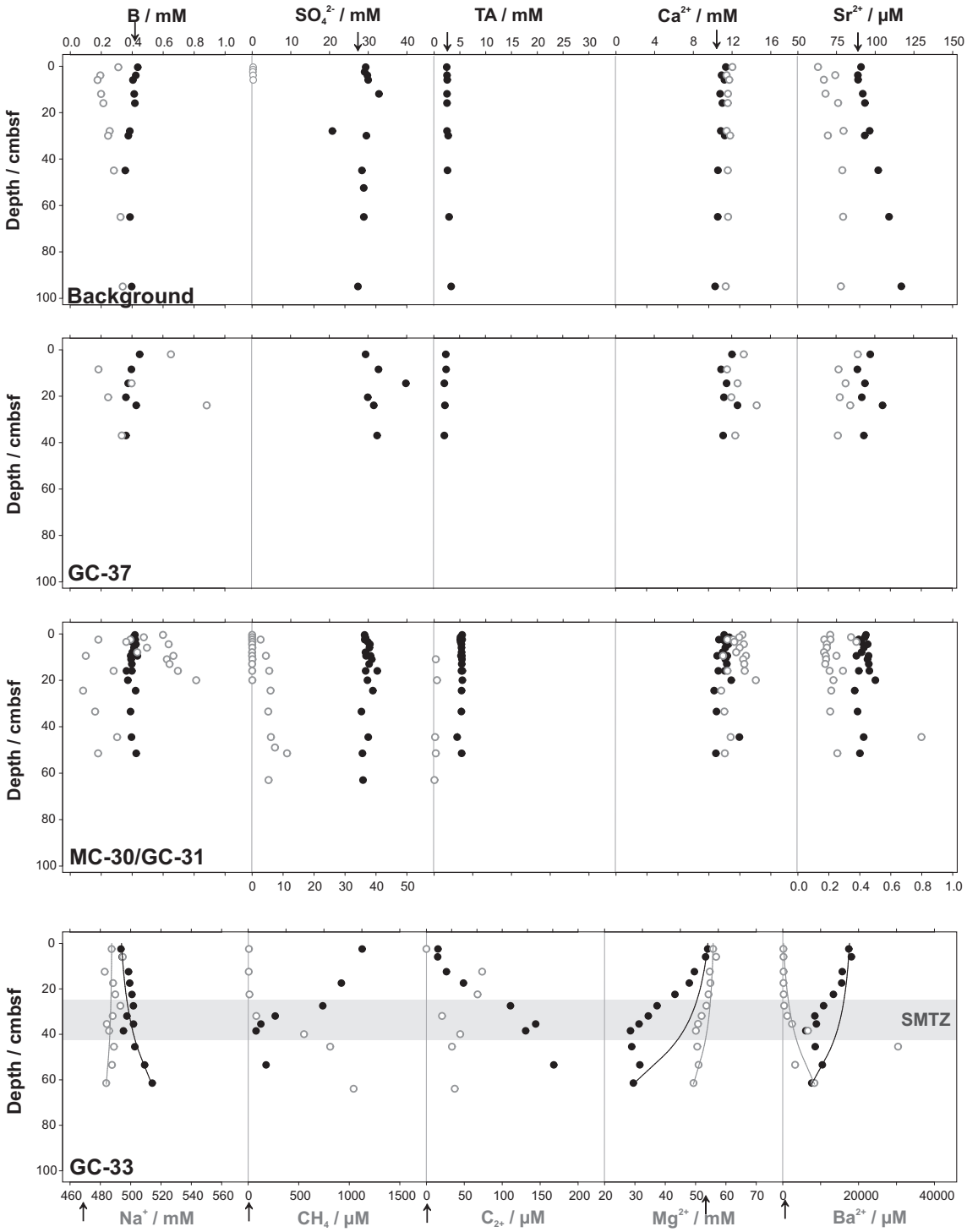

Figure 5.2 Pore water depth profiles of boron (B), sodium (Na^+), sulphate (SO_4^{2-}), methane (CH_4), total alkalinity (TA) , higher hydrocarbons (C_{2+}), calcium (Ca^{2+}), magnesium (Mg^{2+}), strontium (Sr^{2+}) and barium (Ba^{2+}) for the three core sites located on the summit of the Darwin MV and the background site. Results of numerical modelling of B, Na^+, Ca^{2+}, Mg^{2+}, Sr^{2+} and Ba^{2+} data at site 33 are plotted as solid lines. Vertical arrows indicate seawater values and the shaded zone corresponds to the sulphate-methane transition zone (SMTZ) at core site 33.

significant increases in TA and Ba^{2+} with depth, up to, respectively, 25.2 and 30.4 mM. In the same core, concentrations of sulphate, Ca^{2+}, Mg^{2+} and Sr^{2+} are observed to decrease with depth. In particular, the pore fluid profiles of sulphate, Ca^{2+} and Sr^{2+} show a steep gradient within the top 40 cm, then slightly increase again at greater depths. The sulphate profile reaches a minimum of 2.1 mM at 38.5 cm depth and the Ca^{2+} concentration drops to less than half that of background seawater (10.3 mM). The Ba^{2+} concentration of the pore fluid samples at 45.5 cm depth is exceptionally high (30.4 mM). Note that the pore fluid sulphate concentrations for all sites, including the background site, are slightly higher ($\sim$30 mM) than standard seawater (28 mM), probably because of evaporation of the sulphate sub-sample in the interval between pore fluid extraction on board and analyses on shore. For this reason, sulphate data are only considered to be qualitative. B concentrations increase with depth at this site, but only slightly (by 0.2 mM). Note that [B] and $[Na^{+}]$ are respectively lower and higher in the surface sample compared to seawater values; this is because these concentrations were measured in pore waters extracted from the top 5 cm of the sediment core. In addition, gravity cores have the tendency to lose the top few cm. Methane and higher hydrocarbon gases (C_{2+}, most notably ethane), were detected in cores GC-33 and GC-31 and MC-30. The methane concentrations increase with depth at all sites. The highest concentrations were measured in core GC-33, up to 1 mM at 64 cm depth. The composition of the headspace gas varies from 100% methane to 98% C_{2+}. A few samples contained trace amounts ($< 1\%$) of propane and butane. Methane concentrations up to a few micromolars were measured in samples from the background station, but only at depths of greater than $\sim$2 m.

5.3.1.1 Pore fluid model results

The pore fluid profiles of B, Na^{+}, Ca^{2+}, Mg^{2+}, Sr^{2+} and Ba^{2+} generated by the transport model are plotted alongside the measured data for core GC-33 in Fig 5.2. Model and fitting parameters are given in Tables 5.2 and 5.3. The model results indicate that the pore fluids rise very slowly at this site, $\sim$0.09 cm yr^{-1}. Note that this is a maximum estimate as the concentration change in Na^{+} is within analytical error. Comparison of the measured and modelled pore fluid data indicates that, at the time of sampling, Ca^{2+}, Mg^{2+} and Sr^{2+} are being extracted from the pore fluids. Meanwhile, at a depth of 45.5 cm, Ba^{2+} appears to be released from the sediments into the pore fluids.

Table 5.3 Parameter values derived by fitting the model results to the data.

Parameter	Symbol	Unit	Site 33
Upward fluid flow velocity	u_0	[cm yr^{-1}]	0.09
Irrigation depth	x_{mix}	[cm]	10
Irrigation mixing coefficient	α'	[yr^{-1}]	1

5.3.2 Authigenic carbonates

5.3.2.1 Petrography and mineralogy

The authigenic carbonates collected from the Darwin MV consist of both solid (e.g. rock 2; Fig 5.3b) and porous rocks with a high abundance of tubular voids (e.g. rock 4, Fig 5.3c). The interior of the rocks tend to be beige-grey in colour and they are covered with a thin dark red-brown coating on the outside, which probably consists of iron-oxides. Two main morphological types can be identified: (1) carbonates with a high abundance of skeletal grains, in particular bivalve shells (rocks 1, 2, 7 and 8; Fig. 5.3a, 5.3b, 5.3e, 5.3f) and (2) carbonates consisting mainly of lithogenic material (rocks 4 and 6, Fig. 5.3c and 5.3d). Within each rock different components could be distinguished from the study of the hand specimens: rocks 2, 6 and 8 have a more white-coloured rim, and particularly rocks 2 and 8 contain clusters of bivalve shells. Rock 7 is notably different in that it consists almost entirely of cemented shells, and it contains distinctive clasts of up to 1.5 cm in diameter.
Thin sections show that all of the rocks have a generally chaotic fabric because of the irregular distribution of bioclasts (Fig. 5.4) and/ or lithoclasts (Fig. 5.5), and also because of the high diversity in cement types (Fig. 5.6) and different amounts of reworking and brecciation. The clasts are generally immersed in a fine-grained matrix, i.e. micrite, a microcrystalline calcite that ranges in colour from light to dark orange-brown and has sometimes a clotted appearance (e.g. Fig. 5.4b). The skeletal grains are generally well preserved and comprise of gastropod (Fig. 5.4c) and bivalve shells (Fig. 5.4a), echinoid spines (Fig. 5.4d) and foraminifera (Fig. 5.4b). The latter are present in all of the rocks whereas gastropod shells are particularly abundant in rock 1. Rock 6 does not contain any bivalve shells and the foraminifera only occur within the micrite matrix. Micritization of shell segments is clearly visible in rock 7 (Fig 5.4a).
Three types of non-skeletal grains were observed within the authigenic carbonates: peloids (including sedimentary peloids and fecal pellets; Fig. 5.5a and b), intraclasts (Fig. 5.5e) and extraclasts (Fig. 5.5c and d). Both peloids (0.5 - 1.5 mm) and intraclasts are very

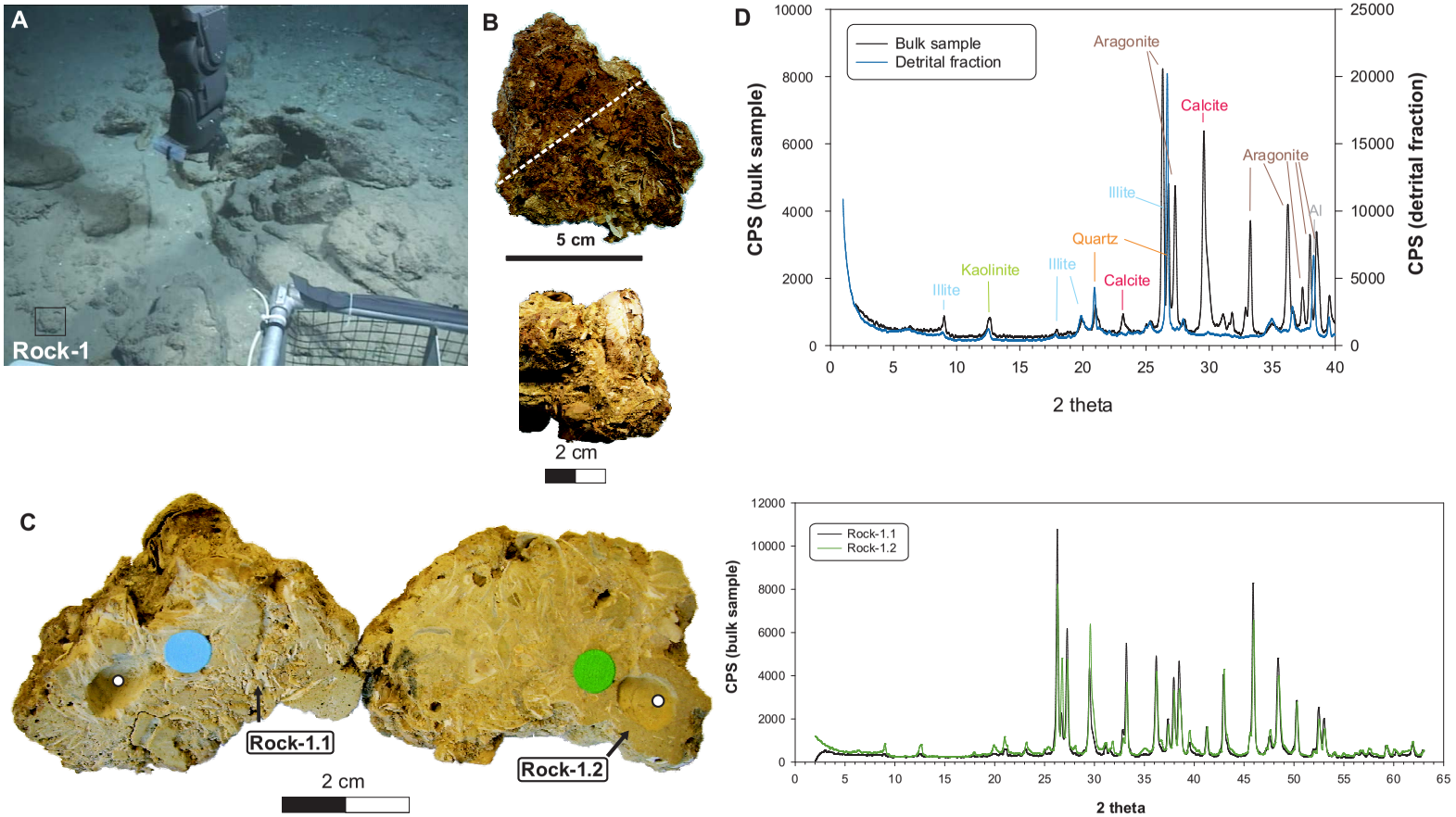

Figure 5.3a Authigenic carbonate samples: Rock-1. **A** Photograph of sample location on the Darwin MV (black box = sample). **B** Photograph of authigenic carbonate sample. **C** Cross sections of carbonate precipitates along the white dashed line shown in B. White dots indicate the positions of the analysed subsamples. **D** X-ray diffraction patterns of the bulk carbonate concretion samples and detrital fraction.

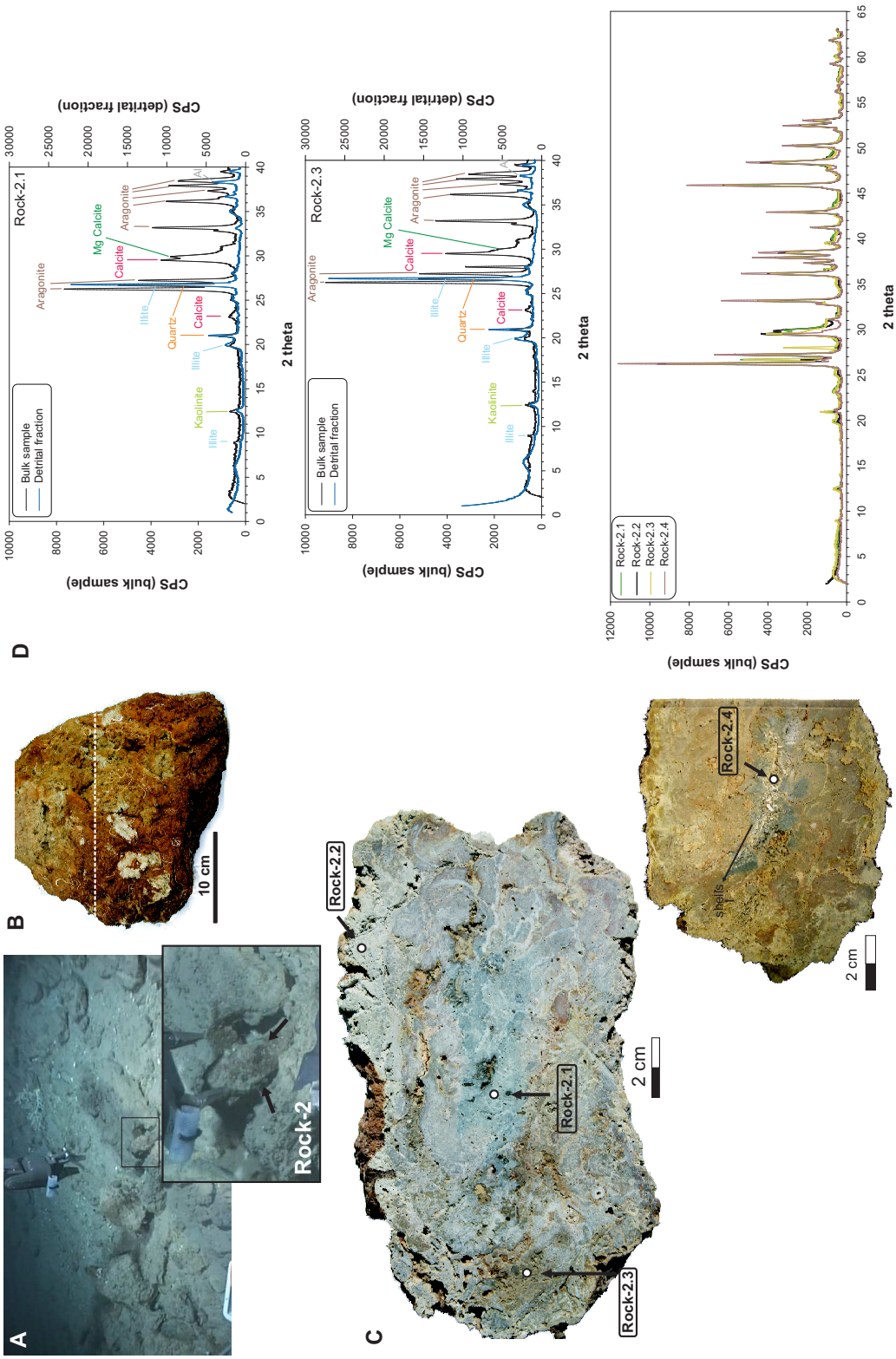

Figure 5.3b Authigenic carbonate samples: Rock-2. **A** Photograph of sample location on the Darwin MV (black box = sample). **B** Photograph of authigenic carbonate sample. **C** Cross sections of carbonate precipitates along the white dashed line shown in B. White dots indicate the positions of the analysed subsamples. **D** X-ray diffraction patterns of the bulk carbonate concretion samples and detrital fraction.

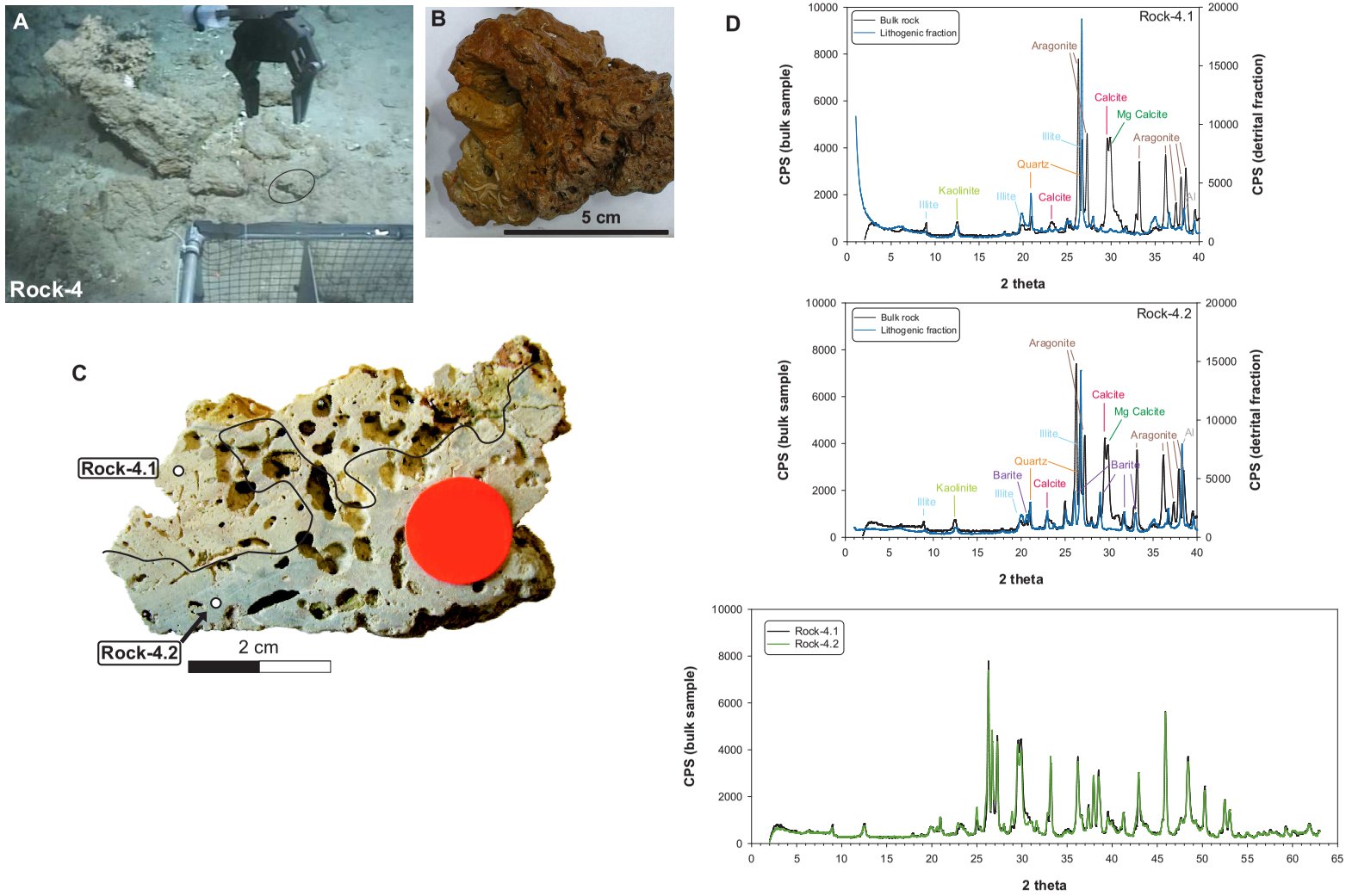

Figure 5.3c Authigenic carbonate samples: Rock-4. **A** Photograph of sample location on the Darwin MV (black oval = sample). **B** Photograph of authigenic carbonate sample. **C** Cross sections of carbonate precipitates along the white dashed line shown in B. White dots indicate the positions of the analysed subsamples. **D** X-ray diffraction patterns of the bulk carbonate concretion samples and detrital fraction.

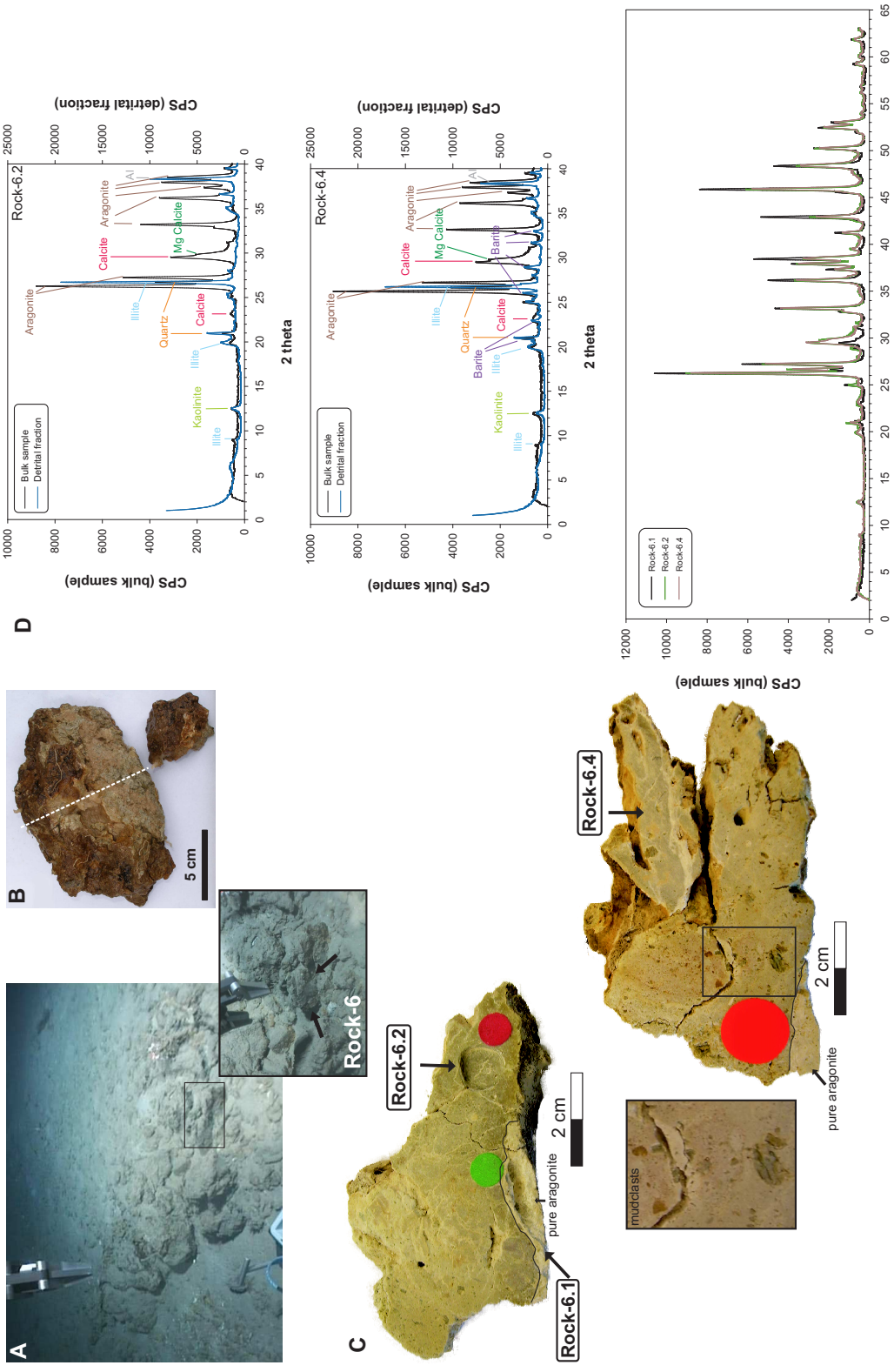

Figure 5.3d Authigenic carbonate samples: Rock-6. **A** Photograph of sample location on the Darwin MV (black box = sample). **B** Photograph of authigenic carbonate sample. **C** Cross sections of carbonate precipitates along the white dashed line shown in B. White dots indicate the positions of the analysed subsamples. **D** X-ray diffraction patterns of the bulk carbonate concretion samples and detrital fraction.

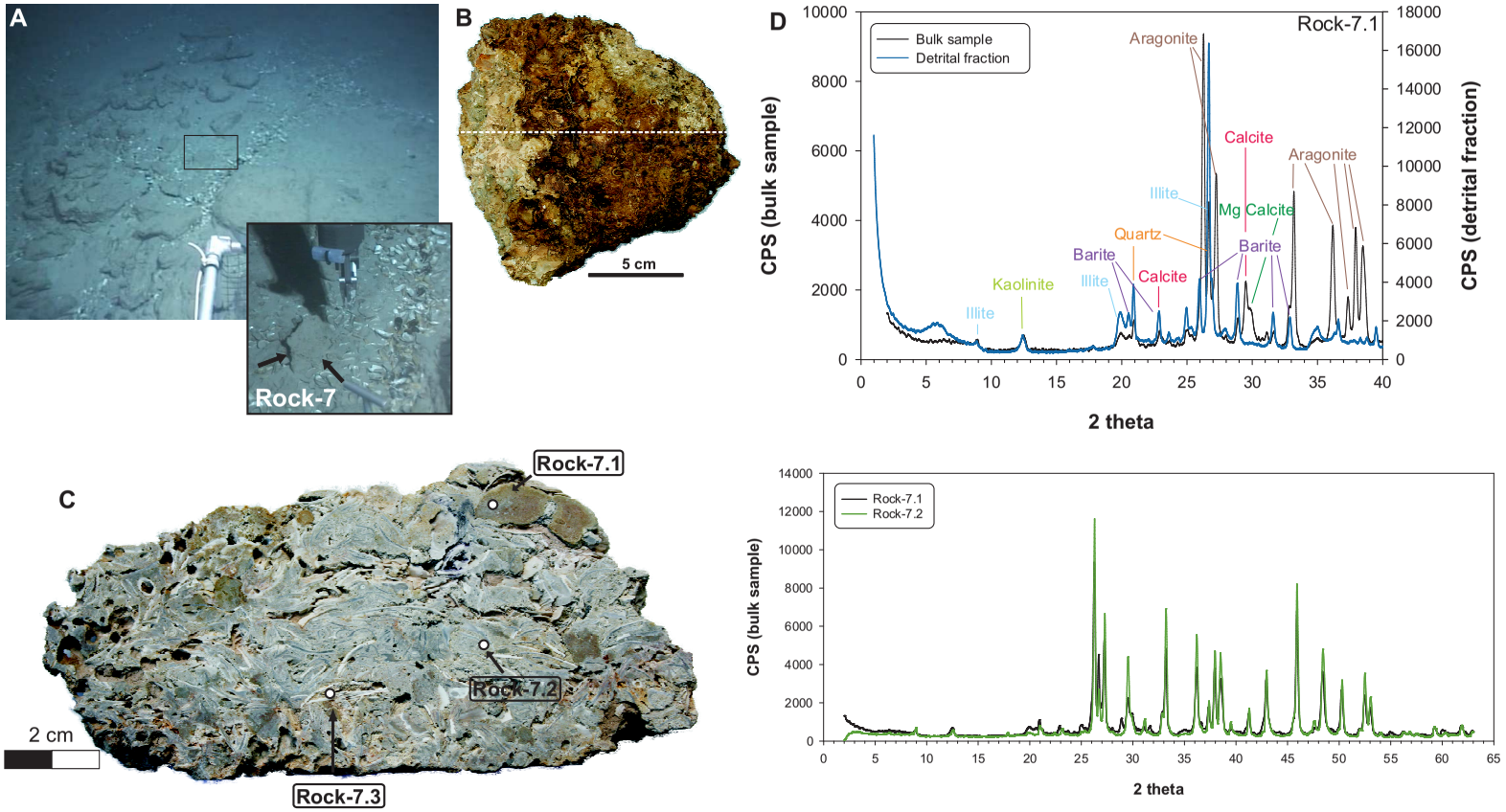

Figure 5.3e Authigenic carbonate samples: Rock-7. **A** Photograph of sample location on the Darwin MV (black box = sample). **B** Photograph of authigenic carbonate sample. **C** Cross sections of carbonate precipitates along the white dashed line shown in B. White dots indicate the positions of the analysed subsamples. **D** X-ray diffraction patterns of the bulk carbonate concretion samples and detrital fraction.

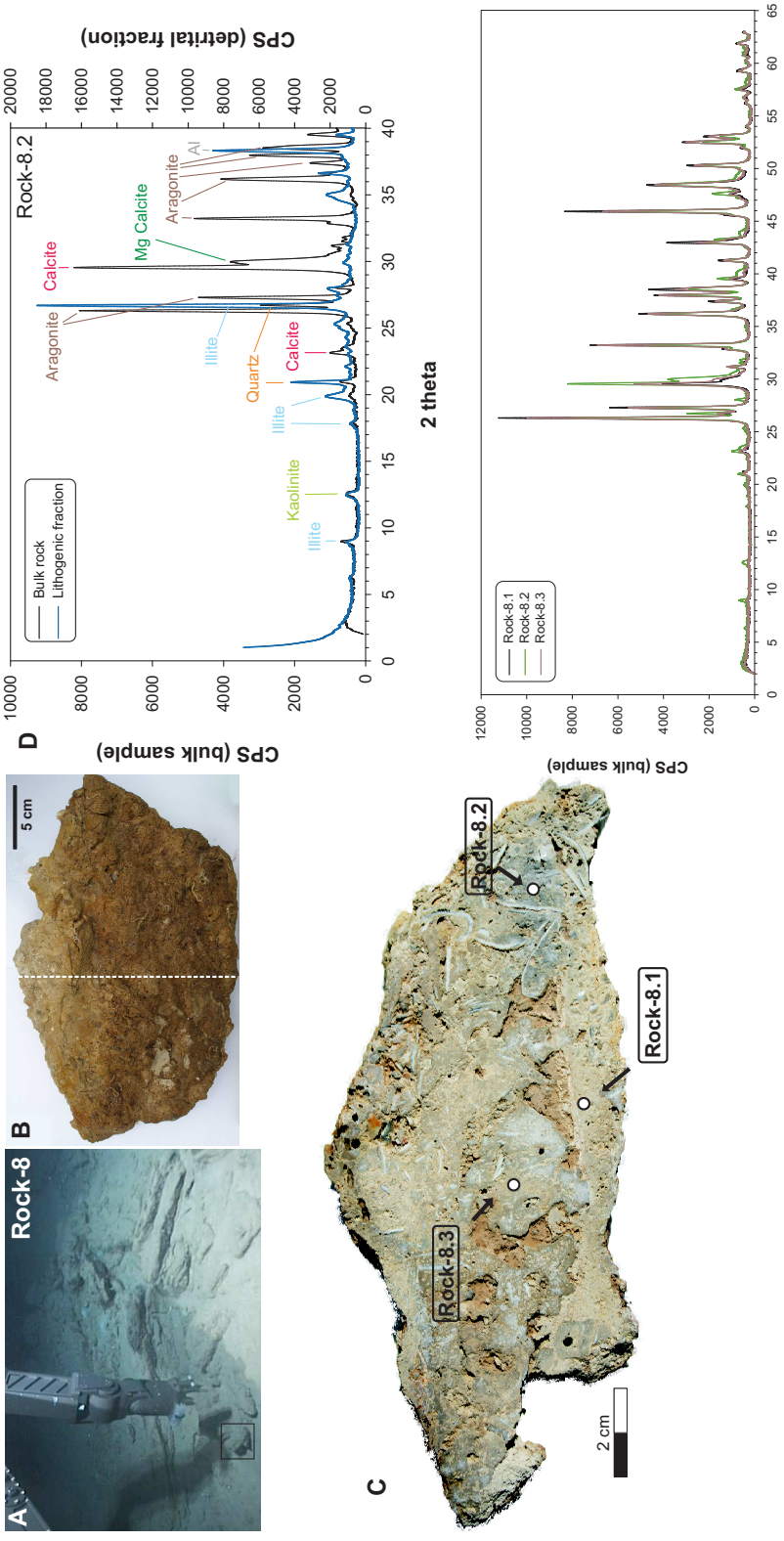

Figure 5.3f Authigenic carbonate samples: Rock-8. **A** Photograph of sample location on the Darwin MV (black box or oval = sample). **B** Photograph of authigenic carbonate sample. **C** Cross sections of carbonate precipitates along the white dashed line shown in B. White dots indicate the positions of the analysed subsamples. **D** X-ray diffraction patterns of the bulk carbonate concretion samples and detrital fraction.

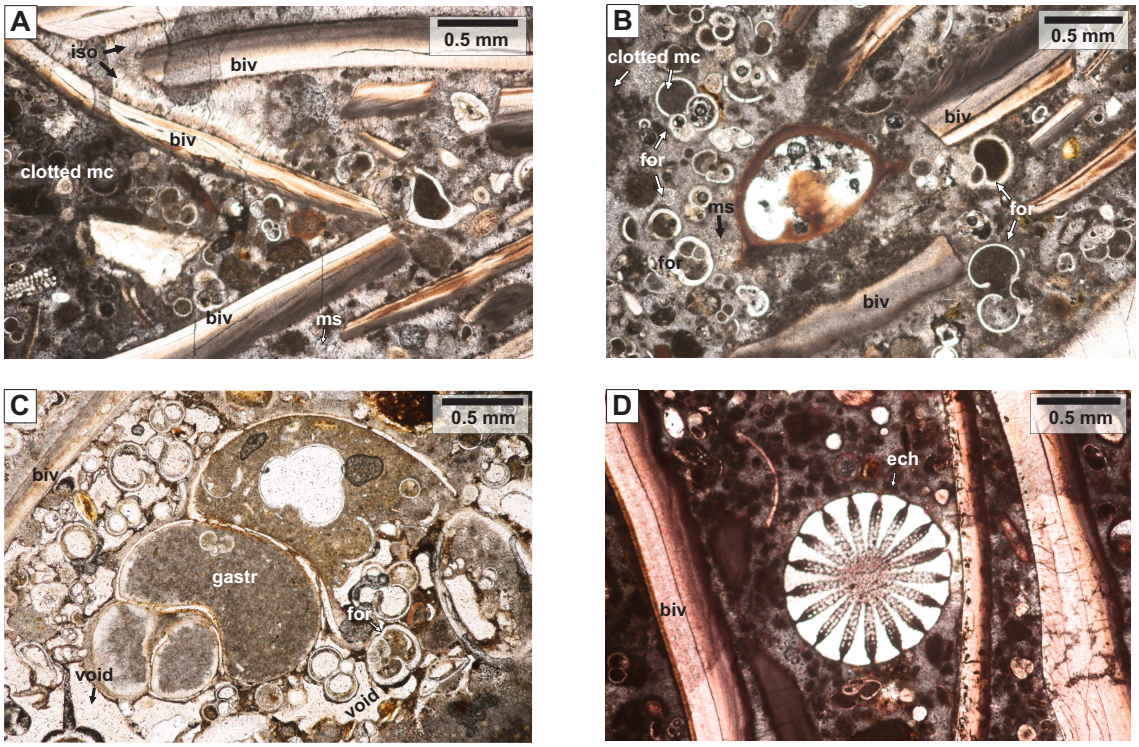

Figure 5.4 Thin section photographs of skeletal grains observed within the carbonate crusts from the Darwin mud volcano. **A** Bivalve shells (biv) immersed in a microsparite (ms) cement. Acicular aragonite occurs as isopachous layers (iso) on bivalve shells. Clotted microcrystalline calcite (micrite = mc) occurs on the left hand side of the photograph (plane-polarized light; rock 7). **B** well-preserved foraminifer tests (for) and bivalve shells immersed in a microsparite cement (plane-polarized light; rock 7). **C** Gastropod shell (gastr) filled with micrite (plane-polarized light; rock 1). **D** Echinoid spine (ech, stained thin section under plane-polarized light; rock 7).

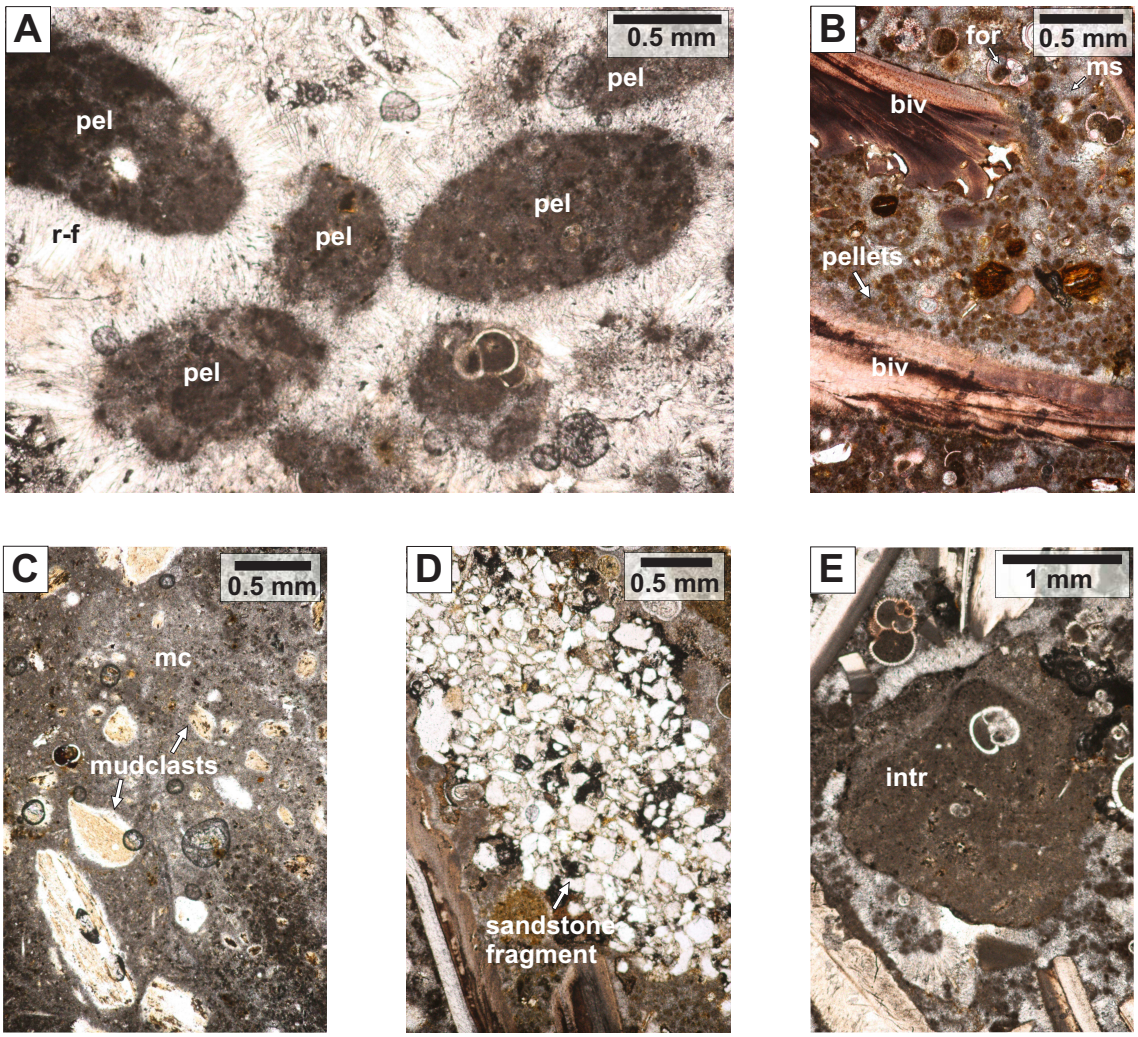

Figure 5.5 Thin section photographs of lithoclasts observed within the carbonate crusts from the Darwin mud volcano. **A** Peloids (pel) with radial fibrous aragonite cement rims (plane-polarized light; rock 6). **B** Fecal pellets, foraminifer (for) tests and bivalve (biv) shells immersed in a microsparite (ms) cement (stained thin section under plane-polarized light, rock 1). **C** Mudclasts within a micrite (mc) matrix (plane-polarised light; rock 6). **D** Sandstone fragment (plane-polarized light; rock 1). **E** Intraclast (intr) consisting of micrite (microcrystalline calcite) and foraminifer tests (plane-polarized light; rock 2).

common. The latter tend to be subrounded to well-rounded and consist of micrite and the remains of foraminifera shells. The majority of the extraclasts are mudclasts which are brown in colour; they are present in all of the rocks and vary greatly in size (0.1 - 5 mm). The biggest clasts are visible by naked eye in the hand specimens (e.g. rock 6, Fig 5.3c). Fragments of dolomitized sandstone were only observed in rocks 1 and 2. The quartz crystals that form the sandstone are overgrown and show undulose extinction under crossed polar light.

Diagenetic carbonate cements are present in all of the rocks but they are particularly abundant and diverse in fabric in rock 6, which is almost entirely composed of carbonate cement. The most common type of cement in all of the rocks is microsparite, (Fig. 5.4b). Botryoidal (Fig. 5.6a and b), isopachous acicular (Fig. 5.5a) and radial (Fig. 5.6c) and splayed fibrous (Fig. 5.6d) cements are also observed. Botryoidal cement characteristically consists of aragonite and it was only observed in rocks 2 and 6, i.e the white rim, and forms a complex structure of dome-shaped hemispheres that consist of thin fibrous brownish-yellowish aragonite crystals and crystal fans. The botryoids nucleate from micritic free surfaces and fill up voids and veins (Fig. 5.6a and 5.7d). Radial and splayed fibrous cements are generally clear in colour and consist of larger crystals than botryoids. They originate from sedimentary peloids and botryoids, while isopachous acicular aragonite forms rims around skeletal grains (Fig. 5.4a). Other microfabrics include burrows, which are often coated with red-brownish iron oxides (Fig. 5.7c). Iron oxides also occur as framboidal (raspberry-like) crystals (Fig. 5.7a). The black coloured (opaque) framboids consist of pyrite and occur in veins (Fig. 5.7e), dispersed within the micrite matrix (Fig 5.7b) and in foraminifera chambers (Fig. 5.7e).

5.3.2.2 Mineralogy and chemical composition

The carbonate content of the authigenic crusts ranges from 77 to 95 wt% (Table 5.4). The X-ray diffractogram of the detrital fraction of the samples, in conjunction with the diffractogram of the bulk sample, shows that the carbonate precipitates from the Darwin MV mainly consist of aragonite and calcite, and both are present in all of the rocks (Fig. 5.3a, 5.3f). The shift in the 2theta position of the calcite d(104) peak indicates substitution of Mg (and/or Fe, which is likely to be negligible as ferroan calcite was rarely observed in the thin sections) for Ca in calcite. LMC was detected in all of the samples (d(104)-values ranging between 3.018 and 3.032 after correction relative to the internal quartz standard, Table D.1 in Appendix D), while HMC mainly occurs in samples R-4.1, R-4.2, R-2.1, R-2.2, R-8.2 and R-8.3, with a d-value ranging from 2.982 to 2.995 Å. Within each rock, aragonite is especially abundant in samples R-1.1, R-2.4, R-6.1, R-7.2 and R-8.1. The detrital phase makes up 5 - 23 wt% of the rocks, and it mainly consists of quartz and clay minerals, usually illite and kaolinite, with mixed layer clays in some samples.

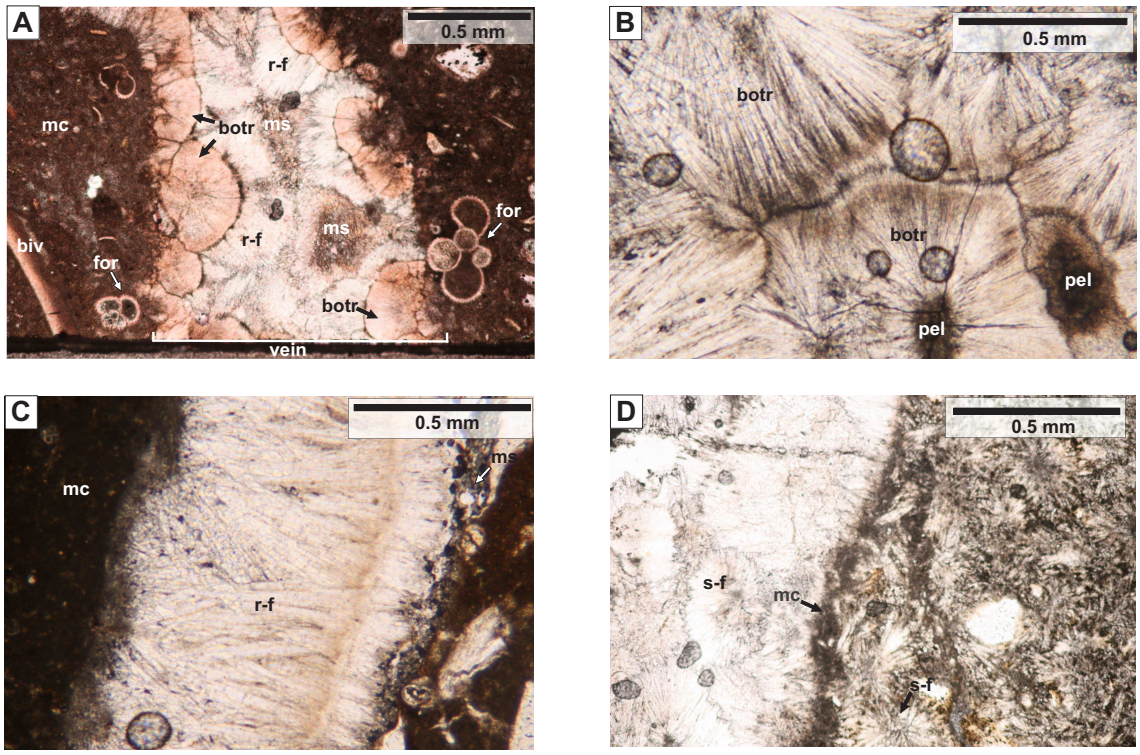

Figure 5.6 Thin section photographs of cement types observed within the carbonate crusts from the Darwin mud volcano. **A** Botryoidal (botr) aragonite cement nucleates from a micrite (mc) free surface, filling up a vein. Radial-fibrous (r-f) aragonite originates from the botryoids and the centre of the vein is filled with microsparite (ms) cement. Foraminifer (for) tests and bivalve (biv) shells are immersed with the micrite matrix (stained thin section under plane-polarized light; rock 2). **B** Botryoidal (botr) cement consisting of thin fibrous brownish-yellowish aragonite crystals nucleating from peloids (pel, plane-polarized light; rock 6). **C** Radial-fibrous (r-f) aragonite crystals originating from a micrite (mc) free surface. Microsparite (ms) occurs at the end of the fibrous aragonite crystals (plane-polarized light; rock 6). **D** shows the sharp boundary between clear splayed-fibrous (s-f) aragonite cement (on the left) and splayed-fibrous aragonite cement imbedded in micrite (mc) matrix (on the right, plane-polarized light, rock 6).

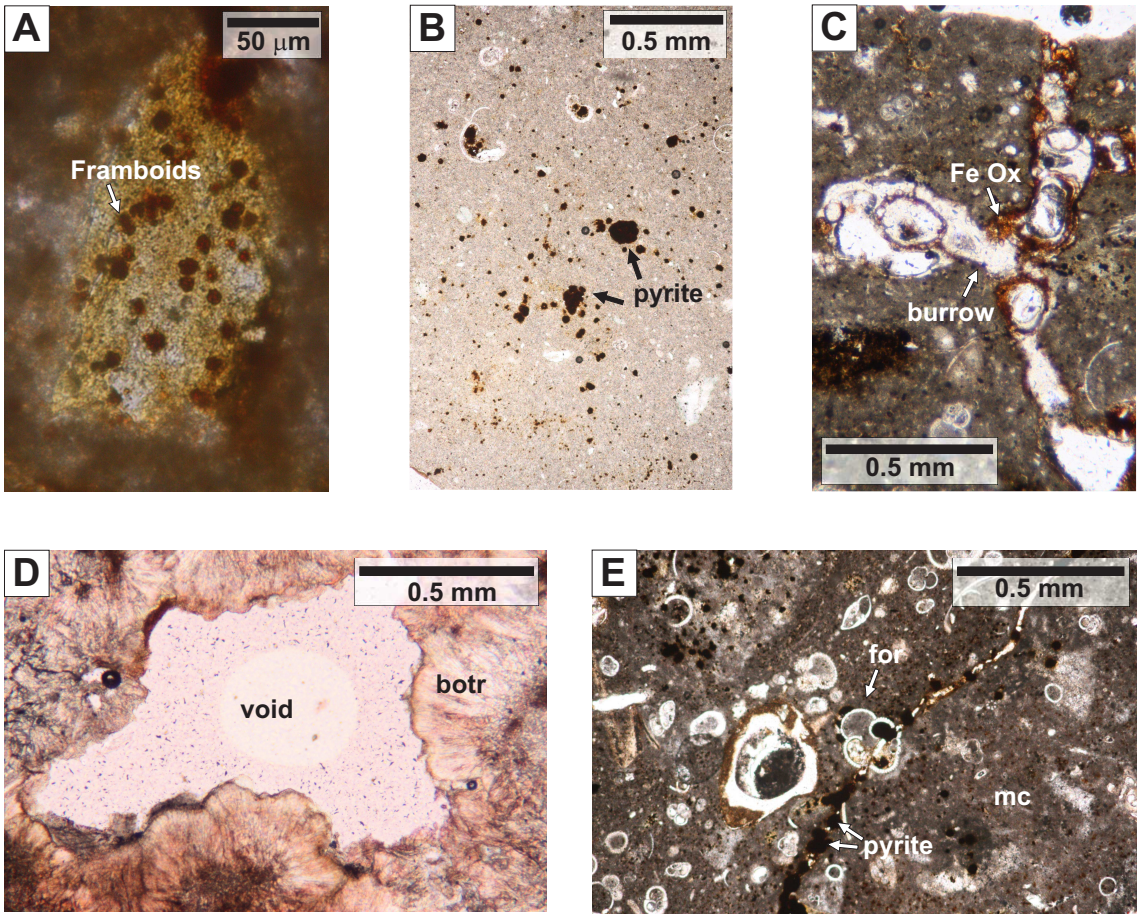

Figure 5.7 Thin section photographs of sulphide minerals and dissolution/deformation **A** Close-up of framboidal iron oxides (plane-polarized light; rock 1). **B** Pyrite and iron oxide framboids scattered in a micrite matrix (plane-polarized light; rock 4). **C** Tubeworm burrow coated with iron-oxides (Fe-Ox, plane-polarized light, rock 4). **D** Void partly filled with botryoidal (botr) aragonite cement (stained thin section under plane-polarized light; rock 6). **E** Fracture cutting through foraminifer (for) test, immersed in micrite (mc) matrix, that has subsequently been filled with pyrite framboids (plane-polarised light; rock 4).

In addition, barite occurs in R-4.2, R-6.1, R-6.2 and R-7.1, while only small amounts were detected in sample R-4.1. The cation content of the carbonate fraction is given in Table 5.4 and shown in Fig. 5.8. The highest Ca concentrations (up to 33.3 wt%) were measured in those samples with a high abundance of bivalve shells (R-7.2, R-2.4, R-8.3 and R-1.1), while samples from the innermost, more homogeneous, parts of the rock have Ca concentrations of as low as 30.9 wt%. Concentrations of Mg and Fe are less than, respectively, 1.5 and 0.5 wt%. A negative correlation is visible between Ca, Mg and Fe in Fig. 5.8a-b: samples with a lower Ca concentration contain higher amounts of Mg and Fe. Sr and Ba concentrations vary greatly between the different rocks, ranging from, respectively, 5360 to 11500 ppm and from 588 to 7990 ppm.

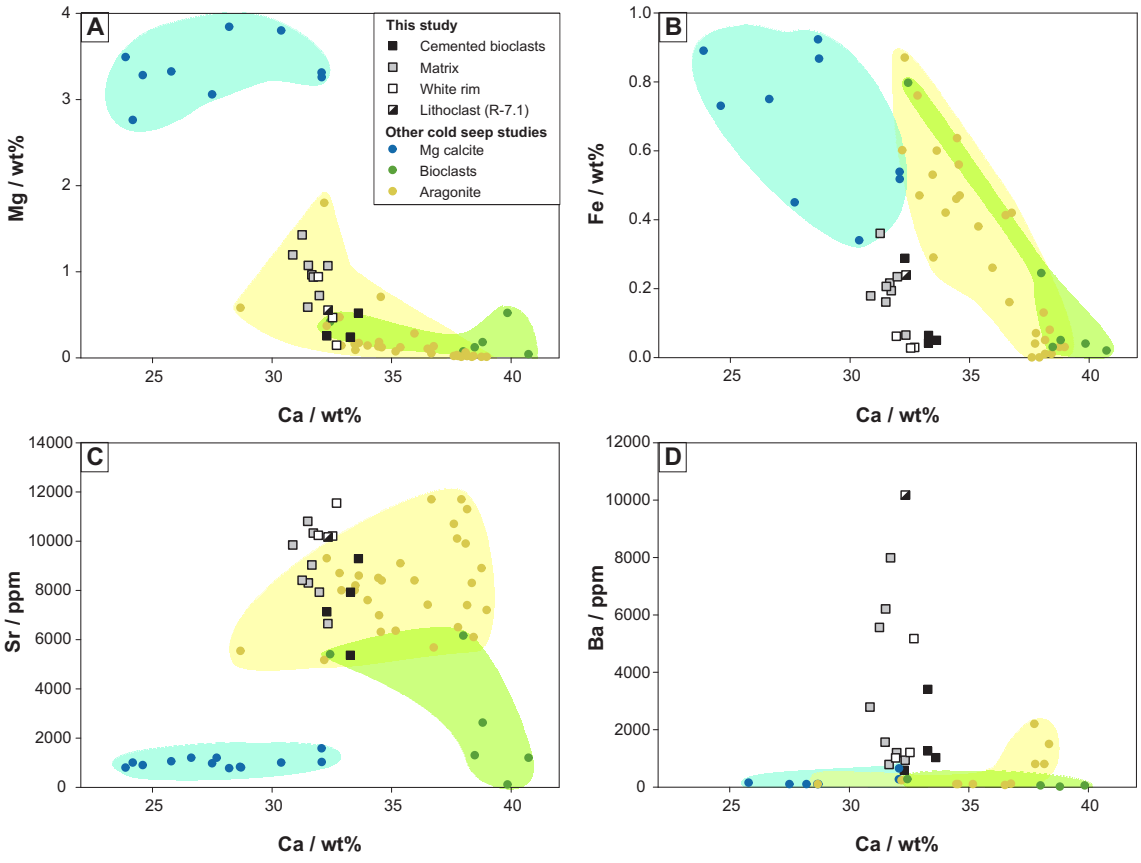

Figure 5.8 Chemical composition of carbonate subsamples from the Darwin mud volcano: calcium (Ca) versus magnesium (Mg; **A**), iron (Fe; **B**), strontium (Sr; **C**) and barium (Ba; **D**). Also shown are data for other hydrocarbon-derived authigenic carbonates (composed of mainly Mg calcite or aragonite) and incorporated bioclasts from seeps in the Niger deep-sea fan (Bayon et al., 2007), Congo Basin (Pierre and Fouquet, 2007), Gulf of Mexico (Feng et al., 2008) and Blake Ridge (Naehr et al., 2000a).

Table 5.4 Major and minor element concentrations of 5% HCl-soluble component of seep carbonate samples from the Darwin mud volcano.

Sample	Detrital fraction	Carbonate fraction	Ca	Mg	K	Fe	Mn	Sr	Ba
	%		weight %				ppm		
Rock-1.1	7	93	33.3	0.2	0.3	0.1	110	7930	3410
Rock-1.2	21	79	32	0.7	0.5	0.2	461	7930	1200
Rock-2.1	16	84	30.9	1.2	0.3	0.2	118	9850	2790
Rock-2.2	9	91	31.9	0.9	0.3	0.1	58.5	10200	1020
Rock-2.3	20	80	31.7	1	0.3	0.2	166	9030	790
Rock-2.4	6	94	32.3	0.3	0.2	0.3	28.4	7130	590
Rock-4.1	21	79	31.3	1.4	0.4	0.4	160	8410	5560
Rock-4.2	21	79	31.5	1.1	0.3	0.2	170	8310	6210
Rock-6.1	6	94	32.7	0.1	0.3	0	32.7	11600	5170
Rock-6.2	19	81	31.7	0.9	0.5	0.2	71.8	10300	7990
Rock-6.4	16	84	31.5	0.6	0.4	0.2	66.3	10800	1570
Rock-7.1	23	77	32.3	0.6	0.4	0.2	91.1	10200	4180
Rock-7.2	9	91	33.3	0.2	0.2	0	58.8	5360	1260
Rock-7.3	n.a.	n.a.	n.a.	n.a.	n.a.	n.a.	n.a.	n.a.	n.a.
Rock-8.1	5	95	32.5	0.5	0.2	0	14.5	10200	1200
Rock-8.2	10	90	32.3	1.1	0.2	0.1	32.6	6650	930
Rock-8.3	6	94	33.6	0.5	0.2	0	25.2	9290	1030

n.a.: not analysed

Table 5.5 Stable carbon and oxygen isotope values of authigenic carbonate crusts, $MgCO_3$ content and calculations of fluid T / $\delta^{18}O$ compositions in present-day bottom/pore waters of the Darwin mud volcano (T=10.3 °C; $\delta^{18}O$ = -0.1 ‰ SMOW)

sample NR	$\delta^{13}C$	$\delta^{18}O$	$MgCO_3$[a]		100 % aragonite		100 % Mg-calcite[b]			
			LCM	HMC	T	$\delta^{18}O_{fluid}$	T_{LMC}[c]	T_{HMC}[c]	$\delta^{18}O_{fluid}$- LMC[d]	$\delta^{18}O_{fluid}$-HMC[d]
	‰ PDB	‰ PDB	mol%	mol%	°C	‰ SMOW	°C	°C	‰ SMOW	‰ SMOW
Rock-1.1	-13.63	4.85	2	n.c.	-1.6	2.68	-3	n.c.	3.35	n.c
Rock-1.2	n.a.	n.a.	1	n.c.	n.c.	n.c.	n.c.	n.c.	n.c.	n.c.
Rock-2.1	-23.94	4.46	3	15	0	2.3	-1.5	1.2	2.96	2.24
Rock-2.2	-19.65	4.44	6	15	0.1	2.28	-0.7	1.3	2.94	2.22
Rock-2.3	-25.45	4.3	4	n.c.	0.7	2.14	-0.7	n.c.	2.8	n.c.
Rock-2.4	-12.21	3.29	3	n.c.	5.1	1.13	2.9	n.c.	1.79	n.c.
Rock-4.1	n.a.	n.a.	4	14	n.c.	n.c.	n.c.	n.c.	n.c.	n.c.
Rock-4.2	-18	5.14	2	14	-2.9	2.97	-4.1	-1.5	3.64	2.97
Rock-6.1	-27.88	4.37	2	n.c.	0.4	2.21	-1.3	n.c.	2.87	n.c.
Rock-6.2	n.a.	n.a.	5	n.c.	n.c.	n.c.	n.c.	n.c.	n.c.	n.c.
Rock-6.4	n.a.	n.a.	3	n.c.	n.c.	n.c.	n.c.	n.c.	n.c.	n.c.
Rock-7.1	n.a.	n.a.	1	n.c.	n.c.	n.c.	n.c.	n.c	n.c.	n.c.
Rock-7.2	-8.83	4.65	3	n.c.	-0.8	2.48	-2.1	n.c	3.15	n.c.
Rock-7.3	-8.07	3.63	n.c.	n.c.	3.6	1.47	n.c.	n.c.	2.13	n.c.
Rock-8.1	-22.64	3.81	2	n.c.	2.8	1.65	0.7	n.c.	2.31	n.c.
Rock-8.2	n.a.	n.a.	3	17	n.c.	n.c.	n.c.	n.c.	n.c.	n.c.
Rock-8.3	-21.14	3.67	3	n.c.	3.5	1.5	1.4	n.c.	2.17	n.c.
Min. value	**-27.88**	**3.29**	**1**	**14**	**-2.9**	**1.13**	**-4.1**	**-1.5**	**1.79**	**2.22**
Max. value	**-8.07**	**5.14**	**6**	**15**	**5.1**	**2.97**	**2.9**	**1.3**	**3.64**	**2.97**

[a] Calculated using the following equation from (Lumsden, 1979): $MgCO_3(mol\%)=100-[333.33 \cdot d(104)-911.99]$

[b] $MgCO_3$ content is assumed to be 3 mol%, i.e. average value of all carbonate sample

[c] Units are converted from $\delta^{18}O$(SMOW) to $\delta^{18}O$(‰PDB) using the following Friedman and O'Neil (1977) equation: $\delta^{18}O_{PDB}=0.97006*\delta^{18}O_{SMOW}-29.94$

[d] Units are converted from $\delta^{18}O$(‰PDB) to $\delta^{18}O$(SMOW) using the following Friedman and O'Neil (1977) equation: $\delta^{18}O_{SMOW}=1.03086*\delta^{18}O_{PDB}-30.86$

n.a.: not analysed

n.c.: not calculated; required data was not available to make the calculation

5.3.2.3 Isotopic composition of pore fluids and authigenic carbonates

Stable oxygen and carbon isotope values of authigenic carbonate samples vary between -27.9 and -8.1‰ V-PDB for δ^{13}C and 3.3 to 5.1 ‰ V-PDB for δ^{18}O (Fig. 5.10; Table 5.5). Samples with a higher abundance of shells tend to be more enriched in ^{13}C compared to samples with a minor shell abundance. A carbon isotopic composition of as low as -8.1‰ was measured in R-7.3; this was a bivalve shell that was extracted from the rock. The lowest δ^{13}C value was measured in R-6.1, i.e. the white coloured rim of rock 6. The δ^{13}C values vary considerably within rock 2, ranging from -12.2‰ in the cluster of shells in the centre of the rock to -25.5‰ in the surrounding matrix. The δ^{18}O value of pore waters from both cores is similar (on average -0.1), while δ^{13}C values were higher in pore fluids from core MC-30 (-17.8 to -21.7‰) than they are in core GC-33 (-28‰ on average; Table 5.6).

Table 5.6 Stable carbon and oxygen isotope values of pore waters from Darwin MV

sample NR (depth)	δ^{13}C ‰ PDB	δ^{18}O ‰ SMOW
MC-30 (2.5 cmbsf)	-21.74	0.00
MC-30 (4.5 cmbsf)	-19.11	0.09
MC-30 (6 cmbsf)	-19.94	-0.13
MC-30 (11 cmbsf)	-17.76	-0.24
GC-33 (12.5 cmbsf)	-27.35	-0.12
GC-33 (17.5 cmbsf)	-28.66	-0.04

5.4 Discussion

5.4.1 Present-day seepage activity at the Darwin MV

Chemical analyses and pore fluid modelling indicate that only one of the three sampling locations on the summit of the Darwin MV was seeping fluids and gases at the time of surveying; site 33 which is located close to the 'black spot' area in the NW corner of the crater. However, the velocity of fluid seepage is low (0.09 cm yr^{-1}, from modelling results). Nevertheless, fluid seepage is sufficient to modify the pore water chemistry of some constituents; for example, there is a rapid decrease in sulphate pore water content with depth accompanied by an enrichment in TA relative to the background core. This also signifies the occurrence of anaerobic oxidation of methane (Eqn. 5.1). In this connection, high levels of methane (up to 1 mM) and higher hydrocarbons were recorded in the pore waters at depth while concentrations were below detection limit in the top 25 cm. In addition, video observations recorded gas bubbles rising from the seabed after disturbing the sediment, suggesting that the pore fluids are saturated in hydrocarbon gases. The

high sulphide concentrations produced by AOM, lead to precipitation of ferrous sulphide deposits, producing the black coloured sediments observed on the seafloor at this site. At the other sites (30/31 and 37), we find no evidence for fluid flow and/or anaerobic oxidation of methane at the time of sampling: pore fluid profiles of the conservative elements (B, Na^+) show no change in concentration with depth, and TA and sulphate pore water concentrations are low and remain constant with depth.
Whether authigenic carbonates are actively precipitating today at site 33 can be assessed by comparing the pore fluid model results with measured pore fluid concentrations of Ca^{2+}, Mg^{2+} and Sr^{2+}. All of these elements appear to be extracted from the pore fluids within the SMTZ, indicating that authigenic carbonates are indeed precipitating within the sediments, fuelled by AOM. Furthermore, the uptake of Mg^{2+} points towards the formation of Mg-calcite, whereas Sr^{2+} is typically incorporated in the aragonite crystal structure (Morse et al., 2007). The increase in pore water $[Ba^{2+}]$ at 45.5 cm depth is most likely the result of dissolution of a Ba-rich mineral such as witherite ($BaCO_3$) and/or barite ($BaSO_4$). The latter is more likely as the high TA concentrations will prevent the dissolution of witherite. Barite precipitates at seep sites are known to record the depth of the sulphate methane transition and hence have been used to get information about the methane flux history at the respective site (Aquilina et al., 1997; Dickens, 2001; Gingele and Dahmke, 1994; Kasten et al., 2003; Torres et al., 1996a; Snyder et al., 2007a) . Although the peak in $[Ba^{2+}]$ might indicated dissolution of barite and thus an upward shift of the SMT, at this point we are unable to make such interpretation based on a single data point.

5.4.2 Formation of authigenic carbonates at the Darwin MV

Laboratory experiments, together with observations from natural environments, indicate that the mineralogy of authigenic carbonates is controlled by a range of environmental parameters (Buczynski and Chafetz, 1991; Burton, 1993; Savard et al., 1996). Accordingly, the mineralogical composition of the authigenic carbonates from the Darwin MV may be used to provide an insight as to the environmental conditions at the MV at the time the carbonates formed, and thus provide a record of past fluid and mudflow activity.

All of the carbonate precipitates recovered from the Darwin MV contain extraclasts such as mudclasts and some have fragments of dolomite cemented sandstone (rocks 1 and 2) embedded in a fine matrix of clays and microcrystalline calcite. Semi-consolidated mudclasts are common in mud breccia and the dolomitisation of the sandstone fragments, as well as the undulating extinction of the quartz grains, are signs of burial and compaction. Accordingly, the mictric matrix of the carbonates can be interpreted as carbonate cemented mud breccia: clasts in a clay mineral-rich matrix originating from deeper loc-

ated stratigraphic layers (Kopf, 2002). This indicates that the Darwin MV was already active before the carbonate crusts were formed. The intraclasts are thought to be the product of brecciation which may be triggered by tectonic and/or vent related disturbances such as ascending mud, increasing fluid flow rates or growing gas hydrate layers as well as the sudden release of trapped fluids and/or gases (Greinert et al., 2001; Matsumoto, 1990; Naehr et al., 2009).The formation of authigenic carbonates at depth may clog up the fluid escape pathways, creating overpressure, which may lead to brecciation of the carbonate seal (Tryon et al., 2002). Consequently, carbonate cementation probably occurred in several stages. The main non-carbonate mineral of note in the rocks recovered from the Darwin MV is barite. As discussed in the previous section, barite is typically formed just above the SMT in cold seep settings and thus its presence in samples R-4.2, R-6.2, R-6.1 and R-7.1 signifies that the carbonate phases formed in the vicinity of the SMT.

The carbonate fraction of all of the rocks sampled from the Darwin MV is composed of the same assortment of carbonate minerals, i.e. aragonite, calcite and Mg-calcite. The low Mg concentrations in the carbonate fraction suggest that Mg calcite is a minor component compared to aragonite and calcite (Fig. 5.8a). As Sr and Ba tend to be preferentially taken up in the orthorhombic aragonite than in the hexagonal calcite crystal structure (Morse et al., 2007), we infer that the high Sr and Ba concentrations measured in the carbonate precipitates (Fig. 5.8c-d) are indicative of an abundance of aragonite relative to calcite. This is in agreement with petrographic observations: the white rim of rock 6 (which has the highest measured Sr concentration, Table 5.4) consists of botryoidal aragonite. Also, Fig. 5.8 shows that the carbonates from the Darwin MV have Mg and Sr concentrations that are comparable to authigenic carbonates from other cold seep sites, which are mainly aragonitic. Note that the soluble fraction of the carbonates from the Darwin MV contains significantly more Ba than carbonates from other seep sites. This might be indicative of witherite, but this would need to be verified by further analysis. Although the parameters that determine carbonate mineralogy and the incorporation of Mg in hydrocarbon-derived carbonates are poorly understood (De Choudens-Sanchez and Gonzalez, 2009), it is commonly accepted that a high degree of carbonate supersaturation in combination with high pore fluid Mg^{2+}/Ca^{2+} ratios and the presence of sulphate promotes aragonite precipitation by inhibiting HMC crystallisation (Aloisi et al., 2002; Burton, 1993; Chafetz et al., 1991; Kralj et al., 2004; Savard et al., 1996). These conditions can be found within sediments that are close to the seafloor, slightly above the base of the sulphate reduction zone. By contrast, calcite and Mg-calcite tend to precipitate at depth below the seafloor, where sulphate concentrations and Mg^{2+}/Ca^{2+} ratios are lower (Aloisi et al., 2000; Burton, 1993; Morse et al., 1997). By analogy, the presence of both $CaCO_3$ polymorphs in the authigenic carbonates from the Darwin MV suggests that there have been several stages of precipitation, both at depth and in the shallow subsurface. The white aragonite-rich rim, enclosing a micritic matrix, observed in rocks 2, 6 and 8, suggests that the rocks initially precipitated at depth, and they were then transported upwards towards the seafloor where the aragonite rim subsequently formed. As the

carbonate ion concentration in pore fluids at MVs is mainly determined by the efficiency of anaerobic oxidation of methane (and thus by the microbial consortia and methane flux from below), the presence of aragonite as a cement in the authigenic carbonates from the Darwin MV suggests that the methane flux and/or the fluid flux from depth has varied over time since the formation of the carbonate precipitates. A positive correlation between aragonite precipitation and seepage rate has been postulated in several cold seep studies (Hovland et al., 1987; Luff and Wallmann, 2003; Terzi et al., 1994). Rapid precipitation and hence aragonite formation (Buczynski and Chafetz, 1991; Given and Wilkinson, 1985) is also implied by the high abundance of well preserved skeletal grains and fecal pellets within the carbonate crusts (Fig. 5.5b). These pellets are produced by organisms, particularly polychaete worms, gastropods and some crustaceans that eat mud, digest organic matter from the mud and excrete the non-digested lime-mud. Besides bacterial decomposition of the organic mucus, fast intragranular cementation is also required to fossilize these originally soft particles (Land and Moore, 1980).

5.4.3 Source of deep fluids at the Darwin MV

The oxygen isotope composition of authigenic carbonates is primarily a function of temperature and the δ^{18}O value of the fluid from which they precipitate. Thus, carbonate δ^{18}O is used to provide information on the temperature of precipitation or, if the temperature is known, carbonate δ^{18}O values can be used to reconstruct the oxygen isotopic composition of the seeping fluids, and hence to assess the origin of the fluids. However, carbonate δ^{18}O also varies as a function of mineralogy (Friedman and O'Neil, 1977). Aragonite is generally enriched in ^{18}O, by 1.4‰ relative to calcite, if both minerals precipitate in isotopic equilibrium from the same solution at the same temperature. The fractionation of oxygen isotopes between aragonite and Mg-calcite is smaller than for aragonite-calcite, and tends to decrease with increasing Mg content (Fig D.2 in Appendix D). The difference between the minimum and maximum measured δ^{18}O value in the carbonates of the Darwin MV is 1.8‰, which cannot be explained solely by differences in carbonate mineralogy. Thus, the oxygen isotopic composition of the carbonate crusts must be affected by additional processes. If the carbonates precipitated in equilibrium with present-day bottom seawater, which has δ^{18}O = -0.1‰ and T = 10.3°C, then the theoretical δ^{18}O values for Mg-calcite (Friedman and O'Neil, 1977) and aragonite (Hudson and Anderson, 1989) are given by:

$$\delta^{18}O_{Mg-Calcite}(V-PDB) = e^{\frac{2.78\cdot(10^6\cdot T^{-2})-2.89+0.06\cdot Mg\%}{1000}}\Big(1000+\delta^{18}O_{fluid}-1000\Big) \quad (5.4)$$

$$\delta^{18}O_{aragonite}(V-PDB) = -\frac{(T-19.7)}{4.34}+\delta^{18}O_{fluid} \quad (5.5)$$

where $\delta^{18}O_{fluid}$ is the isotopic composition of the ambient fluid (‰ V-PDB in Eqn 5.4 and SMOW in Eqn 5.5) and T is the fluid temperature (K in Eqn. 5.4 and °C in Eqn. 5.5). Mg% is the $MgCO_3$ content of the calcite (mol%), which is assumed to be equal to 3 mol%, the average concentration in samples from the Darwin MV (Table 5.5).

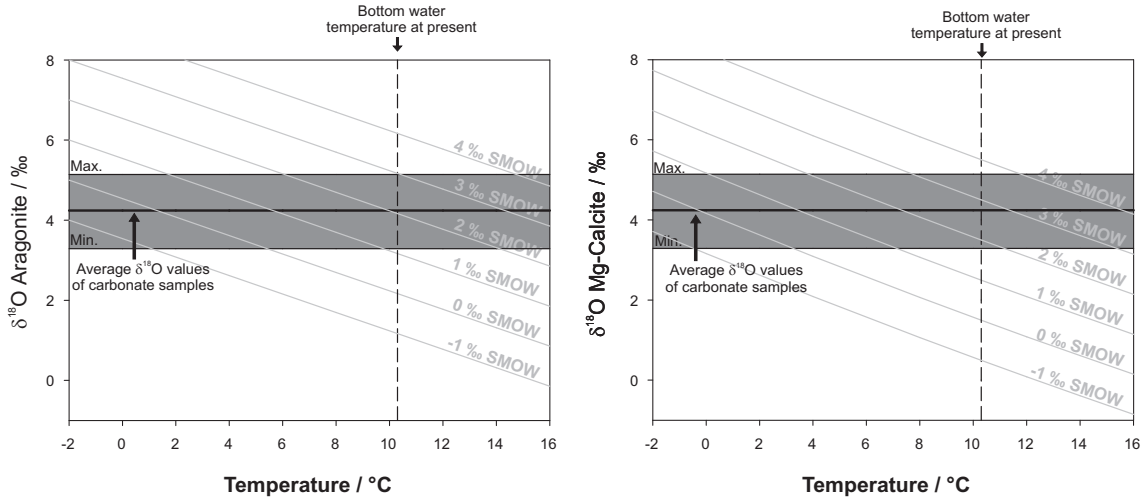

Figure 5.9 Plots showing the relationship between carbonate precipitation temperature and carbonate δ^{18}O, for different values of seawater δ^{18}O. (A) aragonite, (B) Mg-calcite. Based on the equations reported in, respectively, Hudson and Anderson (1989) and Friedman and O'Neil (1977).

As the relative abundances of aragonite and Mg-calcite are not known for Darwin MV carbonates, δ^{18}O and temperature values are calculated for both extremes: 100% - 0% aragonite-Mg calcite and vice versa (Table 5.5, Fig. 5.9). The equilibrium δ^{18}O value for Mg-calcite is 1.4‰, and for aragonite it is 2.1‰. Both values are significantly lower than those measured in the carbonates (which range from 3.3‰ to 5.1‰ PDB), so either fluid temperatures were lower and/or fluid δ^{18}O values were higher than they are at present. If the fluid δ^{18}O value has not changed, then fluid temperatures must have been 0.2 °C, on average, to produce the δ^{18}O values measured in the carbonate samples. Minimum bottom water temperatures of as low as 4 °C are thought to have occurred during glacial periods in the Gulf of Cadiz (Voelker et al., 2006). Thus, it seems unlikely that the δ^{18}O values of the carbonates are principally controlled by temperature. However, during the Last Glacial Maximum (LGM), δ^{18}O of seawater was characteristically 1.05 ± 0.2 ‰ heavier than today (Duplessy et al., 2002). Assuming that carbonate precipitation occurred during the LGM, aragonite and Mg-calcite would have δ^{18}O values of 4.56 and 4.04 ‰, respectively, i.e. 0.5 ‰ lower than the maximum measured δ^{18}O value in the carbonates. Alternatively, if the crusts precipitated at the same temperature as present-day bottom seawater, their high δ^{18}O values must be produced by precipitation from δ^{18}O-rich fluids; δ^{18}O = 1.13 to 3.64‰ SMOW. The pore waters could have been enriched in ^{18}O due to gas hydrate dissociation (Davidson et al., 1983; Hesse and Harrison, 1981). During the formation of gas hydrates

in the sediment column, water with high δ^{18}O is preferentially incorporated into the gas hydrate structure (Davidson et al., 1983). Hence dissociation of gas hydrate releases ^{18}O-rich water (and methane gas), promoting the precipitation of ^{18}O-enriched carbonates. Although the Darwin MV is located within the gas hydrate stability zone (Fig. 5.1b), no gas hydrates have been sampled at this location. However, even if gas hydrates do not occur at present, they might have formed during cooler periods in the past. The presence of authigenic carbonates at other sites in the Gulf of Cadiz has been attributed to the dissociation of gas hydrates as a result of increased bottom water temperatures during the transition from glacial to interglacial conditions (Magalhães, 2007). Lower bottom water temperatures during glacial times permit the formation of gas hydrates near the seafloor; these are destabilised by warming of bottom waters during subsequent interglacial periods and they therefore dissociate (Magalhães, 2007). However, other processes can also lead to the formation of ^{18}O-rich pore fluids. These include clay mineral dehydration (Savin and Epstein, 1970), which seems to be the main source of freshwater in mud volcanoes in the Gulf of Cadiz (Hensen et al., 2007; Scholz et al., 2009). Nevertheless, future investigations are necessary to decipher the importance of both potential sources of enriched fluids and an age determination is essential to find out whether these carbonates were formed during the LGM.

5.4.4 Is authigenic carbonate formation driven by methane seepage?

Authigenic carbonates derive their carbon from the pore water $\sum CO_2$ pool (Suess and Whiticar, 1989). This pool is, in surface sediments affected by methane seepage, mainly controlled by the microbially driven anaerobic oxidation of methane. Isotopic fractionation of carbon occurs during both anaerobic and aerobic oxidation of methane, concentrating the lighter ^{12}C isotope in the CO_2 that is produced (Alperin and Reeburgh, 1988; Whiticar et al., 1986). As a consequence, oxidation of methane reduces the $\delta^{13}C \sum CO_2$ value of the remaining $\sum CO_2$ pool. As the carbon isotopic composition of methane is determined by its source, carbonate δ^{13}C values may give an insight as to changes in the origin of the methane in the past. However, pore waters also contain $\sum CO_2$ derived from seawater (0±3‰; Anderson and Arthur, 1983) and $\sum CO_2$ derived from the degradation of organic matter via sulphate reduction ($\sim$ -20‰; Claypool and Kaplan, 1974 and references therein).

The carbon isotopic composition of the carbonates from Darwin MV varies between -8.1‰ and -27.9‰. The similarity between the δ^{13}C values of the majority of the carbonate precipitates and the pore water $\sum CO_2$ (Table **??**) indicates that the carbonates are likely to have formed from this $\sum CO_2$ pool. Results from gas chromatographic analyses demonstrate that both methane and higher hydrocarbons are present in the subsurface at Darwin MV indicating that the methane is in part of thermogenic origin ($\delta^{13}C_{CH_4}$: -30 to -50‰

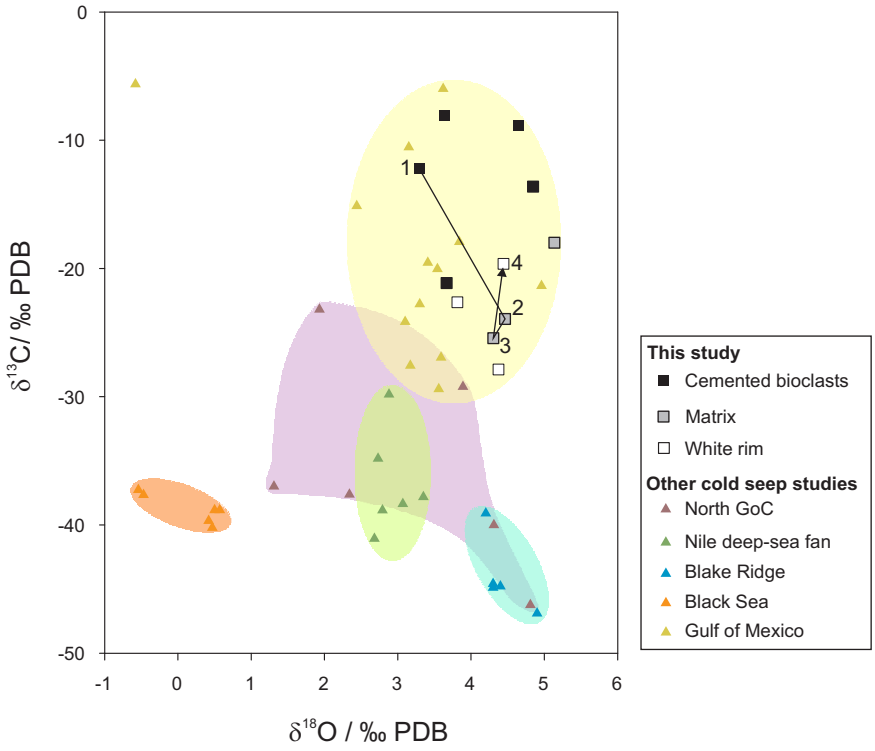

Figure 5.10 Carbon (δ^{13}C) and oxygen (δ^{18}O) isotopic compositions of authigenic carbonates from the Darwin mud volcano. Fields to show the δ^{13}C and δ^{18}O values of authigenic carbonates from other seep sites across the world are also shown. These data are from the Iberian margin in the Gulf of Cadiz (Díaz-del Río et al., 2003), the Nile deep-sea fan (Gontharet et al., 2007), the Blake Ridge (Naehr et al., 2000a), the Black Sea (Bahr et al., 2009) and the Gulf of Mexico (Feng et al., 2009b). The arrow indicates the change in carbon and oxygen isotopic compositions within rock 2, from the centre of the crust (#1) to the rim (# 4).

PDB; Whiticar, 1994). δ^{13}C values of methane in pore fluids from the Darwin MV have not been determined so far but the carbon isotopic signature of methane and higher hydrocarbons from other MVs in the Gulf of Cadiz ranges, respectively, from -23‰ to -73‰ and -11‰ to -34‰ (Nuzzo et al., 2009; Stadnitskaia et al., 2006). Thus although the oxygen isotope data indicates that no deep sourced fluids are seeping at the Darwin MV at the present-day (Table 5.6), the source of hydrocarbons is similar to the one at the time of carbonate precipitation. The less negative δ^{13}C values in the shell-dominated samples (Fig. 5.10), most likely reflects higher carbon input from seawater relative to the other samples, as these shells form at the seafloor. The matrix enclosing the cluster of shells in the centre of rock 2 is more depleted in δ^{13}C (R-2.3 and R-2.1 respectively -25.5‰ and -23.9‰) and thus presumably precipitated at a greater depth. The rim is slightly enriched in ^{13}C which corresponds to precipitation near the seafloor and is in agreement with its aragonite composition.

In addition, Fig. 5.10 compares the δ^{13}C values of authigenic carbonates recovered from cold seep areas from all over the world. The δ^{13}C values of the Darwin MV carbonates are similar to those measured in carbonates recovered from the Bush Hill seeps in the Gulf of Mexico (Feng et al., 2009a), which are thought to reflect the microbial degradation

of crude oil, which has an average -25 ‰ (Feng et al., 2009b; Joye et al., 2004; Roberts and Aharon, 1994). Although no trace of biodegrade crude oil was observed within the carbonates from the Darwin MV, previous studies have provided evidence for petroleum seepage at MVs in the Gulf of Cadiz (Nuzzo et al., 2009). The authigenic carbonates from the other seep areas are generally more depleted in ^{13}C than the precipitates from the Darwin MV. The carbon in the carbonates from the Blake Ridge (Naehr et al., 2000a) and the Black Sea (Bahr et al., 2009) is probably derived from the anaerobic oxidation of biogenic methane ($\delta^{13}C_{CH_4}$: -50 to -120‰ PDB; Whiticar, 1994), while a thermogenic origin is suggested for the Nile deep-sea fan (Gontharet et al., 2007), and a mixture of both for the chimney carbonates on the Iberian margin of the Gulf of Cadiz (Díaz-del Río et al., 2003).

Evidence for microbially induced precipitation of carbonates at the Darwin MV comes also from the presence of particular sedimentary microfabrics. These include peloids (Fig. 5.5a), clotted micrite (Fig. 5.4a), botryoidal aragonite (Fig. 5.6a-b) and framboidal pyrite (Fig. 5.7b and e), which have been reported in other modern and ancient seep carbonates (Hovland et al., 1987; Ritger et al., 1987; Roberts and Aharon, 1994). The formation of peloids and clotted microfabrics is considered to be typical features of microbial carbonates (Burne and Moore, 1987; Chafetz, 1986; Folk and Chafetz, 2000), and therefore may be related to the existence of microenvironments caused by microbial metabolism (Peckmann et al., 2001). The nuclei of marine peloids are thought to have originated as a fine-grained precipitate of high-Mg calcite within and around active clumps of bacteria, influenced by the vital activity of the bacteria (Chafetz, 1986). Framboidal pyrite indicates that sulphate reduction was active during carbonate precipitation as sedimentary pyrite formation results from the reaction of hydrogen sulphide with reactive detrital iron minerals (Berner, 1970). As sulphate reduction is coupled to AOM at cold seeps, resulting in the production of HS^- , the occurrence of pyrite framboids at seep sites has been linked to a biogenic origin (Feng et al., 2010; Naehr et al., 2000a). Furthermore botryoidal aragonite cements in seep carbonates have also been suggested to be a microbial product (Aharon, 2000). Hydrolysis of ammonia, produced from organic nitrogen compounds by actively metabolizing cells, can convert CO_2 to carbonate resulting in aragonite formation on the bacteria cells (Ehrlich, 1990; Krumbein, 1974). These may in turn serve as nuclei for further $CaCO_3$ precipitation. Accordingly, the dark centres in the botryoids can be interpreted as dead bacterial bodies (Roberts et al., 1993). In addition they tend to have anomalously negative δ^{13}C values, indicative of a methane-derived carbon source (Aharon and Sengupta, 1994).

In addition to carbonate precipitation, microbial processes can also lead to episodic dissolution of carbonates. This is because the CO_2 that is produced during methanogenesis and methane oxidation (Higgins and Quayle, 1970) lowers the pH of the pore fluids, causing partial dissolution of carbonates (Aharon, 2000). This might explain the voids and dissolved surfaces of bivalve shells observed in the carbonate samples from the Darwin MV (Fig 5.7d-e). Aerobic methanotrophs, which oxidize methane to CO_2, generally live as symbionts in the gill epithelial cells of *Bathymodiolus* sp. (e.g. Cavanaugh et al., 1987;

Childress et al., 1986). The high abundance of bivalve shells within the carbonates, as well as within the cracks of the carbonate pavement (Fig 5.1a), indicates that methane oxidation takes place at the Darwin MV. Hence, methane fluxes must have been high enough for methane to reach the seafloor and nourish these organisms. Other processes that can cause dissolution of carbonates include the interaction of sulphide-rich pore fluids with oxygenated seawater (Paull and Neumann, 1987):

$$HS^- + 2O_2 \quad \rightarrow \quad SO_4^{2-} + H^+ \tag{5.6}$$

and/or the oxidation of pyrite (FeS_2) by dissolved oxygen (Eqn. 5.7) or ferric iron (Fe^{3+}; Eqn. 5.8; Moses et al., 1987), both processes increasing the local acidity:

$$FeS_2(s) + 7/2O_2(aq) + H_2O \quad \rightarrow \quad Fe^{2+} + 2SO_4^{2+} + 2H^+ \tag{5.7}$$

$$FeS_2(s) + 14Fe^{3+} + 8H_2O \quad \rightarrow \quad 15Fe^{2+} + 2SO_4^{2+} + 16H^+ \tag{5.8}$$

The occurrence of pyrite oxidation is in line with the observation of red-brownish coloured iron-oxide framboids in the carbonate precipitates (Fig. 5.7a). Their coexistence with pyrite and the fact that the framboidal texture is one of the principal morphologies of sedimentary pyrite (e.g. Rickard et al., 1995), suggests that these framboids are the result of pyrite oxidation (Luther Iii et al., 1982). Goethite framboids have been identified in authigenic carbonates from the Iberian continental margin in the Gulf of Cadiz, and they are thought to be produced as a result of pseudomorphism of pyrite (Merinero et al., 2008).

5.4.5 A conceptual model for the formation of authigenic carbonates at the Darwin MV

In this section, I develop a conceptual model that describes the temporal evolution of authigenic carbonate formation at the Darwin MV. The model is based on the results of the petrographic, chemical and isotope analyses discussed in the previous sections. The formation of the carbonates takes place in three distinct stages; these are illustrated in Fig. 5.11 and described below.

(1) As a result of the seepage of methane charged fluids at the Darwin MV, anaerobic oxidation of methane occurs in the subsurface of the sediments, causing pore fluid TA and hydrogen sulphide concentrations to increase. As the pore fluids become oversaturated with respect to carbonate, the mud breccia is cemented together and a carbonate crust with a micritic fabric forms within the SMTZ. The hydrogen sulphide in the pore fluid reacts with detrital iron forming pyrite framboids. In areas where pore fluids are enriched in Ba, barite precipitates at the top of the SMT and it is incorporated into the authigenic carbonates. At the seafloor, cold seep biota thrive where hydrocarbon-rich fluids escape across the sediment-seawater interface.

(2) Activity at the mud volcano increases, and deep-sourced fluids and mud ascend and break up the carbonate crust. Carbonate fragments are transported towards the seafloor and deposited at the surface in a newly formed mudflow. The fields of bivalves are buried. The mudflow degasses and carbonate cements precipitate in the subsurface incorporating micritic intraclasts, mud clasts and skeletal grains. In areas where bivalves were abundant at the seafloor, shells are incorporated in the carbonates as clusters (e.g. rocks 2 and 8 in which the shell clusters are embedded in a micritic matrix). The cements precipitate very fast, so the skeletal grains and fecal pellets are well preserved. During this stage, a reasonably thick carbonate crust forms close to the seafloor, covering the crater area of the Darwin MV.

(3)The MV was then affected, in all probability, by a new pulse of pressure release, causing fracturing of the carbonate slab, and tilting of the fragmented slabs in some areas. Advection of methane-saturated fluids continued, but the seepage was now focussed along the newly formed cracks in the carbonate pavement which was now exposed at the seafloor. As a consequence, pure aragonite cements could precipitate forming white rims around the carbonate (e.g. rocks 2, 6 and 8) as well as infilling pore spaces (e.g. the acicular and botryoidal cements in rocks 1 and 2). Exposure of the carbonate crust at the seafloor is also indicated by the presence of tubeworm burrows which are coated with iron-oxides. Fractures generated by the uplift are partly filled with pyrite, suggesting that conditions were anoxic in the shallow subsurface beneath the carbonate crust.

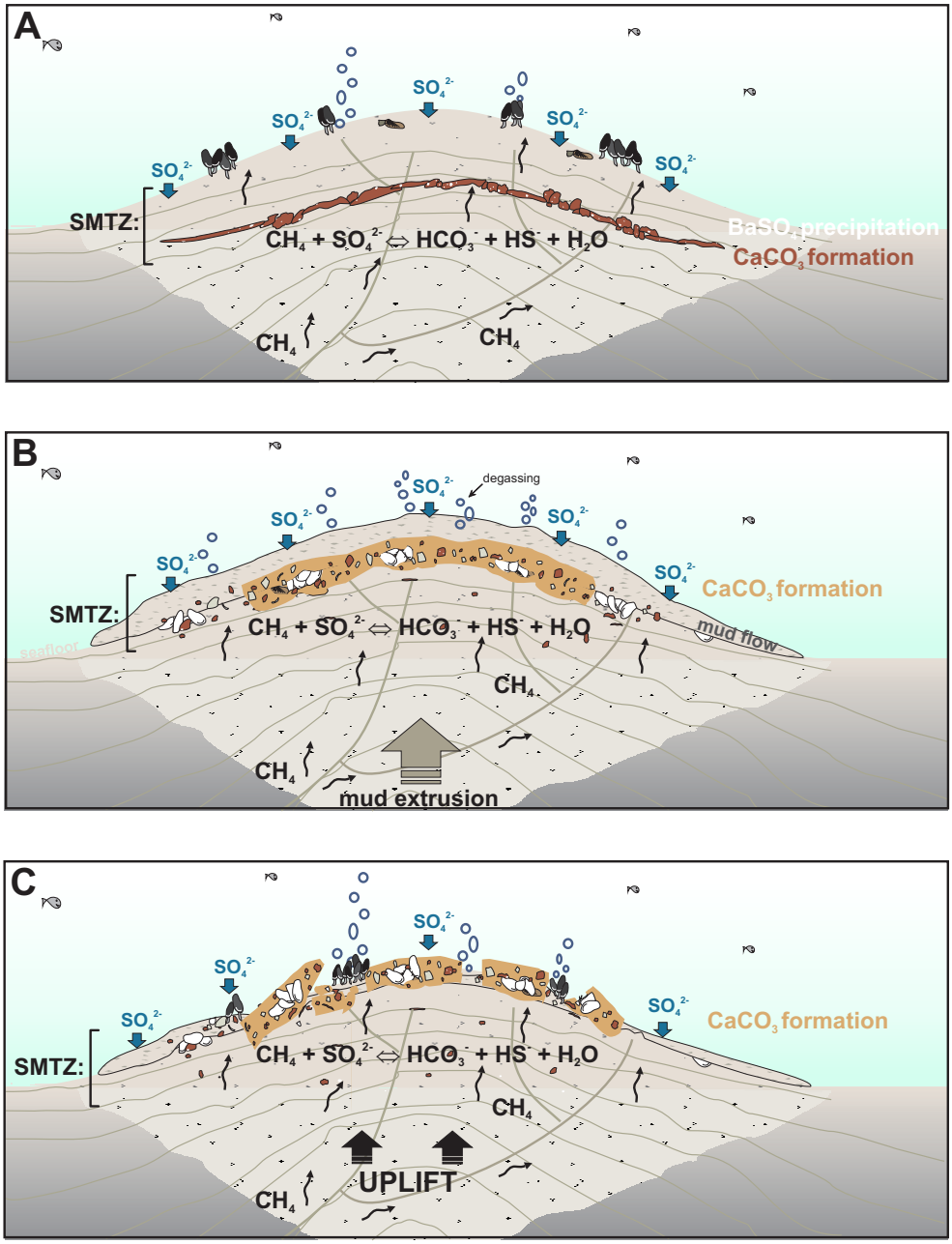

Figure 5.11 Sequence of events in the history of the formation of authigenic carbonates at the Darwin mud volcano. **A** Methane-saturated fluids rise from depth at the Darwin MV. At the seafloor cold seep biota thrive where seepage occurs. In the subsurface anaerobic oxidation of methane by a microbial consortium increases pore fluid total alkalinity concentrations promoting carbonate precipitation. Mud breccia is cemented together forming carbonate crusts with a micritic fabric. The Ba-rich fluids react with seawater sulphate to form barite at the top of the SMT which is eventually incorporated into the carbonates. **B** A new mud flow event breaks up the carbonate crust, transporting it towards the seafloor. The fields of bivalves are buried and as a result of the increased activity, the carbonates now form close to the seafloor, incorporating mudclasts, micritic intraclasts and skeletal grains in a carbonate cement. **C** A pulse of overpressure release lifts up the carbonate platform breaking it up into slabs, and tilting of these slabs occurs at some locations. Methane seepage continues, resulting in the precipitation of bodryoidal aragonite layers around the existing carbonate crusts. Veins and voids formed by dissolution and fracturing are partly filled with aragonite cement. Iron-oxides coat tubeworm burrows.

5.5 Conclusions

Authigenic carbonate crusts and pore waters were collected from several sites on the Darwin mud volcano (Gulf of Cadiz) to assess its venting activity in space and time. The presence of carbonate crusts on the summit of the MV records both the activity at the present time, as well as providing a record of past events that document the fluid and mud extrusion history of the MV.

Chemical data for pore fluids and the results of geochemical modelling indicate that seepage activity at the Darwin MV today is currently limited to an area in the northwest corner of the MV crater. The exposure of black coloured sediments at the seafloor and the escape of gas bubbles triggered by sampling activity indicate that anaerobic oxidation of methane occurs close to the seafloor and the pore fluids are supersaturated with respect to hydrocarbons. On the contrary, pore fluid profiles of conservative constituents (B, Na) show hardly any evidence for advection of fluids, and modelled rates of pore fluid advection are also low ($\sim$0.09 cm yr^{-1}). Thus, today, the Darwin MV seems to be relatively dormant in terms of fluid seepage and mud extrusion, and emission of methane gas occurs only at localised sites on the MV. Where extrusion of methane does occur, anaerobic oxidation of methane supports vent fauna and results in the formation of authigenic carbonates.

Petrographic investigations and chemical and isotope analyses indicate that the authigenic carbonates at the Darwin MV are formed by the interaction between fluid seepage and AOM, which in turn is regulated by the activity of microbial consortia. The carbonates have a brecciated appearance and mainly consist of aragonite. The δ^{13}C values of the carbonates indicate that they derived their carbon from a $\sum CO_2$ pool that has a δ^{13}C value which is similar to that recorded in the present day pore fluids, which reflects the oxidation of thermogenic methane and higher hydrocarbons. The ^{18}O enrichment of the authigenic carbonates indicates that they were more likely formed from ^{18}O-rich fluids rather than that they precipitated during the LGM. With the current data set it is however impossible to discriminate between the different sources of ^{18}O-rich fluids.Three stages of precipitation are proposed: (1) cementation of mud breccia at depth; (2) brecciation and upward transport of the carbonate crusts by the extrusion of mud, followed by the formation of a carbonate platform covering the crater of the MV in the vicinity of the seafloor; (3) uplift and break up of carbonate platform resulting in focused gas seepage along fissures and the precipitation of pure aragonite at the seafloor.

Chapter 6

Conclusions and future perspectives

Mud volcanoes occur worldwide, onshore as well as in coastal and deep sea environments. They are built up of a mixture of extruded material including mud, clasts, pore fluids and hydrocarbon gases, all of which provide unique information on geological and chemical processes that occur at depths that are usually inaccessible by direct sampling. In addition, the release of methane at submarine MVs nourishes dynamic chemosynthetic ecosystems which are characterised by a high biodiversity. Although MVs have been studied for decades, the possible impacts of gas and fluid seepage from the MV on the local environment (e.g. precipitation of authigenic carbonate pavement) and on element inventories of the ocean are still not well understood. This study aims to improve this situation by focusing on the spatial and temporal variability of mud eruptions and seepage activity at two MVs, Carlos Ribeiro and Darwin, located in the Gulf of Cadiz. In particular, I assess the effects of mud volcanism on the transfer of lithium (Li^+), boron (B) and methane (CH_4) from deep within the lithosphere into the water column. To this end, sediment and pore fluid samples were collected from both MVs, and authigenic carbonates from the Darwin MV, and studied using various geochemical, sedimentological, petrographical and numerical modelling techniques. The main achievements and findings of this work are summarized below. I then go on to propose some future directions for mud volcano studies.

6.1 Conclusions

• Active fluid flow has been detected at the CRMV. Although upward advection of fluids is no longer occurring at the Darwin MV, the escape of streams of gas bubbles triggered by sampling activity at this site, indicates that the pore waters at this mud volcano are saturated with methane and that the Darwin MV seems to be 'actively' degassing even today. 1-D transport modelling results show that the fluids from the CRMV are advected towards the seafloor at speeds of up to 4 cm yr^{-1} at the eye of the MV; this value is modest relative to those recorded at other MVs from across the world. Radiocarbon dating of

the hemipelagic drape on top of the CRMV shows that mud has been extruded recently from the eye of the MV. Thus, CRMV can be considered as being an active MV while the Darwin MV is currently in a dormant phase.

- The spatial variation in fluid flow and geochemical fluxes across the sediment-seawater interface at the time of sampling was assessed at the Carlos Ribeiro MV by sampling along a transect that connects the crater of the MV with the mudflow that is located to the SE of the summit. 1-D transport modelling results show that fluid flow velocities vary across the MV: they are highest at the eye of the MV (4 cm yr^{-1}) and rapidly decrease towards its periphery (0.4 cm yr^{-1}). Hence geochemical fluxes will vary across the surface of the mud volcano, generating a pattern of concentric zonation, which seems to be a characteristic of so-called mud pies. This is an important observation as it needs to be taken into consideration when estimating element fluxes from MVs and it is also of great value for biologists studying the distribution of organisms across the MV surface. The distribution of seepage activity at the Darwin MV can be inferred from several observations. First of all, the escape of a stream of gas bubbles, triggered by sampling activity, was witnessed at a sediment patch in the north-western corner of the MV, and several patches of living *Bathomodiolus* species were observed colonising cracks in the carbonate platform indicating elevated methane concentrations in the subsurface. It is clear that the spatial variation in venting activity at this MV is controlled by the carbonate platform. Hence, seepage activity at both MVs seems to be focussed in their centres.

- Results of pore fluid analyses show that the fluids being expelled at the CRMV at the present day are enriched in Li^+ and B and extremely depleted in chloride (Cl^-). Although this behaviour has been observed at other submarine MVs, Cl^- concentrations as low as 200 mM and B concentrations as high as 10 mM are amongst, respectively, the lowest and highest ever reported for cold seep environments. These fresher fluids (compared to seawater) are sourced at depth by the transformation of smectite to illite, a process that takes place at temperatures of between ∼60 and 150 °C. The pore fluid data indicate that Li $^+$and B are leached from marine sediments during this process. The oxygen and strontium isotopic composition of the authigenic carbonates at the Darwin MV also indicate that they formed from a deep fluid source. Li^+ and B fluxes from the CRMV into the overlying water column are 7-301 and 0.5-6 mmol m^{-2} yr^{-1}. This study shows that submarine mud volcanism may be an important source of Li^+ and B on a global scale as MVs are continuously being discovered.
Furthermore pore fluids from the CRMV and the Darwin MV are saturated with methane that has a thermogenic origin. Consumption of this methane by anaerobic oxidation supports a distinct vent fauna at both MVs. Equilibrium calculations indicate that both MVs lie within the gas hydrate stability zone: however, no gas hydrates were sampled and no other evidence for their presence was detected. Estimates for methane emissions into the overlying water column via quiescent dewatering from submarine MVs in the Gulf of Cadiz is significantly lower than for MV clusters in other parts of the ocean. Overall

methane emissions via quiescent dewatering seem to be quantitatively as important as gas ebullition, although more work needs to be done to better quantify methane release via degassing of mud flows. Submarine MVs are estimated to account for ∼8% of methane release into the ocean. However a better understanding of the controls on anaerobic oxidation of methane is needed, as this process is an important filter on methane emissions from the seafloor into the ocean.

- Several approaches were applied in this study to provide insight into the temporal variation in fluid fluxes and mudflow activity at the CRMV and the Darwin MV. Firstly, radiocarbon dating of the hemipelagic drape on top of the CRMV suggests that mud has been extruded recently from the eye of the MV and that episodes of mud extrusion have occurred frequently over the past ∼1000 Cal yr BP. Secondly, although the CRMV is still active at the present day, a drop in the methane flux is inferred from the presence of a barite front in the subsurface sediments at the periphery of the summit. Over the past 340 Cal yrs methane emissions are estimated to have dropped by one order of magnitude. On the other hand, the Darwin MV seems to be in a dormant phase at the moment. My work suggests that it formed during a sequence of events, including periods dominated by high fluid flow (accompanied by authigenic carbonate formation), alternating with phases of mud extrusion and overpressure release.

6.2 Future perspectives

Our understanding of mud volcanism and the associated chemical and biological processes has increased exponentially in the last 10 years, mainly because of an improvement in technology e.g. the use of submersibles and remotely operated underwater vehicles (ROVs) which enable targeted sampling. Despite the recent advances in research on MVs, there are still many unknowns. One major issue, is the size of methane emissions from the subsurface into the overlying water column. This study has determined that there are three important methane sources related to mud volcanism: dissolved methane in the advecting fluids, gas ebullition and degassing of mud flows. Methane fluxes are particularly difficult to quantify as most of the methane is lost during sample recovery. This issue can however be overcome by using pressurised cores (e.g. Heeschen et al., 2007) and/or by in situ measurements (e.g. Boetius and Wenzhofer, 2009) which to date have only been applied in a handful of studies. Thus a systematic use of these technologies in the future will reduce the uncertainty on measurements of the methane flux from MVs. In addition, this would allow a better estimate of the anaerobic consumption of sulphate by methane which seems to significantly control methane emissions from MVs. The use of pressurised cores might also help to determine whether gas hydrates are present in the subsurface of Carlos Ribeiro MV, as well as many other MVs in the Gulf of Cadiz, which are all located within the gas hydrate stability zone. There is the possibility that gas hydrates occur as small crystals within the pore spaces of the sediment. Upon core retrieval the signal of gas hydrate dissociation is dispersed and thus very difficult to detect.

It is also important to determine the sources of the elements enriched in the fluids. To date there is a general consensus that clay mineral dehydration-transformation reactions are important sources of freshwater. However, in the Gulf of Cadiz, it is still unclear whether or not fluids originating from greater depths, i.e. from the basement, are also seeping in. A possible approach to verify the input of hydrothermal fluids is the measurement of helium isotopes in the pore fluids seeping at the MVs. The predominant source of ^{4}He in the Earth is from the radioactive decay of uranium and thorium, whereas most of the ^{3}He is primordial in origin. Owing to their chemical inertness and distinct composition in various earth reservoirs, helium isotopes have been used extensively as tracers of mantle volatile inputs and to provide information on fluid origin (Bayon et al., 2008; Chaduteau et al., 2009)). Whether or not the fluids seeping at the MVs contain a trace of interaction with oceanic and/or continental crust is particularly of interest in the Gulf of Cadiz as the location of the boundary between oceanic and continental crust in the Gulf is still uncertain.
Interpretation of geochemical data regarding fluid sources and sediment-pore fluid interactions has also been hampered by the lack of information on the stratigraphy of the Gulf of Cadiz. Accordingly it would be of great use in MV studies of the Gulf, to take long sediment cores within and on the side of the accretionary wedge and log them in detail. This would also be of great help in identifying the source layer of the extruded mud breccia.
Lithium and boron are generally enriched in pore fluids seeping at cold seeps. However to date, the majority of experimental studies have focused on the alteration of sediments at high temperatures. As the results in this study suggest that Li^{+} and B were leached from sediments at moderate temperatures at great depths, it could be interesting to mimic these conditions in the lab and analyse the effects on pore fluid element concentrations and the behaviour of Li, B and Sr isotopes as well as investigating the role of clay minerals.

Authigenic products of hydrocarbon seepage occur around the world on the seafloor and on land. However, it remains difficult to reconstruct the seep environment of the past based on studies of these precipitates. For instance, how can we deduce the origin of the fluids from which the minerals precipitated, in particular, do they record the effects of gas hydrate dissociation? The physicochemical factors that control the mineralogy (aragonite versus calcite versus Mg-calcite) of seep carbonates are also still not well understood. And what is the role of bacteria and microorganisms in authigenic carbonate precipitation? What processes control the microfacies of the carbonates (e.g. botryoids)? Laboratory experiments in which a range of parameters (temperature, pressure, bacterial activity, carbonate concentration) are controlled may help to increase our knowledge about how mineral formation takes place in cold seep settings.

Appendices: A

Analytical procedures

A.1 Cleaning procedure for pots and bottles used for chemical analyses

Teflon pots:
Before using, Teflon pots are cleaned in several steps. First they are rinsed with MILLI-Q water and left overnight in a glass beaker with a 5% Decon solution to remove remains of organic material. The following morning the pots are rinsed with MILLI-Q water and scrubbed with a soft cloth. Subsequently they are left overnight in a beaker filled with a 1:1 mixture of MILLI-Q water and HCl on a hot plate at 150°C. After rinsing the pots three times with MILLI-Q water they are left for several days in a 10% HNO_3 solution on the hot plate at 150°C. Eventually the pots are rinsed three times with MILLI-Q water and left to dry under the fume hood.

Scintillation vials, LDPE and HDPE bottles:
Scintillation vials, LDPE and HDPE bottles are acid cleaned by leaving them in a 30% HNO_3 solution for several days up to a couple of weeks. Subsequently, they are rinsed three times with MILLI-Q water, dried under the fume hood and double bagged up for future use.

A.2 Pore fluid extraction

Two techniques were applied to extract the pore water from the collected sediment cores: 1) by pressure filtration and 2) with Rhizon samplers. The former technique was the standard procedure during Cruise JC10 on board of the RRS *James Cook* while the application of Rhizon samplers was used as a backup method when not enough processing time was available. The pore water extraction took place either immediately or within 3 hours of sub-sampling. The obtained pore waters were transferred within the glove bag into the appropriate containers for the onboard determination of hydrogen sulphide (H_2S) and total alkalinity (TA). A pair of 1.8 ml Cronus crimp glass vials were filled for

stable isotope and anion determination onshore. The sub-samples for cation analysis were acidified for preservation with hydrochloric acid (1 μl conc HCl per ml of sample). All sub-samples were stored at 6°C. On board four people were responsible for the pore fluid analysis i.e. Heleen Vanneste, Douglas Connelly, Darryl Green and Belinda Alker.

A.2.1 Pore water extraction by pressure filtration

The majority of the pore waters were extracted by pressure filtration in a glove bag under a N_2-atmosphere at 6 °C. First, a gauze followed by a 0.2 μm cellulose acetate membrane filter and a plastic ring go onto the bottom of the tray on which the sediment sample is placed (Fig. A.1). On top of the sample goes a parafilm and subsequently a rubber disk. When all trays are filled, a screw at the top secures the pile tightly. Then, the nitrogen gas pressure was switched on and set to 3-4 bars. All pore water is pressed out of the sediment after a couple of hours.

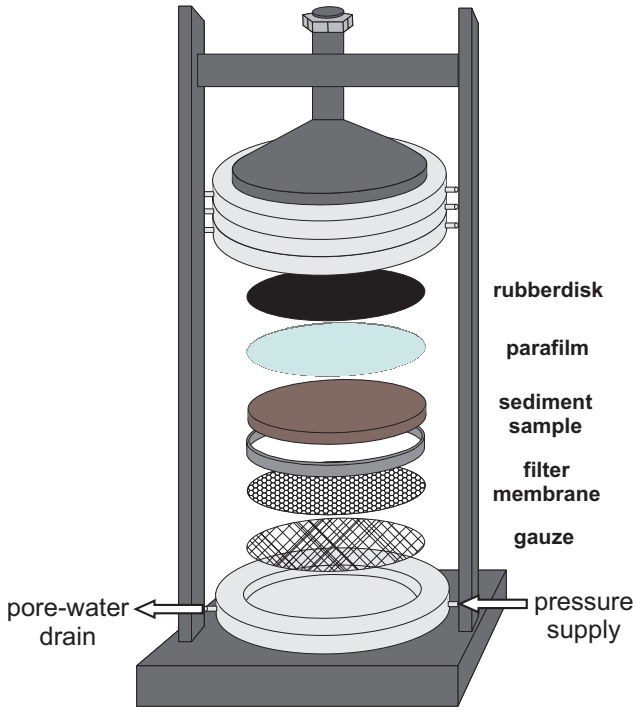

Figure A.1 Sketch of pore water extractor used in this study.

Pressure-filtration is a commonly used technique to extract pore water from marine sediments (Mudroch and Azcue, 1995). Nevertheless it is time consuming: 1) it takes some time to fill the trays with samples and stack the pile (its important not to overfill the trays to be able to put the pile under pressure) and 2) the trays and tubes (transferring the pore water from the trays to the sample containers) need to be cleaned after each batch.

A.2.2 Rhizon sampling of pore waters

Rhizon samplers are an unconventional method to collect pore water samples from sediment cores under vacuum. They consist out of four parts (Fig. A.2): 1) a thin tube containing glass fibre wire; 2) a wire to support the tube; 3) a flexible hose to pass water from the tube and 4) a connector. The porous tube was inserted into the sediment and then a syringe was attached to each tube connector and held open by a wooden spacer. The created vacuum by pulling open the syringe makes the pore water flow into the tube. As the pore size of the Rhizon samplers is small (0.15 μm), they likewise serve as a filter. The usage of Rhizon samplers has been assessed by several studies (Dickens et al., 2007; Seeberg-Elverfeldt et al., 2005) where no problems have been experienced concerning geochemical characteristics of the collected pore water. One discomfort associated with the use of Rhizon samplers is the speed of extraction that slows down significantly with decreasing porosity and permeability (e.g. with increasing depth). Only the pore waters from core PC-59 were extracted by means of Rhizon samplers.

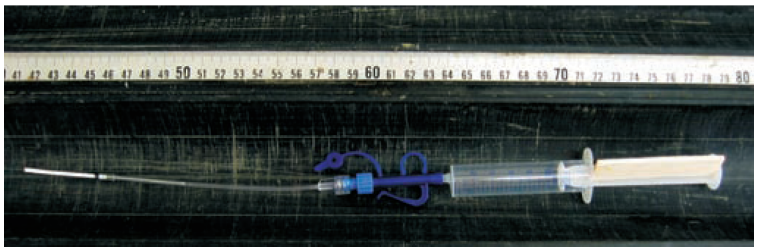

Figure A.2 Rhizon Sampler (Dickens et al., 2007).

A.3 Onboard pore water analyses

Onboard analyses were performed for the most sensitive parameters i.e total alkalinity (TA) and hydrogen sulphide (H_2S), immediately after pore water extraction.

A.3.1 Total alkalinity

Total alkalinity was determined by manual titration, using the special titration vessel after Galina Pavlova, of 1 ml of pore water and 2 ml of MILLI-Q water with 0.05M HCl according to Ivanenkoy and Lyakhin (1978). 20 μl of the following indicator solution was added so that a stable pale pink colour occurred when the equivalence point was reached:

- Indicator solution: 4.8 ml of solution 2 is mixed with 80 ml of solution 1 and a greenish-brown solution is obtained.
- Solution 1: 32 mg Methyl Red is mixed with 1.19 ml NaOH-solution (0.1M) and dissolved in 80 ml Ethanol (96%).

- Solution 2: 10 mg Methylene Blue is dissolved in 10 ml ethanol (96%).

The generated CO_2 and/or H_2S were removed by continuously bubbling nitrogen gas through the sample. The method was standardized by the titration of a seawater standard with an alkalinity of 2.33 mM. As the oxidation of H_2S and $CaCO_3$ precipitation can affect the measurements the determination has to be performed immediately after sampling.

A.3.2 Spectrophotometric determination of hydrogen sulphide

Concentrations of hydrogen sulphide were analysed using standard photometric procedures (Grasshoff et al., 1999) adapted for pore waters with high (∼mM) levels of dissolved sulphide. Spectrophotometric determinations are based on the Beer-Lamberts law (Eqn. A.1), which describes the linear correlation between the absorbance (the ratio of the light intensities before and after passage through the sample solution) and the concentration of the absorbing component.

$$log\frac{I_0}{I} = \varepsilon \cdot c \cdot d \tag{A.1}$$

where I_0 is the initial light intensity, I is the intensity after passage through the sample solution, ε and c are the molar absorptivity and the concentration of the absorbing compound respectively and d is the optical path length (cuvette length).
The H_2S in 1 ml of sample was fixed by the addition of 50 μl of zinc acetate gelatine solution immediately after pore water recovery and kept as ZnS in colloidal solution. For the zinc acetate gelatine solution, 50 mg of gelatine and 261 mg ZnAc were dissolved in 25 ml of O_2-free MILLI-Q water. After adding 10 μl of N,N-Dimethyl-1,4-phenylenediamine-dihydrochloride (colour reagent) and 10 μl of $FeCl_3$ (catalyst), the sulphide concentration was determined photometrically by measuring the absorbance after 1 hour at 670 nm. In case of high concentrations of hydrogen sulphide, samples were diluted with O_2-free salt water. The amount of reagents added to the sample should be adjusted according to the expected hydrogen sulphide concentration.
The analyses were calibrated against 5 standards which are prepared as follow:

- stock standard: 75 mg of $Na_2S{\cdot}9H_2O$ dissolved in 100 ml of O_2-free salt water.
- working standard: 25 ml of stock standard mixed with 25 ml of zinc acetate gelatine solution.
- calibration standards (#5): 0.1, 0.2, 0.5, 1 and 1.5 ml of working standard made up to 20 ml with O_2-free salt water.

To know the exact sulphide concentration of the calibration standard, the working solution was titrated against a 0.1 M $Na_2S_2O_3$-solution.

A.4 Porosity analyses

Minor sediment quantities were transferred in pre-weighed containers immediately after core recovery for onshore porosity measurements. The sediment porosity (φ) was calculated from the loss of water after freeze-drying of the sediment at NOCS. A mineral density (ρ_s) of 2.65 g cm^{-3} was assumed to calculate porosity using the following equation.

$$\varphi = \frac{volume of pore space}{total sample volume} = \frac{V_{pw}}{V_T} = \frac{\frac{m_{pw}}{\rho_{pw}}}{\frac{m_{pw}}{\rho_{pw}} + \frac{m_s}{\rho_s}} \quad \text{(A.2)}$$

Where m_{pw}= mass of pore fluid (= $m_{wetsediment}$ - $m_{drysediment}$), ρ_{pw} is the density of the extracted fluids (= 1.00 g cm^{-3}) and m$_s$ is mass of dry sediment. ρ_{pw} is set to 1.00 g cm^{-3} which is the density of freshwater as the water that is evaporated by freeze-drying is fresh, the salt crystals stay in the sediment.

A.5 Determination of dissolved hydrocarbon gas content

Principle

The headspace extraction technique has become the most common method for all oceanic methane measurements (Reeburgh, 2007). The method is based on the equilibration of the sediment sample with the headspace of the gas-tight glass vial. Once at equilibrium, the gas sample is extracted from the headspace and analysed using gas chromatography. In this study the alkaline extraction protocol was applied, which uses an alkaline solution to inhibit further microbial activity (Hoehler et al., 2000). Gas chromatography is based on the principle of the migration of components in vaporised samples at different rates in a gas stream (= carrier gas, e.g. N_2) through a column containing a stationary liquid or solid phase due to differences in boiling point, solubility or adsorption (Fifield and Kealey, 2000). Samples are introduced into the gas flow via a sample loop connected to the injector. The later is heated to 150-250°C causing the volatile sample solutes to vaporise which are subsequently transported into the column. Once through the column in which the separation process occurs, the carrier gas elutes the components to a detector connected to a recording system. The output consists of the retention time (i.e. the time between the introduction of the sample and the detection of the different components) which is characteristic for each compound, and the signal intensity resulting in a chromatogram.

Procedure

Sediment samples from CRMV and Darwin MV for hydrocarbon gas analyses (ca.3 cm^3) were taken immediately after opening the cores using plastic cut-off syringes and stored in 20 ml crimp cap glass vials containing 5 ml 1M NaOH to prevent further microbial activity (Hoehler et al., 2000). After closing and vigorous manual shaking for several minutes the dissolved gases become enriched in the headspace of the vial. The hydrocarbon gas

abundances ($C_1 - C_5$) in the headspace were measured using an HP Agilent® 6850 gas chromatograph equipped with a 30 m x 32 mm column and a flame ionization detector. The carrier gas was nitrogen. Peak identification and processing was performed using the ChemStation® software (Agilent®).
As the hydrocarbon composition varies significantly among the samples two methods were applied to optimise the determination of the respective components. Samples from deeper sediment horizons were run through a 20 min lasting method, using temperature programming, which measures the full range of hydrocarbons from methane (C_1) to pentane (C_5). The oven was programmed from an initial temperature of 40°C to 80°C (3 min hold), 100°C (3 min hold) and 120°C (6 min hold) at a rate of 20°C/min. Samples from shallower horizons in which higher hydrocarbon concentrations are below the detection limit, were analysed using a 2 min programme with the aim to get a higher precision for lower methane concentrations. Calibration was performed daily, by injecting different amounts of certified gas standard purchased from Air Products® UK. For the long method, a standard made up of a mixture of gases was used while for the short method the standard consisted of 20 ppm of CH_4 in N_2. These standards in addition to a blank (nitrogen gas) were run at the beginning and at the end of each batch as many times as necessary to obtain the required reproducibility (Table A.1). Measurements were performed by Douglas Connelly and Heleen Vanneste.

Concentrations of methane, ethane, propane and higher hydrocarbons were calculated using the following equations:

- Volume of hydrocarbon in headspace (V_{Hhead}; ml):

$$V_{Hhead} = \frac{[H] \times Vhead}{10^6} \tag{A.3}$$

with $V_{head} = V_{vial} - (V_{sed} + V_{NaOH})$, the volume of the headspace in the vial (ml); V_{vial}, the volume of the vial (10 ml); V_{sed}, volume of the sediment sample (ml); $VNaOH$, volume of added NaOH to vial (=5 ml); [H], the hydrocarbon concentration calculated from the GC output (ppmv).

- The hydrocarbon volume fraction in headspace (χ_H):

$$\chi_H = \frac{V_{Hhead}}{V_{head}} \tag{A.4}$$

- The hydrocarbon concentration ([H]; mol $l^{-1}_{porewater}$) (Hoehler et al., 2000):

$$[H] = \frac{P_{atm} \times V_{head} \times \chi_M}{R \times T \times V_{sed}} \cdot \frac{1}{\varphi} \tag{A.5}$$

with, P_{atm}, the pressure in the vial headspace at the time of measurement (1 bar = 0.9869 atm); R = universal gas constant (0.08206 l atm K^{-1} mol^{-1}); T, temperature of the vial headspace at time of measurement (=298.15 K); φ, sediment porosity.

Table A.1 Reproducibility of Gas Chromatography measurements (RSD)

	Long method		Short method	
Gas components	Batch 1 (n=4)	Batch 2 (n=4)	Batch 1 (n=3)	Batch 2 (n=3)
methane	2.2	1	3.3	1.1
ethane	1.7	1.3	-	-
propane	1.8	1.6	-	-
isobutane	2.2	1.7	-	-
butane	2	2.6	-	-
isopentane	2.1	1.8	-	-
pentane	3	2.9	-	-

Note that depressurisation and warming of the core during sediment retrieval is likely to have led to degassing, so the measured concentrations of CH_4 (which is generally oversaturated in the pore waters) are minimum values.

A.6 Sediment geochemistry

For the analyses described below, sediment samples were retrieved either straight from the core which are stored in BOSCORF at NOCS or from the squeeze cakes (the sediment leftover after pore fluid extraction). The subsamples from the required intervals were dried in an oven at 50-60°C for 24 hours and ground to a powder using an agate mortar and pestle.

A.6.1 Total sediment digestion

Sediment samples were digested applying the following procedure, to determine bulk sediment concentrations of major, minor and trace elements. Approximately 0.1 g of sediment was weighed out on weighing paper and transferred into Teflon containers. Note samples are not weighed out in the Teflon containers directly as they often cause static problems. In the first step, organic matter is removed from the samples by adding 5 ml of aqua regia (1 conc HNO_3: 3 conc HCl) using a plastic pastette. Once the reaction has subsided,

the pots are placed on a hot plate at approximately 80°C with lids tightened and left for overnight. The following day, lids are removed and the samples are dried down on a hot plate at 100°C.
For the digestion of the residue 3 ml of hydrofluoric acid and 2.25 ml of perchloric acid are added. The samples are left overnight on a hot plate at 150°C with closed lids. Subsequently, lids are removed and the samples are heated up to 160-170°C. Once each sample produces white perchloric acid smoke, temperature is increased to 180-190°C to dry down the samples. Then, 2 ml of perchloric acid is added and once more the samples are dried down.
To track down procedural errors during the sediment leaching, a procedural blank and two international certified reference materials (a marine mud standard, MAG-1 and a silty marine shale standard, Cody Shale Sco-1 from USGS; Gladney and Roelandts, 1988) were treated simultaneously with the samples (results are given in Tables A.4 and A.3 see section A.8). 44 samples were digested in total, this in two batches of respectively 24 and 20 samples. No replicates were taken through the digestion procedure as this receipt is well established at NOCS.

A.6.2 Barite separation

Barite crystals were chemically extracted from three bulk sediment samples from core GC-60 collected from the Carlos Ribeiro MV following the protocol slightly modified from Paytan et al.(1993) as follows:
Approximately 15 mg of sediment sample was weighed out of which the calcium carbonate fraction was removed with a 4 M acetic acid solution (500 ml). The residue is thoroughly washed with MILLI-Q water and centrifuged to remove all the leachant. This step was repeated after each of the following leaching steps. To oxidize the organic matter, the samples were treated with 5% sodium hypochlorite (125 ml), the bottles were covered loosely and put in the oven at 50°C overnight. The washed residue is leached with 0.2% hydroxylamine hydrochloride in 25% acetic acid to remove Fe-Mn oxyhydroxides. After mixing, the bottles were covered loosely and left in the oven overnight at 80°C. Silicates are removed in three steps: 1) a 50 ml 2:1 solution of 0.1 M HNO_3 and concentrated HF was added and left overnight at room temperature. 2) After decanting the leachant, the residue was digested overnight with a mixture of 1:3 HNO_3 (0.1 M) and concentrated HF. 3) For the third leach, a mixture of 1:5 HNO_3 (0.1 M) and concentrated HF was added. After washing the residue thoroughly, the formed fluorides were dissolved by the addition of 1:1 mixture of saturated $AlCl_3$ and HNO_3 (1 M) and left in the oven at 100°C for 2 hours. Finally the washed residue is ashed in a muffle furnace at 700°C for 1 hour to remove any refractory residue.

A.6.3 Total inorganic carbon determination

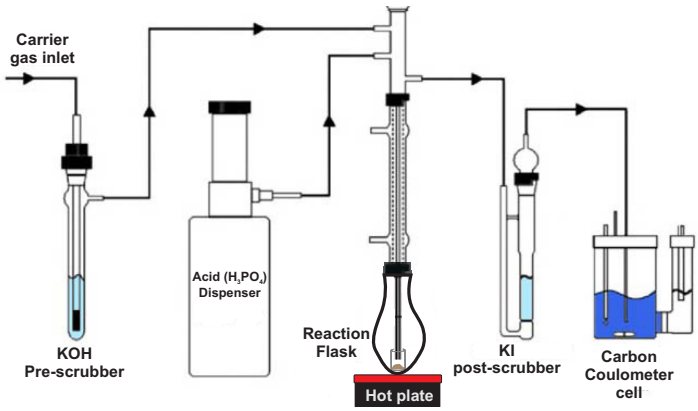

Figure A.3 Simplified schematic illustration of the coulometric titration technique for the determination of TIC.

The total inorganic carbon content (TIC) of 24 sediment samples from Carlos Ribeiro MV was determined at NOCS using a UIC CM 5012 CO2 coulometer applying the following procedure. Of each sediment sample, an aliquot of 10-55 mg is weighed out, depending on the expected carbonate concentration of the sample, into an aluminium cup which is subsequently placed into a clean pear-shaped flask. The flask with the sample is attached to the apparatus ensuring that the end of the injection tube descends into the foil cup and lowered down onto the hot plate (Fig. A.3), 5 ml of 10% phosphoric acid is added to the sample causing the inorganic carbon present in the sample to evolve into CO_2 gas. The reaction products are then transported by a CO_2-free carrier gas through a potassium iodide scrubber to remove potential interferences and ultimately into the reaction cell of the coulometer. At the start of each batch a couple of blanks (empty foil cups) were run until a low and consistent reading was reached followed by the measurement of a pure calcium carbonate standard to calibrate the instrument. Every five samples a blank and $CaCO_3$ standard were run to check for drift during the period of analysis. The TIC concentration (%) is calculated from the 'counts of CO_2' given by the coulometer which is a measurement of electrical activity in the cell directly related to the amount of produced CO_2, using the following formula.

$$TIC(wt\%) = \frac{count - blank}{(M_S \cdot 10000)} \tag{A.6}$$

Where M_s is the mass of the dry sediment sample (g).
Subsequently the carbonate concentration is calculated as follow.

$$CO_3(wt\%) = TIC \cdot (\frac{60.01}{12.01}) \tag{A.7}$$

The reproducibility of the TIC measurements is given in the table below.

Table A.2 Reproducibility of TIC analysis

Sample NR	TIC wt%	SD
Batch 1		
58(17-18)	0.95	0.01
	0.96	
	0.96	
Batch 2		
60(172-173)	1.19	0.01
	1.17	
	1.19	

A.7 Carbonate petrography and mineralogy

Thin section preparation

A stained (using the Dicksons method; Dickson, 1966)and an un-stained thin section of the same rock surface were prepared at NOCS for each rock. The Dicksons staining technique uses Alizarin red S to differentiate slightly different kinds of calcite (varying from very pale pink to red) due to e.g. crystallite size and structure and the optical orientation. Potassium ferricyanide highlights the presence of iron in calcite by colours varying from mauve through purple to royal blue. Dolomite stays colourless while ferroan dolomite colours pale to deep turquoise with increasing Fe content.

X-ray powder diffraction

The identification of the mineralogical composition of sediment samples by X-ray powder diffraction is based on the principle that an X-ray beam, directed at the sample, will be diffracted by the mineral planes when at appropriate angles according to Braggs Law: $n\lambda = 2dsin\theta$ where λ is the wavelength of the X-rays (for a CuKα target, i.e. 1.542Å), d is the lattice spacing (Å) and θ is the angle of diffraction. Accordingly the lattice spacing can be calculated from the diffractometer output, i.e. 2θ. As d is characteristic for each mineral, the minerals making up the sediment sample can be identified. The chemical composition of the minerals can be derived from the relative intensity of the refracted X-rays (Cullity, 1956). The bulk mineralogy of the carbonate precipitates was determined by X-ray powder diffraction on randomly oriented powder slides using a diffractometer

with cupper Kα-radiation at SIO.

A.8 Determination of cation concentrations in pore waters, sediments and carbonate samples

Major (Mg, K, Ca, Na, Al, Ti and Fe) and minor element (Li, Ba and Sr) concentrations were determined using a Perkin Elmer Optima 4300V Inductively Coupled Plasma Optical Emission Spectrometer based at NOCS (operated by Darryl Green). This analysis is based on the principle that excited atoms and ions emit radiation of characteristic wavelength when the electrons return to lower energy orbitals. First the sample solution is taken up by an autosampler and pumped to the nebulizer where it is converted into an aerosol. Subsequently, it is injected into the plasma torch, which contains an inductively coupled argon plasma that atomizes the sample. The emitted photons are then detected radially or axially through an Echelle polychromator that separates the light into its component wavelengths.

Sediments

The digested sediment samples are redissolved in 10 ml 6M HCl solution and left in the oven overnight at a temperature of about 75°C to complete dissolution. Approximately, 2 ml of the mother solution is subsampled into scintillation vials and diluted up to 20 ml with MILLI-Q water. Stock 1000 μg l^{-1} standards (Specpure, Spex) of each element of interest were diluted into four different concentration solutions (in 0.6 M HCl) which were used for instrument calibration. To correct for drift and blank, the same standard (mostly midrange standard # 2 or 3) and an acid blank (0.6 M HCl) were measured every ten samples and at the end of the run. Tables A.3 and A.5 show respectively the accuracy and precision obtained during the analysis. The limit of determination (LOD) of the analysis, i.e. the smallest signal that can be quantitatively measured, is shown in Table A.4 and is determined by the repeat analysis of an acid blank (n=10) using the following formula (Potts, 1987):

$$\bar{X_B} +^* SD_B$$

with $\bar{X_B}$ and SD_B respectively the average and standard deviation of the 10 acid blank measurements.

Table A.3 Accuracy on the sediment analyses by ICP-OES determined by the analysis of certified reference materials MAG-1 and Sco-1.

Elements	MAG-1			Sco-1			
	Measured (ppm)	Certified (ppm)	%	Measured (ppm)	Certified (ppm)		%
Mg	17998	18093	99.5	15797	16404.3	1085.6	96.3
Ca	9577	9791	97.8	17837	18725.1	1429.4	95.3
Al	85093	86630	98.2	71981	72341.6	1111.3	99.5
Ti	4495	4502	99.9	3607	3764.9	359.7	95.8
Fe	50389	47559	106	36983	35879.2	1258.9	103.1
Ba	495	479	103.3	574	57030		100.7
Sr	144	146	98.7	168	17016		99

Table A.4 Limit of determination (LOD) and procedural blank results for ICP-OES analyses.

	Batch 1		Batch 2	
	LOD (n=10) (ppm)	Procedural blank (ppm)	LOD (n=10) (ppm)	Procedural blank (ppm)
Ca	0.7	0	0	0
Mg	0.1	0	0	0
Al	0.2	0	0	0
Ti	0	0	0	0
Fe	-0.1	0	0	0
Ba	0	0	0	0
Sr	0	0	0	0

Pore fluids

Pore water concentrations of the following elements: sodium (Na^+), potassium (K^+), calcium (Ca^{2+}), magnesium (Mg^{2+}), lithium (Li^+), boron (B), strontium (Sr^{2+}) and barium (Ba^{2+}) were determined by ICP-OES using a Perkin Elmer optima 4300DV at NOCS (operated by Darryl Green). Approximately, 1 ml of sample was diluted up to 20 ml with a 0.3M HCl solution. Stock 1000 $\mu g\ L^{-1}$ standards (Specpure, Spex) of each element of interest were diluted into six different concentration solutions (in 0.3 M HCl) which were used for instrument calibration. To correct for drift and blank, the same standard (standard # 3) and an acid blank (0.3 M HCl) were measured every ten samples and at the end of the run. The precision was determined by the repeat analysis (n=3) of 2 samples in each batch and is better than 5% on average (Table A.6). LOD results are also given in table A.6. The accuracy of the analyses was determined by the repeat analysis (n=3) of

Table A.5 Reproducibility of ICP-OES analyses for the determination of the bulk sediment concentrations of major and minor elements

Elements	Batch 1						Batch 2			
	58(215-219)		**43(224-227)**		**49(11-12)**		**58(50-51)**		**60(87-88)**	
	Measured (n=3) (ppm)	RSD %	Measured (n=3) (ppm)	RSD %	Measured (n=3) (ppm)	RSD %	Measured (n=3) (ppm)	RSD %	Measured (n=3) (ppm)	RSD %
Mg	14500	0.6	13800	0.6	16100	0.5	16800	0.9	16700	0.7
Ca	27500	0.7	104000	0.1	18000	0.5	39300	1.3	28600	0.8
Al	82300	0.9	63300	0.7	89300	0.3	86000	0.8	87300	0.5
Ti	4840	1.5	3640	0.5	5170	0.4	4940	0.7	5040	0.9
Fe	45300	0.8	34300	0.5	49500	0.4	45600	0.7	46700	0.9
Ba	232	0.8	477	0.5	245	0.4	129	0.8	764	0.9
Sr	266	0.9	458	0.5	145	0.4	211	0.8	222	0.9

a CRM seawater standard and is given in table A.7.

Table A.6 Reproducibility and limit of determination (LOD) of ICP-OES analyses of major and trace elements in pore waters.

			Batch 1			Batch 2		
			33 (34-37) n=3	73(1-5) n=3	LOD	23 (123-127) n=3	44 (14-16) n=3	LOD
Li^+	Measured	μM	25	25.2	0.14	27.6	25.9	0.26
	RSD	%	5.2	4.6		2.3	1.7	
B	Measured	mM	0.4	0.5	0	0.4	0.5	0
	RSD	%	3.9	1.4		3.5	1.1	
Na^+	Measured	mM	484	479	0	499	472	0
	RSD	%	0.4	1.2		1.6	1.1	
Mg^{2+}	Measured	mM	50.8	53.7	0	54.5	54.5	0
	RSD	%	0.6	1.3		2.4	1.1	
K^+	Measured	mM	9.2	9.9	0	10.6	10.3	0
	RSD	%	0.9	1.4		2.2	0.9	
Ca^{2+}	Measured	mM	3.6	10.7	0	9.7	10.7	0
	RSD	%	0.9	1		3.4	1.3	
Sr^{2+}	Measured	μM	72.2	94.3	0	124	86.7	0
	RSD	%	0.8	1.3		2.4	1.1	
Ba^{2+}	Measured	μM	2.5	0.2	0	0.3	0.2	0
	RSD	%	0.5	7		2.2	0.5	

Table A.7 Accuracy on the pore waters analyses of major and trace elements by ICP-OES.

Element	Unit	CRM seawater		
		Measured	Certified	%
Li^+	uM	15.1	13.7-15.1	105
Na^+	mM	457	455-459	100
Mg^{2+}	mM	51.3	51.2-51.7	99.7
K^+	mM	9.7	9.7-9.8	99.5
Ca^{2+}	mM	10	9.9-10.0	101
Sr^{2+}	uM	137	136-138	100
Ba^{2+}	uM	0.43	0.36-0.37	118

Authigenic carbonates

Approximately 200 mg of carbonate powder was dissolved in 50 ml 5% HCl and separated from the insoluble residue by vacuum filtration through a filter 0.45 μm pore size. The obtained carbonate solution was further diluted with 1% HNO_3 for major (Mg, Ca, K, Fe, Mn) and trace (Sr, Ba, Li) element analyses using a Perkin Elmer Optima 3000DV ICP-OES at SIO. Five calibration standards (in 1% HNO_3) were prepared from 1000 μg l^{-1} stock standards (Specpure, Spex) of the elements of interest covering the range of expected sample concentrations. To correct for drift and blank, a standard and a blank were run every 10 samples. The reproducibility of the analyses is given in Table A.8.

A.9 Determination of anion concentrations in pore waters by Ion Chromatography (IC)

Principle

The separation of anions by ion chromatography depends on the basic principle of the variation in rate at which the anions in the sample migrate through the ion exchange column under the influence of a mobile phase. The separation of the analytes is achieved using an anion-exchange resin (in hydrogen carbonate form) in the column and eluting with a sodium carbonate solution. Once through the column, the eluent passes through the suppressor (i.e a cartridge containing a porous polymeric cation-exchange membrane in the H^+ form) where the 'background' electrolyte is effectively removed by converting it into water (sodium ions are replaced with hydronium ions). The suppressing of ionized species other than the sample ions in the eluting mobile phase, facilitates detection of the sample anions by a conductivity detector (Fifield and Kealey, 2000).

Procedure

In this study the anions: chloride (Cl^-) and sulphate (SO_4^{2-}) were determined using a Dionex ICS2500 Ion Chromatography at NOCS which is provided by an auto sampler. 1% solutions were prepared by adding 200 μl pore water sample to 20 ml MILLI-Q water in a scintillation vial. The samples were subsequently transferred into auto-sampler tubes. The measurements were calibrated using a seawater standard and corrected for drift by measuring a standard every ten samples. The reproducibility of these measurements was assessed through repeat analysis of samples as well as single anion standards (NaCl, KBr, Na_2SO_4) and is better than 0.1% for chloride and 1.0% for sulphate (Table A.9). The analytical accuracy was checked by measuring three single anion standards in every batch. Measurements deviate from the theoretical values by on average 0.2 and 0.8% for respectively chloride and sulphate (Table A.10).

Table A.8 Reproducibility of major and minor element concentration determination by ICP-OES of carbonate precipitates

	R2_3		R7_1		R6_22		R7_2	
	Measured (n=3) (ppm)	RSD %	Measured (n=4) (ppm)	RSD %	Measured (n=3) (ppm)	RSD %	Measured (n=3) (ppm)	RSD %
Ca	317000	0.7	323000	0.4	-		-	
Ba	787	1.5	4180	1.3	-		-	
Sr	9030	0.8	10200	0.8	-		-	
Fe	-		-		1940	0.7	415	0.6
Mg	-		-		7020	1.1	735	1.5

Table A.9 Reproducibility of pore water analyses by IC.

Batch	Sample		Chloride		Sulphate	
			Measured mM	RSD %	Measured mM	RSD %
1	49(63-67)	n=3	324	0.3	0.4	2.6
	60(65-69)	n=3	539	0.1	21.5	0.1
2	43(344-348)	n=3	598	0	22.6	0.3
	43(123-127)	n=3	556	0.1	25.5	0.1
3	53(240-245)	n=3	199	0	0.2	5.5
4	58(38-42)	n=3	521	0.1	13.2	0.2
5	57(28-30)	n=3	505	0.1	13.7	0
	63(12-14)	n=3	548	0.1	27.5	0.2
6	63(18-20)	n=3	543	0.2	26.7	0.3
7	63(2-4)	n=3	553	0.2	28.2	0.2
	58(53-57)	n=3	504	0	2.8	0.9
8	23(95)	n=3	599	0.2	0.9	0.5
	26(6)	n=3	591	0	0.9	0.9
	26(30)	n=3	591	0.1	0.9	0.6
9	31(51.5)	n=3	562	0.1	0.8	1.1
	31(2.5)	n=3	584	0.2	0.9	0.6
10	33(2.5)	n=3	581	0.1	0.9	2.6
	37(20.5)	n=3	581	0.1	0.9	2

Table A.10 Accuracy of single anion standard analyses by IC

Bacth	NaCl				KBr				Na_2SO_4			
		Measured	Theoretical			Measured	Theoretical			Measured	Theoretical	
		mM	mM	%		uM	uM	%		mM	mM	%
1	n=3	143.1	143.8	99.5	n=3	1.3	1.3	99.4	n=3	67.1	66.8	100.4
2	n=1	144.1	143.8	100.2	n=1	1.3	1.3	99.7	n=1	67.3	66.8	100.7
3	n=1	143.9	143.8	100.1	n=1	0.5	0.5	99.8	n=1	67.3	66.8	100.8
4	n=1	143.3	143.8	99.6	n=1	1.4	1.3	108.3	n=1	67.1	66.8	100.4
5	n=1	143.6	143.8	99.8	n=1	1.3	1.3	98.7	n=1	67.3	66.8	100.7
6	n=1	144	143.8	100.1	n=1	0.8	0.8	97.6	n=1	67.8	66.8	101.6
7	n=1	143.7	143.8	99.9	n=1	0.5	0.5	99	n=1	67.4	66.8	100.9
8	n=3	141.2	140.8	100.3	n=1	5.8	5.9	98.3	n=1	63	62.6	100.7
9	n=1	141.6	140.8	100.6	n=3	5.9	5.9	99.8	n=1	63.2	62.6	101
10	n=1	140.8	140.8	100	n=1	6.1	5.9	102.2	n=3	63.2	62.6	101.1

Appendices: B

Supplementary data (1)

B.1 Determination of lithium content in sediments from Carlos Ribeiro mud volcano

The Li content was determined in 35 sediment samples from Carlos Ribeiro mud volcano (Table B.1). Each sample was dried in an oven at 50-60°C for 24 hours and ground into powder using an agate mortar and pestle. Approximately 0.1 g of sediment was weighed out per sample and subjected to a combined Aqua Regia, HF and $HClO_4$ total digestion and analysed by Inductively Coupled Plasma Optical Emission Spectrometry (ICP-OES) using a Perkin Elmer Optima 4300V ICP-OES at NOCS. The analytical precision estimated from replicate analyses (n=3) is better than 1.1%. Accuracy of these measurements was assessed through analysing two internationally certified standards (MAG-1 and Sco-1) and is better than 2%.

B.2 Code of numerical 1-D transport-reaction model

The code of the numerical model will be included in the final thesis on cd-rom.

Table B.1 Li content of sediment from Carlos Ribeiro mud volcano

Core	Depth [cm]	Li [ppm]
GC-52	10	59.5
	70	62.6
	172	77.5
PC-53	372.5	59.5
	507.5	62.3
GC-49	11.5	66.7
	17.5	61.8
	24.5	61.4
	52.5	62.4
	57	61.6
	62.5	62.5
	100.5	62
PC-58	2.5	56.8
	13.5	65.6
	17.75	61.9
	30	60.5
	35.75	59.5
	40.5	55.6
	44.5	59.1
	50.5	58.6
	72.5	59.3
	125	60
	217	58.3
GC-60	1	48.6
	36	81.5
	45	60
	52	59.8
	80	59.6
	85	59.6
	87.5	59.8
	91	60.3
	123	61.2
	130	60.9
	135.5	60.7
	172.5	63.1

Appendices: C

Description of sediment cores from Carlos Ribeiro MV

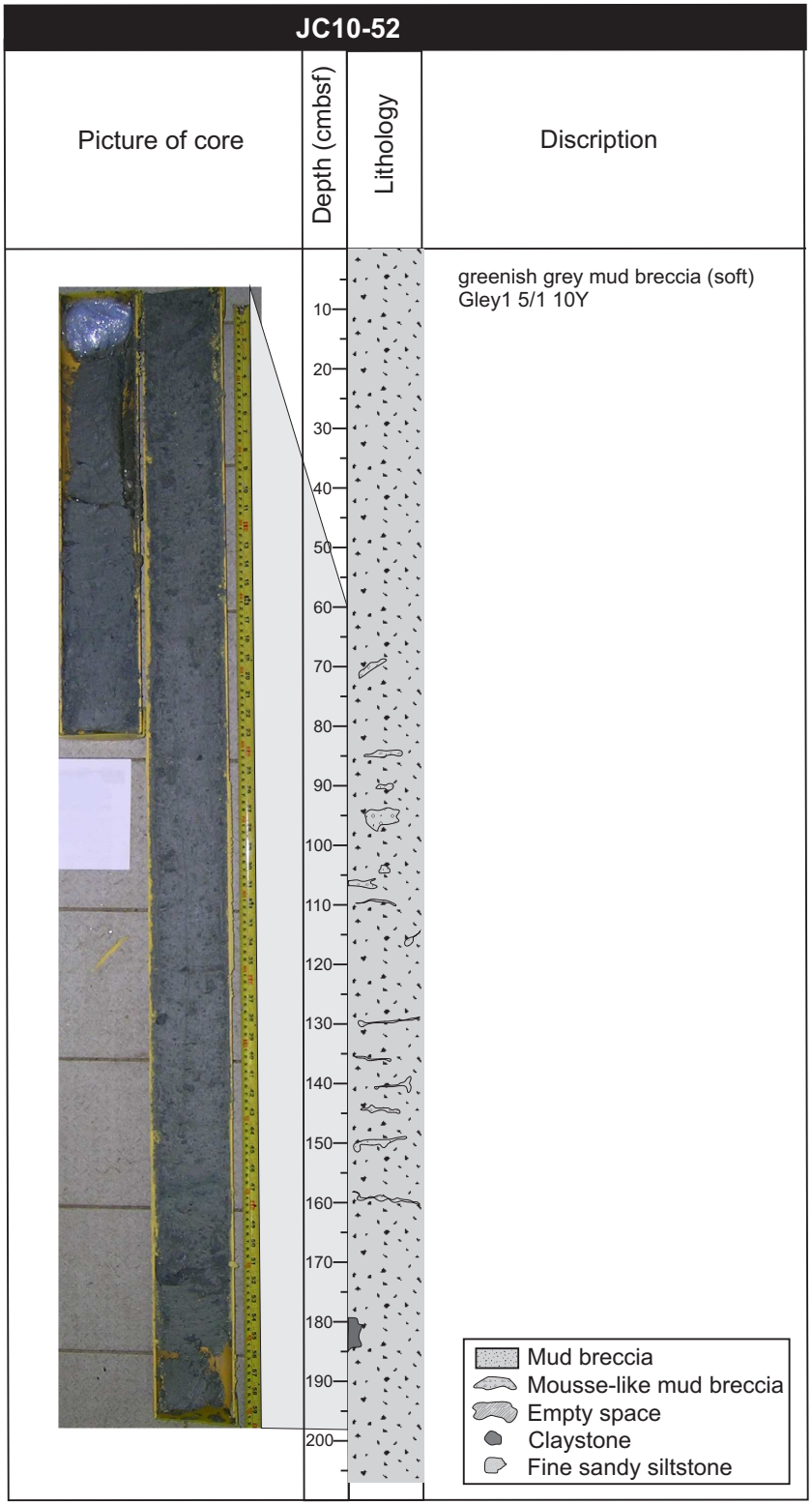

Figure C.1 Eye site

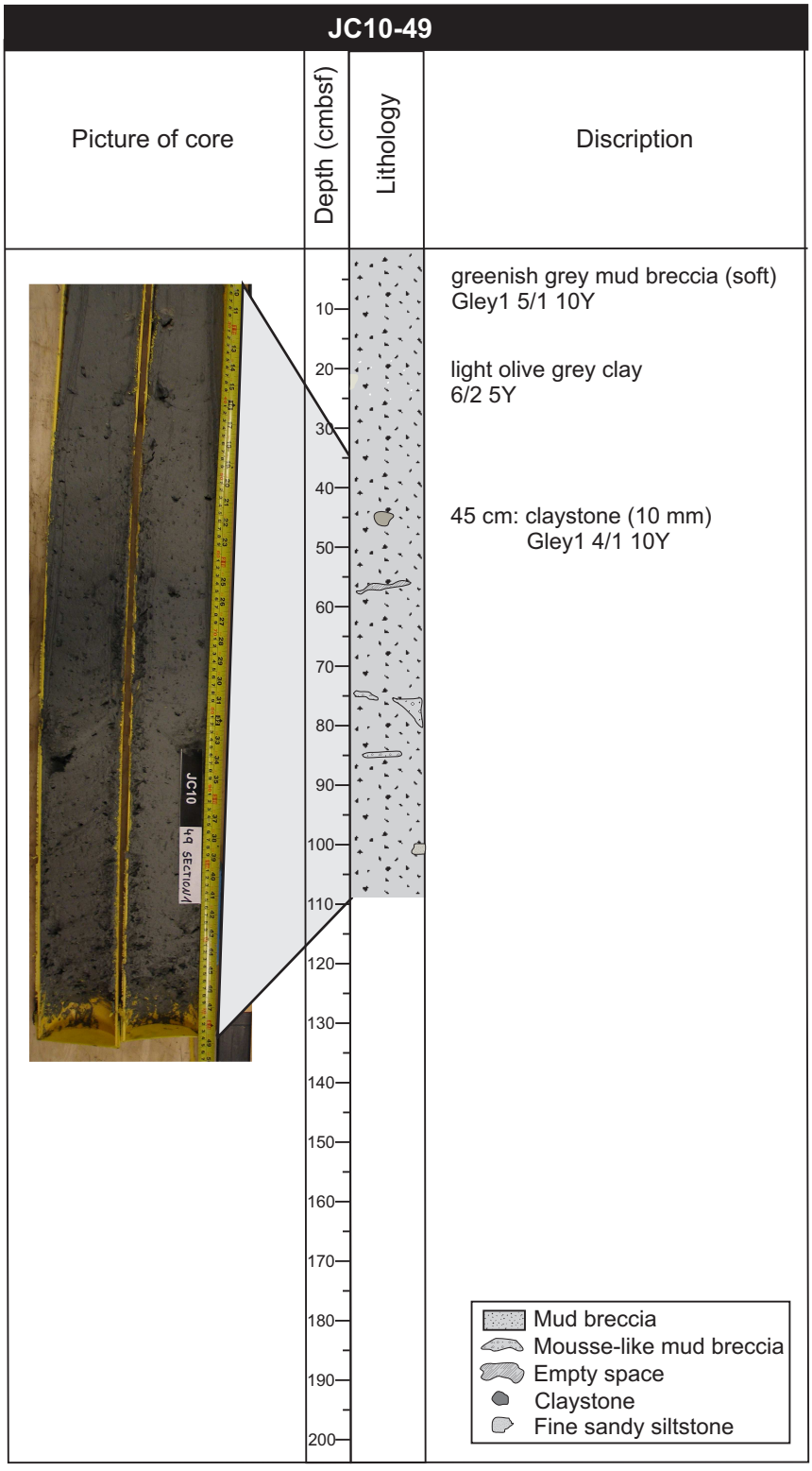

Figure C.2 Off-centre site

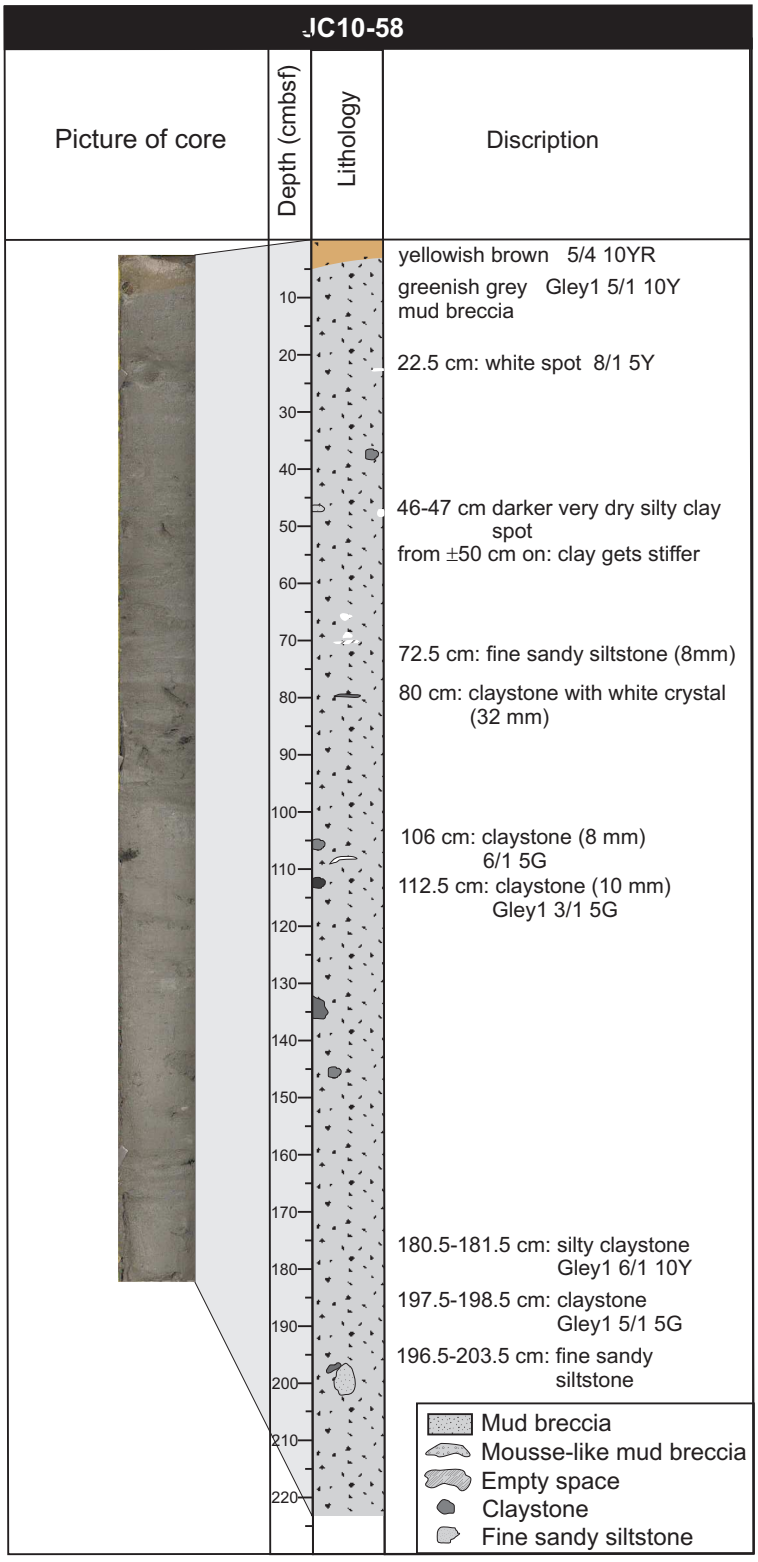

Figure C.3 Margin site

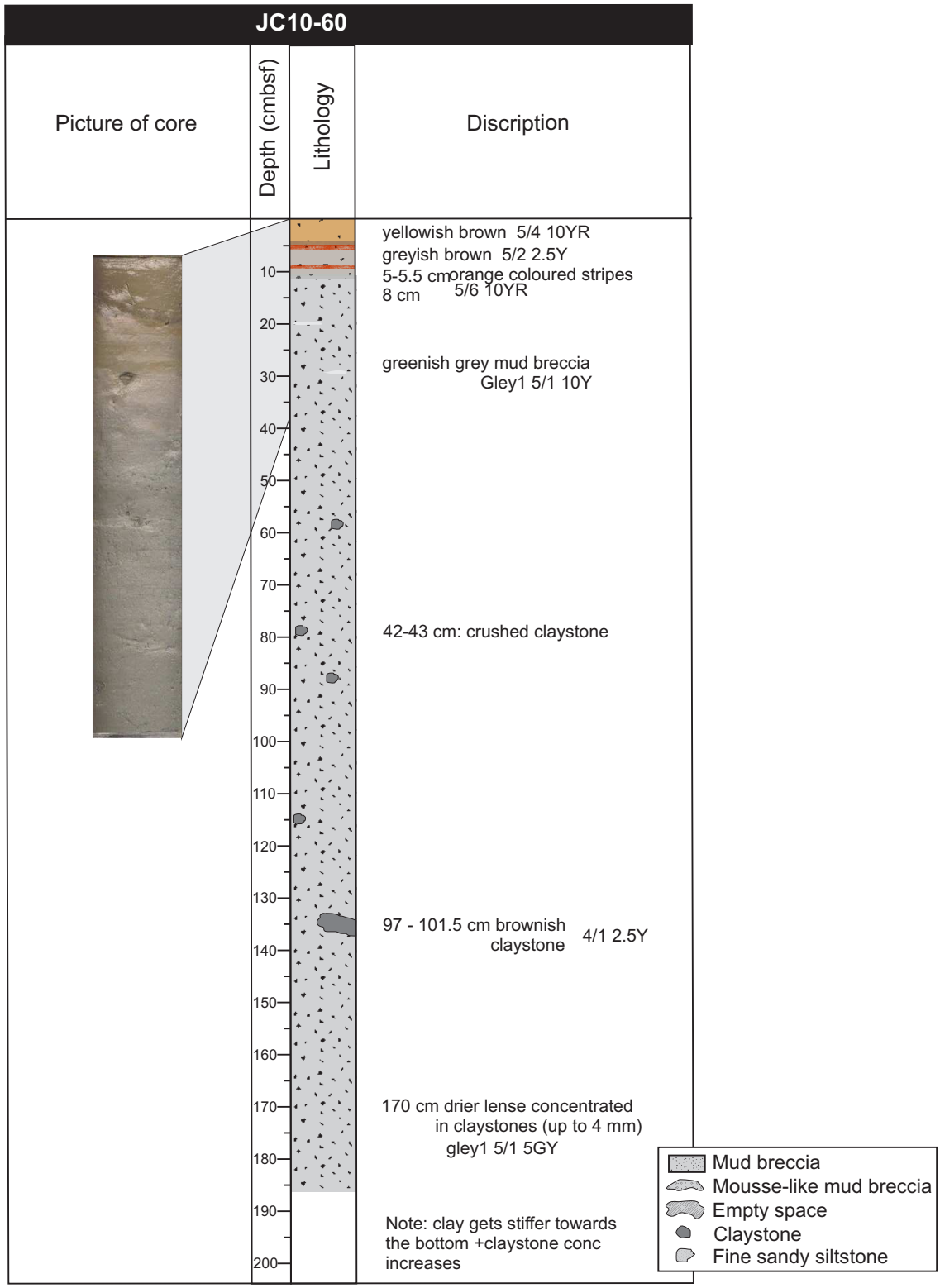

Figure C.4 Mudflow site

Appendices: D

Supplementary data (2)

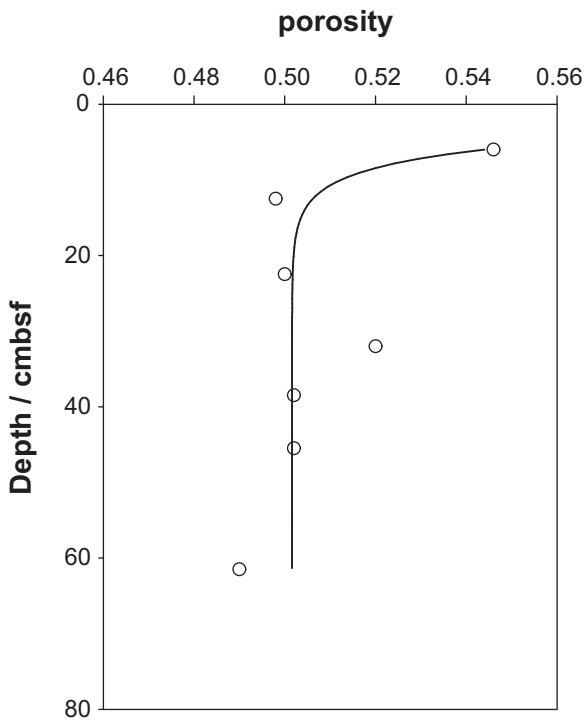

Figure D.1 Porosity depth profile: measured data (open circles) and model results (solid line) for core site GC-33 on the Darwin mud volcano.

Table D.1 X-ray diffraction results: 2theta position d(104) of calcite corrected for alignment using 2theta position of d(101) of quartz

sample NR	Quartz d(101) Å	Correction factor[a]	$d(104)_{LMC}$ Å	$d(104)_{LMC}$- corrected[b] Å	$d(104)_{HMC}$ Å	$d(104)_{HMC}$ - corrected[b] Å
Rock-1.1	3.338	1.002	3.024	3.029	n.d.	n.c.
Rock-1.2	3.327	1.005	3.018	3.033	n.d.	n.c.
Rock-2.1	3.340	1.001	3.023	3.026	2.9875	2.990
Rock-2.2	3.349	0.998	3.024	3.018	2.9966	2.991
Rock-2.3	3.343	1.000	3.025	3.025	n.d.	n.c.
Rock-2.4	3.343	1.000	3.027	3.027	n.d.	n.c.
Rock-4.1	3.335	1.003	3.017	3.025	2.9874	2.995
Rock-4.2	3.336	1.002	3.022	3.029	2.9886	2.995
Rock-6.1	3.347	0.999	3.032	3.029	n.d.	n.c.
Rock-6.2	3.348	0.999	3.024	3.020	n.d.	n.c.
Rock-6.4	3.339	1.001	3.024	3.028	n.d.	n.c.
Rock-7.1	3.337	1.002	3.026	3.032	n.d.	n.c.
Rock-7.2	3.337	1.002	3.022	3.027	n.d.	n.c.
Rock-7.3	n.d.	n.c.	n.d.	n.c.	n.d.	n.c.
Rock-8.1	3.337	1.002	3.023	3.029	n.d.	n.c.
Rock-8.2	3.336	1.002	3.022	3.028	2.9798	2.986
Rock-8.3	3.340	1.001	3.024	3.026	n.d.	n.c.

[a] Correction factor = $d(101)_{samples}$-$d(101)_{theoretical}$; $d(101)_{theoretical}$: 3.343Å
[b] $d(104)_{LMC/HMC}$ corrected = $d(104)_{LMC/HMC}$*correction factor
n.d.: not determined
n.c.: not calculated

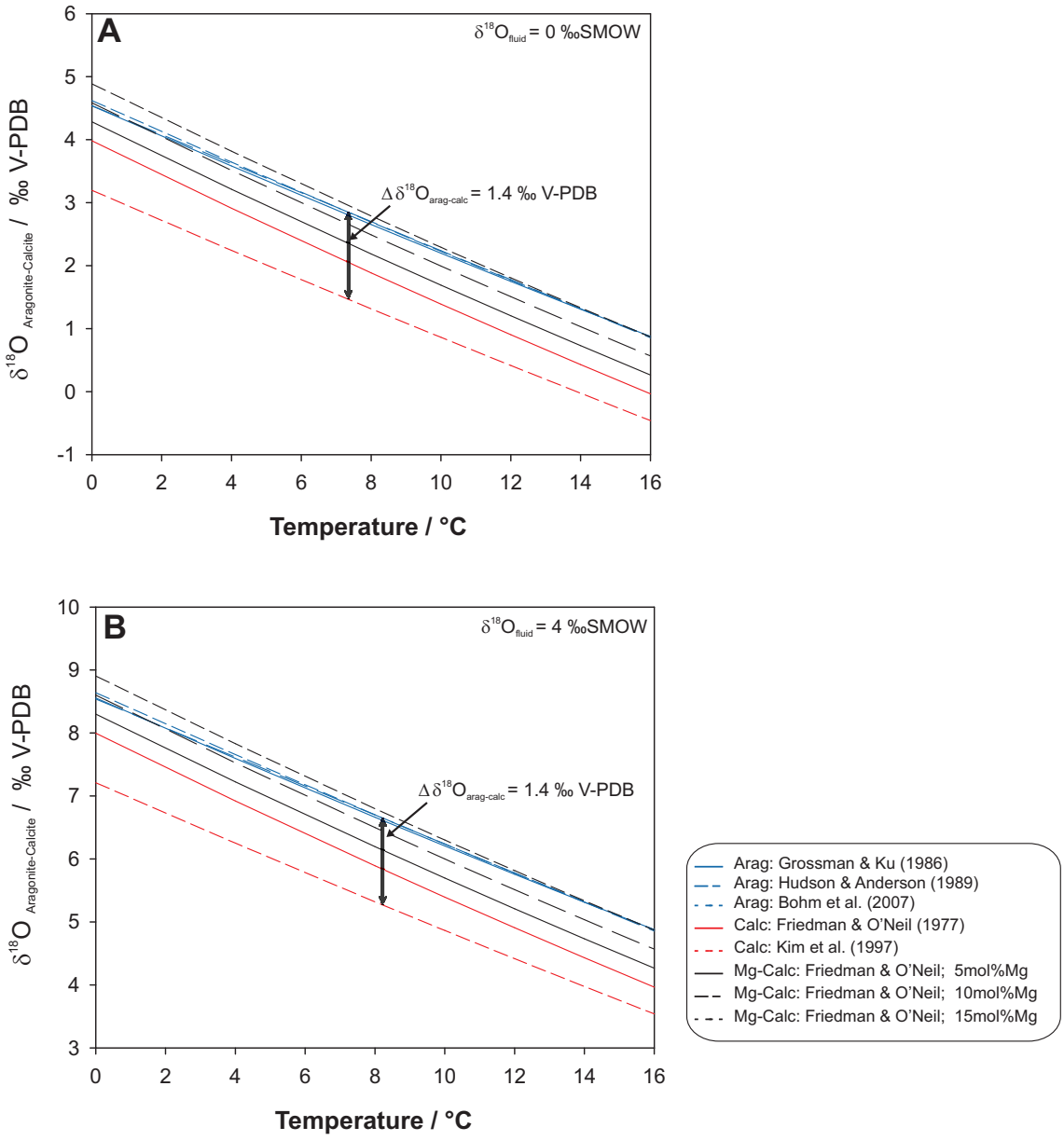

Figure D.2 Comparison of oxygen isotope fractionation relationships for aragonite-water and calcite-water and the influence of the magnesium (Mg) concentration in function of temperature. **A** Precipitation from water with a δ^{18}O value of 0‰ SMOW. **B** Precipitation from water with a δ^{18}O value of 4‰ SMOW. $\Delta\delta^{18}O_{arag-calc}$ is the maximum difference in δ^{18}O between aragonite and calcite.

Appendices: E

Pore water concentration-depth profiles for all coring sites on the Carlos Ribeiro mud volcano and the background site

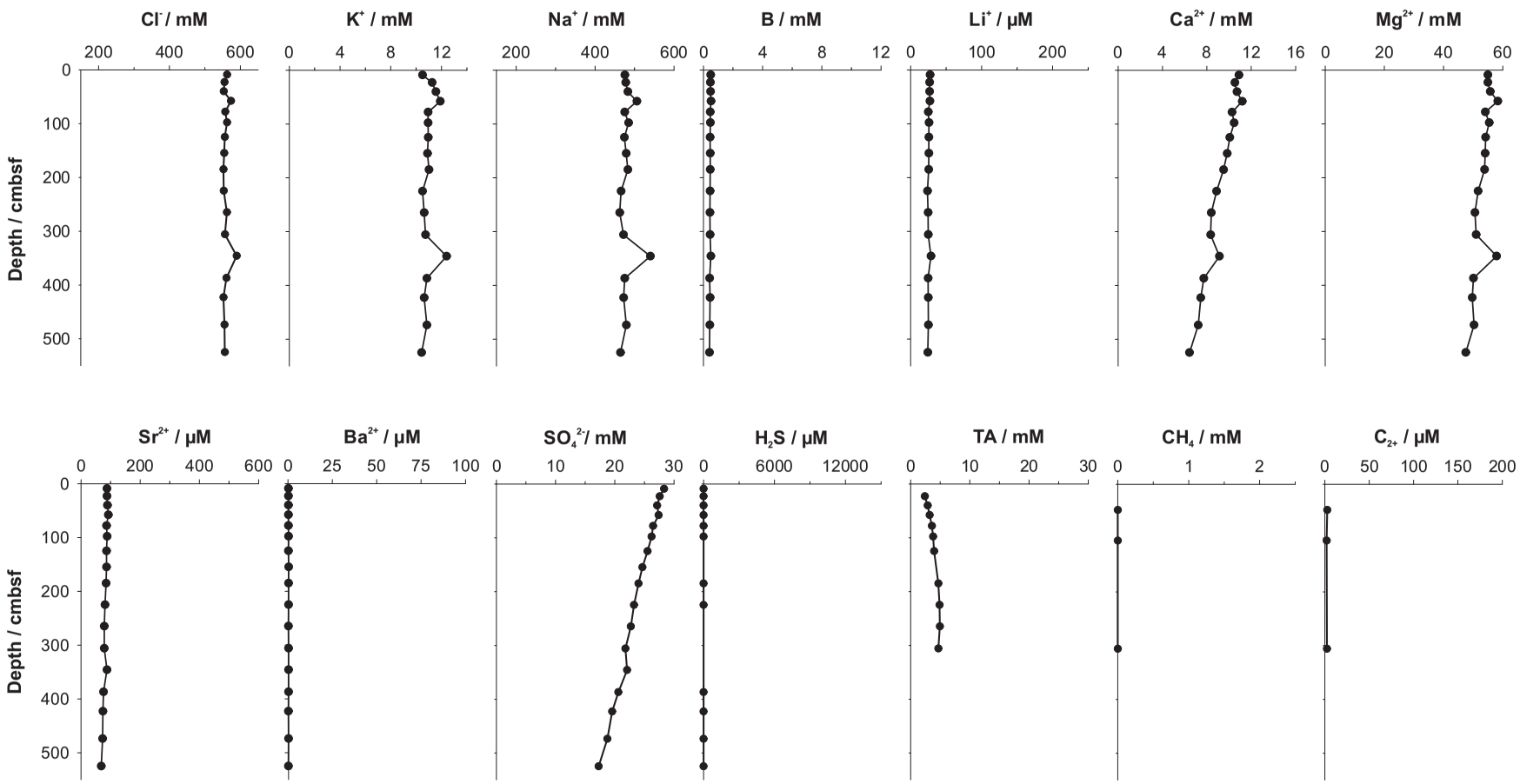

Figure E.1 Pore water depth profiles of chloride (Cl^-), potassium (K^+), sodium (Na^+), boron (B), lithium (Li^+), calcium (Ca^{2+}), magnesium (Mg^{2+}), strontium (Sr^{2+}), barium (Ba^{2+}), sulphate (SO_4^{2-}), hydrogen sulphide (H_2S), total alkalinity (TA), methane (CH_4) and higher hydrocarbons (C_{2+}) for coring site PC-43, i.e. 2.9 km SW of Carlos Ribeiro mud volcano.

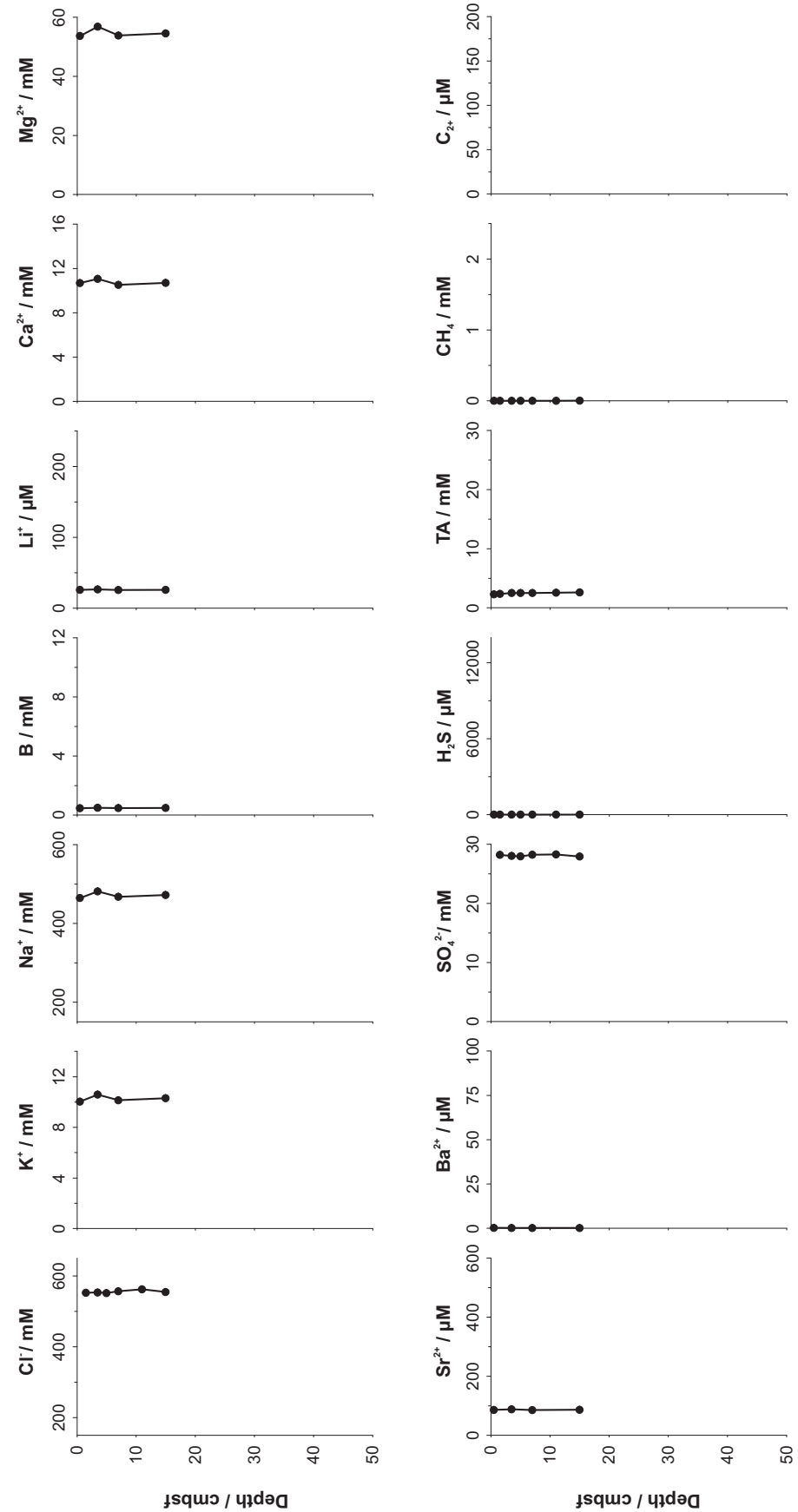

Figure E.2 Pore water depth profiles of chloride (Cl^-), potassium (K^+), sodium (Na^+), boron (B), lithium (Li^+), calcium (Ca^{2+}), magnesium (Mg^{2+}), strontium (Sr^{2+}), barium (Ba^{2+}), sulphate (SO_4^{2-}), hydrogen sulphide (H_2S), total alkalinity (TA), methane (CH_4) and higher hydrocarbons (C_{2+}) for coring site MC-44, i.e. 2.9 km SW of Carlos Ribeiro mud volcano.

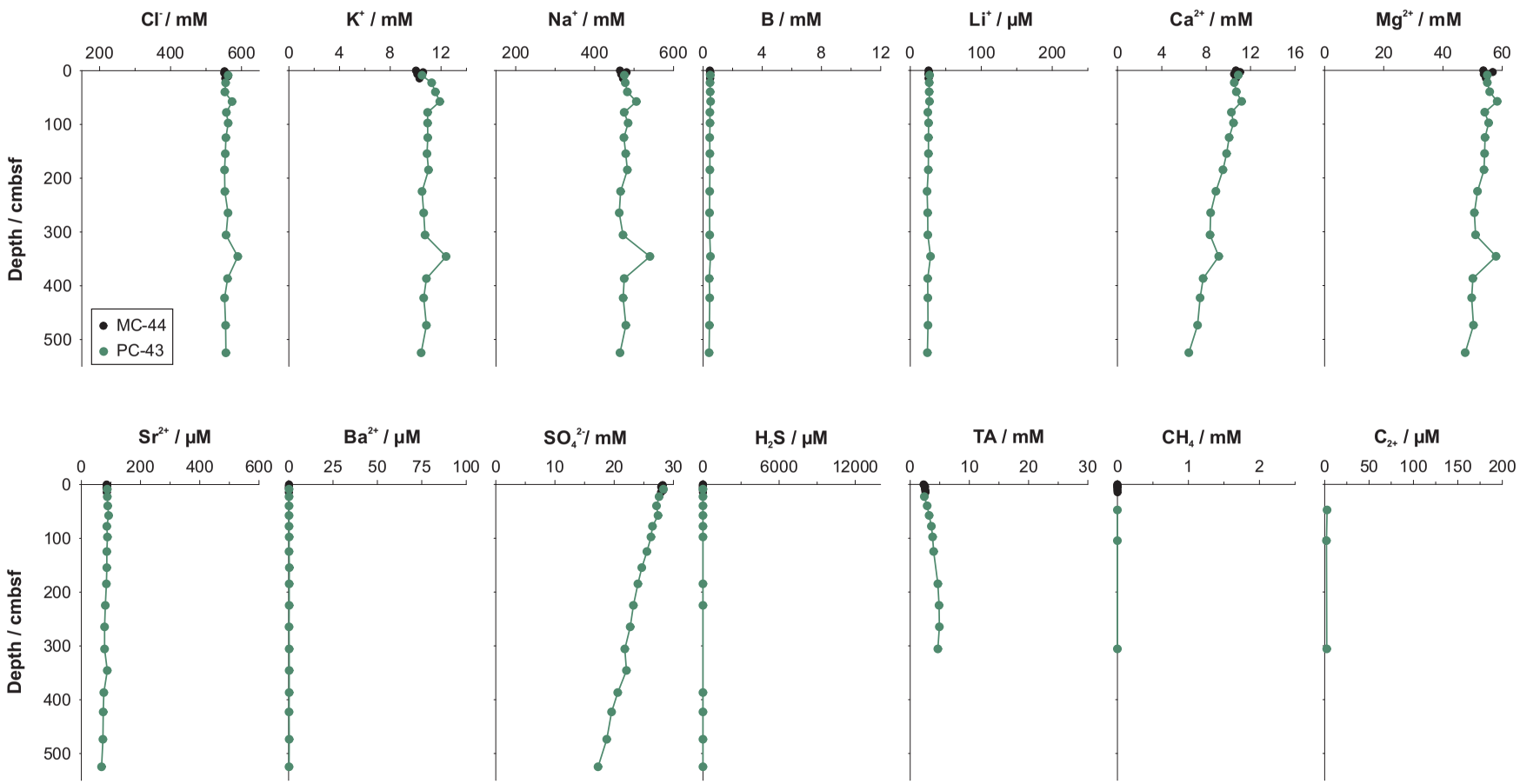

Figure E.3 Pore water depth profiles of chloride (Cl^-), potassium (K^+), sodium (Na^+), boron (B), lithium (Li^+), calcium (Ca^{2+}), magnesium (Mg^{2+}), strontium (Sr^{2+}), barium (Ba^{2+}), sulphate (SO_4^{2-}), hydrogen sulphide (H_2S), total alkalinity (TA), methane (CH_4) and higher hydrocarbons (C_{2+}) for the background site, i.e. 2.9 km SW of Carlos Ribeiro mud volcano.

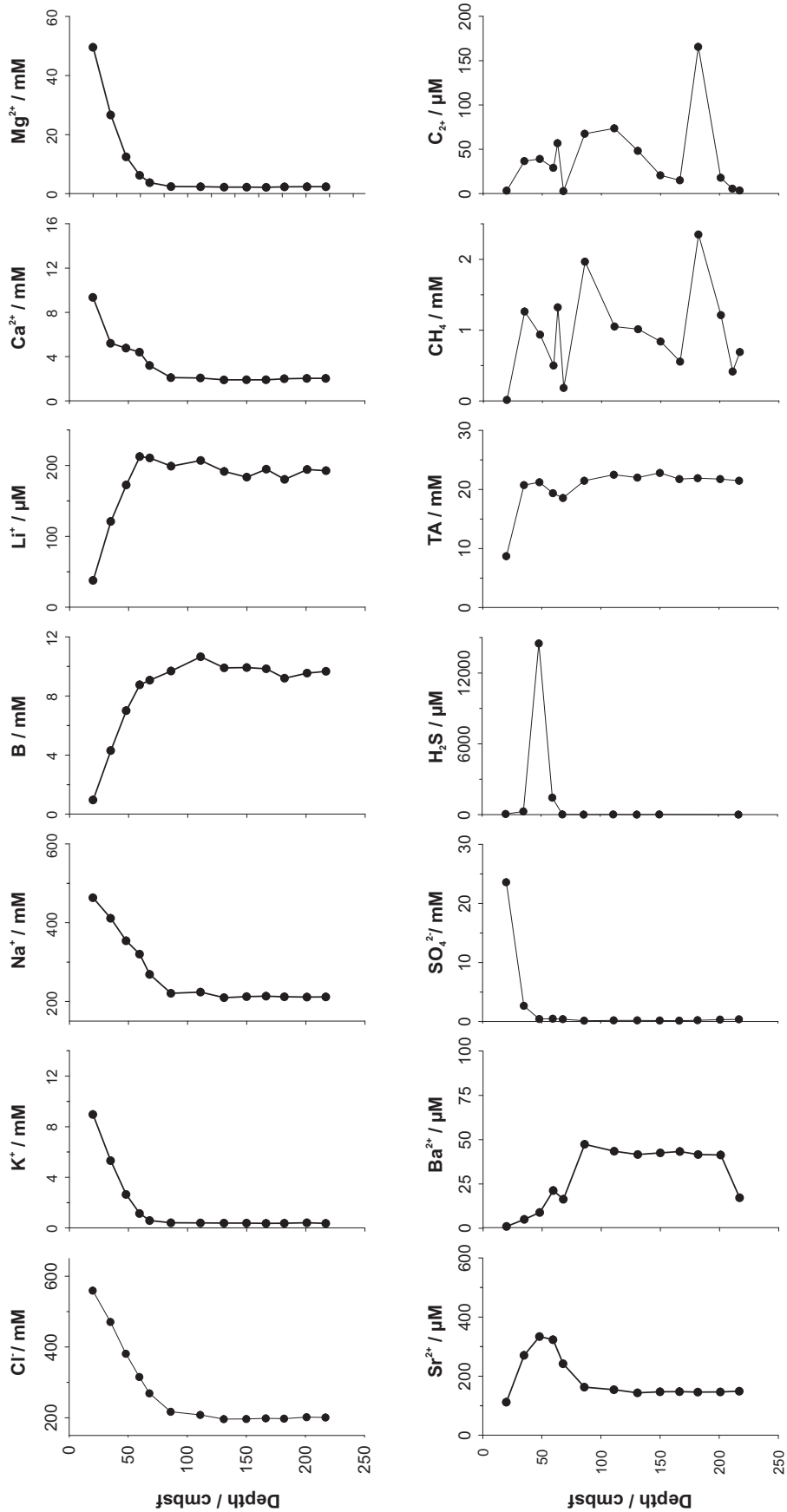

Figure E.4 Pore water depth profiles of chloride (Cl^-), potassium (K^+), sodium (Na^+), boron (B), lithium (Li^+), calcium (Ca^{2+}), magnesium (Mg^{2+}), strontium (Sr^{2+}), barium (Ba^{2+}), sulphate (SO_4^{2-}), hydrogen sulphide (H_2S), total alkalinity (TA), methane (CH_4) and higher hydrocarbons (C_{2+}) for coring site GC-52 on the Carlos Ribeiro mud volcano.

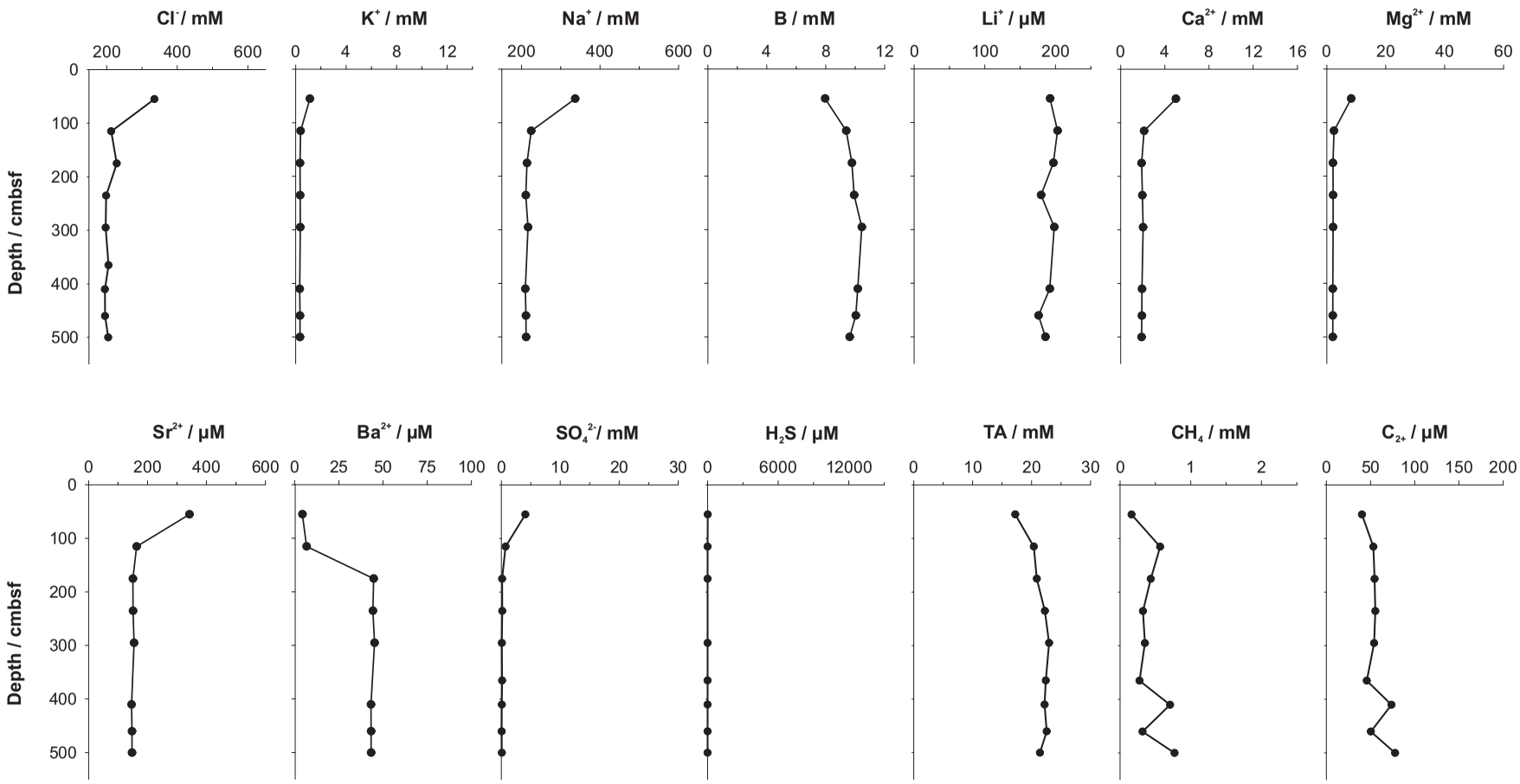

Figure E.5 Pore water depth profiles of chloride (Cl^-), potassium (K^+), sodium (Na^+), boron (B), lithium (Li^+), calcium (Ca^{2+}), magnesium (Mg^{2+}), strontium (Sr^{2+}), barium (Ba^{2+}), sulphate (SO_4^{2-}), hydrogen sulphide (H_2S), total alkalinity (TA), methane (CH_4) and higher hydrocarbons (C_{2+}) for coring site PC-53 on the Carlos Ribeiro mud volcano.

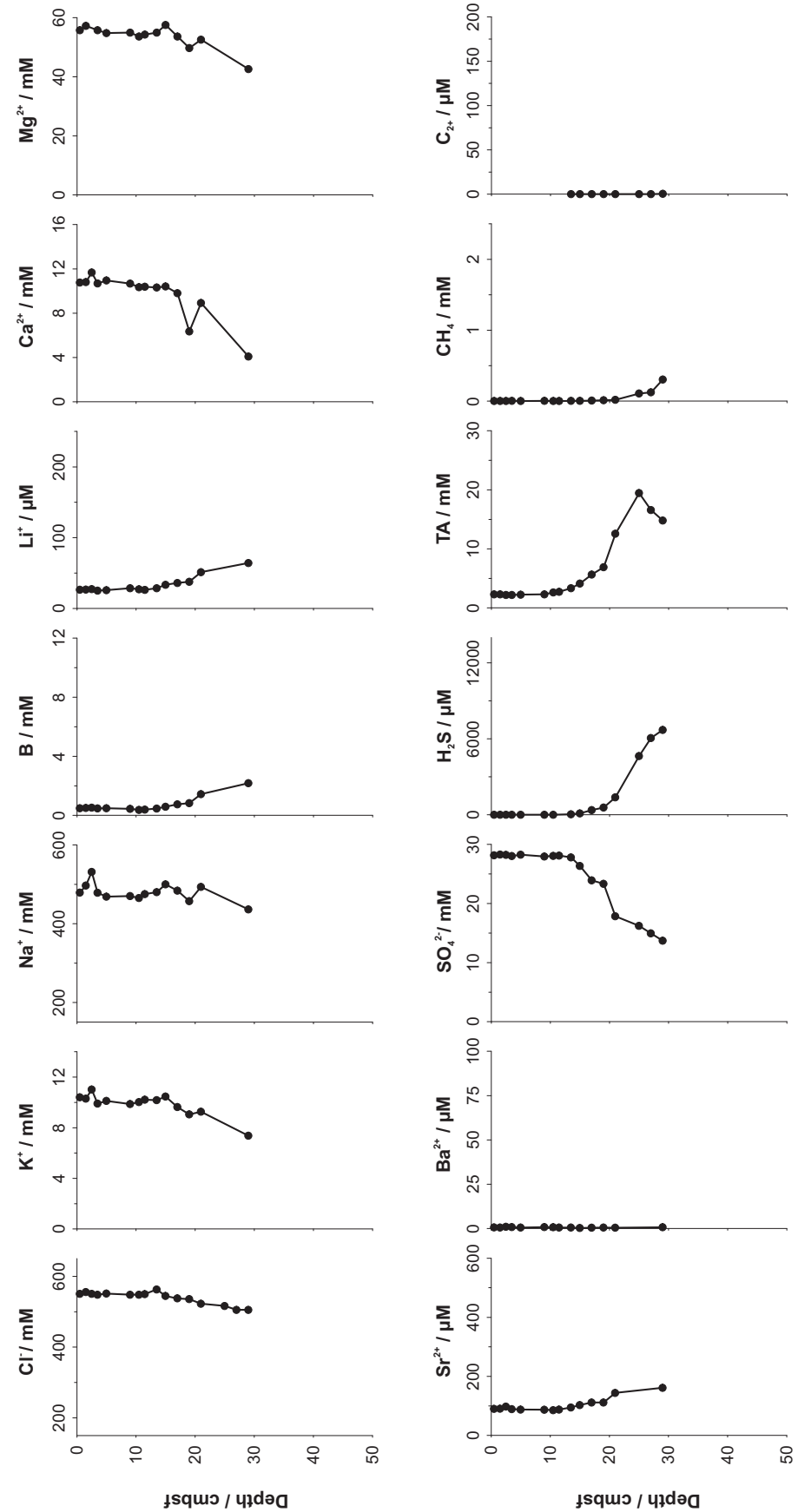

Figure E.6 Pore water depth profiles of chloride (Cl^-), potassium (K^+), sodium (Na^+), boron (B), lithium (Li^+), calcium (Ca^{2+}), magnesium (Mg^{2+}), strontium (Sr^{2+}), barium (Ba^{2+}), sulphate (SO_4^{2-}), hydrogen sulphide (H_2S), total alkalinity (TA), methane (CH_4) and higher hydrocarbons (C_{2+}) for coring site MC-57 on the Carlos Ribeiro mud volcano.

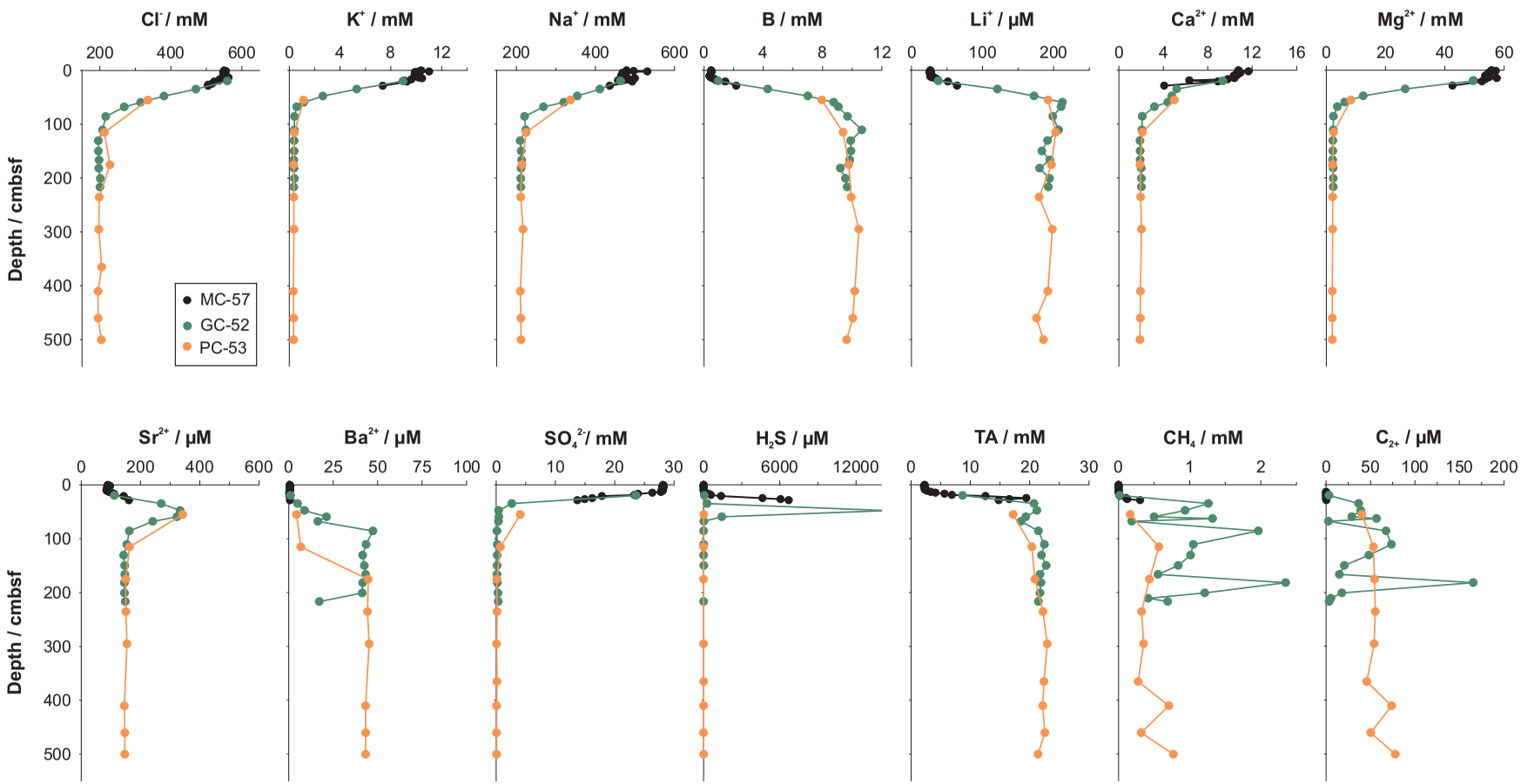

Figure E.7 Pore water depth profiles of chloride (Cl^-), potassium (K^+), sodium (Na^+), boron (B), lithium (Li^+), calcium (Ca^{2+}), magnesium (Mg^{2+}), strontium (Sr^{2+}), barium (Ba^{2+}), sulphate (SO_4^{2-}), hydrogen sulphide (H_2S), total alkalinity (TA), methane (CH_4) and higher hydrocarbons (C_{2+}) for the eye site on the Carlos Ribeiro mud volcano.

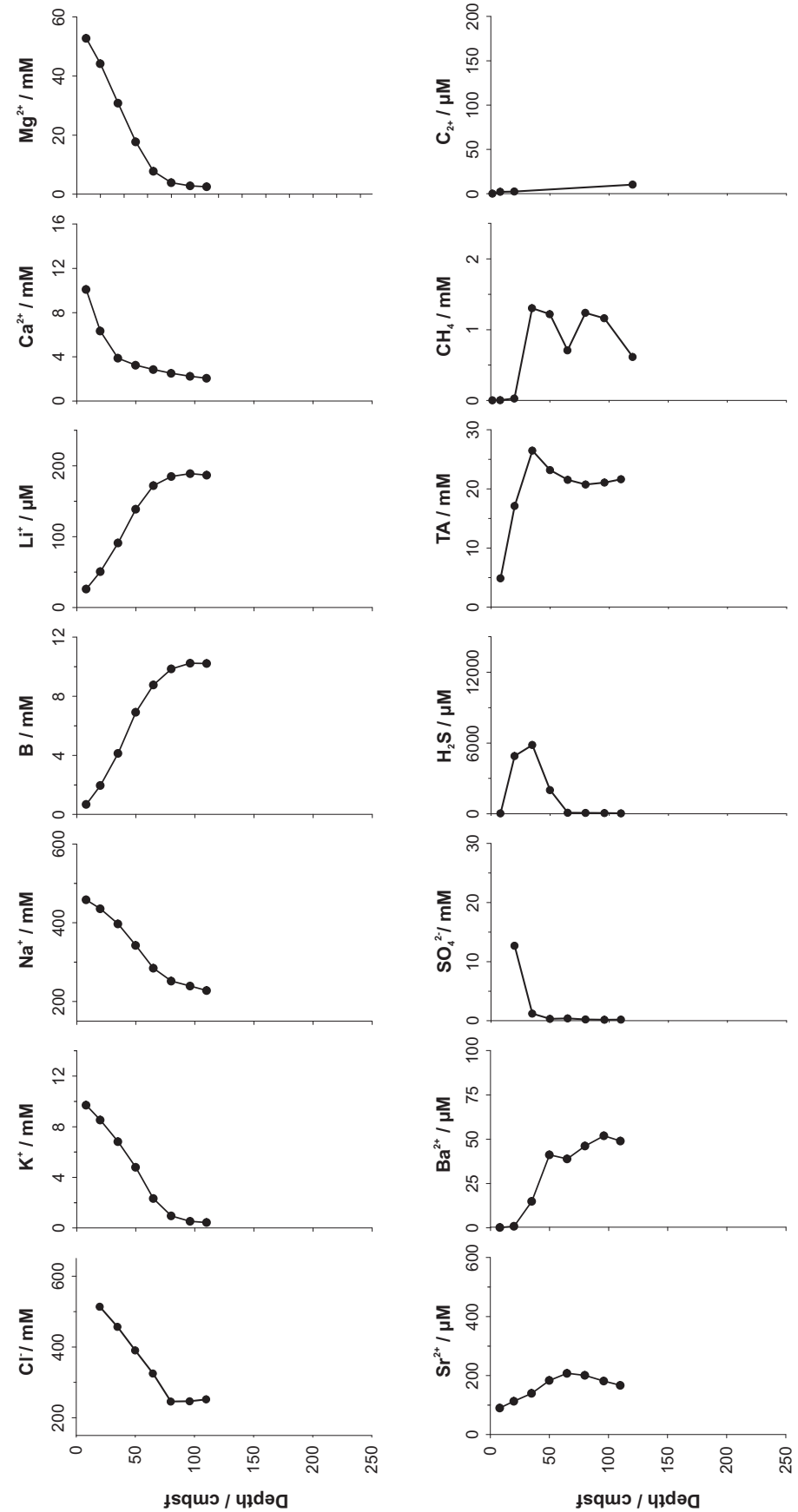

Figure E.8 Pore water depth profiles of chloride (Cl^-), potassium (K^+), sodium (Na^+), boron (B), lithium (Li^+), calcium (Ca^{2+}), magnesium (Mg^{2+}), strontium (Sr^{2+}), barium (Ba^{2+}), sulphate (SO_4^{2-}), hydrogen sulphide (H_2S), total alkalinity (TA), methane (CH_4) and higher hydrocarbons (C_{2+}) for coring site GC-49 on the Carlos Ribeiro mud volcano.

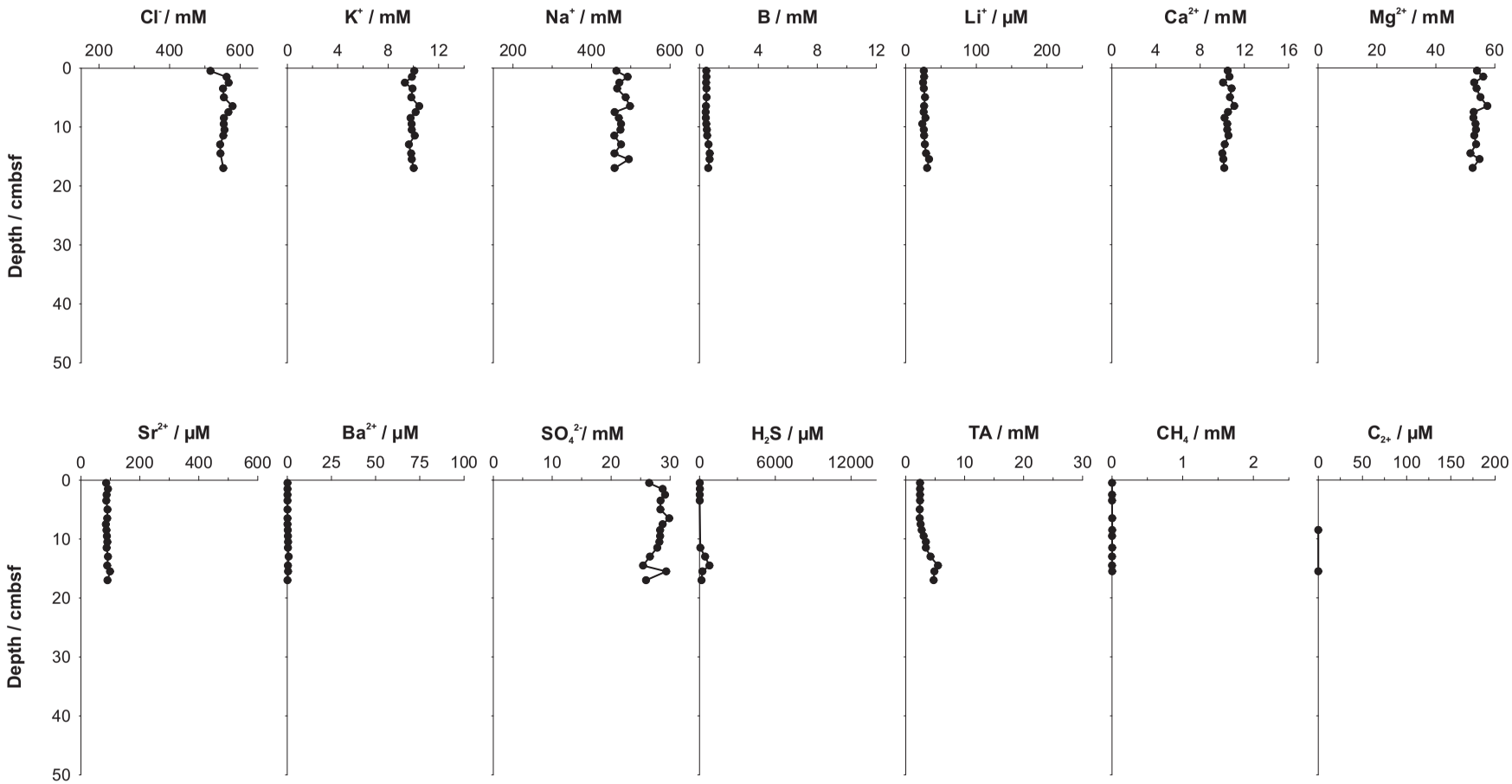

Figure E.9 Pore water depth profiles of chloride (Cl^-), potassium (K^+), sodium (Na^+), boron (B), lithium (Li^+), calcium (Ca^{2+}), magnesium (Mg^{2+}), strontium (Sr^{2+}), barium (Ba^{2+}), sulphate (SO_4^{2-}), hydrogen sulphide (H_2S), total alkalinity (TA), methane (CH_4) and higher hydrocarbons (C_{2+}) for coring site MC-50 on the Carlos Ribeiro mud volcano.

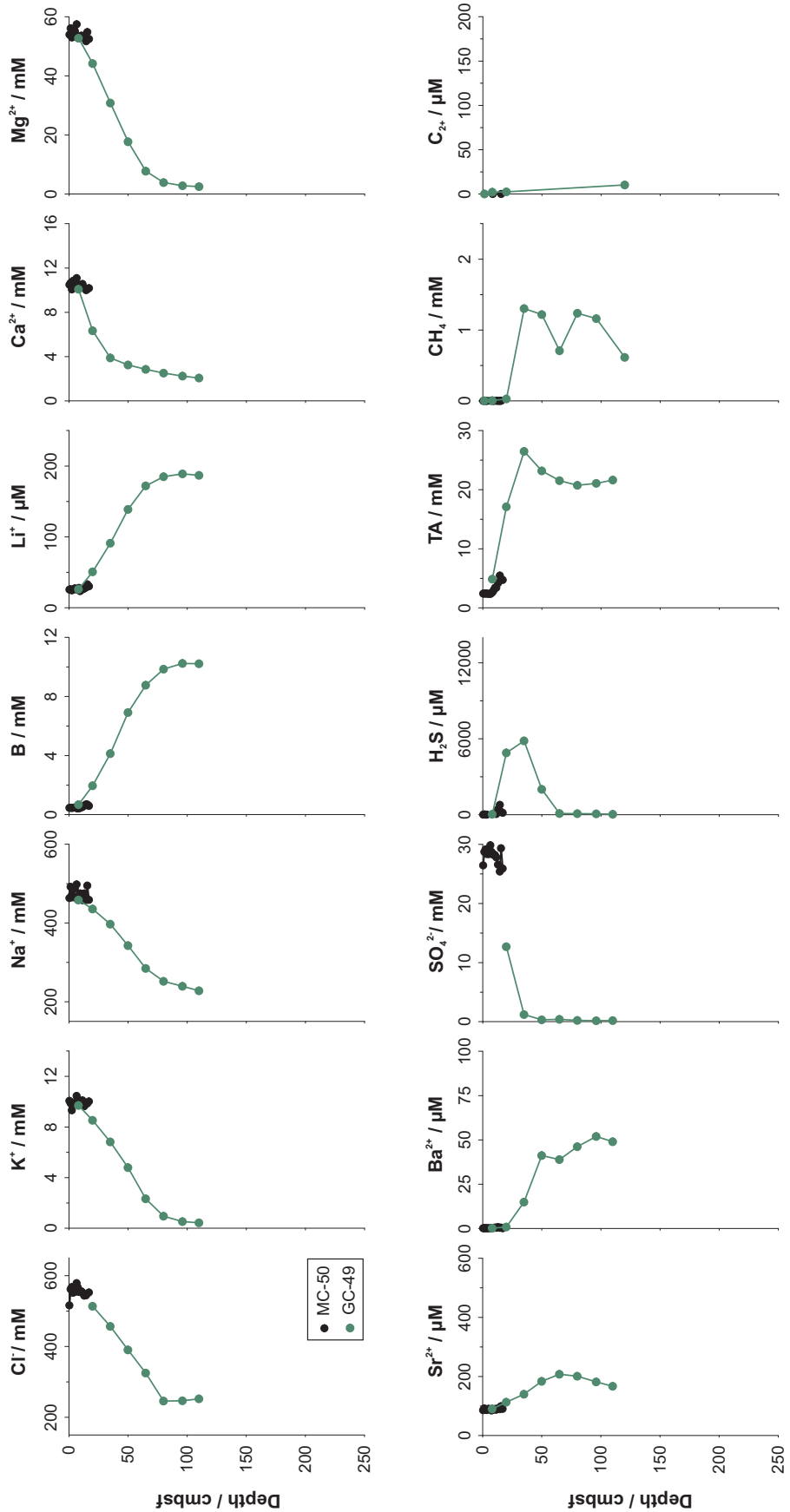

Figure E.10 Pore water depth profiles of chloride (Cl^-), potassium (K^+), sodium (Na^+), boron (B), lithium (Li^+), calcium (Ca^{2+}), magnesium (Mg^{2+}), strontium (Sr^{2+}), barium (Ba^{2+}), sulphate (SO_4^{2-}), hydrogen sulphide (H_2S), total alkalinity (TA), methane (CH_4) and higher hydrocarbons (C_{2+}) for the off-centre site on the Carlos Ribeiro mud volcano.

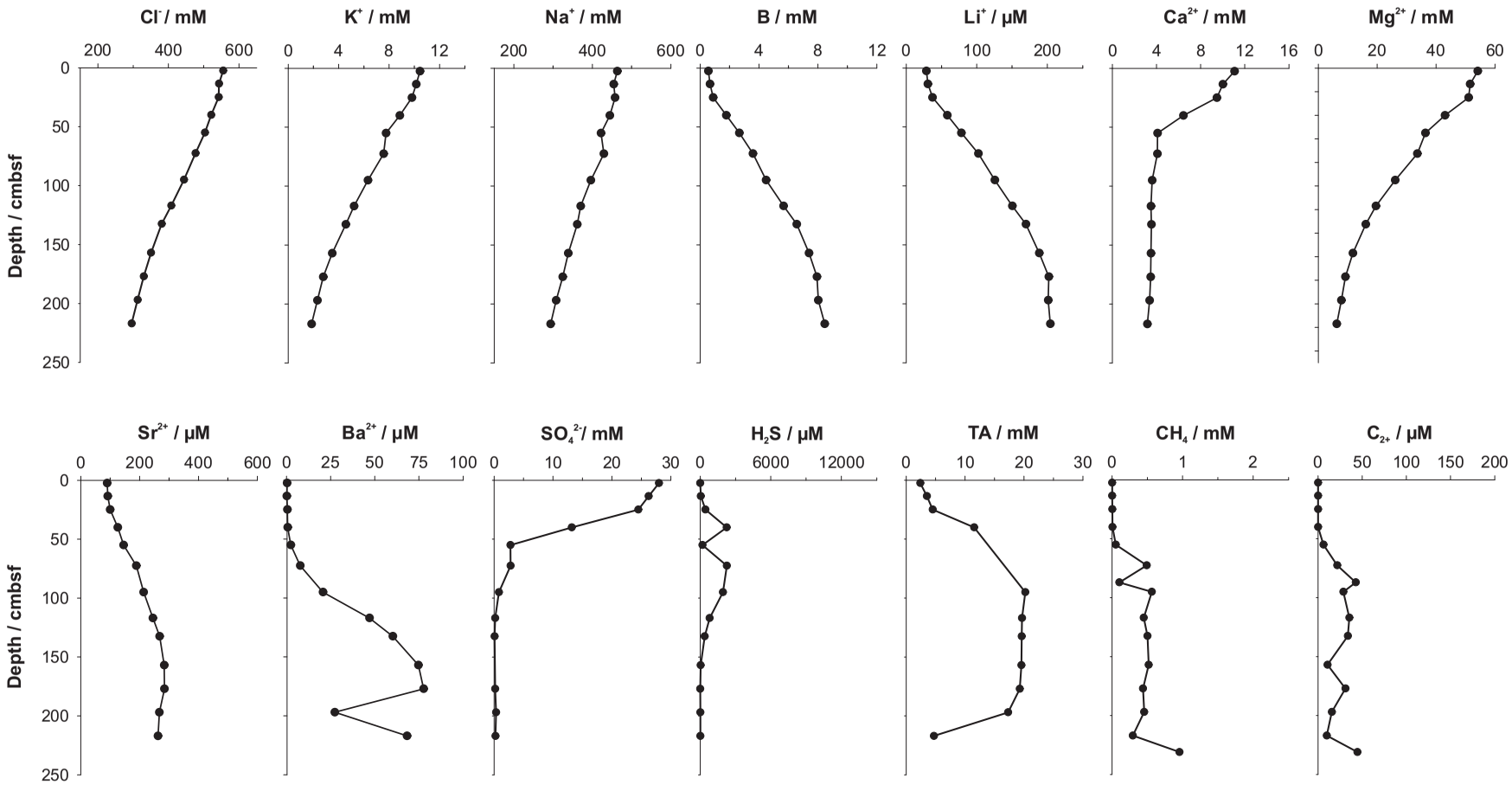

Figure E.11 Pore water depth profiles of chloride (Cl^-), potassium (K^+), sodium (Na^+), boron (B), lithium (Li^+), calcium (Ca^{2+}), magnesium (Mg^{2+}), strontium (Sr^{2+}), barium (Ba^{2+}), sulphate (SO_4^{2-}), hydrogen sulphide (H_2S), total alkalinity (TA), methane (CH_4) and higher hydrocarbons (C_{2+}) for coring site PC-58 on the Carlos Ribeiro mud volcano.

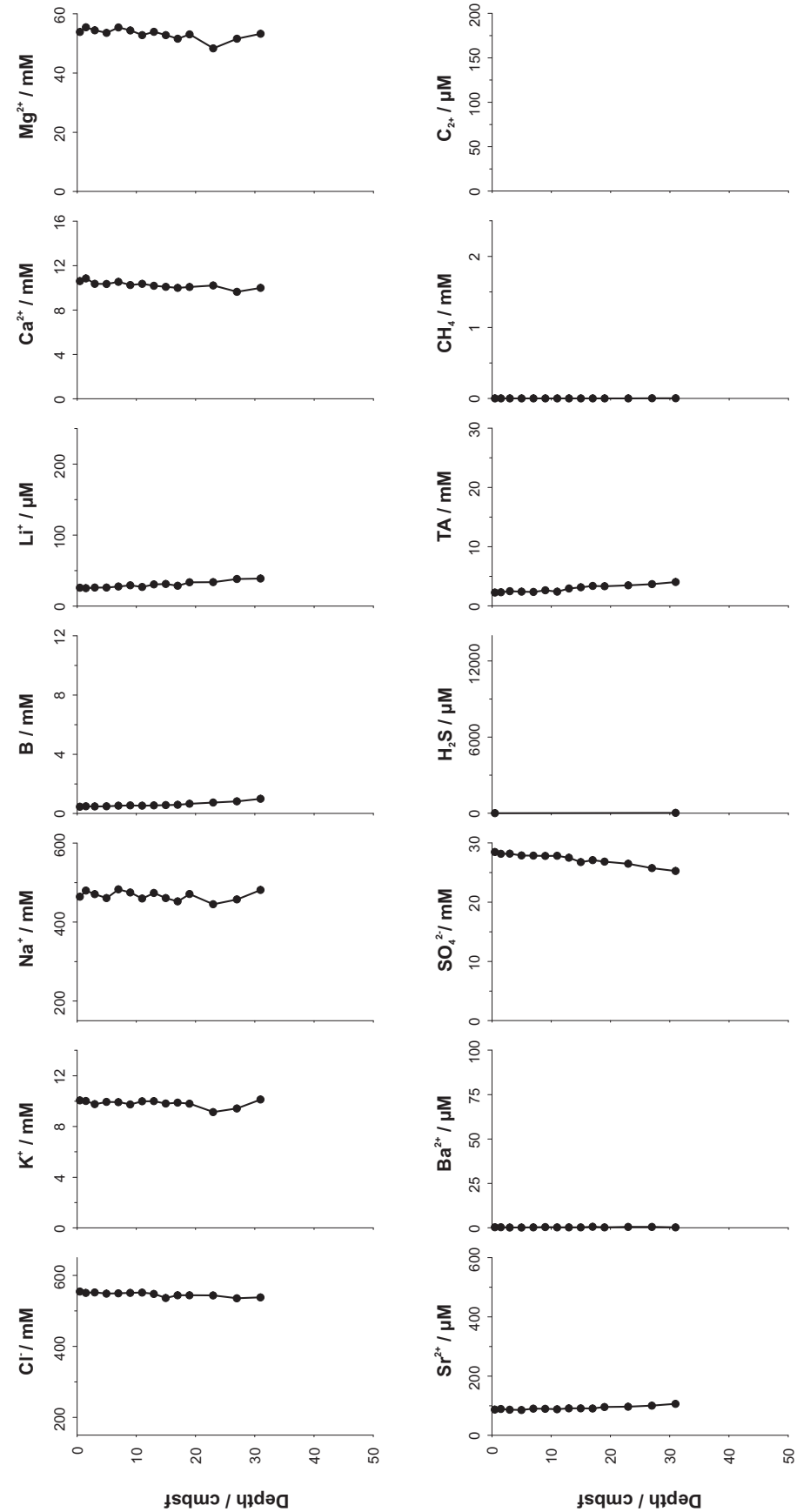

Figure E.12 Pore water depth profiles of chloride (Cl^-), potassium (K^+), sodium (Na^+), boron (B), lithium (Li^+), calcium (Ca^{2+}), magnesium (Mg^{2+}), strontium (Sr^{2+}), barium (Ba^{2+}), sulphate (SO_4^{2-}), hydrogen sulphide (H_2S), total alkalinity (TA), methane (CH_4) and higher hydrocarbons (C_{2+}) for coring site MC-63 on the Carlos Ribeiro mud volcano.

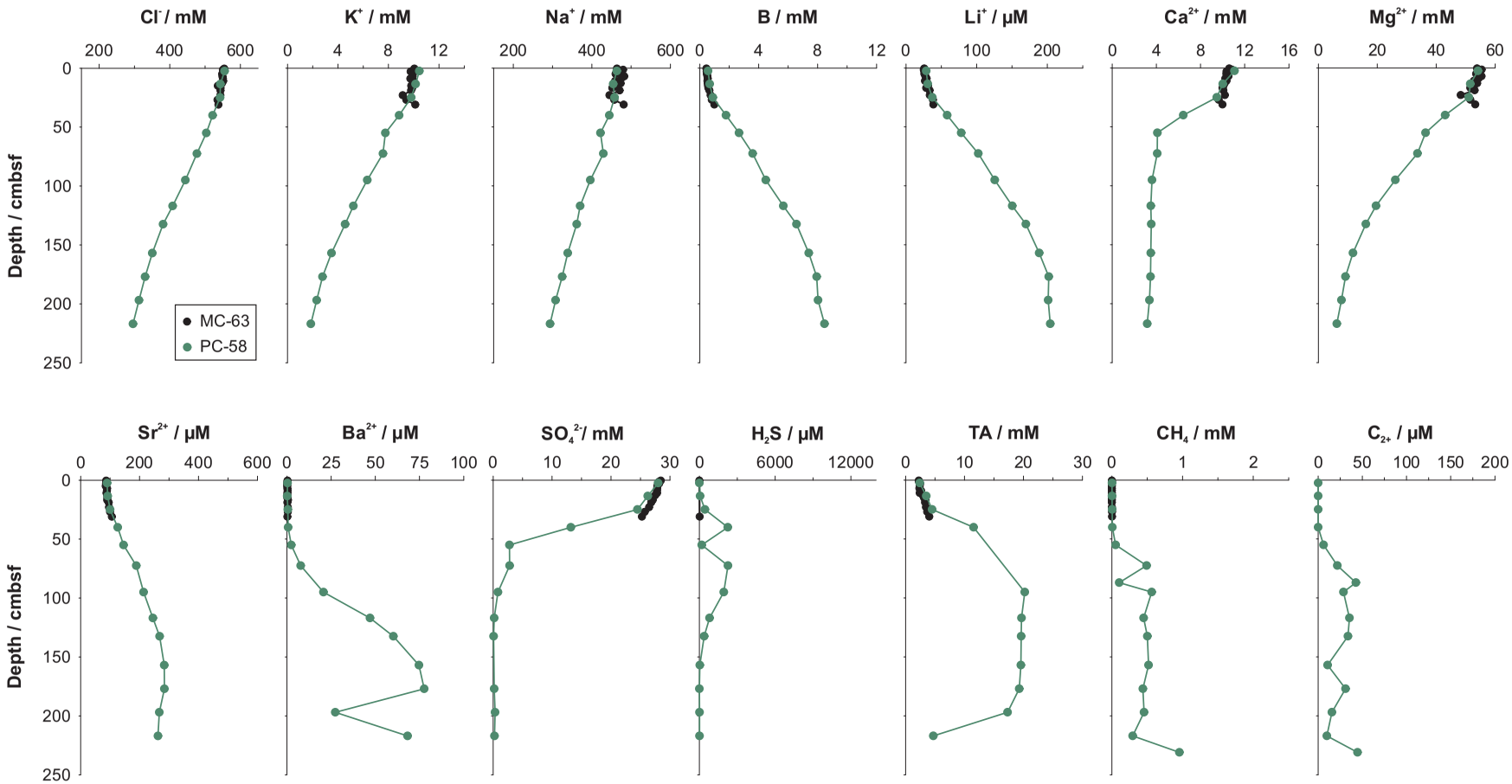

Figure E.13 Pore water depth profiles of chloride (Cl^-), potassium (K^+), sodium (Na^+), boron (B), lithium (Li^+), calcium (Ca^{2+}), magnesium (Mg^{2+}), strontium (Sr^{2+}), barium (Ba^{2+}), sulphate (SO_4^{2-}), hydrogen sulphide (H_2S), total alkalinity (TA), methane (CH_4) and higher hydrocarbons (C_{2+}) for the margin site on the Carlos Ribeiro mud volcano.

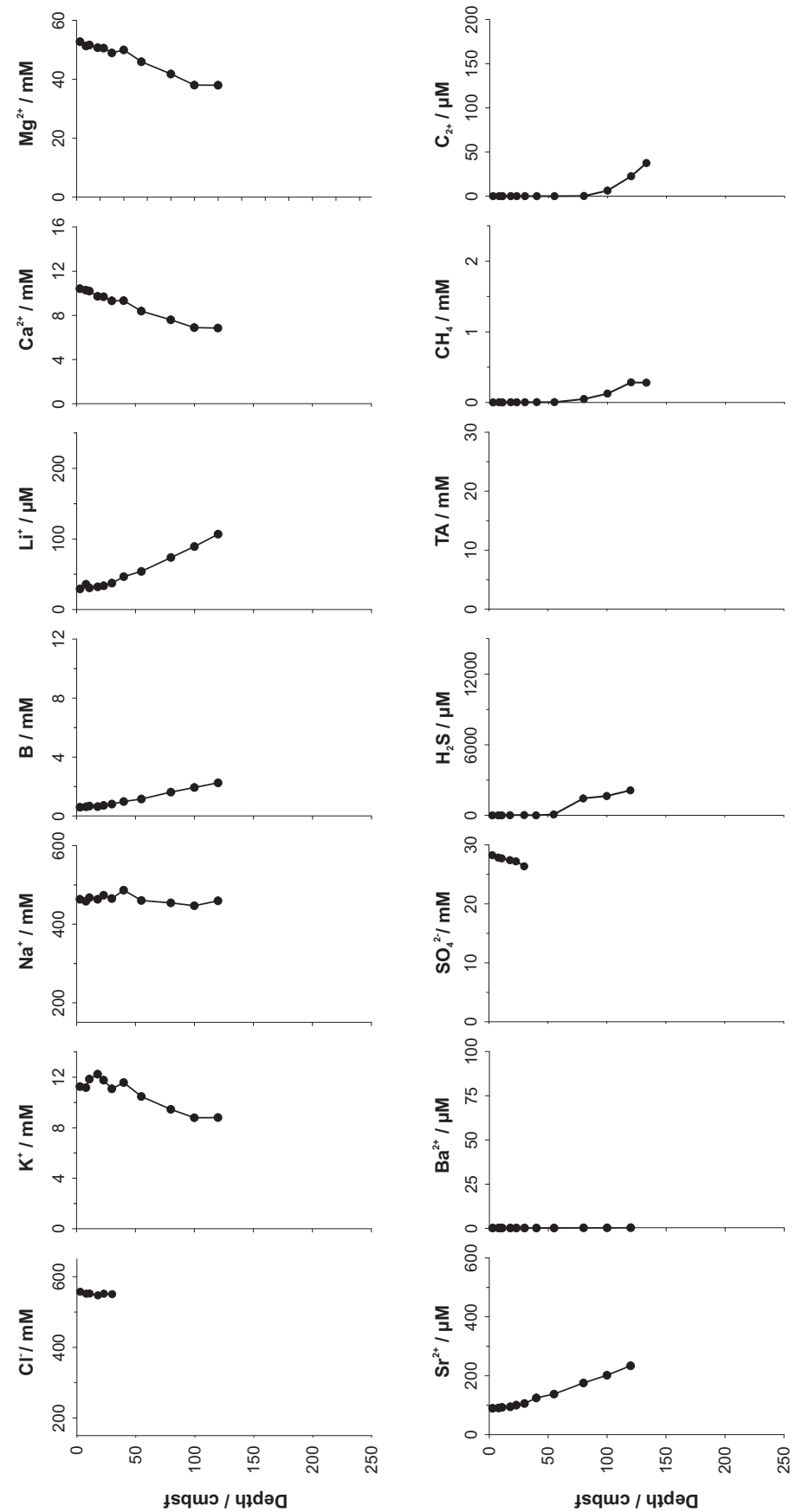

Figure E.14 Pore water depth profiles of chloride (Cl^-), potassium (K^+), sodium (Na^+), boron (B), lithium (Li^+), calcium (Ca^{2+}), magnesium (Mg^{2+}), strontium (Sr^{2+}), barium (Ba^{2+}), sulphate (SO_4^{2-}), hydrogen sulphide (H_2S), total alkalinity (TA), methane (CH_4) and higher hydrocarbons (C_{2+}) for coring site PC-59 on the Carlos Ribeiro mud volcano.

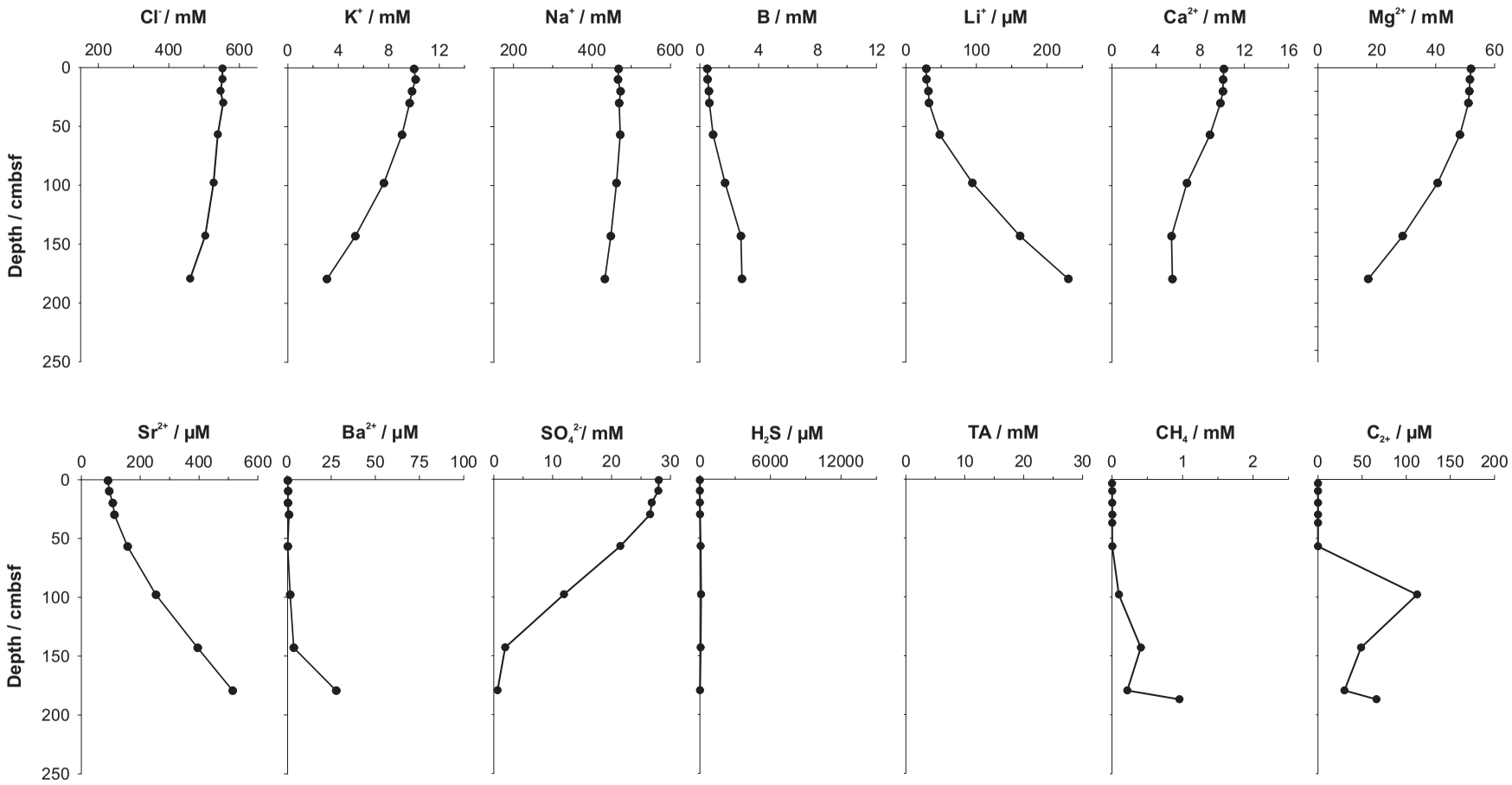

Figure E.15 Pore water depth profiles of chloride (Cl^-), potassium (K^+), sodium (Na^+), boron (B), lithium (Li^+), calcium (Ca^{2+}), magnesium (Mg^{2+}), strontium (Sr^{2+}), barium (Ba^{2+}), sulphate (SO_4^{2-}), hydrogen sulphide (H_2S), total alkalinity (TA), methane (CH_4) and higher hydrocarbons (C_{2+}) for coring site GC-60 on the Carlos Ribeiro mud volcano.

Bibliography

Aharon, P., 2000. Microbial processes and products fueled by hydrocarbons at submarine seeps. In: Riding, R., Awramik, S. (Eds.), Microbial sediments. Springer-Verlag, Berlin, pp. 270–281.

Aharon, P., Schwarcz, H. P., Roberts, H. H., 1997. Radiometric dating of submarine hydrocarbon seeps in the Gulf of Mexico. Geological Society of America Bulletin 109 (5), 568–579.

Aharon, P., Sengupta, B. K., 1994. Bathymetric Reconstructions of the Miocene-Age Calcari a Lucina (Northern Apennines, Italy) from Oxygen Isotopes and Benthic Foraminifera. Geo-Marine Letters 14 (2-3), 219–230.

Akhmetzhanov, A., Ivanov, M., Kenyon, N., Mazzini, A., 2007. Deep-water cold seeps, sedimentary environments and ecosystems of the Black and Tyrrhenian Sea and the Gulf of Cadiz, Preliminary results of investigations during the TTR-15 cruise, RV "Prof Logachev", June-Aug 2005.

Aliyev, A., Guliyev, I., Belov, I., 2002. Catalogue of Recorded Eruptions of Mud Volcanoes of Azerbaijan (for Period of Years 1810 to 2001).

Aller, R. C., 1980. Quantifying Solute Distributions in the Bioturbated Zone of Marine-Sediments by Defining an Average Micro-Environment. Geochimica et Cosmochimica Acta 44 (12), 1955–1965.

Aloisi, G., Bouloubassi, I., Heijs, S. K., Pancost, R. D., Pierre, C., Damste, J. S. S., Gottschal, J. C., Forney, L. J., Rouchy, J. M., 2002. CH_4-consuming microorganisms and the formation of carbonate crusts at cold seeps. Earth and Planetary Science Letters 203 (1), 195–203.

Aloisi, G., Drews, M., Wallmann, K., Bohrmann, G., 2004a. Fluid expulsion from the Dvurechenskii mud volcano (Black Sea) Part I. Fluid sources and relevance to Li, B, Sr, I and dissolved inorganic nitrogen cycles. Earth and Planetary Science Letters 225 (3-4), 347–363.

Aloisi, G., Pierre, C., Rouchy, J. M., Foucher, J. P., Woodside, J., Party, M. S., 2000. Methane-related authigenic carbonates of eastern Mediterranean Sea mud volcanoes

and their possible relation to gas hydrate destabilisation. Earth and Planetary Science Letters 184 (1), 321–338.

Aloisi, G., Wallmann, K., Bollwerk, S. M., Derkachev, A., Bohrmann, G., Suess, E., 2004b. The effect of dissolved barium on biogeochemical processes at cold seeps. Geochimica et Cosmochimica Acta 68 (8), 1735–1748.

Aloisi, G., Wallmann, K., Haese, R. R., Saliège, J. F., 2004c. Chemical, biological and hydrological controls on the ^{14}C content of cold seep carbonate crusts: numerical modeling and implications for convection at cold seeps. Chemical Geology 213 (4), 359–383.

Alperin, M., Reeburgh, W., 1988. Carbon and hydrogen isotope fractionation resulting from anaerobic methane oxidation. Global Biogeochemical Cycles 2 (3), 279–288.

Ambar, I., 1983. A Shallow Core of Mediterranean Water Off Western Portugal. Deep-Sea Research Part a-Oceanographic Research Papers 30 (6), 677–680.

Ambar, I., Howe, M. R., 1979. Observations of the Mediterranean Outflow .2. Deep Circulation in the Vicinity of the Gulf of Cadiz. Deep-Sea Research Part A - Oceanographic Research Papers 26 (5), 555–568.

Ambar, I., Serra, N., Brogueira, M. J., Cabecadas, G., Abrantes, F., Freitas, P., Goncalves, C., Gonzalez, N., 2002. Physical, chemical and sedimentological aspects of the Mediterranean outflow off Iberia. Deep-Sea Research Part II-Topical Studies in Oceanography 49 (19), 4163–4177.

Anderson, T., Arthur, M., 1983. Stable isotopes of oxygen and carbon and their application to sedimentologic and paleoenvironmental problems. In: Arthur, M., Anderson, T., Kaplan, I., Veizer, J. (Eds.), Stable Isotopes in Sedimentary Geology. Society of Economic Paleontologists and Mineralogists, Dallas, pp. 1–151.

Aquilina, L., Dia, A. N., Boulegue, J., Bourgois, J., Fouillac, A. M., 1997. Massive barite deposits in the convergent margin off Peru: Implications for fluid circulation within subduction zones. Geochimica et Cosmochimica Acta 61 (6), 1233–1245.

Bahr, A., Pape, T., Bohrmann, G., Mazzini, A., Haeckel, M., Reitz, A., Ivanov, M., 2009. Authigenic carbonate precipitates from the NE Black Sea: a mineralogical, geochemical, and lipid biomarker study. International Journal of Earth Sciences 98 (3), 677–695.

Baraza, J., Ercilla, G., 1996. Gas-charged sediments and large pockmark-like features on the Gulf of Cadiz slope (SW Spain). Marine and Petroleum Geology 13 (2), 253–261.

Baraza, J., Ercilla, G., Nelson, C. H., 1999. Potential geologic hazards on the eastern Gulf of Cadiz slope (SW Spain). Marine Geology 155 (1-2), 191–215.

Baringer, M. O., Price, J. F., 1999. A review of the physical oceanography of the Mediterranean outflow. Marine Geology 155 (1-2), 63–82.

Barnes, R., Goldberg, E., 1976. Methane production and consumption in anoxic marine-sediments. Geology 4 (5), 297–300.

Bayon, F. E. B., See, F., Margo, G., Pennisi, M., 2008. Noble gas and boron isotopic signatures of the Bacon-Manito geothermal fluid, Philippines. Geofluids 8 (4), 230–238.

Bayon, G., Pierre, C., Etoubleau, J., Voisset, M., Cauquil, E., Marsset, T., Sultan, N., Le Drezen, E., Fouquet, Y., 2007. Sr/Ca and Mg/Ca ratios in Niger Delta sediments: Implications for authigenic carbonate genesis in cold seep environments. Marine Geology 241 (1-4), 93–109.

Berástegui, X., Banks, C., Puig, C., Taberner, C., Waltham, D., Fernàndez, M., 1998. Lateral diapiric emplacement of Triassic evaporites at the southern margin of the Gaudalquivir Basin, Spain. In: Mascle, A., Puigdefàbregas, C., Luterbacher, H., Fernàndez, M. (Eds.), Cenozoic Foreland Basins of Western Europe. Vol. 134. Geological Society, London, Special Publications, pp. 49–68.

Berelson, W. M., Prokopenko, M., Sansone, F. J., Graham, A. W., McManus, J., Bernhard, J. M., 2005. Anaerobic diagenesis of silica and carbon in continental margin sediments: Discrete zones of TCO_2 production. Geochimica et Cosmochimica Acta 69 (19), 4611–4629.

Berner, R. A., 1970. Sedimentary Pyrite Formation. American Journal of Science 268 (1), 1– 23.

Berner, R. A., 1980. Early Diagenesis: A Theoretical Approach. Princeton University Press, Chichester.

Bird, P., 2003. An updated digital model of plate boundaries. Geochemistry Geophysics Geosystems 4, 1027.

Bishop, J. K. B., 1988. The Barite-Opal-Organic Carbon Association in Oceanic Particulate Matter. Nature 332 (6162), 341–343.

Boetius, A., Ravenschlag, K., Schubert, C. J., Rickert, D., Widdel, F., Gieseke, A., Amann, R., Jorgensen, B. B., Witte, U., Pfannkuche, O., 2000. A marine microbial consortium apparently mediating anaerobic oxidation of methane. Nature 407 (6804), 623–626.

Boetius, A., Wenzhofer, F., 2009. In Situ Technologies for Studying Deep-Sea Hotspot Ecosystems. Oceanography 22 (1), 177–177, oceanography.

Böhm, F., Joachimski, M. M., Dullo, W.-C., Eisenhauer, A., Lehnert, H., Reitner, J., Wörheide, G., 2007. Oxygen isotope fractionation in marine aragonite of coralline sponges. Geochimica et Cosmochimica Acta 64 (10), 1695–1703.

Bohrmann, G., Ivanov, M., Foucher, J. P., Spiess, V., Bialas, J., Greinert, J., Weinrebe, W., Abegg, F., Aloisi, G., Artemov, Y., Blinova, V., Drews, M., Heidersdorf, F., Krabbenhoft, A., Klaucke, I., Krastel, S., Leder, T., Polikarpov, I., Saburova, M., Schmale,

O., Seifert, R., Volkonskaya, A., Zillmer, M., 2003. Mud volcanoes and gas hydrates in the Black Sea: new data from Dvurechenskii and Odessa mud volcanoes. Geo-Marine Letters 23 (3-4), 239–249.

Bohrmann, G., Torres, M. E., 2006. Gas hydrates in marine sediments. In: Schulz, H. D., Zabel, M. (Eds.), Marine Geochemistry. Springer-Verlag, Berlin Heidelberg, pp. 481–512.

Borenas, K. M., Wahlin, A. K., Ambar, I., Serra, N., 2002. The Mediterranean outflow splitting - a comparison between theoretical models and CANIGO data. Deep-Sea Research Part II-Topical Studies in Oceanography 49 (19), 4195–4205.

Borowski, W. S., Paull, C. K., Ussler, W., 1996. Marine pore-water sulfate profiles indicate in situ methane flux from underlying gas hydrate. Geology 24 (7), 655–658.

Borowski, W. S., Paull, C. K., Ussler, W., 1999. Global and local variations of interstitial sulfate gradients in deep-water, continental margin sediments: Sensitivity to underlying methane and gas hydrates. Marine Geology 159 (1-4), 131–154.

Boudreau, B. P., 1996. A method-of-lines code for carbon and nutrient diagenesis in aquatic sediments. Computers & Geosciences 22 (5), 479–496.

Boudreau, B. P., 1997. Diagenetic Models and Their Implementation: Modelling Transport and Reactions in Aquatic Sediments. Springer-Verlag, Berlin.

Boudreau, B. P., Algar, C., Johnson, B. D., Croudace, I., Reed, A., Furukawa, Y., Dorgan, K. M., Jumars, P. A., Grader, A. S., Gardiner, B. S., 2005. Bubble growth and rise in soft sediments. Geology 33 (6), 517–520.

Boudreau, B. P., Canfield, D. E., 1988. A Provisional Diagenetic Model for pH in Anoxic Porewaters - Application to the Foam Site. Journal of Marine Research 46 (2), 429–455.

Bower, A. S., Serra, N., Ambar, I., 2002. Structure of the Mediterranean Undercurrent and Mediterranean Water spreading around the southwestern Iberian Peninsula. Journal of Geophysical Research-Oceans 107 (C10), 3160.

Bray, C. J., Karig, D. E., 1985. Porosity of Sediments in Accretionary Prisms and Some Implications for Dewatering Processes. Journal of Geophysical Research-Solid Earth and Planets 90 (Nb1), 768–778.

Brooks, J. M., Kennicutt, M. C., Fay, R. R., Mcdonald, T. J., Sassen, R., 1984. Thermogenic Gas Hydrates in the Gulf of Mexico. Science 225 (4660), 409–411.

Brown, K., 1994. Fluids in deforming sediments. In: Maltman, A. (Ed.), The Geological Deformation of sediments. Chapman & Hall, London, pp. 205–237.

Brown, K., Westbrook, G. K., 1988. Mud Diapirism and Subcretion in the Barbados Ridge Accretionary Complex - the Role of Fluids in Accretionary Processes. Tectonics 7 (3), 613–640.

Brown, K. M., 1990. The Nature and Hydrogeologic Significance of Mud Diapirs and Diatremes for Accretionary Systems. Journal of Geophysical Research-Solid Earth and Planets 95 (B6), 8969–8982.

Brown, K. M., Saffer, D. M., Bekins, B. A., 2001. Smectite diagenesis, pore-water freshening, and fluid flow at the toe of the Nankai wedge. Earth and Planetary Science Letters 194 (1-2), 97–109.

Brumsack, H. J., 1989. Geochemistry of Recent Toc-Rich Sediments from the Gulf of California and the Black-Sea. Geologische Rundschau 78 (3), 851–882.

Buczynski, C., Chafetz, H. S., 1991. Habit of Bacterially Induced Precipitates of Calcium-Carbonate and the Influence of Medium Viscosity on Mineralogy. Journal of sedimentary petrology 61 (2), 226–233.

Burne, R. V., Moore, L., 1987. Microbialites: organo-sedimentary deposits of benthic microbial communities. Palaios 2, 241–254.

Burton, E. A., 1993. Controls on Marine Carbonate Cement Mineralogy - Review and Reassessment. Chemical Geology 105 (1-3), 163–179.

Burton, E. A., Walter, L. M., 1987. Relative Precipitation Rates of Aragonite and Mg Calcite from Seawater - Temperature or Carbonate Ion Control. Geology 15 (2), 111–114.

Camerlenghi, A., Cita, M. B., Hieke, W., Ricchiuto, T., 1992. Geological Evidence for Mud Diapirism on the Mediterranean Ridge Accretionary Complex. Earth and Planetary Science Letters 109 (3-4), 493–504.

Campbell, K. A., Farmer, J. D., Des Marais, D., 2002. Ancient hydrocarbon seeps from the Mesozoic convergent margin of California: carbonate geochemistry, fluids and palaeoenvironments. Geofluids 2 (2), 63–94.

Campbell, K. A., Francis, D. A., Collins, M., Gregory, M. R., Nelson, C. S., Greinert, J., Aharon, P., 2008. Hydrocarbon seep-carbonates of a Miocene forearc (East Coast Basin), North Island, New Zealand. Sedimentary Geology 204 (3-4), 83–105.

Casas, D., Ercilla, G., Baraza, J., 2003. Acoustic evidences of gas in the continental slope sediments of the Gulf of Cadiz (E Atlantic). Geo-Marine Letters 23 (3-4), 300–310.

Castellini, D. G., Dickens, G. R., Snyder, G. T., Ruppel, C. D., 2006. Barium cycling in shallow sediment above active mud volcanoes in the Gulf of Mexico. Chemical Geology 226 (1-2), 1–30.

Castrec, M., Dia, A. N., Boulegue, J., 1996. Major- and trace-element and Sr isotope constraints on fluid circulation in the Barbados accretionary complex .2. Circulation rates and fluxes. Earth and Planetary Science Letters 142 (3-4), 487–499.

Cavanaugh, C. M., Levering, P. R., Maki, J. S., Mitchell, R., Lidstrom, M. E., 1987. Symbiosis of Methylotrophic Bacteria and Deep-Sea Mussels. Nature 325 (6102), 346–348.

Chaduteau, C., Jean-Baptiste, P., Fourre, E., Charlou, J., Donval, J., 2009. Helium transport in sediment pore fluids of the Congo-Angola margin. Geochemistry Geophysics Geosystems 10 (1), 1–12.

Chafetz, H. S., 1986. Marine Peloids - a Product of Bacterially Induced Precipitation of Calcite. Journal of sedimentary petrology 56 (6), 812–817.

Chafetz, H. S., Rush, P. F., Utech, N. M., 1991. Microenvironmental Controls on Mineralogy and Habit of $CaCO_3$ Precipitates - an Example from an Active Travertine System. Sedimentology 38 (1), 107–126.

Chan, L. H., 1994. Lithium isotope characteristics of marine sediments. EOS 75, 314.

Chan, L.-H., Alt, J. C., Teagle, D. A. H., 2002a. Lithium and lithium isotope profiles through the upper oceanic crust: a study of seawater-basalt exchange at ODP Sites 504B and 896A. Earth and Planetary Science Letters 201 (1), 187–201.

Chan, L. H., Kastner, M., 2000. Lithium isotopic compositions of pore fluids and sediments in the Costa Rica subduction zone: Implications for fluid processes and sediment contribution to the arc volcanoes. Earth and Planetary Science Letters 183 (1-2), 275–290.

Chan, L.-H., Starinsky, A., Katz, A., 2002b. The behavior of lithium and its isotopes in oilfield brines: evidence from the Heletz-Kokhav field, Israel. Geochimica et Cosmochimica Acta 66 (4), 615–623.

Childress, J. J., Fisher, C. R., Brooks, J. M., Kennicutt, M. C., Bidigare, R., Anderson, A. E., 1986. A Methanotrophic Marine Molluscan (Bivalvia, Mytilidae) Symbiosis - Mussels Fueled by Gas. Science 233 (4770), 1306–1308.

Cifci, G., Limonov, A., Dimitrov, L., Gainanov, V., 1997. Mud volcanoes and dome-like structures at the eastern Mediterranean Ridge. Marine Geophysical Researches 19 (5), 421–438.

Cita, M. B., Ryan, W. B. F., Paggi, L., 1981. Prometheus mud breccia: an example of shale diapirism in the western Mediterranean ridge. Annal Géologie des Pays Helléniques 3, 543–570.

Claypool, C. K., 1996. Influence of water solubility, phase equilibriaand capillary pressure on methane occurrence in sediments. In: AAPG Annual Convention, San Diego, Program with Abstracts. San Diego, p. A27.

Claypool, G. E., Kaplan, I., 1974. The origin and distribution of methane in marine sediments. In: Kaplan, I. (Ed.), Natural gases in marine sediments. Plenum, New York, pp. 99–139.

Clennell, M., Judd, A., Howland, M., 2000. Movement and accumulation of methane in marine sediments: relation to gas hydrate systems. In: Max, M. (Ed.), Natural gas hydrate in oceanic and permafrost environments. Kluwer Academic, Dordrecht, pp. 105–122.

Coleman, D. D., Liu, C. L., Riley, K. M., 1988. Microbial Methane in the Shallow Paleozoic Sediments and Glacial Deposits of Illinois, USA. Chemical Geology 71 (1-3), 23–40.

Colten-Bradley, V. A., 1987. Role of Pressure in Smectite Dehydration - Effects on Geopressure and Smectite-to-Illite Transformation. American Association of Petroleum Geologists Bulletin 71 (11), 1414–1427.

Coplen, T. B., Hanshaw, B. B., 1973. Ultrafiltration by a compacted clay membrane - I. Oxygen and hydrogen isotopic fractionation. Geochimica et Cosmochimica Acta 37, 2295–2310.

Criado-Aldeanueva, F., Garcia-Lafuente, J., Vargas, J. M., Del Rio, J., Vazquez, A., Reul, A., Sanchez, A., 2006. Distribution and circulation of water masses in the Gulf of Cadiz from in situ observations. Deep Sea Research Part II: Topical Studies in Oceanography 53 (11-13), 1144–1160.

Croudace, I. W., Rindby, A., Rothwell, R. G., 2006. ITRAX: description and evaluation of a new multi-function X-ray core scanner. In: Rothwell, R. (Ed.), New Techniques in Sediment Core Analysis. Vol. 267. Geological Society, London, Special Publications, pp. 51–63.

Cullity, B., 1956. Elements of x-ray diffraction. Addison-Wesley Publishing Company, Inc. Reading.

Dählmann, A., de Lange, G. J., 2003. Fluid-sediment interactions at Eastern Mediterranean mud volcanoes: a stable isotope study from ODP Leg 160. Earth and Planetary Science Letters 212, 377–391.

Damm, E., Budéus, G., 2003. Fate of vent-derived methane in seawater above the Håkon Mosby mud volcano (Norwegian Sea). Marine Chemistry 82 (1-2), 1–11.

Daniault, N., Maze, J. P., Arhan, M., 1994. Circulation and Mixing of Mediterranean Water West of the Iberian Peninsula. Deep-Sea Research Part I-Oceanographic Research Papers 41 (11-12), 1685–1714.

Davidson, D. W., Leaist, D. G., Hesse, R., 1983. O18 Enrichment in the Water of a Clathrate Hydrate. Geochimica et Cosmochimica Acta 47 (12), 2293–2295.

Davie, M., Buffett, B., 2001. A numerical model for the formation of gas hydrate below the seafloor. Journal of Geophysical Research 106 (B1), 497–514.

Davies, R. J., Brumm, M., Manga, M., Rubiandini, R., Swarbrick, R., Tingay, M., 2008. The East Java mud volcano (2006 to present): An earthquake or drilling trigger? Earth and Planetary Science Letters 272 (3-4), 627–638.

de Beer, D., Sauter, E., Niemann, H., Kaul, N., Foucher, J. P., Witte, U., Schluter, M., Boetius, A., 2006. In situ fluxes and zonation of microbial activity in surface sediments of the Hakon Mosby Mud Volcano. Limnology and Oceanography 51 (3), 1315–1331.

De Choudens-Sanchez, V., Gonzalez, L. A., 2009. Calcite and Aragonite Precipitation under Controlled Instantaneous Supersaturation: Elucidating the Role of $CaCO_3$ Saturation State and Mg/Ca Ratio on Calcium Carbonate Polymorphism. Journal of Sedimentary Research 79 (5-6), 363–376.

de Roo, J. L., Peters, C. J., Lichtenthaler, R. N., Diepen, G. A. M., 1983. Occurrence of Methane Hydrate in Saturated and Unsaturated Solutions of Sodium-Chloride and Water in Dependence of Temperature and Pressure. Aiche Journal 29 (4), 651–657.

Deer, W., Howie, R., Zussman, J., 1992. An introduction to the rock-forming minerals. 2nd ed. Addison Wesley Longman, Harlow.

Dehairs, F., Chesselet, R., Jedwab, J., 1980. Discrete Suspended Particles of Barite and the Barium Cycle in the Open Ocean. Earth and Planetary Science Letters 49 (2), 528–550.

Dewey, J., Helman, M., Turco, E., Hutton, D., Knott, S., 1989. Kinematics of the western Mediterranean. In: Coward, M., Dietrich, D., Park, R. (Eds.), Alpine Tectonics. Vol. 45. Geological Society, London, Special Publication, pp. 265–283.

Deyhle, A., Kopf, A., 2002. Strong B enrichment and anomalous $\delta^{11}B$ in pore fluids from the Japan Trench forearc. Marine Geology 183 (1-4), 1–15.

Dia, A. N., Aquilina, L., Boulegue, J., Bourgois, J., Suess, E., Torres, M., 1993. Origin of Fluids and Related Barite Deposits at Vent Sites Along the Peru Convergent Margin. Geology 21 (12), 1099–1102.

Dia, A. N., Castrec, M., Boulegue, J., Boudou, J. P., 1995. Major and Trace-Element and Sr Isotope Constraints on Fluid Circulations in the Barbados Accretionary Complex .1. Fluid Origin. Earth and Planetary Science Letters 134 (1-2), 69–85.

Díaz-del Río, V. V., Somoza, L., Martínez-Frias, J., Mata, M., Delgado, A., Hernandez-Molina, F., Lunar, R., Martín-Rubí, J., Maestro, A., M.C., F.-P., León, R., Llave, E., Medialdea, T., Vázquez, J., 2003. Vast fields of hydrocarbon-derived carbonate chimneys related to the accretionary wedge/olistostrome of the Gulf of Cádiz. Marine Geology 195, 177–200.

Dickens, G., Koelling, M., Smith, D., Schneiders, L., Scientists, 2007. Rhizon sampling of pore water on scientific drilling expeditions: An example from IODP Expedition 302, Arctic Coring Expedition (ACEX). Scientific Drilling IODP Expedition 302 (4), 22–25.

Dickens, G. R., 2001. Sulfate profiles and barium fronts in sediment on the Blake Ridge: present and past methane fluxes through a large gas hydrate reservoir. Geochimica et Cosmochimica Acta 65 (4), 529–543.

Dickson, J., 1966. Carbonate identification and genesis as revealed by staining. Journal of Sedimentary Petrology 36, 491–505.

Dimitrov, L., 2002. Mud volcanoes-the most important pathway for degassing deeply buried sediments. Earth-Science Reviews 59, 49–76.

Dimitrov, L., 2003. Mud volcanoes-a significant source of atmospheric methane. Geo-Marine Letters 23, 155–161.

Duan, Z., Miller, N., Greenberg, J., Waere, J., 1992. The prediction of methane solubility in natural waters to high ionic strengths from 0 to 250 C and from 0 to 1600 bar. Geochimica et Cosmochimica Acta 56, 1451–1460.

Duplessy, J.-C., Labeyrie, L., Waelbroeck, C., 2002. Constraints on the ocean oxygen isotopic enrichment between the Last Glacial Maximum and the Holocene: Paleoceanographic implications. Quaternary Science Reviews 21, 315–330.

Dymond, J., Suess, E., Lyle, M., 1992. Barium in deep-sea sediment: a geochemical proxy for paleoproductivity. Paleoceanography 7 (2), 163–181.

Eagle, M., Paytan, A., Arrigo, K. R., van Dijken, G., Murray, R. W., 2003. A comparison between excess barium and barite as indicators of carbon export. Paleoceanography 18 (1), 1021.

Egorov, A. V., Crane, K., Vogt, P. R., Rozhkov, A. N., 1999. Gas hydrates that outcrop on the sea floor: stability models. Geo-Marine Letters 19 (1-2), 68–75.

Ehrlich, H., 1990. Geomicrobiology. Marcel Dekker, New York.

Emeis, K., Robertson, A., Richter, C., 1996. Site970. Proceedings of the Ocean Drilling Program, Initial Reports 106.

Etiope, G., 2009. Natural emissions of methane from geological seepage in Europe. Atmospheric Environment 43 (7), 1430–1443.

Etiope, G., Caracausi, A., Favara, R., Italiano, F., Baciu, C., 2002. Methane emission from the mud volcanoes of Sicily (Italy). Geophysical Research Letters 29 (8), 1215.

Etiope, G., Milkov, A. V., 2004. A new estimate of global methane flux from onshore and shallow submarine mud volcanoes to the atmosphere. Environmental Geology 46 (8), 997–1002.

Evans, R. J., Stewart, S. A., Davies, R. J., 2008. The structure and formation of mud volcano summit calderas. Journal of the Geological Society 165, 769–780.

Feng, D., Chen, D., Peckmann, J., Bohrmann, G., 2010. Authigenic carbonates from methane seeps of the northern Congo fan: Microbial formation mechanism. Marine and Petroleum Geology 27 (4), 748–756.

Feng, D., Chen, D., Roberts, H. H., 2008. Sedimentary fabrics in the authigenic carbonates from Bush Hill: implication for seabed fluid flow and its dynamic signature. Geofluids 8 (4), 301–310.

Feng, D., Chen, D. F., Peckmann, J., 2009a. Rare earth elements in seep carbonates as tracers of variable redox conditions at ancient hydrocarbon seeps. Terra Nova 21 (1), 49–56.

Feng, D., Chen, D. F., Roberts, H. H., 2009b. Petrographic and geochemical characterization of seep carbonate from Bush Hill (GC 185) gas vent and hydrate site of the Gulf of Mexico. Marine and Petroleum Geology 26 (7), 1190–1198.

Fernandez-Puga, M. C., Vazquez, J. T., Somoza, L., del Rio, V. D., Medialdea, T., Mata, M. P., Leon, R., 2007. Gas-related morphologies and diapirism in the Gulf of Cadiz. Geo-Marine Letters 27 (2-4), 213–221.

Feseker, T., Dählmann, A., Foucher, J. P., Harmegnies, F., 2009. In-situ sediment temperature measurements and geochemical porewater data suggest highly dynamic fluid flow at Isis mud volcano, eastern Mediterranean Sea. Marine Geology 261 (1-4), 128–137.

Feseker, T., Foucher, J. P., Harmegnies, F., 2008. Fluid flow or mud eruptions? Sediment temperature distributions on Hakon Mosby mud volcano, SW Barents Sea slope. Marine Geology 247 (3-4), 194–207.

Fifield, F., Kealey, D., 2000. Principles and practice of analytical chemistry, 5th Edition. Blackwell Science, Oxford.

Fitts, T. G., Brown, K. M., 1999. Stress-induced smectite dehydration: ramifications for patterns of freshening and fluid expulsion in the N-Barbados accretionary wedge. Earth and Planetary Science Letters 172 (1-2), 179–197.

Fiuza, A. F. D., Demacedo, M. E., Guerreiro, M. R., 1982. Climatological Space and Time-Variation of the Portuguese Coastal Upwelling. Oceanologica Acta 5 (1), 31–40.

Flinch, J. F., 1993. Tectonic evolution of the Gilbraltar Arc. Ph.D. thesis, Rice University, Houston, Texas.

Flinch, J. F., Bally, A. W., Wu, S. G., 1996. Emplacement of a passive-margin evaporitic allochthon in the Betic Cordillera of Spain. Geology 24 (1), 67–70.

Folk, R. L., Chafetz, H. S., 2000. Bacterial induced microscale and nanoscale carbonate precipitates. In: Riding, R. E., Awramik, S. (Eds.), Microbial Sediments. Springer-Verlag, Berlin Heidelberg, pp. 40–49.

Foubert, A., Depreiter, D., Beck, T., Maignien, L., Pannemans, B., Frank, N., Blamart, D., Henriet, J.-P., 2008. Carbonate mounds in a mud volcano province off north-west Morocco: Key to processes and controls. Marine Geology 248 (1-2), 74–96.

Foucher, J. P., Westbrook, G. K., Boetius, A., Ceramicola, S., Dupre, S., Mascle, J., Mienert, J., Pfannkuche, O., Pierre, C., Praeg, D., 2009. Structure and Drivers of Cold Seep Ecosystems. Oceanography 22 (1), 92–109, oceanography.

Friedman, I., O'Neil, J., 1977. Compilation of stable isotope fractionation factors of geochemical interest. In: Fleischer, M. (Ed.), Data of Geochemistry 6th Ed. U.S. Geological Survey Professional Paper, Reston.

Fu, B. S., Aharon, P., Byerly, G. R., Roberts, H. H., 1994. Barite Chimneys an the Gulf-of-Mexico Slope - Initial Report on Their Petrography and Geochemistry. Geo-Marine Letters 14 (2-3), 81–87.

Gardner, J., 1999. Mud volcanoes on the Moroccan Margin. EOS Trans. AGU 80, 483.

Gardner, J., Jung, W.-Y., Somoza, L., 2001. The possible effect of the mediterranean outflow water (MOW) on gas hydrate dissociation in the Gulf of Cadiz. In: AGU Fall meeting. San Francisco, USA.

German, C. R., Damm, K. V., 2003. Hydrothermal Processes. In: Holland, H., Turekian, K., Elderfield, H. (Eds.), Treatise on Geochemistry. Vol. 6. Elsevier-Pergamon, Oxford, pp. 181–222.

Gingele, F., Dahmke, A., 1994. Discrete Barite Particles and Barium as Tracers of Paleoproductivity in South-Atlantic Sediments. Paleoceanography 9 (1), 151–168.

Ginsburg, G. D., Milkov, A. V., Soloviev, V. A., Egorov, A. V., Cherkashev, G. A., Vogt, P. R., Crane, K., Lorenson, T. D., Khutorskoy, M. D., 1999. Gas hydrate accumulation at the Hakon Mosby Mud Volcano. Geo-Marine Letters 19 (1-2), 57–67.

Given, R. K., Wilkinson, B., 1985. Kinetic control of morphology, composition, and mineralogy of abiotic sedimentary carbonates. Journal of Sedimentary Petrology 55 (1), 109–119.

Gladney, E., Roelandts, I., 1988. 1987 Compilation of elemental concentration data for USGS BHVO-1, MAG-1, QLO-1, RGM-1, SCo-1, SDC-1, SGR-1 and STM-1. Geostandards Newsletter-the Journal of Geostandards and Geoanalysis 12 (2), 253–362.

Goldsmith, J., Graf, D., Heard, H., 1961. Lattice constants of the calcium-magnesium carbonates. American Mineralogist 46, 453–457.

Gonneea, M. E., Paytan, A., 2006. Phase associations of barium in marine sediments. Marine Chemistry 100 (1-2), 124–135.

Gontharet, S., Pierre, C., Blanc-Valleron, M. M., Rouchy, J. M., Fouquet, Y., Bayon, G., Foucher, J. P., Woodside, J., Mascle, J., 2007. Nature and origin of diagenetic carbonate crusts and concretions from mud volcanoes and pockmarks of the Nile deep-sea fan (eastern Mediterranean Sea). Deep-Sea Research Part Ii-Topical Studies in Oceanography 54 (11-13), 1292–1311.

Gonzalez, A., Torne, M., Cordoba, D., Vidal, N., Matias, L. M., Diaz, J., 1996. Crustal thinning in the Southwestern Iberia Margin. Geophysical Research Letters 23 (18), 2477–2480.

Gracia, E., Danobeitia, J., Verges, J., Bartolome, R., Cordoba, D., 2003. Crustal architecture and tectonic evolution of the Gulf of Cadiz (SW Iberian margin) at the convergence of the Eurasian and African plates. Tectonics 22 (4).

Grasshoff, K., Kremling, K., Ehrhardt, M., et al., 1999. Methods of seawater analysis. 3rd ed. Wiley VCH, Weinheim, Germany.

Graue, K., 2000. Mud volcanoes in deepwater Nigeria. Marine and Petroleum Geology 17 (8), 959–974.

Greinert, J., Bohrmann, G., Elvert, M., 2002. Stromatolitic fabric of authigenic carbonate crusts: result of anaerobic methane oxidation at cold seeps in 4,850 m water depth. International Journal of Earth Sciences 91 (4), 698–711.

Greinert, J., Bohrmann, G., Suess, E., 2001. Gas Hydrate-Associated Carbonates and Methane-Venting at Hydrate Ridge: Classification, Distribution, and Origin of Authigenic Lithologies. In: Paull, C., Dillon, W. (Eds.), Natural gas hydrates: occurence, distribution and detection. Vol. 124 of AGU Geophysical Monograph. American Geophysical Union, Washington, DC, pp. 99–113.

Grossman, E. L., Ku, T. L., 1986. Oxygen and Carbon Isotope Fractionation in Biogenic Aragonite - Temperature Effects. Chemical Geology 59 (1), 59–74.

Gutscher, M.-A., Dominguez, S., Westbrook, G. K., Gente, P., Babonneau, N., Mulder, T., Gonthier, E., Bartolome, R., Luis, J., Rosas, F., Terrinha, P., 2009. Tectonic shortening and gravitational spreading in the Gulf of Cadiz accretionary wedge: Observations from multi-beam bathymetry and seismic profiling. Marine and Petroleum Geology 26 (5), 647–659.

Gutscher, M. A., Malod, J., Rehault, J. P., Contrucci, I., Klingelhoefer, F., Mendes-Victor, L., Spakman, W., 2002. Evidence for active subduction beneath Gibraltar. Geology 30 (12), 1071–1074.

Haeckel, M., Berndt, C., Liebetrau, V., Linke, P., Reitz, A., Schonfeld, J., Vanneste, H., 2007. Genesis and rates of fluid flow at the Mercator mud volcano, Gulf of Cadiz. Geochimica et Cosmochimica Acta 71 (15), A367–A367.

Haeckel, M., Suess, E., Wallmann, K., Rickert, D., 2004. Rising methane gas bubbles from massive hydrate layers at the seafloor. Geochimica et Cosmochimica Acta 68 (21), 4335–4345.

Haese, R. R., Hensen, C., Lange, G. J. d., 2006. Pore water geochemistry off eastern Meditrranean mud volcanoes: Implications for fluid transport and fluid origin. Marine Geology 225, 191–208.

Haese, R. R., Meile, C., Van Cappellen, P., De Lange, G. J., 2003. Carbon geochemistry of cold seeps: Methane fluxes and transformation in sediments from Kazan mud volcano, eastern Mediterranean Sea. Earth and Planetary Science Letters 212 (3-4), 361–375.

Hathorne, E. C., James, R. H., 2006. Temporal record of lithium in seawater: A tracer for silicate weathering? Earth and Planetary Science Letters 246 (3-4), 393–406.

Hayduk, W., Laudie, H., 1974. Prediction of Diffusion-Coefficients for Nonelectrolytes in Dilute Aqueous-Solutions. Aiche Journal 20 (3), 611–615.

Hayes, D. E., Pimm, A. C., Beckmann, J. P., Benson, W. E., Berger, W. H., Roth, P. H., Supko, P. R., Rad, U. v., 1972. Shipboard Site Reports: Site 135. Initial Reports of the Deep Sea Drilling Project 14, 15–48.

Hedberg, H. D., 1974. Relation of Methane Generation to Undercompacted Shales, Shale Diapirs, and Mud Volcanoes. American Association of Petroleum Geologists Bulletin 58 (4), 661–673.

Heeschen, K. U., Collier, R. W., Angelis, M. A. d., Suess, E., Rehder, G., Linke, P., Klinkhammer, G. P., 2005. Methane sources, distribution, and fluxes from cold vent sites at Hydrate Ridge, Cascadia Margin. Global Biogeochemical Cycles 19, GB2016.

Heeschen, K. U., Hohnberg, H. J., Haeckel, M., Abegg, F., Drews, M., Bohrmann, G., 2007. In situ hydrocarbon concentrations from pressurized cores in surface sediments, Northern Gulf of Mexico. Marine Chemistry 107 (4), 498–515.

Henry, P., LePichon, X., Lallemant, S., Lance, S., Martin, J. B., Foucher, J. P., FialaMedioni, A., Rostek, F., Guilhaumou, N., Pranal, V., Castrec, M., 1996. Fluid flow in and around a mud volcano field seaward of the Barbados accretionary wedge: Results from Manon cruise. Journal of Geophysical Research-Solid Earth 101 (B9), 20297–20323.

Hensen, C., Nuzzo, M., Hornibrook, E., Pinheiro, L. M., Bock, B., Magalhaes, V. H., Bruckmann, W., 2007. Sources of mud volcano fluids in the Gulf of Cadiz–indications for hydrothermal imprint. Geochimica et Cosmochimica Acta 71 (5), 1232–1248.

Hensen, C., Wallmann, K., 2005. Methane formation at Costa Rica continental margin-constraints for gas hydrate inventories and cross-décollement fluid flow. Earth and Planetary Science Letters 236, 41–60.

Hensen, C., Wallmann, K., Schmidt, M., Ranero, C. R., Suess, E., 2004. Fluid expulsion related to mud extrusion off Costa Rica - A window to the subducting slab. Geology 32 (3), 201–204.

Hernandez-Molina, F. J., Llave, E., Stow, D. A. V., Garcia, M., Somoza, L., Vazquez, J. T., Lobo, F. J., Maestro, A., Diaz del Rio, V., Leon, R., Medialdea, T., Gardner, J., 2006. The contourite depositional system of the Gulf of Cadiz: A sedimentary model related to the bottom current activity of the Mediterranean outflow water and its interaction with the continental margin. Deep Sea Research Part II: Topical Studies in Oceanography 53 (11-13), 1420–1463.

Hesse, R., 2003. Pore water anomalies of submarine gas-hydrate zones as tool to assess hydrate abundance and distribution in the subsurface - What have we learned in the past decade? Earth-Science Reviews 61 (1-2), 149–179.

Hesse, R., Harrison, W. E., 1981. Gas Hydrates (Clathrates) Causing Pore-Water Freshening and Oxygen Isotope Fractionation in Deep-Water Sedimentary Sections of Terrigenous Continental Margins. Earth and Planetary Science Letters 55 (3), 453–462.

Heyman, M., 1989. Tectonic and depositional history of the Moroccan continental margin. In: Tankard, A., Balkill, H. (Eds.), Extensional tectonics and stratigraphy of the north Atlantic margins. Vol. 46. American Association of Petroleum Geologists, Tulsa, pp. 323–340.

Higgins, G., Saunders, J., 1974. Mud volcanoes - Their nature and origin. Verhandlungen Naturforschenden Gesselschaft in Basel 84, 101–152.

Higgins, I. G., Quayle, J. R., 1970. Oxygenation of Methane by Methane-Utilizing Bacteria. Biochemical Journal 118 (2), P28.

Hinrichs, K. U., Hayes, J. M., Sylva, S. P., Brewer, P. G., DeLong, E. F., 1999. Methane-consuming archaebacteria in marine sediments. Nature 398 (6730), 802–805.

Hoehler, F. K., Borowski, C., Alperin, M., Rodriguez, N. M., Paull, C. K., 2000. Model, stable isotope, and radiotracer characterization of anaerobic methane oxidation in gas hydrate-bearing sediments of the Blake Ridge. Proceedings of the Ocean Drilling Program Scientific Results 164, 79–85.

Hornafius, J. S., Quigley, D., Luyendyk, B. P., 1999. The world's most spectacular marine hydrocarbon seeps (Coal Oil Point, Santa Barbara Channel, California): Quantification of emissions. Journal of Geophysical Research-Oceans 104 (C9), 20703–20711.

Horwitz, E. P., Chiarizia, R., Dietz, M. L., 1992. A Novel Strontium-Selective Extraction Chromatographic Resin. Solvent Extraction and Ion Exchange 10 (2), 313–336.

Hovland, M., Judd, A., 1988. Seabed pockmarks and seepages: impact on geology, biology and the marine environment. Graham and Trotman Ltd., London.

Hovland, M., Judd, A. G., Burke, R. A., 1993. The Global Flux of Methane from Shallow Submarine Sediments. Chemosphere 26 (1-4), 559–578.

Hovland, M., Talbot, M. R., Qvale, H., Olaussen, S., Aasberg, L., 1987. Methane-Related Carbonate Cements in Pockmarks of the North-Sea. Journal of sedimentary petrology 57 (5), 881–892.

Hower, J., Eslinger, E. V., Hower, M. E., Perry, E. A., 1976. Mechanism of Burial Metamorphism of Argillaceous Sediment .1. Mineralogical and Chemical Evidence. Geological Society of America Bulletin 87 (5), 725–737.

Hudson, J. D., Anderson, T. F., 1989. Ocean Temperatures and Isotopic Compositions through Time. Environments and Physiology of Fossil Organisms 80, 183–192 329.

Hughen, K. A., Baillie, M. G. L., Bard, E., Beck, J. W., Bertrand, C. J. H., Blackwell, P. G., Buck, C. E., Burr, G. S., Cutler, K. B., Damon, P. E., Edwards, R. L., Fairbanks, R. G., Friedrich, M., Guilderson, T. P., Kromer, B., McCormac, G., Manning, S., Ramsey, C. B., Reimer, P. J., Reimer, R. W., Remmele, S., Southon, J. R., Stuiver, M., Talamo, S., Taylor, F. W., van der Plicht, J., Weyhenmeyer, C. E., 2004. Marine04 marine radiocarbon age calibration, 0-26 cal kyr BP. Radiocarbon 46 (3), 1059–1086.

Huguen, C., 1998. Volcanisme boueux et déformation récente à actuelle au sein de la Ride Méditerranéenne, d'après les données de la campagne PRISMED II. Ph.D. thesis, Univ. Pierre et Marie Curie, Paris.

Huh, Y., Chan, L.-H., Zhang, L., Edmond, J. M., 1998. Lithium and its isotopes in major world rivers: implications for weathering and the oceanic budget. Geochimica et Cosmochimica Acta 62 (12), 2039–2051.

Hunt, J., 1996. Petroleum geochemistry and geology. 2nd ed. W.H. Freeman and Company.

Huseynov, D. A., Guliyev, I. S., 2004. Mud volcanic natural phenomena in the South Caspian Basin: geology, fluid dynamics and environmental impact. Environmental Geology 46 (8), 1012–1023.

Iorga, M. C., Lozier, M. S., 1999. Signatures of the Mediterranean outflow from a North Atlantic climatology 1. Salinity and density fields. Journal of Geophysical Research-Oceans 104 (C11), 25985–26009.

Iribarren, L., Vergés, J., Camurri, F., Fullea, J., Fernàndez, M., 2007. The structure of the Atlantic-Mediterranean transition zone from the Alboran Sea to the Horseshoe Abyssal Plain (Iberia-Africa plate boundary). Marine Geology 243 (1-4), 97–119.

Ivanenkov, V., Lyakhin, Y., 1978. Determination of total alkalinity in seawater. In: Bordovsky, O., Ivanenkov, V. (Eds.), Methods of Hydrochemical Investigations in the Ocean (in Russian). Nauka Publication House, Moscow, pp. 110–114.

Jakubov, A., AliZade, A., Zeinalov, M., 1971. Mud volcanoes of the Azerbaijan SSR, (in russian) Edition. Azerbaijan Academy of Sciences, Baku.

James, R. H., Allen, D. E., Seyfried, W. E., 2003. An experimental study of alteration of oceanic crust and terrigenous sediments at moderate temperatures (51 to 350 °C): insights as to chemical processes in near-shore ridge-flank hydrothermal systems. Geochimica et Cosmochimica Acta 67 (4), 681–691.

James, R. H., Palmer, M. R., 2000. Marine geochemical cycles of the alkali elements and boron: the role of sediments. Geochimica et Cosmochimica Acta 64 (18), 3111–3122.

Jenden, P., Kaplan, I., 1986. Comparison of microbial gases from the Middle American Trench and Scripps Submarine Canyon: Implications for the origin of natural gas. Applied Geochemistry 1, 631–646.

Jiménez-Munt, I., Fernàndez, M., Torne, M., Bird, P., 2001. The transition from linear to diffuse plate boundary in the Azores-Gilbraltar region: results from a thin-sheet model. Earth and Planetary Science Letters 192, 175–189.

Joye, S. B., Boetius, A., Orcutt, B. N., Montoya, J. P., Schulz, H. N., Erickson, M. J., Lugo, S. K., 2004. The anaerobic oxidation of methane and sulfate reduction in sediments from Gulf of Mexico cold seeps. Chemical Geology 205 (3-4), 219–238.

Judd, A., Croker, P., Tizzard, L., Voisey, C., 2007. Extensive methane-derived authigenic carbonates in the Irish Sea. Geo-Marine Letters 27 (2-4), 259–267.

Judd, A., Hovland, M., 2007. Seabed fluid flow: the impact of geology, biology and the marine environment. Cambridge University Press, Cambridge.

Kasten, S., Zabel, M., Heuer, V., Hensen, C., 2003. Processes and signals of nonsteady-state diagenesis in deep-sea sediments and their pore waters. In: Wefer, G., Mulitza, S., Ratmeyer, V. (Eds.), The South Atlantic in the Late Quaternary: Reconstruction of Material Budgets and Current Systems. Springer-Verlag, Berlin Heidelberg New York Tokyo, pp. 431–459.

Kastner, M., 1981. Authigenic silicates in deep-sea sediments: formation and diagenesis. In: Emiliani, C. (Ed.), The Sea: The oceanic lithosphere. Vol. 7. John Wiley & Sons, New York, pp. 915–980.

Kastner, M., Elderfield, H., Martin, J. B., 1991. Fluids in convergent margins: what do we know about their composition, origin, role in diagenesis and importance for oceanic chemical fluxes? Philosophical Transactions of the Royal Society of London, Series A: Physical Sciences and Engineering 335 (1638), 243–259.

Keir, R. S., Greinert, J., Rhein, M., Petrick, G., Sültenfuß, J., Fürhaupter, K., 2005. Methane and methane carbon isotope ratios in the Northeast Atlantic including the Mid-Atlantic Ridge (50 °N). Deep-Sea Research Part I Oceanographic Research Papers 52 (6), 1043–1070.

Kenyon, N., Ivanov, M., Akhmetzhanov, A., Akhmanov, G., 2000. Multidisciplinary study of geological processes on the North East Atlantic and western Mediterranean margins.Preliminary results of geological and geophysical investigations during the TTR-9 cruise of R/V "Professor Logachev", June-July, 1999.

Kenyon, N., Ivanov, M., Akhmetzhanov, A., Akhmanov, G., 2002. Geological processes in the Mediterranean and Black Seas and North East Atlantic: preliminary results of investigations during the TTR-11 cruise of RV "Professor Logache", July-September 2001.

Kenyon, N., Ivanov, M., Akhmetzhanov, A., Akhmanov, G., 2003. Interdisciplinary geoscience research on the north east Atlantic margin, Mediterranean Sea and Mid-Atlantic Ridge. Preliminary results of investigations during the TTR-12 cruise of RV "Professor Logachev", June-August 2002.

Kenyon, N., Ivanov, M., Akhmetzhanov, A., Kozlova, E., 2006. Interdisciplinary geoscience studies of the Gulf of Cadiz and Western Mediterranean basins, Preliminary results of investigations during the TTR-14 cruise, RV "Prof Logachev", Jul-Sep 2004.

Kholodov, V., 2002a. Mud Volcanoes: Distribution Regularities and Genesis (Communication 2. Geological–Geochemical Peculiarities and Formation Model). Lithology and Mineral Resources 37 (4), 339–358.

Kholodov, V. N., 2002b. Mud Volcanoes, Their Distribution Regularities and Genesis: Communication 1. Mud Volcanic Provinces and Morphology of Mud Volcanoes. Lithology and Mineral Resources 37 (3), 197–209.

Kim, S. T., ONeil, J. R., 1997. Equilibrium and nonequilibrium oxygen isotope effects in synthetic carbonates. Geochimica et Cosmochimica Acta 61 (16), 3461–3475.

Knittel, K., Boetius, A., 2009. Anaerobic Oxidation of Methane: Progress with an Unknown Process. Annual Review of Microbiology 63, 311–334.

Knittel, K., Losekann, T., Boetius, A., Kort, R., Amann, R., 2005. Diversity and distribution of methanotrophic archaea at cold seeps. Applied and Environmental Microbiology 71 (1), 467–479.

Kobayashi, K., Ashi, J., Boulegue, J., Cambray, H., Chamotrooke, N., Fujimoto, H., Furuta, T., Iiyama, J. T., Koizumi, T., Mitsuzawa, K., Monma, H., Murayama, M., Naka, J., Nakanishi, M., Ogawa, Y., Otsuka, K., Okada, M., Oshida, A., Shima, N., Soh, W., Takeuchi, A., Watanabe, M., Yamagata, T., 1992. Deep-Tow Survey in the

Kaiko-Nankai Cold Seepage Areas. Earth and Planetary Science Letters 109 (3-4), 347–354.

Kopf, A., 2003. Global methane emission through mud volcanoes and its past and present impact on the Earth's climate. International Journal of Earth Sciences 92, 806–816.

Kopf, A., Behrmann, J., 2000. Extrusion dynamics of mud volcanoes on the Mediterranean Ridge accretionary complex. In: Vendeville, B., Mart, Y., Vigneresse, J.-L. (Eds.), Salt, shale and igneous diapirs in and around Europe. Vol. 174. Geological Society, London, Special Publications, pp. 169–204.

Kopf, A., Deyhle, A., 2002. Back to the roots: boron geochemistry of mud volcanoes and its implications for mobilization depth and global B cycling. Chemical Geology 192 (3-4), 195–210.

Kopf, A. J., 2002. Significance of mud volcanism. Reviews of Geophysics 40 (2), 1005.

Kralj, D., Kontrec, J., Brecevic, L., Falini, G., Nothig-Laslo, V., 2004. Effect of inorganic anions on the morphology and structure of magnesium calcite. Chemistry-a European Journal 10 (7), 1647–1656.

Krumbein, W. E., 1974. Precipitation of Aragonite on Surface of Marine Bacteria. Naturwissenschaften 61 (4), 167–167.

Kugler, H., 1933. Contribution to the knowledge of sedimentary volcanism in Trinidad. Journal of the Institute of Petroleum Technology, Trinidad. 19, 743–760.

Kvenvolden, K. A., 1995. A review of the geochemistry of methane in natural gas hydrate. Organic Geochemistry 23 (11-12), 997–1008.

Kvenvolden, K. A., Barnard, L. A., 1983. Hydrates of Natural Gas in Continental Margins. In: Watkins, J., Drake, C. (Eds.), Studies in Continental Margin Geology. Vol. 34. Tulsa, Oklahoma U.S.A. American Association of Petroleum Geologists, pp. 631–640.

Kvenvolden, K. A., Kastner, M., 1990. Gas hydrates of the Peruvian outer continental margin. Proceedings of the Ocean Drilling Program Scientific Results 112, 517–526.

Lanaja, J., Querol, R., Navarro, A., 1987. Contribución de la exploración petrolífera al conocimiento de la geología de España. Instituto geológico y minero de España, 1–465.

Lance, S., Henry, P., Le Pichon, X., Lallemant, S., Chamley, H., Rostek, F., Faugeres, J. C., Gonthier, E., Olu, K., 1998. Submersible study of mud volcanoes seaward of the Barbados accretionary wedge: sedimentology, structure and rheology. Marine Geology 145 (3-4), 255–292.

Land, L., Moore, C., 1980. Lithification, micritization and syndepositional diagenesis of biolithites on the Jamaican island slope. Journal of Sedimentary Research 50/2, 357–370.

Le Pichon, X., Foucher, J. P., Boulegue, J., Henry, P., Lallemant, S., Benedetti, M., Avedik, F., Mariotti, A., 1990. Mud Volcano Field Seaward of the Barbados Accretionary Complex - a Submersible Survey. Journal of Geophysical Research-Solid Earth and Planets 95 (B6), 8931–8943.

Lemarchand, D., Gaillardet, J., Lewin, E., Allegre, C. J., 2000. The influence of rivers on marine boron isotopes and implications for reconstructing past ocean pH. Nature 408 (6815), 951–954.

Leon, R., Somoza, L., Gimenez-Moreno, C. J., Dabrio, C. J., Ercilla, G., Praeg, D., Diaz-del Rio, V., Gomez-Delgado, M., 2009. A predictive numerical model for potential mapping of the gas hydrate stability zone in the Gulf of Cadiz. Marine and Petroleum Geology 26 (8), 1564–1579.

León, R., Somoza, L., Medialdea, T., Gonzalez, F., Diaz-del Rio, V., Fernandez-Puga, M. C., Maestro, A., Mata, M. P., 2007. Sea-floor features related to hydrocarbon seeps in deepwater carbonate-mud mounds of the Gulf of Cadiz: from mud flows to carbonate precipitates. Geo-Marine Letters 27 (2-4), 237–247.

León, R., Somoza, L., Medialdea, T., Maestro, A., del Río, V. D., del Carmen Fernández-Puga, M., 2006. Classification of sea-floor features associated with methane seeps along the Gulf of Cádiz continental margin. Deep Sea Research Part II: Topical Studies in Oceanography 53, 1464–1481.

Levin, L. A., 2005. Ecology of cold seep sediments: Interactions of fauna with flow, chemistry and microbes. Oceanography and Marine Biology - an Annual Review, Vol. 43 43, 1–46.

Lichtschlag, A., Felden, J., Wenzhöfer, F., Schubotz, F., Ertefai, T. F., Boetius, A., de Beer, D., 2010. Methane and sulfide fluxes in permanent anoxia: In situ studies at the Dvurechenskii mud volcano (Sorokin Trough, Black Sea). Geochimica et Cosmochimica Acta 74 (17), 5002–5018.

Linke, P., Wallmann, K., Suess, E., Hensen, C., Rehder, G., 2005. In situ benthic fluxes from an intermittently active mud volcano at the Costa Rica convergent margin. Earth and Planetary Science Letters 235 (1-2), 79–95.

Lloyd, K. G., Lapham, L., Teske, A., 2006. Anaerobic methane-oxidizing community of ANME-1b archaea in hypersaline Gulf of Mexico sediments. Applied and Environmental Microbiology 72 (11), 7218–7230.

Loget, N., Van Den Driessche, J., 2006. On the origin of the Strait of Gibraltar. Sedimentary Geology 188-189, 341–356.

Lonsdale, P., 1979. A deep-sea hydrothermal site on a strike-slip fault. Nature 281 (5732), 531–534.

Luff, R., Haeckel, M., Wallmann, K., 2001. Robust and fast FORTRAN and MATLAB (R) libraries to calculate pH distributions in marine systems. Computers & Geosciences 27 (2), 157–169.

Luff, R., Wallmann, K., 2003. Fluid flow, methane fluxes, carbonate precipitation and biogeochemicalturnover in gas hydrate-bearing sediments at Hydrate Ridge, Cascadia Margin: Numerical modeling and mass balances. Geochimica et Cosmochimica Acta 67 (18), 3403–3421.

Lumsden, D. N., 1979. Discrepancy between Thin-Section and X-Ray Estimates of Dolomite in Limestone. Journal of sedimentary petrology 49 (2), 429–436.

Luther Iii, G. W., Giblin, A., Howarth, R. W., Ryans, R. A., 1982. Pyrite and oxidized iron mineral phases formed from pyrite oxidation in salt marsh and estuarine sediments. Geochimica et Cosmochimica Acta 46 (12), 2665–2669.

Lykousis, V., Alexandri, S., Woodside, J., de Lange, G., Dahlmann, A., Perissoratis, C., Heeschen, K., Ioakim, C., Sakellariou, D., Nomikou, P., Rousakis, G., Casas, D., Ballas, D., Ercilla, G., 2009. Mud volcanoes and gas hydrates in the Anaximander mountains (Eastern Mediterranean Sea). Marine and Petroleum Geology 26 (6), 854–872.

Macdonald, I. R., Guinasso, N. L., Sassen, R., Brooks, J. M., Lee, L., Scott, K. T., 1994. Gas Hydrate That Breaches the Sea-Floor on the Continental-Slope of the Gulf-of-Mexico. Geology 22 (8), 699–702.

MacDonald, I. R., Peccini, M. B., 2009. Distinct activity phases during the recent geologic history of a Gulf of Mexico mud volcano. Marine and Petroleum Geology 26 (9), 1824–1830.

Mackin, J. E., 1986. The Free-Solution Diffusion-Coefficient of Boron - Influence of Dissolved Organic-Matter. Marine Chemistry 20 (2), 131–140.

Madelain, F., 1970. Influence de la topographie du fond sur l'ecoulement méditerranéen entre le Detroit de Gibraltar et le Cap Saint-Vincent. Cahiers Océanographiques 22, 43–61.

Maekawa, T., 2004. Experimental study on isotopic fractionation in water during gas hydrate formation. Geochemical Journal 38 (2), 129–138.

Maestro, A., Somoza, L., Medialdea, T., Talbot, C. J., Lowrie, A., Vázquez, J. T., Díaz-del Río, V., 2003. Large-scale slope failure involving Triassic and Middle Miocene salt and shale in the Gulf of Cádiz (Atlantic Iberian Margin). Terra Nova 15, 380–391.

Magalhães, V. H. d. S., 2007. Authigenic carbonates and fluid escape structures in the Gulf of Cadiz. Ph.D. thesis, University of Aveiro.

Maldonado, A., Nelson, C. H., 1999. Interaction of tectonic and depositional processes that control the evolution of the Iberian Gulf of Cadiz margin. Marine Geology 155, 217–242.

Maldonado, A., Somoza, L., Pallarés, L., 1999. The Betic orogen and the Iberian-African boundary in the Gulf of Cadiz: geological evolution (central North Atlantic). Marine Geology 155, 9–43.

Malod, J. A., Mauffret, A., 1990. Iberian Plate Motions during the Mesozoic. Tectonophysics 184 (3-4), 261–278.

Martin, J. B., Kastner, M., Elderfield, H., 1991. Lithium: Sources in pore fluids of Peru slope sediments and implications for oceanic fluxes. Marine Geology 102, 281–292.

Martin, J. B., Kastner, M., Henry, P., LePichon, X., Lallement, S., 1996. Chemical and isotopic evidence for sources of fluids in a mud volcano field seaward of the Barbados accretionary wedge. Journal of Geophysical Research-Solid Earth 101 (B9), 20325–20345.

Matsumoto, R., 1990. Vuggy Carbonate Crust Formed by Hydrocarbon Seepage on the Continental-Shelf of Baffin Island, Northeast Canada. Geochemical Journal 24 (3), 143–158.

Mau, S., Sahling, H., Rehder, G., Suess, E., Linke, P., Soeding, E., 2006. Estimates of methane output from mud extrusions at the erosive convergent margin off Costa Rica. Marine Geology 225 (1-4), 129–144.

Mazurenko, L., Soloviev, V., Beienkaya, I., Ivanov, M., Pinheiro, L., 2002. Mud volcano gas hydrates in the Gulf of Cadiz. Terra Nova 14, 321–329.

Mazurenko, L., Soloviev, V., Gardner, J., Ivanov, M., 2003. Gas hydrates in the Ginsburg and Yuma mud volcano sediments (Moroccan Margin): results of chemical and isotopic studies of pore water. Marine geology 195, 201–210.

Mazzini, A., 2009. Mud volcanism: Processes and implications. Marine and Petroleum Geology 26 (9), 1677–1680.

Mazzini, A., Ivanov, M. K., Parnell, J., Stadnitskaia, A., Cronin, B. T., Poludetkina, E., Mazurenko, L., van Weering, T. C. E., 2004. Methane-related authigenic carbonates from the Black Sea: geochemical characterisation and relation to seeping fluids. Marine Geology 212 (1-4), 153–181.

Mazzini, A., Svensen, H., Planke, S., Guliyev, I., Akhmanov, G. G., Fallik, T., Banks, D., 2009. When mud volcanoes sleep: Insight from seep geochemistry at the Dashgil mud volcano, Azerbaijan. Marine and Petroleum Geology 26 (9), 1704–1715.

McGinnis, D. F., Greinert, J., Artemov, Y., Beaubien, S. E., Wuest, A., 2006. Fate of rising methane bubbles in stratified waters: How much methane reaches the atmosphere? Journal of Geophysical Research-Oceans 111 (C9), C09007.

McManus, J., Berelson, W. M., Klinkhammer, G. P., Johnson, K. S., Coale, K. H., Anderson, R. F., Kumar, N., Burdige, D. J., Hammond, D. E., Brumsack, H. J., McCorkle, D. C., Rushdi, A., 1998. Geochemistry of barium in marine sediments: Implications for its use as a paleoproxy. Geochimica et Cosmochimica Acta 62 (21-22), 3453–3473, geochim. Cosmochim. Acta.

Medialdea, T., Somoza, L., Pinheiro, L. M., Fernandez-Puga, M. C., Vazquez, J. T., Leon, R., Ivanov, M. K., Magalhaes, V., Diaz-del Rio, V., Vegas, R., 2009. Tectonics and mud volcano development in the Gulf of Cadiz. Marine Geology 261 (1-4), 48–63.

Medialdea, T., Vegas, R., Somoza, L., Vázquez, J., Maldonado, A., Díaz-del Río, V., Maestro, A., Córdoba, D., Fernández-Puga, M., 2004. Structure and evolution of the "Olistostrome" complex of the Gibraltar Arc in the Gulf of Cádiz (eastern Central Atlantic): evidence from two long seismic cross-sections. Marine Geology 209, 173–198.

Meile, C., Berg, P., Van Cappellen, P., Tuncay, K., 2005. Solute-specific pore water irrigation: Implications for chemical cycling in early diagenesis. Journal of Marine Research 63 (3), 601–621.

Merinero, R., Lunar, R., Martínez-Frías, J., Somoza, L., Díaz-del Río, V., 2008. Iron oxyhydroxide and sulphide mineralization in hydrocarbon seep-related carbonate submarine chimneys, Gulf of Cadiz (SW Iberian Peninsula). Marine and Petroleum Geology 25 (8), 706–713.

Meysman, F. J. R., Boudreau, B. P., Middelburg, J. J., 2005. Modeling reactive transport in sediments subject to bioturbation and compaction. Geochimica et Cosmochimica Acta 69, 3601–3617.

Middelburg, J. J., 1989. A Simple Rate Model for Organic-Matter Decomposition in Marine-Sediments. Geochimica et Cosmochimica Acta 53 (7), 1577–1581.

Milkov, A. V., 2000. Worldwide distribution of submarine mud volcanoes and associated gas hydrates. Marine Geology 167, 29–42.

Milkov, A. V., Claypool, G. E., Lee, Y. J., Sassen, R., 2005. Gas hydrate systems at Hydrate Ridge offshore Oregon inferred from molecular and isotopic properties of hydrate-bound and void gases. Geochimica Et Cosmochimica Acta 69 (4), 1007–1026.

Milkov, A. V., Dickens, G. R., Claypool, G. E., Lee, Y.-J., Borowski, W. S., Torres, M. E., Xu, W., Tomaru, H., Tréhu, A. M., Schultheiss, P., 2004a. Co-existence of gas hydrate, free gas, and brine within the regional gas hydrate stability zone at Hydrate Ridge (Oregon margin): evidence from prolonged degassing of a pressurized core. Earth and Planetary Science Letters 222 (3-4), 829–843.

Milkov, A. V., Sassen, R., Apanasovich, T. V., Dadashev, F. G., 2003. Global gas flux from mud volcanoes: A significant source of fossil methane in the atmosphere and the ocean. Geophysical Research Letters 30 (2), 1037.

Milkov, A. V., Vogt, P. R., Crane, K., Lein, A. Y., Sassen, R., Cherkashev, G. A., 2004b. Geological, geochemical, and microbial processes at the hydrate-bearing Håkon Mosby mud volcano: a review. Chemical Geology 205 (3-4), 347–366.

Moore, G. W., Gieskes, J. M., 1980. Interaction between sediment and interstitial water near the Japan Trench Leg 57. Initial Reports of the Deep Sea Drilling Project 56/57, 1269–1275.

Moore, J. C., Vrolijk, P., 1992. Fluids in Accretionary Prisms. Reviews of Geophysics 30 (2), 113–135.

Morse, J. W., Arvidson, R. S., Luttge, A., 2007. Calcium carbonate formation and dissolution. Chemical Reviews 107 (2), 342–381.

Morse, J. W., Wang, Q. W., Tsio, M. Y., 1997. Influences of temperature and Mg:Ca ratio on $CaCO_3$ precipitates from seawater. Geology 25 (1), 85–87.

Moses, C. O., Nordstrom, D. K., Herman, J. S., Mills, A. L., 1987. Aqueous Pyrite Oxidation by Dissolved-Oxygen and by Ferric Iron. Geochimica et Cosmochimica Acta 51 (6), 1561–1571.

Mudroch, A., Azcue, J. M., 1995. Manual of aquatic sediment sampling. CRC Press, Florida.

Naehr, T. H., Birgel, D., Bohrmann, G., MacDonald, I. R., Kasten, S., 2009. Biogeochemical controls on authigenic carbonate formation at the Chapopote "asphalt volcano", Bay of Campeche. Chemical Geology 266 (3-4), 390–402.

Naehr, T. H., Rodriguez, N., Bohrmann, G., Paull, C., Botz, R., 2000a. Methane derived authigenic carbonates associated with gas hydrate decomposition and fluid venting above the Blake Ridge Diapir. Proceedings of the Ocean Drilling Program Scientific Results 164, 285–300.

Naehr, T. H., Stakes, D. S., Moore, W. S., 2000b. Mass wasting, ephemeral fluid flow, and barite deposition on the California continental margin. Geology 28 (4), 315–318.

Nauhaus, K., Boetius, A., Kruger, M., Widdel, F., 2002. In vitro demonstration of anaerobic oxidation of methane coupled to sulphate reduction in sediment from a marine gas hydrate area. Environmental Microbiology 4 (5), 296–305.

Niemann, H., Duarte, J., Hensen, C., Omoregie, E., Magalhaes, V., Elvert, M., Pinheiro, L., Kopf, A., Boetius, A., 2006a. Microbial methan turnover at mud volcanoes of the Gulf of Cadiz. Geochimica et Cosmochimica Acta 70, 5336–5355.

Niemann, H., Losekann, T., de Beer, D., Elvert, M., Nadalig, T., Knittel, K., Amann, R., Sauter, E. J., Schluter, M., Klages, M., Foucher, J. P., Boetius, A., 2006b. Novel microbial communities of the Haakon Mosby mud volcano and their role as a methane sink. Nature 443 (7113), 854–858.

Nuzzo, M., Hornibrook, E. R. C., Gill, F., Hensen, C., Pancost, R. D., Haeckel, M., Reitz, A., Scholz, F., Magalhães, V. H., Brückmann, W., Pinheiro, L. M., 2009. Origin of light volatile hydrocarbon gases in mud volcano fluids, Gulf of Cadiz – Evidence for multiple sources and transport mechanisms in active sedimentary wedges. Chemical Geology 266 (3-4), 350–363.

Nuzzo, M., Hornibrook, E. R. C., Hensen, C., Parkes, R. J., Cragg, B. A., Rinna, J., von Deimling, J. S., Sommer, S., Magalhaes, V. H., Reitz, A., Bruckmann, W., Pinheiro, L. M., 2008. Shallow microbial recycling of deep-sourced carbon in Gulf of Cadiz mud volcanoes. Geomicrobiology Journal 25 (6), 283–295.

Oehler, D. Z., Allen, C. C., 2010. Evidence for pervasive mud volcanism in Acidalia Planitia, Mars. Icarus 208 (2), 636–657.

Olu, K., Sibuet, M., Harmegnies, F., Foucher, J. P., Fiala-Medioni, A., 1996. Spatial distribution of diverse cold seep communities living on various diapiric structures of the southern Barbados prism. Progress in Oceanography 38 (4), 347–376.

Omoregie, E. O., Niemann, H., Mastalerz, V., de Lange, G. J., Stadnitskaia, A., Mascle, J., Foucher, J.-P., Boetius, A., 2009. Microbial methane oxidation and sulfate reduction at cold seeps of the deep Eastern Mediterranean Sea. Marine Geology 261 (1-4), 114–127.

Orphan, V. J., House, C. H., Hinrichs, K. U., McKeegan, K. D., DeLong, E. F., 2001. Methane-consuming archaea revealed by directly coupled isotopic and phylogenetic analysis. Science 293 (5529), 484–487.

Ovsyannikov, D., Yu, A., Sadekov, Kozlova, E., 2003. Rock fragments from mud volcanic deposits of the Gulf of Cadiz: an insight into the Eocene-Pliocene sedimentary succession of the basin. Marine geology 195, 211–221.

Park, A., Dewers, T., Ortoleva, P., 1990. Cellular and Oscillatory Self-Induced Methane Migration. Earth-Science Reviews 29 (1-4), 249–265.

Park, H., Schlesinger, W. H., 2002. Global biogeochemical cycle of boron. Global Biogeochemical Cycles 16 (4), 1072.

Paull, C., 1997. Drilling for gas hydrates: offshore drilling program Leg 164. In: Proceeding of the Offshore Technology Conference. Houston, TX.

Paull, C., Dillon, W., 2001. Natural gas hydrates: occurrence, distribution and detection. No. 124 in AGU Geophysical Monograph. American Geophysical Union, Washington, DC.

Paull, C., Ussler, W., Borowski, W., 1994. Sources of biogenic methane to form marine gas hydrates: in situ production or upward migration? In: Natural Gas Hydrates. Vol. 715 of Annals of the New York Academy of Science. New York, pp. 392–409.

Paull, C. K., Neumann, A. C., 1987. Continental-Margin Brine Seeps - Their Geological Consequences. Geology 15 (6), 545–548.

Paytan, A., Kastner, M., Martin, E. E., Macdougall, J. D., Herbert, T., 1993. Marine Barite as a Monitor of Seawater Strontium Isotope Composition. Nature 366 (6454), 445–449.

Pearson, P. N., Palmer, M. R., 2000. Atmospheric carbon dioxide concentrations over the past 60 million years. Nature 406 (6797), 695–699.

Peckmann, J., Goedert, J. L., Thiel, V., Michaelis, W., Reitner, J., 2002. A comprehensive approach to the study of methane-seep deposits from the Lincoln Creek Formation, western Washington State, USA. Sedimentology 49 (4), 855–873.

Peckmann, J., Paul, J., Thiel, V., 1999. Bacterially mediated formation of diagenetic aragonite and native sulfur in Zechstein carbonates (Upper Permian, Central Germany). Sedimentary Geology 126 (1-4), 205–222.

Peckmann, J., Reimer, A., Luth, U., Luth, C., Hansen, B. T., Heinicke, C., Hoefs, J., Reitner, J., 2001. Methane-derived carbonates and authigenic pyrite from the northwestern Black Sea. Marine Geology 177 (1-2), 129–150.

Pelegrí, J. L., Marrero-Díaz, A., Ratsimandresy, A., Antoranz, A., Huguen, C., Gordo, C., Grisolía, D., Hernández-Guerra, A., Láiz, I., Martínez, A., Parrilla, G., Pérez-Rodríguez, P., Rodríguez-Santana, A., Sangrà, P., 2005. Hydrographic cruises off northwest Africa: the Canary Current and the Cape Ghir region. Journal of Marine Systems 54 (1-4), 39–63.

Perry, E. A., Hower, J., 1972. Late-Stage Dehydration in Deeply Buried Pelitic Sediments. American Association of Petroleum Geologists Bulletin 56 (10), 2013–2021.

Pierre, C., Fouquet, Y., 2007. Authigenic carbonates from methane seeps of the Congo deep-sea fan. Geo-Marine Letters 27 (2-4), 249–257.

Pinheiro, L., Ivanov, M., Sautkin, A., Akhmanov, G., Magalhães, V., Volkonskaya, A., Monteiro, J., Somoza, L., Gardner, J., Hamouni, N., Cunha, M., 2003. Mud volcanism in the Gulf of Cadiz: results from the TTR-10 cruise. Marine geology 195, 131–151.

Potts, P., 1987. A Handbook of silicate rock analysis. Blackie & Son, Glasgow.

Pruysers, P. A., Delange, G. J., Middelburg, J. J., Hydes, D. J., 1993. The Diagenetic Formation of Metal-Rich Layers in Sapropel-Containing Sediments in the Eastern Mediterranean. Geochimica et Cosmochimica Acta 57 (3), 527–536.

Reeburgh, W. S., 1976. Methane Consumption in Cariaco Trench Waters and Sediments. Earth and Planetary Science Letters 28 (3), 337–344.

Reeburgh, W. S., 2007. Oceanic methane biogeochemistry. Chemical Reviews 107 (2), 486–513.

Reed, D. L., Silver, E. A., Tagudin, J. E., Shipley, T. H., Vrolijk, P., 1990. Relations between mud volcanoes, thrust deformation, slope sedimentation, and gas hydrate, offshore north Panama. Marine and Petroleum Geology 7 (1), 44–54.

Rickard, D., Schoonen, M. A. A., Luther, G. W., 1995. Chemistry of iron sulfides in sedimentary environments. Geochemical Transformations of Sedimentary Sulfur 612, 168–193.

Ritger, S., Carson, B., Suess, E., 1987. Methane-Derived Authigenic Carbonates Formed by Subduction Induced Pore-Water Expulsion Along the Oregon Washington Margin. Geological Society of America Bulletin 98 (2), 147–156.

Roberts, H., Aharon, P., Walsh, M., 1993. Cold-seep carbonates of the Louisiana continental slope-to-basin floor. In: Rezak, R., Lavoie, D. (Eds.), Carbonate Microfabrics. Springer, Berlin, pp. 95–104.

Roberts, H. H., Aharon, P., 1994. Hydrocarbon-Derived Carbonate Buildups of the Northern Gulf-of-Mexico Continental-Slope - a Review of Submersible Investigations. Geo-Marine Letters 14 (2-3), 135–148.

Roberts, H. H., Carney, R. S., 1997. Evidence of episodic fluid, gas, and sediment venting on the northern Gulf of Mexico continental slope. Economic Geology and the Bulletin of the Society of Economic Geologists 92 (7-8), 863–879.

Rodriguez, N., Paull, C., Borowski, W., 2000. Zonation of authigenic carbonates within gas hydrate-bearing sedimentary sections on the Blake Ridge: offshore southeastern North America. Proceedings of the Ocean Drilling Program Scientific Results 164, 301–311.

Rosas, F. M., Duarte, J. C., Terrinha, P., Valadares, V., Matias, L., 2009. Morphotectonic characterization of major bathymetric lineaments in Gulf of Cadiz (Africa-Iberia plate boundary): Insights from analogue modelling experiments. Marine Geology 261 (1-4), 33–47.

Rutten, A., de Lange, G. J., 2002. A novel selective extraction of barite, and its application to eastern Mediterranean sediments. Earth and Planetary Science Letters 198 (1-2), 11–24.

Sahling, H., Bohrmann, G., Artemov, Y. G., Bahr, A., Brüning, M., Klapp, S. A., Klaucke, I., Kozlova, E., Nikolovska, A., Pape, T., Reitz, A., Wallmann, K., 2009. Vodyanitskii mud volcano, Sorokin trough, Black Sea: Geological characterization and quantification of gas bubble streams. Marine and Petroleum Geology 26 (9), 1799–1811.

Sartori, R., Torelli, L., Zitellini, N., Peis, D., Lodolo, E., 1994. Eastern Segment of the Azores-Gibraltar Line (Central-Eastern Atlantic) - an Oceanic Plate Boundary with Diffuse Compressional Deformation. Geology 22 (6), 555.

Sauter, E. J., Muyakshin, S. I., Charlou, J. L., Schluter, M., Boetius, A., Jerosch, K., Damm, E., Foucher, J. P., Klages, M., 2006. Methane discharge from a deep-sea submarine mud volcano into the upper water column by gas hydrate-coated methane bubbles. Earth and Planetary Science Letters 243 (3-4), 354–365.

Sautkin, A., Talukder, A. R., Comas, M. C., Soto, J. I., Alekseev, A., 2003. Mud volcanoes in the Alboran Sea: evidence from micropaleontological and geophysical data. Marine Geology 195 (1-4), 237–261.

Savard, M. M., Beauchamp, B., Veizer, J., 1996. Significance of aragonite cements around Cretaceous marine methane seeps. Journal of Sedimentary Research 66 (3), 430–438.

Savin, S. M., Epstein, S., 1970. Oxygen and Hydrogen Isotope Geochemistry of Clay Minerals. Geochimica Et Cosmochimica Acta 34 (1), 25.

Savin, S. M., Hsieh, J. C. C., 1998. The hydrogen and oxygen isotope geochemistry of pedogenic clay minerals: principles and theoretical background. Geoderma 82 (1-3), 227–253.

Schmidt, M., Hensen, C., Morz, T., Muller, C., Grevemeyer, I., Wallmann, K., Mau, S., Kaul, N., 2005. Methane hydrate accumulation in "Mound 11" mud volcano, Costa Rica forearc. Marine Geology 216 (1-2), 83–100.

Schoell, M., 1980. The Hydrogen and Carbon Isotopic Composition of Methane from Natural Gases of Various Origins. Geochimica Et Cosmochimica Acta 44 (5), 649–661.

Schoell, M., 1988. Multiple Origins of Methane in the Earth. Chemical Geology 71 (1-3), 1–10.

Scholz, F., Hensen, C., Lu, Z. L., Fehn, U., 2010. Controls on the $^{129}I/I$ ratio of deep-seated marine interstitial fluids: 'Old' organic versus fissiogenic 129-iodine. Earth and Planetary Science Letters 294 (1-2), 27–36.

Scholz, F., Hensen, C., Reitz, A., Romer, R. L., Liebetrau, V., Meixner, A., Weise, S. M., Haeckel, M., 2009. Isotopic evidence ($^{87}Sr/^{86}Sr$, δ^7Li) for alteration of the oceanic crust at deep-rooted mud volcanoes in the Gulf of Cadiz, NE Atlantic Ocean. Geochimica et Cosmochimica Acta 73 (18), 5444–5459.

Schwarcz, H., Agyei, E., McMullen, C., 1969. Boron isotopic fractionation during clay adsorption from sea-water. Earth and Planetary Science Letters 6, 1–5.

Seeberg-Elverfeldt, J., Schluter, M., Feseker, T., Kolling, M., 2005. Rhizon sampling of porewaters near the sediment-water interface of aquatic systems. Limnology and Oceanography-Methods 3, 361–371.

Seyfried, W. E., Janecky, D. R., Mottl, M. J., 1984. Alteration of the Oceanic-Crust - Implications for Geochemical Cycles of Lithium and Boron. Geochimica Et Cosmochimica Acta 48 (3), 557–569.

Shih, T., 1967. A survey of the active mud volcanoes in Taiwan and a study of their types and the character of the mud. Petroleum Geology of Taiwan 5, 259–311.

Sibuet, M., Olu, K., 1998. Biogeography, biodiversity and fluid dependence of deep-sea cold-seep communities at active and passive margins. Deep-Sea Research Part II-Topical Studies in Oceanography 45 (1-3), 517–567.

Skinner, J. A., Tanaka, K. L., 2007. Evidence for and implications of sedimentary diapirism and mud volcanism in the southern Utopia highland-lowland boundary plain, Mars. Icarus 186 (1), 41–59.

Sloan, E., 1998. Clathrate hydrates of natural gases. 2nd ed. Vol. 73 of Chemical Industries. Marcel Dekker Inc, New York, NY.

Snyder, G. T., Dickens, G. R., Castellini, D. G., 2007a. Labile barite contents and dissolved barium concentrations on Blake Ridge: New perspectives on barium cycling above gas hydrate systems. Journal of Geochemical Exploration 95 (1-3), 48–65.

Snyder, G. T., Hiruta, A., Matsumoto, R., Dickens, G. R., Tomaru, H., Takeuchi, R., Komatsubara, J., Ishida, Y., Yu, H., 2007b. Pore water profiles and authigenic mineralization in shallow marine sediments above the methane-charged system on Umitaka Spur, Japan Sea. Deep Sea Research Part II: Topical Studies in Oceanography 54 (11-13), 1216–1239.

Solomon, E. A., Kastner, M., Jannasch, H., Robertson, G., Weinstein, Y., 2008. Dynamic fluid flow and chemical fluxes associated with a seafloor gas hydrate deposit on the northern Gulf of Mexico slope. Earth and Planetary Science Letters 270 (1-2), 95–105.

Sommer, S., Linke, P., Pfannkuche, O., Schleicher, T., von Deimling, J. S., Reitz, A., Haeckel, M., Flogel, S., Hensen, C., 2009. Seabed methane emissions and the habitat of frenulate tubeworms on the Captain Arutyunov mud volcano (Gulf of Cadiz). Marine Ecology Progress Series 382, 69–86.

Somoza, L., Díaz-del Río, V., Hernandez-Molina, F., León, R., Lobato, A., Alveirinho, J., Rodero, J., team, T., 2000. New discovery of a mud-volcano field related to gas venting in the Gulf of Cadiz: Imagery of multibeam data and ultra-high resolution data. In: Final Proceedings 3rd International Symposium Iberian Atlantic continental Margin. Faro, Portugal, pp. 397–398.

Somoza, L., Díaz-del Río, V., León, R., Ivanov, M., Fernández-Puga, M., Gardner, J., Hernández-Molina, F., Pinheiro, L., Rodero, J., Lobato, A., Maestro, A., Vázquez, J., Medialdea, T., Fernández-Salas, L., 2003. Seabed morphology and hydrocarbon seepage in the Gulf of Cádiz mud volcano area: Acoustic imagery, multibeam and ultra-high resolution seismic data. Marine geology 195, 153–176.

Somoza, L., Diaz-Del-Rio, V., Vaszquez, J., Pinheiro, L. M., Hernandez-Molina, F. J., 2002. Numerous methane gas-related sea floor structures indentified in Gulf of Cadiz. EOS 83, 541–547.

Spinelli, G. A., Underwood, M. B., 2004. Character of sediments entering the Costa Rica subduction zone: Implications for partitioning of water along the plate interface. Island Arc 13 (3), 432–451.

Spivack, A., Palmer, M., Edmond, J., 1987. The sedimentary cycle of the boron isotopes. Geochimica et Cosmochimica Acta 51, 1939–1949.

Spivack, A., You, C., Smith, J., 1993. Foraminiferal boron isotope ratios as a proxy for surface ocean pH over the past 21 Myr. Nature 363, 149–151.

Srivastava, S. P., Roest, W. R., Kovacs, L. C., Oakey, G., Levesque, S., Verhoef, J., Macnab, R., 1990. Motion of Iberia since the Late Jurassic - Results from Detailed Aeromagnetic Measurements in the Newfoundland Basin. Tectonophysics 184 (3-4), 229–260.

Srodon, J., 1999. Nature of mixed-layer clays and mechanisms of their formation and alteration. Annual Review of Earth and Planetary Sciences 27, 19–53.

Stadnitskaia, A., Ivanov, M. K., Blinova, V., Kreulen, R., Weering, T. C. E. v., 2006. Molecular and carbon isotopic variability of hydrocarbon gases from mud volcanoes in the Gulf of Cadiz, NE Atlantic. Marine and Petroleum Geology 23, 281–296.

Stadnitskaia, A., Ivanov, M. K., Sinninghe Damsté, J. S., 2008. Application of lipid biomarkers to detect sources of organic matter in mud volcano deposits and post-eruptional methanotrophic processes in the Gulf of Cadiz, NE Atlantic. Marine Geology 255 (1-2), 1–14.

Stoffyn-Egli, P., Mackenzie, F. T., 1984. Mass balance of dissolved lithium in the oceans. Geochimica et Cosmochimica Acta 48 (4), 859–872.

Stuiver, M., Reimer, P. J., 1993. Extended ^{14}C Data-Base and Revised Calib 3.0 ^{14}C Age Calibration Program. Radiocarbon 35 (1), 215–230.

Suess, E., Bohrmann, G., von Huene, R., Linke, P., Wallmann, K., Lammers, S., Sahling, H., Winckler, G., Lutz, R. A., Orange, D., 1998. Fluid venting in the eastern Aleutian subduction zone. Journal of Geophysical Research-Solid Earth 103 (B2), 2597–2614.

Suess, E., Whiticar, M. J., 1989. Methane-Derived CO2 in Pore Fluids Expelled from the Oregon Subduction Zone. Palaeogeography Palaeoclimatology Palaeoecology 71 (1-2), 119–136.

Teichert, B. M. A., Torres, M. E., Bohrmann, G., Eisenhauer, A., 2005. Fluid sources, fluid pathways and diagenetic reactions across an accretionary prism revealed by Sr and B geochemistry. Earth and Planetary Science Letters 239 (1-2), 106–121.

Terzi, C., Aharon, P., Lucchi, F. R., Vai, G. B., 1994. Petrography and Stable-Isotope Aspects of Cold Vent Activity Imprinted on Miocene Age Calcari-a-Lucina from Tuscan and Romagna Apennines, Italy. Geo-Marine Letters 14 (2-3), 177–184.

Thiebot, E., Gutscher, M. A., 2006. The Gibraltar Arc seismogenic zone (part 1): Constraints on a shallow east dipping fault plane source for the 1755 Lisbon earthquake provided by seismic data, gravity and thermal modeling. Tectonophysics 426 (1-2), 135–152.

Tishchenko, P., Hensen, C., Wallmann, K., Wong, C. S., 2005. Calculation of the stability and solubility of methane hydrate in seawater. Chemical Geology 219 (1-4), 37–52.

Torelli, L., Sartorit, R., Zitellini, N., 1996. The giant chaotic body in the Atlantic Ocean off Gibraltar: new results from a deep seismic reflection survey. Marine and Petroleum Geology 14 (2), 125–138.

Torres, M., McManus, J., Hammond, D., Angelis, M. d., Heeschen, K., Colbert, S., Tryon, M., Brown, K., Suess, E., 2002. Fluid and chemical fluxes in and out of sediments hosting methane hydrate deposits on Hydrate Ridge, OR, I: Hydrological provinces. Earth and Planetary Science Letters 201, 525–540.

Torres, M. E., Bohrmann, G., Dube, T. E., Poole, F. G., 2003. Formation of modern and Paleozoic stratiform barite at cold methane seeps on continental margins. Geology 31 (10), 897–900.

Torres, M. E., Bohrmann, G., Suess, E., 1996a. Authigenic barites and fluxes of barium associated with fluid seeps in the Peru subduction zone. Earth and Planetary Science Letters 144 (3-4), 469–481.

Torres, M. E., Brumsack, H. J., Bohrmann, G., Emeis, K. C., 1996b. Barite fronts in continental margin sediments: A new look at barium remobilization in the zone of sulfate reduction and formation of heavy barites in diagenetic fronts. Chemical Geology 127 (1-3), 125–139.

Tortella, D., Torne, M., PerezEstaun, A., 1997. Geodynamic evolution of the eastern segment of the Azores-Gibraltar zone: The Gorringe Bank and the Gulf of Cadiz region. Marine Geophysical Researches 19 (3), 211–230.

Treude, T., Boetius, A., Knittel, K., Wallmann, K., Jorgensen, B. B., 2003. Anaerobic oxidation of methane above gas hydrates at Hydrate Ridge, NE Pacific Ocean. Marine Ecology Progress Series 264, 1–14.

Trotsyuk, V., Avilov, V., 1988. Disseminated flux of hydrocarbon gases from the sea bottom and a method of measuring it. Transactions (Doklady) USSR Academy of Sciences, Earth Sciences Section 291, 281–220.

Tryon, M. D., Brown, K. M., Torres, M. E., 2002. Fluid and chemical flux in and out of sediments hosting methane hydrate deposits on Hydrate Ridge, OR, II: Hydrological processes. Earth and Planetary Science Letters 201 (3-4), 541–557.

Ussler, W., Paull, C. K., 1995. Effects of Ion-Exclusion and Isotopic Fractionation on Pore-Water Geochemistry during Gas Hydrate Formation and Decomposition. Geo-Marine Letters 15 (1), 37–44.

Van Cappellen, P., Gaillard, J.-F., Rabouille, C., 1993. Biogeochemical transformations in sediments: kinetic models of early diagenesis. In: Wollast, R., Mackenzie, F., Chou, L. (Eds.), Interactions of C, N, P and S Biogeochemical Cycles and Global Change. Springer-Verlag, Berlin Heidelberg, pp. 401–445.

Van Der Weijden, C., Wolf, K., Chilingarian, G., 1992. Chapter 2 Early diagenesis and Marine Pore Water. In: Developments in Sedimentology. Vol. 47. Elsevier, pp. 13–134.

Van der Weijden, C. H., 2002. Pitfalls of normalization of marine geochemical data using a common divisor. Marine Geology 184 (3-4), 167–187.

Van Rensbergen, P., Depreiter, D., Pannemans, B., Henriet, J. P., 2005a. Seafloor expression of sediment extrusion and intrusion at the El Arraiche mud volcano field, Gulf of Cadiz. Journal of Geophysical Research-Earth Surface 110 (F2), F02010.

Van Rensbergen, P., Depreiter, D., Pannemans, B., Moerkerke, G., Van Rooij, D., Marsset, B., Akhmanov, G., Blinova, V., Ivanov, M., Rachidi, M., Magalhaes, V., Pinheiro, L., Cunha, M., Henriet, J. P., 2005b. The El arraiche mud volcano field at the Moroccan Atlantic slope, Gulf of Cadiz. Marine Geology 219 (1), 1–17.

Van Rensbergen, P., Morley, C. K., Ang, D. W., Hoan, T. Q., Lam, N. T., 1999. Structural evolution of shale diapirs from reactive rise to mud volcanism: 3D seismic data from the Baram delta, offshore Brunei Darussalam. Journal of the Geological Society 156, 633–650.

Vanreusel, A., Andersen, A. C., Boetius, A., Connelly, D., Cunha, M. R., Decker, C., Hilario, A., Kormas, K. A., Maignien, L., Olu, K., Pachiadaki, M., Ritt, B., Rodrigues, C., Sarrazin, J., Tyler, P., Van Gaever, S., Vanneste, H., 2009. Biodiversity of Cold Seep Ecosystems Along the European Margins. Oceanography 22 (1), 110–127.

Vigier, N., Decarreau, A., Millot, R., Carignan, J., Petit, S., France-Lanord, C., 2008. Quantifying Li isotope fractionation during smectite formation and implications for the Li cycle. Geochimica et Cosmochimica Acta 72 (3), 780–792.

Voelker, A. H. L., Lebreiro, S. M., Schonfeld, J., Cacho, I., Erlenkeuser, H., Abrantes, F., 2006. Mediterranean outflow strengthening during northern hemisphere coolings: A salt source for the glacial Atlantic? Earth and Planetary Science Letters 245 (1-2), 39–55.

Von Breymann, M. T., Brumsack, H. J., Emeis, K.-C., 1992a. Deposition and diagenetic behavior of barium in the Japan Sea. Proceedings of the Ocean Drilling Program Scientific Results 127/128, 651–665.

Von Breymann, M. T., Emeis, K.-C., Suess, E., 1992b. Water depth and diagenetic constraints on the use of barium as a palaeoproductivity indicator. In: Summerhayes, C., Prell, W., Emeis, K. (Eds.), Upwelling Systems: evolution Since the Early Miocene. Vol. 64. Geological Society, London, Special Publications, pp. 273–284.

von Huene, R., Lee, H., 1983. The possible significance of pore fluid pressures in subduction zones. AAPG Memoires 34, 781–791.

Wallmann, K., Aloisi, G., Haeckel, M., Obzhirov, A., Pavlova, G., Tishchenko, P., 2006a. Kinetics of organic matter degradation, microbial methane generation, and gas hydrate formation in anoxic marine sediments. Geochimica et Cosmochimica Acta 70 (15), 3905–3927.

Wallmann, K., Drews, M., Aloisi, G., Bohrmann, G., 2006b. Methane discharge into the Black Sea and the global ocean via fluid flow through submarine mud volcanoes. Earth and Planetary Science Letters 248 (1-2), 545–560.

Wallmann, K., Linke, P., Suess, E., Bohrmann, G., Sahling, H., Schluter, M., Dahlmann, A., Lammers, S., Greinert, J., von Mirbach, N., 1997. Quantifying fluid flow, solute mixing, and biogeochemical turnover at cold vents of the eastern Aleutian subduction zone. Geochimica et Cosmochimica Acta 61 (24), 5209–5219.

Weaver, P. P. E., Boetius, A., Danovaro, R., Freiwald, A., Gunn, V., Heussner, S., Morato, T., Schewe, I., van den Hove, S., 2009. The Future of Integrated Deep-Sea Research in Europe The HERMIONE Project. Oceanography 22 (1), 178–191.

Weaver, P. P. E., Masson, D., 2007. RRS"James Cook" Cruise 10, 13 May-07 June 2007. Hotspot ecosystems in the NE Atlantic, UK contribution to the HERMES project: Mud volcanoes in the Gulf of Cadiz; submarine canyons west of Portugal; submarine canyons in the northern Bay of Biscay. Cruise report No. 22.

Werne, J. P., Haese, R. R., Zitter, T., Aloisi, G., Bouloubassi, I., Heijs, S., Fiala-Médioni, A., Pancost, R. D., Sinninghe Damsté, J. S., de Lange, G., Forney, L. J., Gottschal, J. C., Foucher, J.-P., Mascle, J., Woodside, J., 2004. Life at cold seeps: a synthesis of biogeochemical and ecological data from Kazan mud volcano, eastern Mediterranean Sea. Chemical Geology 205 (3-4), 367–390.

Whiticar, M. J., 1994. Correlation of Natural Gases with their Sources. In: Magoon, L., Dow, W. (Eds.), The petroleum system - from source to trap. Vol. 60 of AAPG Memoir. Tulsa, OK: American Association of Petroleum, pp. 261–283.

Whiticar, M. J., 1999. Carbon and hydrogen isotope systematics of bacterial formation and oxidation of methane. Chemical Geology 161, 291–314.

Whiticar, M. J., Faber, E., Schoell, M., 1986. Biogenic Methane Formation in Marine and Fresh-Water Environments - CO_2 Reduction Vs Acetate Fermentation Isotope Evidence. Geochimica Et Cosmochimica Acta 50 (5), 693–709.

Wienberg, C., Frank, N., Mertens, K. N., Stuut, J.-B., Marchant, M., Fietzke, J., Mienis, F., Hebbeln, D., 2010. Glacial cold-water coral growth in the Gulf of Cádiz: Implications of increased palaeo-productivity. Earth and Planetary Science Letters In Press, Corrected Proof.

Woltemate, I., Whiticar, M. J., Schoell, M., 1984. Carbon and Hydrogen Isotopic Composition of Bacterial Methane in a Shallow Fresh-Water Lake. Limnology and Oceanography 29 (5), 985–992.

Woodside, J., Ivanov, M., Limonov, A., 1997. Neotectonics and fluid flow through seafloor sediments in the Eastern Mediterranean and Black Sea, part II: Black Sea.

Yassir, 2003. The role of shear stress in mobilizing deep-seated mud volcanoes: geological and geomechanical evidence from Trinidad and Taiwan. In: Van Rensbergen, P., Hillis, R., Maltman, A. J., Morley, C. K. (Eds.), Subsurface Sediment Mobilization. Vol. 216. The Geological Society, London, Special Publications, pp. 461–474.

You, C. F., Castillo, P., Gieskes, J., Chan, L. H., Spivack, A., 1996a. Trace element behavior in hydrothermal experiments: Implications for fluid processes at shallow depths in subduction zones. Earth and Planetary Science Letters 140, 41–52.

You, C. F., Chan, L. H., Spivack, A. J., Gieskes, J. M., 1995a. Lithium, Boron, and Their Isotopes in Sediments and Pore Waters of Ocean Drilling Program Site-808, Nankai Trough - Implications for Fluid Expulsion in Accretionary Prisms. Geology 23 (1), 37–40.

You, C. F., Gieskes, J., Chen, R., Spivack, A., Gamo, T., 1993a. Iodide, bromide, maganese, boron, and dissolved organic carbon in interstitial waters of organic carbon-rich marine sediments: observations in the Nankai accretionary prism.

You, C.-F., Gieskes, J. M., Lee, T., Yui, T.-F., Chen, H.-W., 2004. Geochemistry of mud volcano fluids in the Taiwan accretionary prism. Applied Geochemistry 19 (5), 695–707.

You, C. F., Spivack, A., Gieseke, A., Rosenbauer, R., 1995b. Experimental study of boron geochemistry: Implications for fluid processes in subduction zones. Geochimica et Cosmochimica Acta 59 (12), 2435–2442.

You, C. F., Spivack, A. J., Gieskes, J. M., Martin, J. B., Davisson, M. L., 1996b. Boron contents and isotopic compositions in pore waters: A new approach to determine temperature induced artifacts - Geochemical implications. Marine Geology 129 (3-4), 351–361.

You, C. F., Spivack, A. J., Smith, J. H., Gieskes, J. M., 1993b. Mobilization of Boron in Convergent Margins - Implications for the Boron Geochemical Cycle. Geology 21 (3), 207–210.

Zenk, W., Armi, L., 1990. The Complex Spreading Pattern of Mediterranean Water Off the Portuguese Continental-Slope. Deep-Sea Research Part A - Oceanographic Research Papers 37 (12), 1805–1823.

Zitellini, N., Gràcia, E., Matias, L., Terrinha, P., Abreu, M. A., DeAlteriis, G., Henriet, J. P., Dañobeitia, J. J., Masson, D. G., Mulder, T., Ramella, R., Somoza, L., Diez, S., 2009. The quest for the Africa-Eurasia plate boundary west of the Strait of Gibraltar. Earth and Planetary Science Letters 280 (1-4), 13–50.

Zuleger, E., Gieskes, J. M., You, C. F., 1996. Interstitial water chemistry of sediments of the Costa Rica accretionary complex off the Nicoya Peninsula. Geophysical Research Letters 23 (8), 899–902.